STRATEGIES TO DEVELOP MATERIALS FOR LITHIUM STORAGE IN HIGH-PERFORMANCE LITHIUM-SULFUR BATTERIES AND PSEUDOCAPACITORS

A thesis submitted

in partial fulfillment for the degree of

Doctor of Philosophy

by

HARITHA H.

Department of Chemistry

Indian Institute of Space Science and Technology
Thiruvananthapuram-695547

July 2020

To Kukku

Achan & Amma

CERTIFICATE

This is to certify that the thesis entitled **“Strategies to Develop Materials for Lithium Storage in High-Performance Lithium-Sulfur Batteries and Pseudocapacitors”** submitted by **Haritha H.** to the Indian Institute of Space Science and Technology Thiruvananthapuram, in partial fulfilment for the award of the degree of **Doctor of Philosophy** is a *bona fide* record of research work carried out by her under my supervision. The contents of this thesis, in full or in parts, have not been submitted to any other Institution or University for the award of any degree or diploma.

Dr. J. Mary Gladis
Supervisor
Associate Professor
Department of Chemistry

Thiruvananthapuram
July 2020

Counter signature of the HOD with seal

DECLARATION

I declare that this thesis entitled **"Strategies to Develop Materials for Lithium Storage in High-Performance Lithium-Sulfur Batteries and Pseudocapacitors"** submitted in partial fulfilment of the degree of **Doctor of Philosophy** is a record of original work carried out by me under the supervision of Dr. J. Mary Gladis, and has not formed the basis for the award of any other degree or diploma, in this or any other Institution or University. In keeping with the ethical practice of reporting scientific information, due acknowledgments have been made wherever the finding of others have been cited.

Haritha H.

SC15D014

Thiruvananthapuram
July 2020

ACKNOWLEDGEMENTS

There are many people to whom I owe a huge debt of gratitude for my academic, intellectual and emotional development during the past few years.

I express my profound gratitude to Dr. J. Mary Gladis for her able guidance and valuable support that enabled me to grow as a researcher. I feel so fortunate to have such a great teacher, who has in-depth knowledge in the subject as my research supervisor. I am particularly indebted to her for offering me the freedom in choosing the research problems to work on, and designing the experiments. She has been there always with her priceless support and care during my peaks and valleys regardless of whether the matter is related to research or personal life.

I thank Dr. K.S. Dasgupta, Former Director, IIST and Dr. V.K. Dhadhwal, Director IIST for providing me opportunity to accomplish my research work in the excellent ambience of IIST with the fine facilities provided. It is my profound privilege to express my extreme sense of gratefulness to Prof. Kuruvilla Joseph, Dean Student activities and Prof. Nirmala Rachael James, Former HOD of Chemistry for their care and support. I express my sincere gratitude to Prof. K. Prabhakaran, HOD Chemistry, for his kind patience and readiness to hear all our problems in lab, finding solutions for the same and providing a healthy working atmosphere. I am immensely obliged to my doctoral committee members, Prof. S. Sampath, Dr. P. Prabhakar Rao, Dr. K.B. Jinesh, and Prof. K. Prabhakaran for their constructive criticism and valuable suggestions at various phases of this research program and for lending me their expertise and intuition to investigate my scientific and technical problems. I render my sincere thanks to all the faculty members of Department of Chemistry for their boundless support during these years.

I owe my special and genuine thanks to my group members Dr. Reshma C., Mrs. Sreekala K., Mr. Parameswaran T. M., Mr. Athul Mohanan and Mrs. Varanya J., without them this research work would not have come to a successful completion. I am

very much thankful to all the staff members of Chemistry Department who have helped me in many ways for the healthy completion of my research works. I am extremely grateful to Dr. A. Manuel Stephan and Ms. Shruti Suriyakumar, CSIR-CECRI, Karaikudi for helping and extending their facility for battery fabrication and analysis, STIC-CUSAT and PSG College of Engineering, Coimbatore for providing TEM analysis, University of Kerala, Thiruvananthapuram and LPSC, Thiruvananthapuram for SEM analysis, NIIST, Thiruvananthapuram for XRD and XPS analyses. I also thank Mrs. Jayasree L from Department of Chemistry for help and support for performing characterizations of my samples

Remembering all my friends (obviously, the list is too big) at IIST who made the campus life livelier and memorable. Thanks to all my friends and lab-mates for their encouragement and support throughout the PhD life.

Nobody has been more important to me in the pursuit of this endeavour, than the members of my family; my mother, father and grandparents, whose prayers and encouragement were what sustained me this far. They are the ultimate pillars of my strength and the prime source of support in my life. I also thank for the heart-warming kindness, care and patience from my mother-in law and father-in law for all of the sacrifices that they have made on my behalf during this long ride. And most of all, special thanks to my husband Rahul for his care, encouragement, faithful support and patience all through the different stages of this research work. Finally, I would like to thank God Almighty for giving me the strength, knowledge, ability and opportunity to undertake this research study and to persevere and complete it satisfactorily. Without his blessings, this achievement would not have been possible.

(Haritha H.)

ABSTRACT

With the rising demand for the hybrid electric vehicles and portable electronic devices, clean and sustainable alternative energy solutions have become indispensable to avoid environment pollution and to mitigate the energy crisis. State-of-the-art electrochemical energy storage systems, such as batteries and supercapacitors, are receiving more attention since they can efficiently store energy and synchronously work as power sources. Lithium-sulfur batteries (LSBs) and lithium-ion capacitors (LICs) are considered as the most viable options due to their high energy and power densities compared to conventional energy storage devices such as lithium-ion batteries and capacitors. This thesis work aims to address the challenges in the LSBs and LICs by the rational selection and development of materials, followed by their electrochemical evaluation. The detailed investigation on the developed materials for LSB and LIC were carried out and the description of the obtained results were presented in six chapters (chapter 2-7).

First chapter provides a general introduction on LSBs and LICs including its principle, limitations and state-of-the-art literature survey. More emphasis is given to aspects which are currently focused on the thesis.

In the second chapter, a highly permselective lithiated poly(2-acrylamido-2-methyl-1-propanesulfonic acid) (LPAMPS) modified Celgard (CG) separator has been developed to improve capacity and cycling stability of LSB. The negatively charged –SO_3^- groups present on the LPAMPS impart selective diffusion of lithium ions, at the same time repelling polysulfide anions via coulombic interactions. Besides, the LPAMPS@CG separator possesses excellent electrolyte wettability, interfacial contact and ionic conductivity. The Li-S cell (areal sulfur loading 0.9 mg cm^{-2}) containing LPAMPS@CG separator exhibited significant improvement in the electrochemical performance, with a high initial capacity of 1486 mAh g^{-1} and coulombic efficiency of ~99%. It is noted that the LPAMPS@CG separator impedes shuttle effect by inhibiting PS crossover towards lithium anode, resulting a stable discharge capacity of 1060 mAh g^{-1} even after 200 cycles. Further, galvanostatic charge-discharge studies were carried out for Li-S cells with higher sulfur loadings of 2.5 and 4.2 mg cm^{-2} (This work was published in *Electrochimica Acta*, 2019).

Poly(3,4-ethylenedioxythiophene):poly(styrene sulfonate) (PEDOT:PSS) is one of the most investigated and extensively used conducting polymer with wide applications. In the third chapter, we propose a novel approach of decorating commercial separator by bifunctional lithiated PEDOT:PSS (Li^+- PEDOT:PSS@CG). Owing to strong chemical interactions of PEDOT with insoluble polysulfides and the electrostatic repulsion between the negatively charged –SO_3^- groups present in PSS and polysulfide anions, the Li-S cell (areal sulfur loading 3.9 mg cm^{-2}) with Li^+-PEDOT:PSS@CG separator demonstrated a high initial discharge capacity of 1360 mAh g^{-1} and coulombic efficiency of ~99%. It is notable that the Li^+-PEDOT:PSS@CG

separator possesses excellent electrolyte wettability, interfacial properties and ionic conductivity, resulting in a stable discharge capacity of 1047 mAh g^{-1} even after 300 cycles at 0.1 C with 77% capacity retention.

In the fourth chapter, we propose a carboxyl functional lithiated polymer, lithiated poly(acrylic acid-co-maleic acid) (LPAM) coated onto Celgard separator (LPAM@CG)for LSBs. The LPAM@CG separator effectively inhibit the shuttle effect of polysulfides, also promote the diffusion of lithium ions. Particularly, the $–COO^{-}$ groups present in the LPAM allow the rapid transfer of positively charged lithium ions while preventing the diffusion of negatively charged PS anions through coulombic interactions. Besides, the LPAM@CG membrane possesses good interfacial properties, ionic conductivity, excellent electrolyte wettability and remarkable electrolyte uptake. The Li-S cell (areal sulfur loading 4.1 mg cm^{-2}) with LPAM@CG separator exhibit significant improvement in the electrochemical performances, with a high initial discharge capacity of 1213 mAh g^{-1}, an excellent rate capability of 637 mAh g^{-1} at 3 C, and a good capacity retention of 957 mAh g^{-1} (~79% over 300 cycles).

Micro and nanocrystalline $LiCoVO_4$ were synthesized via conventional solid-state reaction and hydrothermal reaction followed by calcination, respectively. In particular, nanocrystalline $LiCoVO_4$ demonstrated better lithium-ion intercalation properties benefited from its small crystallite size with highly exposed lithium-ion selective crystallographic pathways towards electrolyte. The nanocrystalline $LiCoVO_4$ electrode demonstrated high specific capacitance (929.58 F g-^{1} at 1 A g^{-1}) and excellent cycling stability in aqueous electrolyte. On the grounds, we fabricated an asymmetric LIC (nanocrystalline $LiCoVO_4$//MWCNT) using aqueous and non-aqueous electrolyte. The LIC cell in non-aqueous electrolyte displays a specific capacitance of 67 F g^{-1} at a current density of 1 A g^{-1}, and good reversibility with a capacitance retention of ~93% after 10000 cycles. The energy performance of the hybrid LIC cell reported here reaches 315.7 Wh kg^{-1} (at a power density of 399.6 W kg^{-1}) (A part of this work was published in *ACS Applied Energy Materials*, 2018).

The nanocrystalline $LiNiVO_4$ was prepared via a hydrothermal route followed by calcination and used as a high-performance pseudocapacitive material for lithium storage in aqueous electrolyte. The electrochemical evaluation of $LiNiVO_4$ electrode in aqueous electrolyte demonstrated good capacitive performance with a specific capacitance of 406 F g^{-1} at 1 A g^{-1}. The cycle stability test reveals exceptional capacitance retention of ~99% even after 1000 cycles owing to the unique structural feature which permit intercalation mechanism. Further, asymmetric LIC cell has been assembled with $LiNiVO_4$ as negative electrode and MWCNT as positive electrode in non-aqueous electrolyte. The assembled hybrid cells exhibited a high energy density of 255 Wh kg^{-1} with maximum power density of 22325 W kg^{-1} and excellent capacitance retention of ~92% after 10000 cycles at 5 A g^{-1} (A part of this work was published in *Journal of Solid State Electrochemistry,* 2018).

In the seventh chapter, nanoscale $LiMnVO_4$ was synthesized by a facile hydrothermal approach and subsequent calcination. The intercalation pseudocapacitive lithium storage behaviour of the $LiMnVO_4$ electrode material was investigated in aqueous electrolyte, which demonstrated a high specific capacitance of 961 F g^{-1} at a current density of 1 A g^{-1} with a capacitance retention of ~99% after 1000 cycles. Further, an asymmetric LIC device has been fabricated with $LiMnVO_4$ as negative electrode and MWCNT as positive electrode in non-aqueous electrolyte. The device delivers a specific capacitance of 81 F g^{-1} (with a wide voltage window of 3 V), and good rate performance of 47 F g^{-1} at 30 A g^{-1}. Further, they show an energy density of 368 Wh kg^{-1} and a maximum power density of 24781 W kg^{-1} in association with superior cycling stability (~97% capacitance retention after 10000 cycles at 5 A g^{-1}).

Finally, the conclusion part of this thesis presents an understanding of, how the logical selection of materials can meet the present energy and power demands and conquer the technical challenges associated with the LSBs and LICs.

TABLE OF CONTENTS

LIST OF FIGURES

LIST OF TABLES

ABBREVIATIONS

3D	Three dimensional
AB	Acetylene black
AC	Activated carbon
AMC	Amorphous carbon
BP	Black phosphorous
BTC	Benzene-1,3,5-tricarboxylate
CG	Commercially available Celgard® 2325 separator
CNF	Carbon nanofiber
CNT	Carbon nanotube
CTF	Covalent triazine-bazed frameworks
CV	Cyclic voltammetry
DGA	Defective graphene aerogel
DME	1,2-Dimethoxyethane
DOE	Department of Energy
DOL	1,3-Dioxolane
EC	Electrochemical capacitors
EDLC	Electric double-layer capacitor
EDS	Energy dispersive spectroscopy
EIS	Electrochemical impedance spectroscopy
ESR	Equivalent series resistance
EV	Electric vehicles
FE-SEM	Field emission scanning electron microscope
FHI	Fuji Heavy Industries
FR-IR	Fourier transform infrared
GDY	Graphdiyne
GF	Glass fiber

GO	Graphene oxide
HEV	Hybrid electric vehicles
H-LCVO	Microsized lithium cobalt vanadate
KB	Ketjan black
LED	Light-emitting diode
Li^+-PEDOT:PSS	Lithiated poly(3,4-ethylenedioxythiophene): poly(styrene sulfonate)
Li^+-PEDOT:PSS@CG	Li^+- PEDOT:PSS coated CG
LIC	Lithium-ion capacitor
Li-S	Lithium-sulfur
LiTFSI	Lithium bis(trifluoromethanesulfonyl)imide
LPAM	Lithiated poly(acrylic acid-co-maleic acid)
LPAM@CG	LPAM coated CG
LPAMPS	Lithiated poly(2-acrylamido-2-methyl-1-propane sulfonic acid)
LPAMPS@CG	LPAMPS coated CG
LSB	Lithium-sulfur battery
mAh g^{-1}	Milliampere hour per gram
MCP	Microporous carbon paper
mg cm^{-2}	Milligram per square centimeter
MMT	Montmorillonite
MOF	Metal-organic frameworks
MPC	Mesoporous carbon
mV	Millivolt
MWCNT	Multi-walled carbon nanotube
NEC	Nippon Electric Company
NMP	N-methyl pyrrolidone
OCV	Open circuit voltage
PAA	Polyacrylic acid
PAH	Poly(allylamine hydrochloride)

PAM	Poly(acrylic acid-co-maleic acid)
PAMPS	Poly(2-acrylamido-2-methyl-1-propanesulfonic acid)
PAN	Polyacrylonitrile
PANi	Polyaniline
PC	Porous carbon
PCNW	Porous carbon nanowires
PDA	Polydopamine
PEDOT:PSS	Poly(3,4-ethylenedioxythiophene):poly(styrene sulfonate)
PEG	Polyethylene glycol
PGC	Porous graphitic carbon
PHCS	Porous hollow carbon sphere
PP	Polypropylene
Ppy	Polypyrrole
PS	Polysulfide
PTFE	Polytetrafluoroethylene
PVDF	Polyvinylidene fluoride
RAPOP	Rich amine porous organic polymer
rGO	Reduced graphene oxide
SAED	Selected area diffraction pattern
S-LCVO	Nanosized lithium cobalt vanadate
SP	Super P
SPEEK	Sulfonated poly(ether ether ketone)
SS	Stainless steel
SSEBS	Sulfonated poly(styrene-ethylene-butylenestyrene)
SWCNT	Single-walled carbon nanotube
TEM	Transmission electron microscopy
TGA	Thermogravimetric analysis
TMO	Transition metal oxide
UPD	Under potential deposition

UPS	Uninterruptible power supply
XPS	X-ray photoelectron spectroscopy
XRD	X-ray diffraction

SYMBOLS AND UNITS

Symbol	**Name**	**Unit**
%	Percentage	
C	Specific capacitance	$F\ g^{-1}$
Cp	Pseudocapacitive element	F
CPE	Constant phase element	$\Omega^{-1}\ s^{n}$
C-rate	Charge/discharge rate	$mAh\ g^{-1}$
D	Diffusion coefficient	$cm^{2}\ s^{-1}$
E	Energy density	$Wh\ kg^{-1}$
ε_0	Permittivity of vacuum	$F\ m^{-1}$
ε_r	Permittivity of electrolyte solution	$F\ m^{-1}$
i	Cathodic peak current	A
I	Current	A
I_p	Peak current	mA
m	Mass of active material in the electrode	g
P	Power density	$W\ kg^{-1}$
Q	Specific capacity	$mAh\ g^{-1}$
R_{ct}	Charge-transfer resistance	Ω
R_e	Bulk/solution resistance	Ω
R_i	Interfacial resistance	Ω
R_{int}	Interface contact resistance	Ω
T	Temperature	°C/K
t	Transference number	
v	Scan rate	$mV\ s^{-1}$
V	Voltage/Potential	V
W_0	Warburg diffusion element	$\Omega^{-1}\ s^{5}$
Z'	Real part of impedance	Ω
Z"	Imaginary part of impedance	Ω

Symbol	**Name**	**Unit**
ΔE	Voltage hysteresis	mV
θ	Angle of diffraction	°/degree
	Current density	A g^{-1}
	Time	s/h
	Wavenumber	cm^{-1}
	Ionic conductivity	Ω^{-1} cm^{-1}

NOMENCLATURE

Ag/AgCl	Silver/Silver chloride
Al_2O_3	Aluminium oxide
$BaTiO_3$	Barium titanate
BN	Boron nitride
C_3N_4	Carbon nitride
CH_3COOLi	Lithium acetate
-CN	Cyano group
$Co(NO_3)_2$	Cobalt nitrate
Co_2B	Cobalt boride
$CoFe_2O_4$	Cobalt ferrite
-COOH	Carboxylic acid group
$-COO^-$	Carboxylate ion
CoS	Cobalt sulfide
Cr_2O_3	Chromium(III) oxide
CuS	Copper(II) sulfide
Fe_3O_4	Iron(II, III) oxide (Magnetite)
In_2O_3	Indium(III) oxide
KBr	Potassium bromide
$LaLiO_2$	Lanthanum lithium oxide
Li	Lithium
Li^+	Lithium ion
Li_2S	Lithium sulfide
$Li_4Ti_5O_{12}$	Lithium titanate
$LiCoO_2$	Lithium cobalt oxide
$LiCoVO_4$	Lithium cobalt vanadate
$LiFePO_4$	Lithium iron phosphate
$LiMnO_2$	Lithium manganese dioxide

$LiMnVO_4$	Lithium manganese vanadate
$LiNiO_2$	Lithium nickel oxide
$LiNiVO_4$	Lithium nickel vanadate
$LiNO_3$	Lithium nitrate
LiOH	Lithium hydroxide
$LiPF_6$	Lithium hexafluorophosphate
MgO	Magnesium oxide
$Mn(CH_3CO_2)_2$	Manganese acetate
MnO	Manganese(II) oxide
MnO_2	Manganese(IV) oxide
MoO_3	Molybdenum trioxide
MoS_2	Molybdenum disulfide
Nb_2O_5	Niobium pentoxide
NbN	Niobium nitride
$-NH_2$	Amino group
NH_4VO_3	Ammonium metavanadate
$Ni(NO_3)_2$	Nickel nitrate
NiOOH	Nickel oxyhydroxide
-OH	Hydroxyl group
RuO_2	Rutheniun oxide
S	Sulfur
S_8	Octasulfur
SiO_2	Silicon dioxide
S_n^{2-}	Polysulfide anion
SnO_2	Tin(IV) oxide
SnS_2	Tin(IV) sulfide
$-SO_3H$	Sulfonic acid group
$-SO_3^-$	Sulfonate ion
Ta_2O_5	Tantalum pentoxide
TiO	Titanium(II) oxide

TiO_2	Titanium(IV) oxide
V_2O_5	Vanadium pentoxide
VN	Vanadium nitride
$VO(C_5H_7O_2)_2$	Vanadyl acetylacetonate
WS_2	Tungsten disulfide
ZnO	Zinc oxide

CHAPTER 1

INTRODUCTION

Increasing demand of portable electronic devices and hybrid electric vehicles trigger the development of next-generation energy storage devices, in terms of energy, power, cycle life, safety, cost, and environmental compatibility. Therefore, it is indispensable to develop materials that can meet the present and future energy needs. Lithium-sulfur batteries (LSBs) and lithium-ion capacitors (LICs) are considered as the most viable options due to their high energy and power densities compared to conventional energy storage devices such as lithium-ion batteries (LIBs) and capacitors. This chapter comprises of the basics and challenges of electrochemical energy storage, particularly LSB and LIC, and a brief state-of-the-art literature survey on various strategies adopted to improve their electrochemical performances. Finally, the chapter briefs about the motivation of our research work, research problem, objectives and the expected outcomes of the proposed work. In addition, the outline of the thesis and a brief introduction of each chapter are provided at the end of the chapter.

1.1. Introduction

Energy may one of the critical factors that will govern the shape of society in the 21st century. With the rapid depletion of fossil fuels and increased environmental pollution resulted from the excessive human reliance on fossil fuels, there arise an unprecedented urgency to figure out alternate energy sources that can substitute fossil fuels to enable the sustainable development of our economy and society (Burke et al., 2018; Goodenough et al., 2014; Lopes et al., 2012). Energy storage can be considered as an intermediary stage to the clean, versatile and efficient use of energy which has acquired global concern and increasing research interest. In a conventional energy storage process, one form of energy is converted into another form that can be stored and drawn upon at a later time when needed (Sterner et al., 2019; Dehghani-Sanij et al., 2019). Therefore, various energy storage systems are being developed aiming at proper utilization of different energy sources.

Driven by the increasing demand for powering systems of portable electronic devices and hybrid electric vehicles (HEVs), electrochemical energy storage devices, including batteries and supercapacitors play a pivotal role (Li et al., 2019a). On the other hand, transforming natural energy from sustainable and renewable resources such as the sun and wind significantly relies on climate/geographical conditions and is not even and continuous (Gielen et al.,2019). Therefore, corresponding high-performance energy storage systems are imperative to store the energy generated. Among the various alternate energy storage technologies, electrochemical energy storage is promising to serve present energy demand, in terms of high efficiency, versatility, and flexibility (Hou et al., 2019). Electrochemical energy storage/release is realized by electron and ion charge/discharge. Batteries and supercapacitors are two major technologies of electrochemical energy storage, both of which store chemical energy and convert it into electrical energy through electrochemical processes (Zuo et al., 2017).

The smallest unit of an electrochemical energy storage device is the electrochemical cell, consisting of two electrodes (an anode and a cathode), which is separated by a porous membrane with both ionic conducting and electrical insulating properties (a separator) and an electrolyte for ion migration. During charging, an accumulation of positive ions occurs at cathode/electrolyte interface. This drives the electrons to move towards the cathode, creating a potential difference between the cathode and the anode. During discharge, electrons are released by passing current from the cathode through an external circuit and back to the anode. While charging, the current flows in the opposite direction (Winter and Brodd, 2004). There are several parameters that need to be discussed for monitoring the electrochemical performance and operating conditions of an electrochemical cell (Dell and Rand, 2001).

Specific capacity (Q). The total amount of current available when the cell is fully discharged or total ampere-hours available when the cell is discharged at a certain discharge current normalized by the mass of active material, in mAh g^{-1}. The theoretical specific capacity of a cell can be calculated by Faraday’s law:

$$Q_{theoretical} = \frac{n \times F}{3600 \times M_w} \text{ mAh g}^{-1} \tag{1.1}$$

where n is the number of charge carrier, F is the Faraday constant (F = 96,485 A.s mol^{-1}) and M_w is the molecular weight of the active material used in the electrode (g mol^{-1}).

In reality, the practical specific capacity of an operating cell can be different from the theoretical one. The practical specific capacity can be calculated by the voltage-time curve from the galvanostatic cycling test.

$$Q_{practical} = \frac{i \times A \times t_{cut-off}}{3600 \times M_w} \text{ mAh g}^{-1} \tag{1.2}$$

where i is the current density (A m^{-2}), A is the area (m^2), $t_{cut\text{-}off}$ is the time required to reach the cut-off voltage ($V_{cut\text{-}off}$) in seconds and M_w is the molecular weight of the active material used in the electrode (g mol^{-1}).

Cut-off voltage ($V_{cut\text{-}off}$). The selected voltage at which charge or discharge is terminated.

C-rate. The discharge rate or charge rate, in amperes. It is a measure of the rate at which a cell is discharged relative to its maximum capacity.

Energy density. The amount of energy stored in the material per unit mass/volume (Wh kg^{-1} or Wh L^{-1}) or the total Watt-hours available when the cell is discharged at a certain discharge current, normalized by the mass of active material or by the volume.

Power density. The amount of energy flow per unit mass/volume per unit time (W kg^{-1} or W L^{-1}). Power density describes how quickly the device can deliver energy.

Coulombic efficiency. The ratio, usually expressed as a percentage, of the ampere-hours removed from a battery during a discharge to the ampere-hours required to restore the initial capacity. It indicates electrochemical reversibility.

1.2. First Great Leap Forward: Lithium-Ion Battery

New technologies often demand more compact, higher capacity, safe, rechargeable batteries. Lithium-ion batteries (LIBs) emerged as a promising candidate and governs the battery market for portable electronics since their launch (Kharbachi et al., 2020). Furthermore, it is believed to be a pertinent option for zero-emissions vehicles and grid energy storage due to their higher energy density compared with other rechargeable battery systems (Figure 1.1).

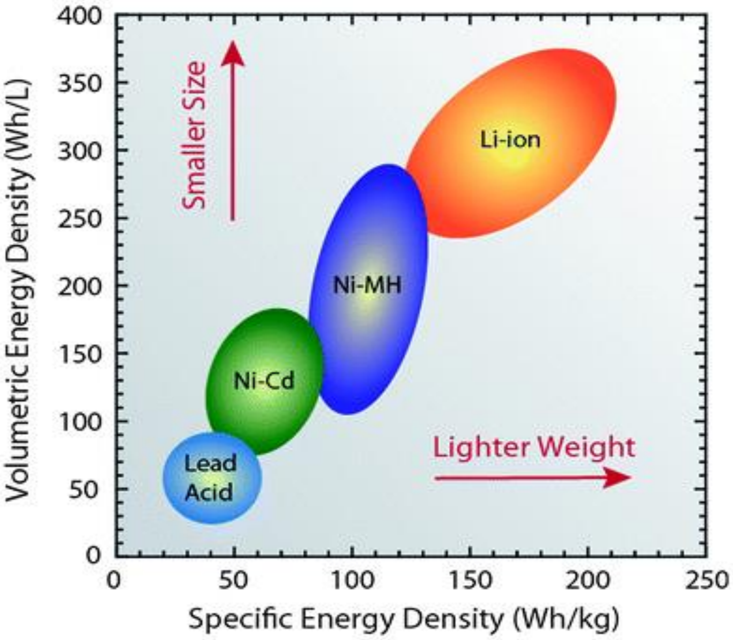

Figure 1.1. Comparison diagram of rechargeable battery technologies as a function of volumetric and specific energy densities (Landi et al., 2009)

A LIB is an advanced battery technology that uses Li-ions as a key component of its electrochemistry. The electrochemistry of the lithium ion results from its small ionic radius and low molecular weight, both are equally important for diffusion. Besides, Li-ion can be easily reduced ($E°(Li^+/Li) = -3.04\ V\ vs.\ SHE$) (Liu et al., 2016; Deng, 2015). The pioneering scientists Whittingham and Goodenough had been developed LIB cathode materials in 1970. The first commercial LIB was produced by Sony corporation in 1991 and was based on $LiCoO_2$ and petroleum coke (Goodenough and Park, 2013; Kamat, 2019).

A conventional LIB composed of four components: negative carbon (usually graphite) as the anode, solid layered transition metal oxide (e.g., $LiCoO_2$, $LiMnO_2$, $LiFePO_4$ and $LiNiO_2$) as the cathode, fine porous polymer membrane as the separator and lithium-salts (e.g., $LiPF_6$) in organic solvents (e.g., ethylene carbonate) as the electrolyte (lithium-ion conductive medium) (Goodenough and Park, 2013). The LIB works based on the intercalation mechanism. While charging, the lithium ions are deintercalated from the cathode (layered lithium intercalation host, for example, $LiCoO_2$) and intercalated between the graphite layers (anode) through the electrolyte. The discharging step involves the reverse process (Deng, 2015; Gopalakrishnan et al., 2016).

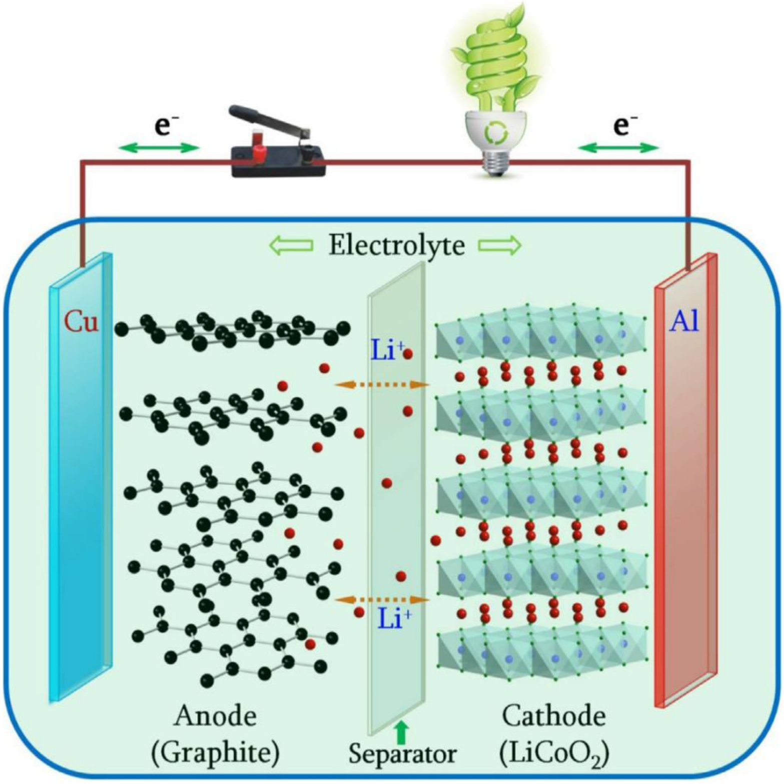

Figure 1.2. Schematic diagram of LIB (Liu et al., 2016)

Over the past two decades, commercial LIBs have continually improved in terms of energy densities, service life, cost and other metrics. Most of the LIB research has focussed on the lithium transition metal oxide-based cathode and a carbon-based anode (He et al., 2012; Roselin et al., 2019). However, LIBs based on Li-ion intercalation materials offer limited capacities and energy densities, specifically gravimetric (Choi et al., 2016). This has led many researchers to believe that massive market adoption of electric vehicles (EVs) will require development of new batteries with higher energy density and lower cost than the current LIBs, the so-called “beyond Li-ion” chemistries (Cano et al., 2018). Theoretically, this can be realised by the conversion-type cathode materials, which give more than three-fold energy density of the intercalation-type cathode materials (Wu et al., 2017a).

1.3. Beyond Li-Ion Batteries: Lithium-Sulfur Battery

In recent years, lithium-sulfur batteries (LSBs) have received considerable interest due to their high theoretical capacity (1675 mAh g^{-1}) and energy density (2600 Wh kg^{-1}). The high abundance of sulfur in conjunction with its non-toxic nature and low cost place LSB research on the top priorities (Kang et al., 2016; Fotouhi et al., 2017; Manthiram et al., 2014). Moreover, the LSB can be operated over a wide range of temperatures, which is crucial for the power demands of battery systems for EVs (Lin et al., 2016). The concept of elemental sulphur as a positive electrode material was first introduced by Helbert and Ulam in 1962 and the first demonstration of LSB was presented in the late 1960s (Manthiram et al., 2014; Singh et al., 2019). The operation of the LSB is based on multiple redox reactions between metallic lithium and elemental sulfur, which can be described by an overall equation:

$$16\ \mathrm{Li} + \mathrm{S_8} + 16\ e^- \rightleftharpoons 8\ \mathrm{Li_2S} \qquad (1.3)$$

The potential lies at an average voltage of 2.15 V with respect to Li^+/Li.

1.4. Fundamental Chemistry of LSB

The LSB, which is composed of lithium metal as anode, sulphur composite as cathode, lithium bis(trifluoromethanesulphonyl)imide (LiTFSI) in ether-based solvents as electrolyte and a porous polypropylene membrane as separator (Figure 1.3).

During discharging process, the Li-ions are stripped from the anode, moves towards the cathode and form lithium sulfide. While charging, the reverse reaction will happen. The reaction between metallic lithium and elemental sulfur is a multistep process. The electrochemical reduction of sulfur occurs through the formation of a series of intermediate lithium polysulfides (PSs) with a general formula Li_2S_n ($8 \geq n \geq 2$) followed by the final reduction product, Li_2S. However, the exact number of stable intermediate PSs during the discharge process has not yet been identified beyond doubt. During discharge, it is assumed that the cyclic octatomic sulfur (S_8) in the solid phase is firstly dissolved in the electrolyte to form solvated S_8, which is then gradually reduced to lithium PS. Intermediate products of higher order lithium PS (Li_2S_n, $4 \leq n \leq 8$) are soluble in the commonly used organic electrolyte, but the lower order lithium sulfides (Li_2S_2 and Li_2S) are insoluble (Akridge et al., 2004; Wild et al., 2015)

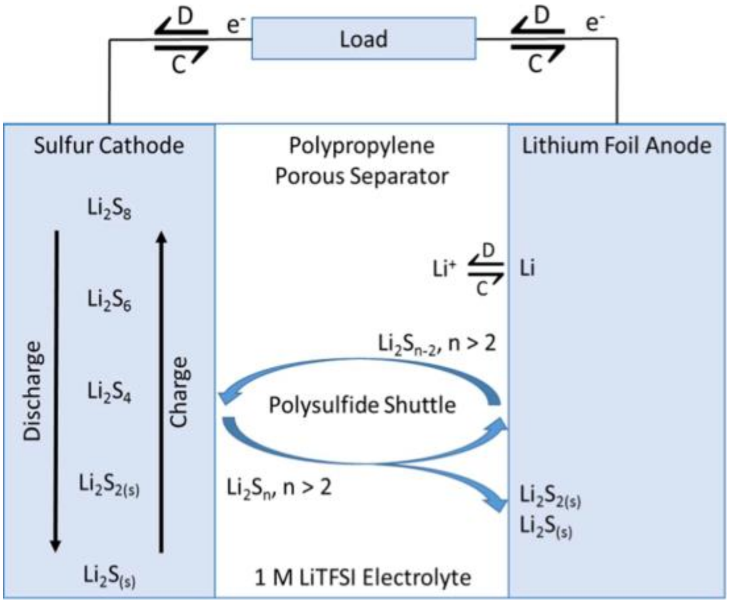

Figure 1.3. Schematic of the electrochemical processes in LSB (Narayan and Moy, 2017)

1.4.1. Voltage Characteristic of LSB

The formation of several chemically distinct species in LSB leads to a complex voltage profile during discharging, which can be divided into four stages, as shown in Figure 1.4 (Barghamadi et al., 2014; Wild et al., 2015).

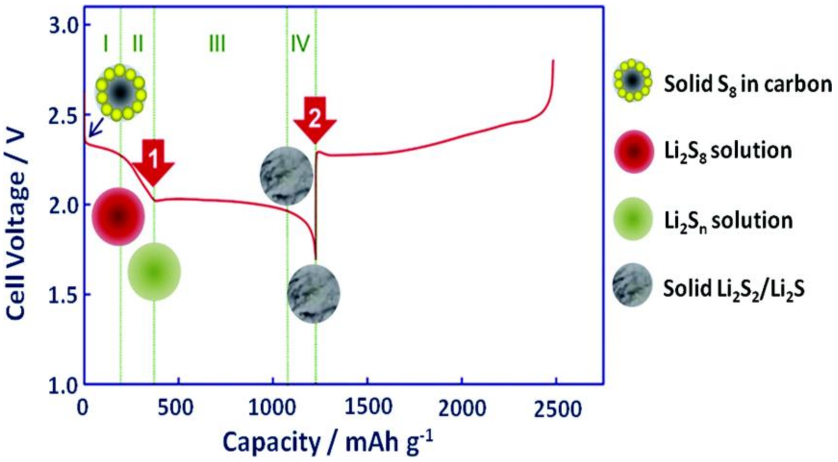

Figure 1.4. Typical discharge-charge voltage profile for a LSB (Barghamadi et al., 2014)

Stage I: Elemental sulfur (S_8) is reduced to higher order PS (Li_2S_8), which is highly soluble in the common organic liquid electrolyte.

$S_8 + 2\ Li^+ \rightarrow Li_2S_8$ (1.4)

Stage II: The dissolved Li_2S_8 is reduced to different order PS (Li_2S_n, $4 \leq n \leq 8$), which are again soluble in the electrolyte. During this stage, the cell voltage linearly decreases.

$Li_2S_8 + 2Li^+ \rightarrow Li_2S_{8-n} + Li_2S_n$ (1.5)

Stage III: The soluble PS are reduced to insoluble lithium sulphides (Li_2S_2 or Li_2S), which accumulates on the cathode surface, forming an insulating passivation layer. This stage corresponds to the second voltage plateau and contributes to the major capacity of the LSB.

$2Li_2S_n + (2n\text{-}4)\ Li^+ \rightarrow n\ Li_2S_2$ (1.6)

$Li_2S_n + (2n\text{-}2)\ Li^+ \rightarrow n\ Li_2S$ (1.7)

Stage IV: The last discharge step involves a solid-to-solid reduction from insoluble Li_2S_2 to insoluble Li_2S. This stage shows a steep voltage drop in the discharge profile.

$Li_2S_2 + 2\ Li^+ \rightarrow 2\ Li_2S$ (1.8)

1.4.2. Polysulfide Shuttle Phenomena

The solubility of PS in the electrolyte is proven to support the electrochemical utilization of insulating sulfur. However, this can root severe redox shuttle between the sulfur cathode and the lithium anode, which leads to low coulombic efficiency and fast self-discharge of LSBs (Shen et al., 2019; Lacey et al., 2016). As previously mentioned, in the early stages of discharging, higher order PS (Li_2S_n, $4 \leq n \leq 8$) are formed, which are highly soluble in the organic electrolyte. The dissolved PS anions (S_n^{2-}) can diffuse through the separator towards lithium anode and undergo chemical reduction with metallic lithium to form lower order PS. The formed lower order PS diffuse back towards the sulfur cathode and get oxidised to regenerate higher order PS (Figure 1.3). This phenomenon, the diffusion back and forth of PS between the two electrodes is termed as the "*polysulfide shuttle*", which is characteristic of LSBs. These parasitic reactions cause severe problems such as poor coulombic efficiency for charging cycle, corrosion of lithium anode and polarization of lithium anode once the formed Li_2S_2/Li_2S deposit on the lithium surface (Mikhaylik and Akridge, 2004).

1.5. Problems and Challenges in LSB

The commercialization of LSB is still impeded due to the following technical challenges (Aurbach et al., 2009; Manthiram et al., 2013; Liu et al., 2018a; Zhao et al., 2019a).

(1) The inherent insulating nature of sulfur (electrical conductivity is 5×10^{-30} S cm^{-1} at 25 °C) often leads to poor utilization of sulfur active material and limited rate capability, which demands intimate contact with conductors (conductive carbon).

(2) The insoluble discharge products (Li_2S_2/Li_2S) deposit on the cathode surface and form a passivation layer on the electrode and reduce the utilization of sulfur active material.

(3) A significant volumetric change of ~79% involve in the conversion process of elemental sulfur to lithium sulfide during cycling (Bini et al., 2015). Due to the continuous dissolution and precipitation of sulfur, the cathode structure can be collapsed or degraded, leading to rapid capacity fading.

(4) PS shuttle between lithium anode and sulfur cathode during cycling (described in section 1.4.2) leads to poor coulombic efficiency and severe self-discharge.

(5) Corrosion of the lithium anode and dendrite morphology after lithium plating, associated to the parasitic reactions with dissolved PS. The reaction of lithium with PS and organic electrolyte form an undesirable passivation layer, which leads to poor cycling efficiency of the lithium electrode, increase in cell resistance and fast capacity fading. Furthermore, the reaction between lithium and PS has been identified as an important factor initializing thermal runaway in LSB at elevated temperatures.

The key challenge associated with LSB is the PS shuttle effect that is responsible for the progressive leakage of sulfur active material from the cathode resulting in low life cycle of the battery. In addition, the shuttle effect can lead to self-discharge and reduce coulombic efficiency, which is not roadworthy for the commercialization of LSBs (Balach et al, 2018). Various strategies are reported in the literature to overcome this detrimental phenomenon occurring in LSB on charge-discharge process.

1.6. Effective Strategies for Suppression of Shuttle Effect in LSBs

The PS shuttle phenomenon occurring in LSB can be summarized into three processes in a loop: the dissolution of PSs, the diffusion of PSs, and side reaction of PSs (Li et al., 2018a; Deng et al., 2019). The shuttle effect can be suppressed by completely blocking one of these three processes. In accordance with the analysis of the statistics available from reported LSB research papers, the potential solutions to supress PS shuttle are divided into four parts (He et al., 2018a):

(1) Design of the cathode architectures
(2) Modification of separators
(3) Anode improvements
(4) Novel electrolyte systems

Broad in scope, the rational design of the cathode composite (i.e., internal modification of the cathode) and the incorporation of interlayers and coatings for the sulfur cathode (i.e., external modification of the cathode) can confine the PSs upon their generation at the cathode by physical adsorption and chemical binding, thereby impede the shuttling of PSs (Dong et al., 2018). The separator having ion selectivity for PSs can be applied to prevent the diffusion of polysulfides towards the lithium anode (He et al., 2018a). The effective passivation of lithium anode surface can restrain the side reactions between PS and lithium, which is favourable to suppress the shuttle effect (Xiong et al., 2019). The solubility of PSs can be reduced by adjusting the electrolyte composition, which can again lower the shuttle of PS (Weller et al., 2019).

The PSs formed at the sulfur cathode undergo dissolution and diffusion processes before reaching the lithium anode for side reactions. Even though the dissolution of PSs can trigger the shuttle effect, it also features some advantages for LSBs (Deng et al., 2019). Compared to the solid phase reaction, the dissolution of PSs can improve the kinetics of the electrochemical reaction (Li et al., 2014a). Therefore, the dissolution of PSs is inevitable in LSB chemistry. During the diffusion process, PSs will drift across the separator towards the lithium metal anode (Berger et al., 2018). Therefore, it is indispensable to quench the diffusion of PSs. The diffusion of PSs can be limited by the modifications of the sulfur cathode and the separator. In brief, a cathode design can generally be realized via two ways: encapsulating sulfur in the conducting scaffolds (e.g. micro/meso-porous carbon, hollow nanostructures, sp^2 carbon of carbon nanotubes (CNTs) and graphene, MXene, conductive polymers) and introducing polysulfide absorbers into the cathode (Wang et al., 2002; Wu et al., 2015; Hu et al., 2016; Zhao et al., 2019b; Díez et al, 2019). However, the cathode framework become unable to trap the PSs within the cathode side upon prolonged cycling, and the introduction of too much inactive material is difficult to achieve the advantage of the high energy density of LSBs. The modification of separator has been proved to efficiently suppress the shuttle effect by physical obstruction or chemical bonding, without influencing the utilization of active materials. Therefore, the functional modification of the separator seems to be more reliable for LSBs with a long cycle life (He et al., 2018a; Xiang et al., 2016). Various materials and approaches have been devoted to modifying commercial separators, and the modified separators with different functions can suppress the shuttle effect in different ways. This thesis focuses on the modification of separator for shuttle effect free long-cycle life LSBs. Hence, the literature review presents a brief overview of the recent advances in the development of the functional separators for LSBs to restrict the PSs in the cathodic region.

1.7. A Brief Review on Functional Separators for LSBs

As an imperative battery component, separator functions as an electrical insulator for preventing internal short circuit and diffusion channels for ion transport (Arora and Zhang, 2004). Porous polymer separators are suitable to meet these requirements in routine LIBs. However, the multi-electron electrochemical reaction takes place in LSB generates PSs. This degrades the battery performance by parasitic reactions of PSs with lithium anode or by irreversible decomposition due to its metastability and forming 'dead' sulfur-containing species (Ma et al., 2015; Kang et al., 2016). In LSB system, separator has to permit the selective passage of lithium ions obstructing the transport of other ions, especially PSs. In effect, separator act as a complete shield between cathode and anode. Thus, separator is a perfect platform for modification that can introduce novel cell configuration for LSBs. Various functionalized barrier coatings have been applied to controllably modify the commercial separators (polyolefin membranes), including carbon materials, polymers, inorganic oxides and their composites (Deng et al., 2016; He et al., 2018b; Rana et al., 2019; Deng et al., 2019).

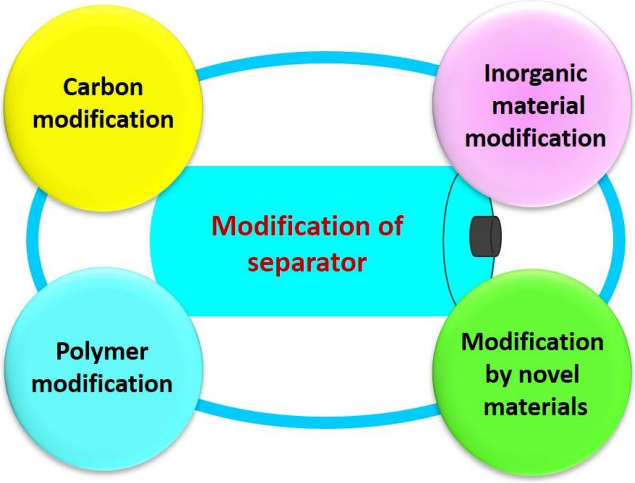

Figure 1.5. Various functional modification of separator for long-cycle life LSB

1.7.1. Carbon Modified Separators

Carbon-based materials have received tremendous interest over the recent years owing to their extraordinary electrical conductivity, large surface area, good thermal stability and chemical stability; therefore, they turn out to be the most widely used material for separators modification (Wen and Li, 2009). Broadly, the carbon coating on the cathodic side of commercial separator (Celgard) has two important roles: (1) acting as a barrier to obstruct the diffusion of PSs from cathode to anode side by physical adsorption/chemical bonding; (2) serving as an upper current collector to provide electrical conduction paths to accelerate the transport of electrons into active material and to facilitate sulfur reutilization. Thus, the carbon coated separator not only suppress the PS shuttling but also contribute to the enhanced utilization of the sulfur active material (Pei et al., 2018; Zhang et al., 2019a). Various types of carbon material suppress the shuttle effect according to their unique physical and/or chemical properties.

Among the carbon-based materials for separator modification, porous carbon (PC) has been extensively explored by several research groups. The main advantage of PC is its small pore structure and large surface area, both favours to capture the migrating PSs (Rana et al., 2019). An early study of PC was reported by Manthiram group in 2012. Their LSB with microporous carbon paper (MCP) interlayer between separator and cathode presented an initial capacity of 990 mAh g^{-1} with a fading rate of 0.28% after 100 cycles at 2C (Su et al., 2012). Later, a highly conductive activated microporous carbon nanofiber (ACNF) coated separator was investigated for LSB, and the cell demonstrate an overall boost in the electrochemical utilization (discharge capacity of 1270 mAh g^{-1}) and polysulfide retention (capacity fade rate of 0.13% per cycle after 200 cycles) (Chung et al., 2015). Since the porous carbon coated separators exhibit good performance, researchers investigated compositing different porous carbon materials to optimise the conductivity and the porosity of the coating layer. A multifunctional separator was prepared by introducing PC/MWCNT onto Celgard separator. The cell with PC/multi-walled carbon nanotube (PC/MWCNT) coated separator exhibited a higher initial discharge capacity of 916 mAh g^{-1} with a 0.14% fading rate after 200 cycles at 0.5C (Tan et al., 2017).

In addition to PC, electrically conductive carbon also plays an important role in improving the initial discharge capacity and long term cyclability of LSBs. The superior electrical conductivity of super P (SP) was considered to coat on a glass fiber (GF) separator. The cell with SP coated separator exhibited an initial discharge capacity of 1200 mAh g^{-1} and a capacity fading rate of 0.19% after 200 cycles at 1C (Zhu et al., 2016a). A simple insertion of acetylene black mesh between cathode and separator resulted in enhanced capacity, cyclability, and rate capability; an initial discharge capacity of 1491 mAh g^{-1} with 71% capacity retention after 50 cycles (Jeong et al., 2013). A routine separator modified by a Ketjen black (KB) layer on the cathode side has been investigated. The cells with the KB coated separator exhibit a high initial discharge capacity of 1318 mAh g^{-1} at 0.1C with a reversible capacity of 815 mAh g^{-1} after 100 cycles at 1C and extraordinary rate capability (capacity of 934 mA h g^{-1} at 2C) (Zhao et al., 2016). A single-walled carbon nanotube (SWCNT)-modified separator was employed to directly suppress the polysulfide migration, owing to the presence of conductive sp^2-carbon scaffold which continuously reactivates and reutilizes the trapped active material. The cell employing SWCNT coated separator exhibits a high discharge capacity of 1132 mAh g^{-1} with a low capacity fade rate of 0.18% per cycle after 300 cycles (Chang et al., 2016). Manthiram group coated ultralight-weight MWCNTs on a conventional separator and the cell displays a high initial discharge capacity of 1324 mAh g^{-1}, excellent rate performance from 0.2C to 1C rates, and superior long-term cycle stability over 300 cycles (Chung et al., 2014).

Graphene has several superior properties, including a high surface area and electrical conductivity, which is exactly why it is designated as the ‘miracle material’ (Novoselov et al., 2012). An effective route for large scale synthesis of graphene is the chemical reduction of graphene oxide, which is referred as reduced graphene oxide (rGO) (Singh et al., 2016). rGO can be synthesized with various negatively charged functional groups making it suitable to suppress PS migration through polar-polar interactions (Rana et al., 2019). A graphene coated separator was reported for LSB with a high sulfur loading of 4 mg cm^{-2}. The cell delivered an initial capacity of 1006 mAh g^{-1} with a fading rate of 0.10% after 300 cycles at a 0.9C rate. The graphene coating serves as a barrier towards the migrating PSs due to its moderate binding with PSs through charge transfer (Zhou et al., 2014). A LSB employing rGO coated separator was reported with an enhanced electrochemical performance, an initial discharge capacity of 1067 mAh g^{-1} at 0.2 C (82% capacity retention after 100 cycles) with a capacity decay rate of 0.18% per cycle (Lin et al., 2015). CNTs have also been composited with rGO to form a separator coating and the cell delivered a discharge capacity of 1030 mAh g^{-1} with a 0.13% fading rate after 200 cycles (Wu et al., 2017b).

Even though pure carbon-based materials are noteworthy, their surface is inherently non-polar which limits the efficiency of PS confinement. By doping or co-doping carbon with elements such as N, O, S, B, Fe and Co (Wang et al., 2014a; Yin et al., 2016; Mi et al., 2017) the non-polar carbon surface can be transformed to polar, thereby attract the PSs through polar-polar interactions. A variety of N-doped carbons have been reported for separator modification, including N-doped mesoporous carbon (MPC) (Balach et al., 2016), N-doped porous hollow carbon sphere (PHCS) (Zhang et al., 2015a) and N-doped porous carbon nanowires (PCNW) (Zhou et al., 2016). The LSB with N-doped MPC separator exhibit an outstanding long lifespan of 1200 cycles with a high reversible capacity of 566 mAh g^{-1} at 0.5C and a degradation rate of only 0.037% per cycle (Balach et al, 2016a). The cells with N-doped PHCS coated separator exhibited an improvement in active material utilization and electrochemical performance, an initial discharge capacity of 1656 mAh g^{-1} (0.2 C) and a low fading rate of 0.11% per cycle within 500 cycles at 1C were achieved (Zhang et al., 2015b). With the N-doped PCNW modified separator, the cell exhibited a high initial discharge capacity of 1430 mAh g^{-1} at 0.2 C and good long-term cycling stability at 0.5 C with 0.08% capacity fading per cycle (Zhou et al., 2016). The B-doped rGO coated separator cell with a high sulfur content of 66% exhibited a long cycle life of 400 cycles at 0.1C rate maintaining a specific capacity of 367 mAh g^{-1} (Han et al., 2017). The LSBs were fabricated with O-doped carbon on the surface of rGO (O-doped C/rGO)-coated separator and exhibited excellent rate performance and good long-term cycling stability with 0.057% capacity decay per cycle at 1.0 C after 600 cycles (Zhang et al., 2018a). N and S co-doped mesoporous carbon (N,S-doped MPC) coating on separator effectively reduced the PS shuttle effect and the cell exhibited a second discharge capacity of 1467 mAh g^{-1} at 1 C with a reversible capacity of 561 mAh g^{-1} at 5 C after 200 cycles (Yuan et al., 2017). Later, Fe-embedded N-doped carbon nanofibers (Fe, N-doped C) was introduced to modify separator and the cell assembled demonstrates a high rate capability and excellent cycling stability, exhibiting a capacity of 848 mAh g^{-1} at 2 C and a low degradation rate of 0.053% per cycle over 500 cycles at 0.5 C (Song et al., 2018a).

Functionalization of carbon with sulfonate ($–SO_3^-$) groups transform the carbon surface suitable for PS trapping. A functional sulfonated acetylene black (SO_3^--AB) coated separator was designed for LSB. Firstly, the permselective $–SO_3^-$ group block the migration of electronegative PSs without affecting the lithium ion conductivity and, second, the $–SO_3^-$ group could anchor PS through the Li bond. This kind of a cell delivers a high initial capacity of 1262 mAh g^{-1} and a superior capacity of 955 mAh g^{-1} was retained after 100 cycles at 0.1C (Zeng et al., 2016). Later, a sulfonated rGO (SO_3^--rGO) interlayer on the separator was adopted by Yang et al. to mitigate the PS shuttle effect. The prototype battery with SO_3^--rGO modified separator exhibited a high reversible discharge capacity of more than 1300 mAh g^{-1} and good capacity retention of 802 mAh g^{-1} after 250 cycles at 0.5 C rate (Lu et al., 2017a).

1.7.2. Polymer Modified Separators

Typically, polymers are used as the binder for cathode materials in LSBs, such as polyvinylidene fluoride (PVDF) and polytetrafluoroethylene (PTFE) (Wang et al., 2014b). Several polymer materials have been recently used as functional coating for Celgard separators. The presence of functional groups on polymeric coatings helps to effectively suppress the shuttle effect by physical separation or chemical bonding. Since, most polymer materials are non-conductive in nature, it cannot act as a secondary current collector to reactivate the trapped active materials (Rana et al., 2019). For this reason, polymer coating materials are often composited with carbonaceous materials to enhance the electronic conductivity.

PVDF is one of the commonly employed cathode binders in LSBs. A novel separator modified with a PVDF-Super P carbon layer was fabricated using a phase inversion process and the resultant LSB cell showed a prolonged cycling capability, with discharge capacities of 918 mAh g^{-1}, 827 mAh g^{-1} and 669 mAh g^{-1} after 100, 200, and 500 cycles, respectively, at 0.5 C (Wei et al., 2014). Later, a rGO-PVDF layer coated separator was reported and the cell exhibited a good initial discharge capacity of 1322 mAh g^{-1} and maintained 646 mAh g^{-1} after 200 cycles with a fading rate of 0.25% at 0.2C (Zhu et al., 2017).

Similarly, polar negatively charged functional groups ($–SO_3^-$ and $–COO^-$) containing polymer coating material is a feasible way to restrain the migration of soluble polysulfides via coulombic repulsion. Besides, the separator modified with negatively charged groups will function as cation-selective membranes providing transport channels for lithium through the coulombic interactions, thereby improving electrochemical performance of LSBs (Park et al., 2015; Deng et al., 2019). Nafion is a sulfonated tetrafluoroethylene based fluoropolymer containing $–SO_3^-$ group. A multifunctional Nafion-based membrane layer was fabricated for an ion selective LSB configuration. The resultant cell exhibited a greatly improved cycling stability with a cyclic decay of 0.08% per cycle within the first 500 cycles. However, the cell deliver a lower initial discharge capacity of 781 mAh g^{-1}, which can be attributed to the insulating nature of Nafion (Huang et al., 2014). The protons present in the Nafion can be exchanged with lithium ions to obtain lithiated Nafion (Li-Nafion) having good lithium ion conductivity. The effect of a Li-Nafion coated separator was investigated for LSB and achieved stable capacities than uncoated separator with an initial discharge capacity of 1100 mAh g^{-1} at low current rate of 0.05C (Bauer et al., 2014). Several groups have coupled Nafion with carbon materials to improve LSB performance. With Nafion/super P-modified separator, a simple elemental sulfur cathode with 70% sulfur content delivered a high initial discharge capacity of 1087 mAh g^{-1} at 0.1 C and a long-term cyclability with only 0.22% capacity fade per cycle over 250 cycles at 0.5 C (Hao et al., 2016). A ternary-layered separator with a macroporous polypropylene (PP) matrix layer, graphene oxide (GO) barrier layer, and Nafion retarding layer (PP/GO/Nafion) was designed as the separator for LSB with high coulombic efficiency and superior cycle stability. The cell with ternary separator produced a discharge capacity of 905 mAh g^{-1} with a fading rate of 0.18% per cycle over 200 cycles (Zhuang et al., 2015). Similar to the Nafion, sulfonated poly(ether ether ketone) (SPEEK) also contain $–SO_3^-$ group. Nafion/SPEEK composite coated separator was designed for LSB and the cell with 6 mg cm^{-2} sulfur loading showed an initial capacity of 1300 mAh g^{-1} and a capacity retention of 650 mAh g^{-1} over 500 cycles (Babu et al., 2018). Poly(3,4-

ethylenedioxythiophene):poly(styrene sulfonate) (PEDOT:PSS) is the another polymer of choice. The $–SO_3^-$ group present in PSS act as an electrostatic shield for soluble PSs through coulombic repulsion, whereas PEDOT provides chemical interactions with insoluble lithium sulfide. The dual PS shielding effect provide excellent battery performance, with an initial discharge capacity of 901 mAh g^{-1} and maintained 596 mAh g^{-1} after 500 cycles with a fading rate of 0.067% at 0.5C (Abbas et al., 2016). A lithium ion conductive block polymer, lithium sulfonated poly(styrene-ethylene-butylenestyrene (Li^+-SSEBS) combined with super P was employed to fabricate a LSB functional separator. The resulted cell displayed a high initial discharge capacity of 1066 mAh g^{-1} with a capacity retention of 72% after 350 cycles at 0.5C and anti-self-discharge capability (Yang et al., 2018a).

There are a wide range of polymers containing other functional groups like –OH, –CN, –COOH, $–NH_2$, etc., that can physically/chemically confine PSs (Hencz et al., 2019). Polyethylene glycol (PEG) is a polyether compound with –OH functional groups. A functional separator was fabricated for LSB employing MWCNT/PEG coating and the cell (S loading: 3.9 mg cm^{-2}) delivered a maximum discharge capacity of 1216 mAh g^{-1} at 0.2C with a low fading rate of 0.17% after 200 cycles (Rana et al., 2019). The commercial Celgard separator modified with poly(allylamine hydrochloride) (PAH) and polyacrylic acid (PAA) was designed for LSB. The PAH and PAA contains amine and hydroxyl groups, respectively. The cell assembled with PAH/PAA-modified separator exhibited a high initial discharge capacity of 1418 mAh g^{-1}, but with very high fading of 1.4% after 50 cycles at 0.05C (Gu et al., 2014). The polypropylene (PP) grafted with PAA (PP-gPAA) separator was designed to physically confine PSs through electrostatic repulsion towards PSs, the resultant cell showed an improved cycling stability with a decay rate of 0.074% per cycle over first 600 cycles at 0.5 C (Song et al., 2018b). The LSB with ultrathin PAA composited with SWCNT (PAA-SWNT) coated separator maintained higher capacity retention over 200 cycles and achieved better retention rate (Kim et al., 2016a). Polydopamine (PDA) provides hydroxyl and amine groups and the cell with the PDA coated separator exhibited a capacity of 752 mAh g^{-1} for the initial cycle, and a high reversible capacity of 603 mAh g^{-1} retained after 100 cycles with 80% capacity retention (Zhang et al., 2015). The separators modified with polypyrrole (PPy) nanotubes were designed for LSBs and the fabricated cells with 2.5-3 mg cm^{-2} sulfur loading displayed an initial discharge capacity of 1110 mAh g^{-1}, and a retained capacity of 801 mAh g^{-1} after 300 cycles at 0.5C (Ma et al., 2016). In-situ vapor-phase polymerization of PPy on Celgard separator was reported for LSB to delivere stable cycling for 250 cycles at 0.5 C with a low capacity decay rate of 0.083% per cycle (Li et al., 2019b). A prototype LSB with carboxyl functional polyamide acid nanofiber separator was developed. The resultant cell displayed a high initial discharge capacity of 1031 mAh g^{-1}, an excellent rate capability of 408 mAh g^{-1} at 5 C, and a good capacity retention of 76% after 200 cycles at 0.2 C (Luo et al., 2018). A polyacrylonitrile/GO (PAN/GO) nanofiber membrane separator was developed for LSB to simultaneously enable an initial discharge capacity of 985 mAh g^{-1} with a fading rate of 0.42% after 100 cycles and excellent anti-self-discharge capability (Zhu et al., 2016b). The LSB with an ultra-lightweight polyaniline nanofiber/MWCNT (PANiNF/MWCNT) coated separator was investigated to deliver an initial discharge capacity of 1020 mAh g^{-1} and a high capacity retention rate of 70% after 100 cycles (Chang et al., 2015). A functional rich amine porous organic polymer/acetylene black-polypropylene (RAPOP/AB-PP) separator was designed. The large number of imine groups present in RAPOP could strongly anchor PSs and the cell with RAPOP/AB-PP separator deliver high capacity of 1322 and 897 mAh g^{-1} after the first and 800th cycle at the current density of 0.2 mA cm^{-2} (Wang et al., 2019a).

1.7.3. Inorganic Materials Modified Separators

The class of inorganic materials including metal oxides, metal chalcogenides, etc. presents a possible barrier coating for PSs. These materials can arrest the PS migration chemically (through strong binding effects on PSs) and/or physically (through the fine porous structure which can trap PSs) (Balach et al., 2018). Additionally, the inorganic materials offer an opportunity to use Lewis acid-base interactions to restrain PSs (Deng et al., 2019).

Oxygen rich inorganic metal oxides or their composites modified separator were reported as an effective strategy to confine PSs because of their ability to chemically adsorb and/or physically obstruct the diffusing PSs (He et al., 2018b). Al_2O_3 is a widely explored functional coating on the separator for LIBs owing to its thermal stability (reduce thermal shrinkage of the separator) and hydrophilicity (improve the electrolyte wettability of the separator). Because of the aforesaid advantages, Al_2O_3 has also been applied as separator coating in LSBs. The LSB with Al_2O_3 coated separator was reported with an initial discharge capacity of 967 mAh g^{-1} but with a high fading rate of 0.77% after 50 cycles at 0.2C (Zhang et al., 2014). A trilayer graphene/PP/Al_2O_3 separator was designed with dual functions. The graphene layer acts as a conductive layer and an electrolyte reservoir, and Al_2O_3 coating enhances the thermal stability and safety. The cell with trilayer coated separator delivered a maximum initial discharge capacity of 1067 mAh g^{-1} and a capacity fading rate of 0.24% after 100 cycles at 0.2C (Song et al., 2016a). A PP separator modified with an Al_2O_3 layer followed by a CNT layer was designed and the resultant LSB produced an initial capacity of 1287 mAh g^{-1} with a retained capacity of 807 mAh g^{-1} after 100 cycles at 0.2C (Xu et al., 2015).

Apart from Al_2O_3 other metal oxides has also been investigated as separator coatings in LSB. A micrometer thick V_2O_5 barrier layer was designed to hinder the diffusion of dissolved PSs permitting the transport of lithium ions. A pouch cell (2 x 2 cm) fabricated with V_2O_5 layer was cycled >300 times over 1 year without noticeable performance degradation at a capacity of 5 mAh (800 mAh g^{-1} of sulfur) (Li et al., 2014b). The routine LSB separator modified with hollow carbon nanofiber@mesoporous δ-MnO_2 nanosheets (HCNF@pδ-MnO_2) delivered a capacity of 856 mAh g^{-1} after 200 cycles at a rate of 0.5 C with enhanced rate capacity and anti-self-discharge feature (Lai et al., 2017). A self-sssembled close-packed MnO_2 nanoparticles anchored polyethylene separator was designed for LSB to suppress the PS shuttling, which greatly improved the capacity and cycling stability of the cells (Song et al., 2018c). The LSB with KB-MnO composite separator displayed an initial capacity of 1059 mAh g^{-1}, and a capacity retention of 85% after 200 cycles at 1C (Qian et al., 2016). A LSB was fabricated with SiO_2 nanoparticle decorated PP separator and the capacity of the configured cell was 937 mAh g^{-1} at the first cycle and 603 mAh g^{-1} at 200 cycles at 0.2C (Li et al., 2017a). A biomass carbon fiber@SiO_2 modified separator was developed for LSB and the resultant cell delivered a high reversible capacity of 1352 mAh g^{-1} at 0.1C and enhanced capacity of 618 mAh g^{-1} after 500 cycles at 1C (Liu et al., 2019a). Nano-TiO_2 decorated carbon coated separator was designed for LSB to physically and chemically suppress the PS shuttle and resultant cell exhibited a retained specific capacity of 883 mAh g^{-1} after 180 cycles at 0.1 C and 762 mAh g^{-1} after 200 cycles at 0.5C (Shao et al., 2018a). LSB cells fabricated with carbonized bacterial cellulose/TiO_2 modified separator showed an initial discharge capacity of 1314 mAh g^{-1} at 0.2 C and a discharge capacity of 475 mAh g^{-1} obtained after 250 cycles at 2 C (Li et al., 2017b). A polar TiO/MWCNT coating on LSB separator produced a relatively high initial discharge capacity of 1527 mAh g^{-1} and excellent cycling stability up to 1000 cycles at 0.5 C with a negligible fading rate of 0.057% per cycle (Li et al., 2019c). Some other inorganic metal oxide-based barrier coating have also been reported for LSB separator to mitigate the diffusion of PSs, such as ZnO (Sun et al., 2019a), MgO (Sun et al., 2019b), SnO_2 (Xiang et al., 2018), Cr_2O_3 (Guan et al., 2019a), Ta_2O_5 (Li et al., 2019d), Fe_3O_4 (Sun et al., 2019c, Cheng et al., 2019), MoO_3 (Kaisar et al., 2019), In_2O_3 (Yang et al., 2018b), RuO_2 (Balach et al, 2016b), $CoFe_2O_4$ (Feng et al., 2019), $LaLiO_2$ (Bizuneh et al., 2019) and $BaTiO_3$ (Yim et al., 2016).

Metal chalcogenides have also been evaluated as LSB separator coatings due to their intrinsic network polarity where the surface metal or chalcogen ions synergistically interact with PSs and lithium (Knoop and Ahn, 2020). MoS_2 is one of the promising candidates to anchor PSs in LSB because its interaction energy with PSs is ~3-5 eV. Besides Li-S interaction, metal (Mo) facets interact with PSs. Moreover, MoS_2 can catalyze the conversion of higher order PSs to lower order PSs and act as a lithium ion conductor. The as-prepared MoS_2 coated separators were designed for LSB to deliver a specific capacity of 796 mAh g^{-1} after 500 cycles with the capacity retention of 93%. The excellent electrolyte wettability of MoS_2 coating favours fast lithium ion diffusion (Liu et al., 2019b). The LSB with N and S-codoped CNTs intertwined with flower-like MoS_2 coated separator exhibited a high reversible capacity of 814 mAh g^{-1} at 1.0 C and long-lasting cycling durability with an ultralow capacity decay of 0.02% per cycle over 1000 cycles (Xiang et al., 2019).

Similar studies were reported with other metal chalcogenides like CoS (Yang et al., 2019), CuS (Li et al., 2019e), SnS_2 (Moorthy et al., 2019) and WS_2 (Ali et al., 2018).

Other inorganic materials like selenides, nitrides, borides and phosphides have also been explored as separator coatings in LSB (Carenco et al., 2013). A rGO@$CoSe_2$ separator coating was proposed for LSB to block the PS shuttling with the help of graphene with physical absorption and $CoSe_2$ particles with strong chemical binding. The resultant LSB assembled with rGO@$CoSe_2$ separator presents a high initial discharge capacity of 1180 mAh g^{-1} at 0.2 C and long cycle stability at 0.5 C with a low capacity decrease rate of 0.0856% per cycle (Zhou et al., 2019). Incorporation of functionalized BN nanosheets with negative charged groups on to LSB separator produced an excellent long-term cycling stability up to 1000 cycles and a high capacity of 718 mAh g^{-1} at a very high current of 7C (Fan et al., 2019). PS confinement via porous VN-modified separator was reported to deliver an average capacity fading of 0.077% per cycle at 1C for 800 cycles (Song et al., 2019). A potent functional separator was developed to restrain the PS by coating Co_2B@CNT layer. The co-adsorption effect of Co sites and B sites in Co_2B enable efficient polysulfides blocking and the LSB showed prolonged cycle life with a capacity degradation of 0.0072% per cycle up to 3000 cycles and a capacity of 1172 mAh g^{-1} preserved at 5C (Guan et al., 2019b). A MoP/rGO coating layer introduced on the separator, which not only impedes the diffusion of PSs to the anode but also improves the sulfur utilization. The resultant cell (sulfur loading of 3.88 mg cm^{-2}) displayed high areal capacity (~3 mAh cm^{-2}) and good rate performance with a capacity decay rate as low as 0.045% per cycle over 300 cycles (Li et al., 2018b).

1.7.4. Other Novel Separator Modifications

Recently, metal-organic frameworks (MOFs) were proposed, comprising an infinite network of metal clusters bridged by simple organic linkers through metal-ligand coordination bonds. MOFs possess rich porosity, nanometer cavity sizes, and high surface areas which allows the MOF to acts as an ionic sieve in LSBs-selectively sieves lithium ions while efficiently blocking PSs migrating towards the anode

(Shrivastav et al., 2019; Rana et al., 2019). In addition, the MOF containing organic functional groups on its surface promotes ionic conductivity. The microporous $Cu_3(BTC)_2$ (BTC: benzene-1,3,5-Tricarboxylate) (HKUST-1) MOF structure has a pore size of ~9 A°, which is large enough to pass lithium ions but smaller than the size of PSs. The LSB with GO and HKUST-1 MOF composite coated separator produced an initial specific capacity of 1207 mA h g^{-1} and a capacity fading rate of 0.02% after 1500 cycles at 0.5C (Bai et al., 2016a). The same design with Zn(II)-MOF based separator exhibited an initial discharge capacity of 1118 mAh g^{-1} and capacity decay of 0.041% per cycle at 1C over 1000 cycles (Bai et al., 2016b). Recently, the separator coated with Mn(II)-BTC was reported and the cells exhibited an initial discharge capacity of 1450 mAh g^{-1} with excellent rate capabilities (Suriyakumar et al., 2019). Li et al. performed a comparison study for the LSBs using the separators coated with different types of MOFs including Y-FTZB ($[Y_6(\mu_3\text{-OH})_8]^{10+}$ clusters with $FTZB^{2-}$ 2-fluoro-4-(tetrazol-5-yl)benzoate) ligands), ZIF-7 (zeolitic imidazolate frameworks), ZIF-8, and HKUST-1 having various pore sizes and chemical structures. The authors observed that the densely packed structure of Y-FTZB played a crucial role to produce an initial discharge capacity of 1127 mAh g^{-1} with a retention capacity of 597 mAh g^{-1} after 300 cycles at 0.25C (Li et al., 2017c). The amine decorated UiO-66-NH_2 MOF with SiO_2 coated separator was developed for LSBs to produce an initial discharge capacity of 1319 mAh g^{-1} and a retained capacity of 571 mAh g^{-1} (fading rate of 0.56%) after 100 cycles at 0.1C (Rana et al., 2019). Covalent triazine-based frameworks (CTFs) are another class of materials with ordered porous structures, large specific surface area, and good thermal/chemical stabilities. The 2D CTFs consisting of benzene derivatives and triazine rings can effectively trap PSs through chemical absorption and lithiophilic interaction of the heteroatoms in their porous structures. The CTFs coated separator exhibited enhanced battery performance- high reversible specific capacity (1249 mAh g^{-1} at 0.5 C), an ideal rate performance (802 mAh g^{-1} at 2 C), good cycling stability with a low capacity fade-rate of 0.052% per cycle over 800 cycles at 1 C and good anti-self-discharge behaviour (Shi et al., 2019).

MXenes are a family of semiconducting or metallic 2D inorganic compounds of early transition-metal carbides, nitrides or carbonitrides obtained through selective etching of the A element from the MAX phases, where M is an early transition metal, A represents group IIIA or IVA element, X stands for C or N (Naguib et al., 2014). These materials possess a highly active 2D surfaces to chemically anchor PSs through strong metal-sulfur bond (Rana et al., 2019). A functional separator for trapping soluble PSs was designed for LSB by coating $Ti_3C_2T_x$ MXene (T stands for the surface termination, such as -O, -OH, and/or -F) nanosheets on Celgard separator and the resultant cell delivered high discharge capacity of 550 mAh g^{-1} after 500 cycles with a capacity decay of 0.062% per cycle at 0.5 C (Song et al., 2016b). CNT incorporated delaminated titanium based MXene nanosheets (Ti_2C, Ti_3C_2, and Ti_3CN) were reported to modify LSB separator. The cell delivered an initial discharge capacity of 1240 (CNT-Ti_2C), 1216 (CNT-Ti_3C_2), and 1263 mAh g^{-1} (CNT-Ti_3CN) at 0.05C and long-term cycling at a 0.5C (Liang et al., 2016). Orthorhombic black phosphorous (BP) is a 2D layered crystal structure composed of phosphorene layers linked through weak interlayer van der Waals attractions. The P atoms present in the phosphorene layers chemically interact with the PS anions (P-S binding energy 285~442 kJ mol^{-1}) to suppress the undesired PS shuttle in LSBs. In addition, BP possesses high electrical conductivity (~300 S m^{-1}) and fast lithium ion diffusivity. The BP-modified separator was designed for LSB to entrap PSs and the assembled cell showed an initial discharge capacity of 947 mAh g^{-1} (S loading of 2 mg cm^{-2}) with a fading rate of 0.17% after 100 cycles at 0.25C (Sun et al., 2016). Introduction of montmorillonite (MMT) ceramic protective film to form an ion selective separator was another approach to minimize diffusion of dissolved PS to the anode side by repulsive electrostatic force between PSs and MMT. The LSB fabricated with MMT-coated separator maintained a discharge capacity of 924 mAh g^{-1} at 200 cycles from the initial capacity of 1380 mAh g^{-1} (Ahn et al., 2015). The light-weight and scalable organic macromolecule, graphitic carbon nitride (g-C_3N_4) with enriched PSs adsorption sites of pyridinic-N was introduced to achieve the effective functionalization of LSB separator. The g-C_3N_4 coated separator cell delivered an initial discharge capacity of 1196 mAh g^{-1} (S loading of 5 mg cm^{-2}) at 1C with a fading rate of 0.07% after 400 cycles (Fan et al., 2016).

1.8. Electrochemical Supercapacitors

Among the various energy-storage devices, batteries and supercapacitors are considered as the two major technologies of choice for practical applications as illustrated in the Ragone plot (Figure 1.6) (Gür, 2018). Because of their high energy density, LIBs are widely used in consumer electronics. However, due to several resistive losses from sluggish electron and ion transport, batteries lead to heat generation and dendrite formation when operated at high power which can give rise to severe safety issues (Dend et al., 2015). On the other side, supercapacitors, also known as electrochemical capacitors (ECs) or ultracpacitors can safely provide high power and rapid charging with extremely long cycle life (>100000 cycles). Hence, they found potential applications in heavy-duty vehicles, hybrid platforms for trucks and buses, load-leveling systems for intermittent renewable energy sources, and storing the regenerative braking energy of EVs and light rail (Hannan et al., 2017; Khaligh and Li, 2010).

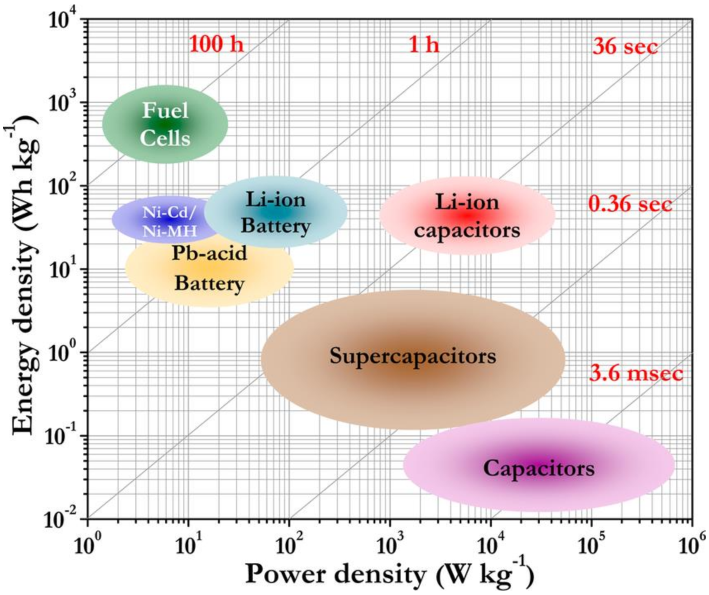

Figure 1.6. Ragone plot showing the performances of specific power *vs.* specific energy for electrochemical energy-storage devices. Times shown in the plot are the discharge time (Aravindan et al., 2014a)

1.8.1. Brief Historic Overview of Supercapacitors

The historical development of supercapacitors is the tale of discovering various charge-storage mechanisms (Shao et al., 2018b). The demonstration of the first capacitor dates back to the middle of the 18th century. The first capacitor, named a "Leyden jar", was invented separately by a German cleric Ewald Georg von Kleist in 1745 and a Dutch scientist Pieter van Musschenbroek in 1746. It was a simple design consisted of two pieces of metal foils, water, and a conductive chain inside a glass jar (Figure 1.7), and static electricity could be generated by rotating the glass jar (Huggins, 2016; Shao et al., 2018b; Xin et al., 2019).

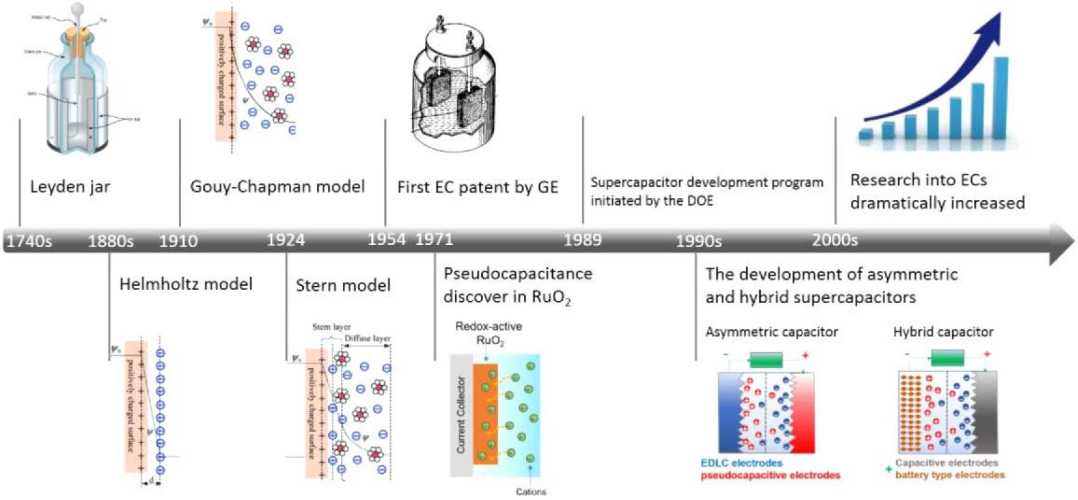

Figure 1.7. Historic timeline for the development of supercapacitors (upper panel) and schematics of various models proposed for the charge-storage mechanism inside a capacitor (lower panel) (Shao et al., 2018b)

After the invention of the Leyden jar, people realized the concept of storing static electricity at the interface between a solid electrode and a liquid electrolyte, and this knowledge aided to establish the initial concept of an electric double layer in 1880s. von Helmholz first studied the electrical charge-storage mechanism in capacitors and built the first electric double-layer model in 1853 (Balakrishnan and Subramanian, 2014). Thereafter, some pioneering interfacial electrochemists, including Gouy, Chapman, Stern, and Grahame, developed the modern theory of electric double-layer capacitance. In 1954, H. I. Becker at General Electric patented the first EC, which employed porous carbon electrodes immersed in an aqueous electrolyte (which functions as dielectric) and stored electric energy at the interfacial electric double layer. The first nonaqueous-electrolyte-based EC was patented by Robert A. Rightmire at the Standard Oil Co. of Ohio and later commercialized by Nippon Electric Company (NEC) in 1978 (Shao et al., 2018b).

A new class of EC termed as pseudocapacitor, which involves Faradaic processes, was discovered based on RuO_2 in 1971. Based on this discovery, the Pinnacle Research Institute (PRI) started a project in the 1980s to develop a high-performance supercapacitor based on ruthenium/tantalum oxide and named it as PRI Ultracapacitor. However, due to the high price of the noble metal, ruthenium, the PRI Ultracapacitor was only used for military applications, such as laser weapons and missile launch systems (Conway, 1991). Later in 1989, the U.S. Department of Energy (DOE) initiated a long-term study on supercapacitor aiming high energy density supercapacitors for applications like electric drivelines as a part of their Electric and Hybrid Vehicle Program (Burke, 2000). Ever since then a variety of supercapacitors have emerged, which includes electric double-layer capacitors (EDLCs), pseudocapacitors, and asymmetric supercapacitors. Each type of supercapacitor has its own significant features and target applications, such as backup energy for portable electronics or uninterrupted power supplies (UPS) and high-power energy sources for heavy loading trucks or cranes. From 2000 onwards there is a continuous and significant increase in the research related to supercapacitors with the increased demand for high-power, and safe energy-storage devices (Shao et al., 2018b).

1.8.2. Charge Storage Mechanisms of Supercapacitors

EC consists of an anode, cathode, and separator in between the anode and cathode to prevent the short circuit, with the electrolyte. On the basis of the energy storage mechanism, ECs can be generally classified into two main types: (i) EDLC and (ii) pseudocapacitors, irrespective of the electrolyte medium employed (aqueous or nonaqueous) (Salinas-Torres et al., 2019).

When an electronically conductive electrode is dipped in an ion-conductive electrolyte solution, a double layer forms spontaneously at the electrode-electrolyte interface due to the organization of charges. In an EDLC, the charge is physically stored by electrostatic adsorption of cations and anions at the interface between electrode and electrolyte (Figure 1.8).

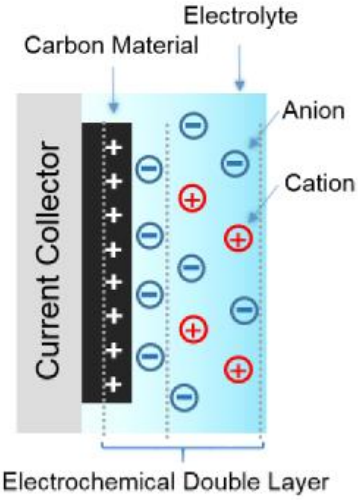

Figure 1.8. Schematics of charge-storage mechanisms for an EDLC (Shao et al., 2018b)

One of the salient characteristics of EDLCs is that no charge transfer reaction between the electrode-electrolyte interfaces, i.e., no Faradaic processes occur (Frackowiak and Béguin, 2001; Su and Schlögl, 2010). Generally, the carbonaceous materials with high specific surface areas are utilized as the electrode material of EDLCs, and the capacitance of an EDLC electrode is calculated according to the following equation (Zhang and Zhao, 2009):

$$C = \frac{A\,(\mathcal{E}_r\,\mathcal{E}_0)}{d}\ \mathrm{F} \tag{1.9}$$

where A is the effective specific surface area of the electrode materials which are accessible to the electrolyte ions, $\mathcal{E}_r$ is the permittivity of electrolyte solution, $\mathcal{E}_0$ is the permittivity of vacuum, and d is the effective charge separation distance between the electrical double layers. Carbon-based materials like commercial activated carbons, carbon aerogels, templated carbon, carbon nanomaterials such as carbon nanotubes and graphene, are the extensively studied active electrode materials for EDLCs owing to their high specific surface areas, desirable electrochemical stabilities, and open porosity accessible to the electrolyte ions (Gu and Yushin, 2013; Borenstein et al., 2017). Moreover, carbon-based materials with high surface area undergoes the formation of electric double layer ensuring a long-term cyclability over 10^6 cycles in aqueous electrolyte (Wu et al., 2017c). In the case of organic electrolytes, EDLC exhibits poor cycle life due to the higher equivalent series resistance (ESR); hence fewer studies have been conducted in non-aqueous electrolyte (Zhong et al., 2015; Pal et al., 2019).

In the 1990s, Conway and co-workers proposed the concept of pseudocapacitance (Brousse et al., 2015). Pseudocapacitive electrode materials store charge through Faradaic processes that involve fast, reversible redox reactions at the surface or near surface of the active electrode materials. This mechanism involves a valence state change of the active electrode material because of electron transfer (Conway et al., 1997; Augustyn et al., 2014). Transition metal oxides and conducting polymers are common pseudocapacitive electrode materials (Wang et al., 2016a). Amongst them, conducting polymers (polyaniline, polypyrrole, etc.) possess a relatively high specific capacitance and electronic conductivity with relatively low ESR values and cost-effectiveness in comparison with carbon-based electrodes (Ramya et al., 2013). Despite that, poor cycling stability of conducting polymers is a major concern. Similar to conducting polymers, transition metal oxides (RuO_2, MnO_2, etc.) also exhibited higher capacitance with lower ESR values, but higher cost and poor cycling stability remain the serious problem that hinder its commercialization (Augustyn et al., 2014). Energy storage mechanism in pseudocapacitors demonstrate an intermediate electrochemical characteristic between pure electrostatic EDLC-type materials and solid-state diffusion controlled by Faradaic reactions in bulk battery-type electrode materials (Jiang and Liu, 2019).

Pseudocapacitance can be accomplished through several faradaic mechanisms: (i) under potential deposition (UPD), (ii) redox pseudocapacitance and (iii) intercalation pseudocapacitance. These processes are demonstrated in Figure 1.9 (Shao et al., 2018b). UPD involves the faradaic absorption/desorption of metal ions on the surface of a different metal to form an adsorbed monolayer above their redox potential (e.g., H^+ on Pt or Pd^{2+} on Au) (Sudha and Sangaranarayanan, 2002). Redox pseudocapacitance occurs when ions electrochemically adsorb on the surface/near surface of electrode material along with faradaic charge transfer process (e.g., RuO_2 or MnO_2, as well as some conducting polymers) (Augustyn et al., 2014). Intercalation pseudocapacitance arises when ions intercalate into the tunnel/layer structure of a redox active material accompanied by a faradaic charge-transfer without any crystallographic phase change and in a time scale close to that of an EDLC. Transition metal oxides with layered or tunnel crystalline structures are interesting electrode materials because of their capability to intercalate/de-intercalate ions in the lattice sites. The ion intercalation occurs along with a change of metal valence to preserve electric neutrality. The ion intercalation pseudocapacitance received significant attention considering its ability to overcome the slow intrinsic solid-state diffusion limited battery kinetics with surface process (Augustyn et al., 2013; Augustyn et al., 2014; Jiang and Liu, 2019).

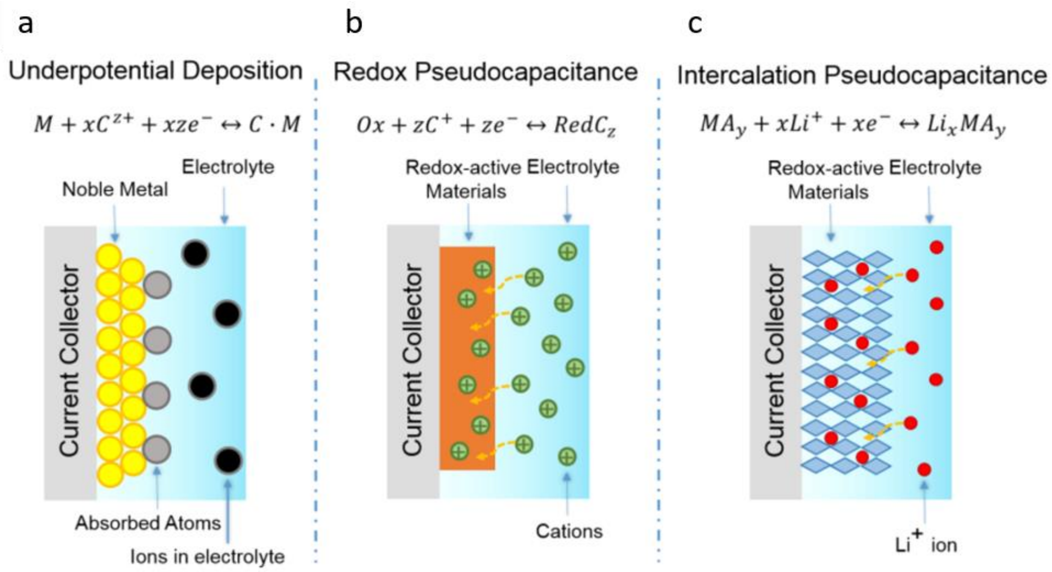

Figure 1.9. Schematics of charge-storage mechanisms for different types of pseudocapacitors (b) underpotential deposition, (c) redox pseudocapacitor, and (d) intercalation pseudocapacitor (Shao et al., 2018b)

From the application perspective, especially to power the zero emission vehicles such as EV and HEV, both EDLC and pseudocapacitive materials suffer inadequate energy density (Lin et al., 2018). Hybrid electrochemical capacitors serves as an interesting alternative to conventional EDLCs or pseudocapacitors by partnering a battery-like electrode (energy source) and a capacitor-like electrode (power source) within the same cell (Cericola and Kötz, 2012). A suitable combination of electrodes can expand the cell’s working voltage range, which further contribute to the enhanced energy and power densities. Presently, two types of electrode combination approaches exist for the development of hybrid systems: (i) pseudocapacitive metal oxides with a capacitive carbon electrode, and (ii) lithium-insertion electrodes with a capacitive carbon electrode (Zuo et al., 2017; An et al., 2019).

1.8.3. Lithium-Ion Capacitors

Since the beginning of the 1990s, many renowned research institutions and large corporations shifted their research focus from EDLC-type to new types of capacitor. In 1995, D.A. Evans suggested a fundamental concept of hybrid electrochemical capacitor by combining an ideal polarized electrode and a Faraday electrode (Shao et al., 2018b; Najib and Erdem, 2019). A Russian company named ESMA, in 1997, published a new hybrid capacitor design (NiOOH/activated carbon (AC)) integrating battery and capacitor chemistries (Burke, 2000). In 2000, Amatucci and co-workers reported a non-aqueous hybrid capacitor employing LIB material (nanostructured $Li_4Ti_5O_{12}$) as negative electrode and AC as positive electrode, which is considered as one the ground-breaking work in the area of hybrid electrochemical capacitor (Amatucci et al., 2001). Following Amatucci’s work, considerable research has been focused on multiple combinations of a lithium-insertion electrode with a capacitive carbon electrode. In 2005, Fuji Heavy Industries (FHI) published a novel hybrid electrochemical capacitor named the lithium-ion capacitor (LIC), using a pre-lithiated high surface area carbon (polyacene) anode together with an AC cathode. The pre-doped lithium-ions improved energy density of the anode by more than 30 times compared to the AC. Moreover, the lithiation can significantly lower the anode potential, which leads to an increment in the cell voltage, thereby improving the energy density (Aida et al., 2007; Jeżowski et al., 2016). In the 21st century, LIC research received considerable attention. At present, carbon-based materials (such as AC, graphene, and graphite), transition metal oxides, and transition metal sulfides have been extensively studied as active electrode materials (Li et al., 2018c).

A LIC, fundamentally, is a hybrid electrochemical capacitor, which can be constructed by substituting the active material in one of the electrodes of a supercapacitor with LIB material and operated in an electrolyte (aqueous and non-aqueous) containing lithium ions (Cericola and Kötz, 2012). The energy storage mechanism of LICs is hybrid in nature, which includes not only redox reaction of LIBs, such as lithium intercalation/conversion, alloying, etc. but also EDLC-type and Faradaic pseudocapacitance (Liu et al., 2018b). The difference between EDLC and LIC is illustrated in Figure 1.10. The configuration of LICs can be divided into two categories, symmetric and asymmetric capacitors, based on the combination of capacitor-type materials and LIB-type materials (Aravindan et al., 2014a).

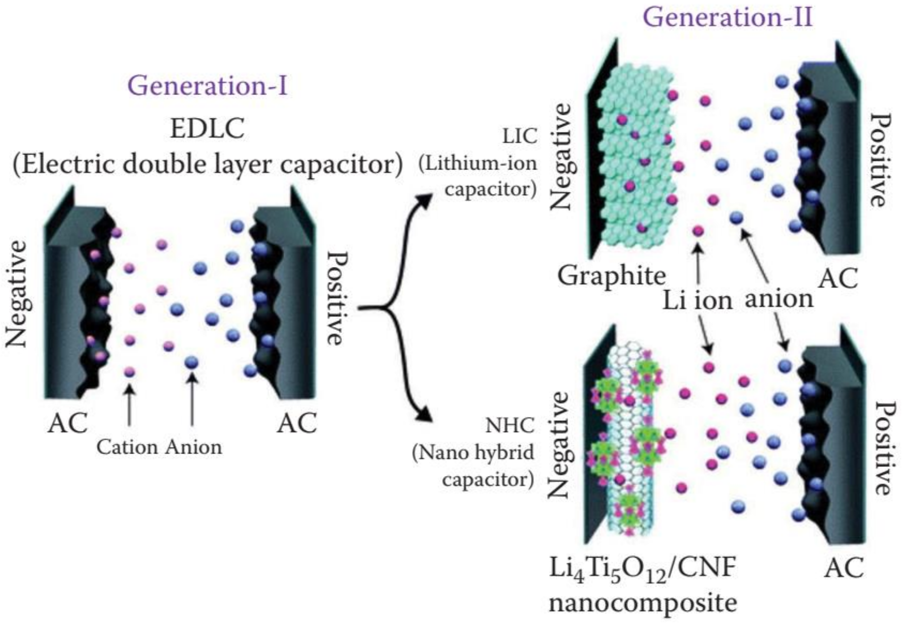

Figure 1.10. Schematic diagram of EDLC, LIC, and lithium-ion based hybrid electrochemical capacitor (which is same as a LIC) (Aravindan et al., 2014a)

Typically, EDLCs utilize high surface area carbon as both cathode and anode materials. LICs utilize high surface area carbon as the anode and an intercalation-type compound supporting the fast reversible intercalation of lithium-ions as the cathode material. The typical intercalation-type compound used in LIC can be classified into four types: (i) lithium-ion containing metal oxides ($LiMO_x$, M = Mn, Co, Ni, etc.), (ii) polyanionic compounds ($Li_xM_y(XO_4)$, M is transition metal, X = P, S, Si, V, Mo, W, etc.), (iii) graphite, and (iv) transition metal oxides (Jagadale et al., 2019). Generally, lithium-ion containing metal oxides and polyanionic compounds function as cathode materials; on the other hand, graphite and transition metal oxides serve as anode materials (Huang and Niederberger, 2019). Irrespective of the electrode, active material is mixed together with the binder and conductive materials to form a slurry. The obtained slurry is then coated on the Al foil, Cu foil, Ti foil, Ni foil or stainless steel substrate. A membrane (separator) is used to separate the positive and negative electrodes and to prevent electron conduction and short circuits. The commonly employed separator materials are polypropylene and cellulose (Simon and Gogotsi, 2008). A LIC can work in aqueous and non-aqueous electrolyte mediums. Aqueous electrolytes hold low viscosity and high ionic conductivity. But, the working potential window of electrode materials was limited to 1 V, which lower energy density. Li_2SO_4, LiOH, and $LiNO_3$ are the frequently used aqueous electrolytes. On the contrary, the non-aqueous electrolyte can widen the potential window up to 3 V, or even 4 V, which can dramatically enhance the energy density of LIC (Pal et al., 2019). The commonly used non-aqueous system is $LiPF_6$ dissolved in ethylene carbonate and dimethyl carbonate. However, the high viscosity and low ionic conductivity of non-aqueous electrolyte affects the power density (Laheäär et al., 2009).

Energy and power densities are the most important characteristics of LIC application, which can be calculated according to the following equations (Gupta et al., 2015):

$$E = \frac{C_{cell}V^2}{2 \times 3.6} \text{ Wh kg}^{-1} \tag{1.10}$$

$$P = \frac{3600 \times E}{\Delta t} \text{ W kg}^{-1} \tag{1.11}$$

where E is the energy density of LIC, C_{cell} is the specific capacitance of the LIC (F g^{-1}), V is the potential window (V), P is the power density of LIC, and Δt is the discharging time (s).

Generally, the specific capacitance can be measured from chronopotentiometry, an electrochemical technique where the electrode is charged and discharged under a constant current to obtain a potential-time curve (Zhang et al., 2018b). In a three-electrode system, the specific capacitance of the electrode can be calculated according to the following equation:

$$C_1 = \frac{I \times \Delta t}{m \times \Delta V} \text{ F g}^{-1} \tag{1.12}$$

In a two-electrode system, the specific capacitance of the electrode can be calculated according to the following equation:

$$C_2 = \frac{4 \times I \times \Delta t}{m \times \Delta V} \text{ F g}^{-1} \tag{1.13}$$

The specific capacitance of capacitor can be calculated according to the following equation:

$$C_{cell} = \frac{1}{4} C_2 \text{ F g}^{-1} \tag{1.14}$$

where C_1 and C_2 are the specific capacitances of the electrode material in the three-electrode and two-electrode system, respectively, C_{cell} is the specific capacitance of the LIC, m is the total active material mass of electrodes (g), I is the constant charging or discharging current (A), Δt is the discharging time (s), ΔV is the potential window (V).

1.9. A Brief Review on Electrode Materials for LICs

1.9.1. Anode

The fundamental prerequisite for selecting anode material is its electrode potential (Zhang et al., 2018b). Lithium titanate and graphitic electrodes are the most investigated materials in the LICs. Lithium titanate possesses relatively higher lithiation potential (1.55 V *vs.* Li/Li^+) than graphite (close to 0 V *vs.* Li/Li^+). The lower potential of the anode materials offer high upper potential window of the LIC cell (Aravindan et al., 2014a; Han et al., 2018a). Therefore, selection of negative electrode materials with low potential are preferred.

Currently, graphite is the most commonly used anode material for LICs owing to its low lithiation potential offering the LIC a high operating potential window in the range of 3.8-4.0 V, which in turn improve energy and power density (Béguin et al., 2014). A LIC based on graphite anode and AC cathode was reported to deliver a gravimetric and volumetric energy densities of 103.8 Wh kg^{-1} and 111.8 Wh L^{-1}, respectively (Khomenko et al., 2008). However, the sluggish nature of lithium-ion intercalation into graphite structure makes it unsuitable to the charge-discharge studies at high current densities. Hence, graphite mixed with other carbonaceous materials were reported. LIC composed of a pre-lithiated MWCNT/graphite composite anode and an AC cathode hold a specific capacitance of 58.2 F g^{-1} at the current density of 100 mA g^{-1} with a power density up to 10.1 kW kg^{-1} at 8000 mA g^{-1}, and retained a capacitance of 86% after 3000 cycles (Cai et al., 2018).

Another promising alternative to graphite anode is amorphous carbon (AMC) with wide interlayer spacing (~0.47 nm), which considerably reduce the lithium-ion insertion barrier (Han et al., 2018a). A variety of amorphous carbon materials have been obtained through pyrolysis and carbonization of polymers and biomass materials. An AMC anode derived from glucose, together with a disordered carbon cathode constitute a high energy efficient LIC with a maximum energy density of 133 Wh kg^{-1} at low power density of 210 W kg^{-1} (Lee et al., 2018a). A LIC assembled by coupling pre-lithiated nitrogen-doped carbonized polyimide microsphere anode and an AC cathode delivered energy densities of 28.5 and 13.1 Wh kg^{-1} at power densities of 348 and 6940 W kg^{-1}, respectively, with a capacity retention of 97.1% even after 5000 cycles (Han et al., 2016). A LIC performance based on recycled olive pit bio-waste derived carbon anode and AC cathode surpasses their EDLC counterpart in terms of energy density throughout the whole range of power density (Ajuria et al., 2017).

Low-dimensional carbon allotropes such as carbon nanofibers (CNFs), CNTs, and graphene were also investigated as anode materials for LIC due to their unique characteristics like high electrical conductivity, good mechanical integrity, and nanostructures with large surface area (Wang et al., 2019b). A 4.5 V symmetric LIC device was constructed using B and N dual-doped carbon nanofibers to deliver a large energy density of 220 Wh kg^{-1} and a power density of 22.5 kW kg^{-1} (at 104 Wh kg^{-1}) with a capacitance retention of ~81% after 5000 cycles (Xia et al., 2017). LIC assembled with pre-lithiated MWCNT anode and AC cathode achieved a specific capacitance of 59.3 F g^{-1} at the current density of 100 mA g^{-1} with a maximum energy density and power density of 96 Wh kg^{-1} and 4035 W kg^{-1}, respectively (Cai et al., 2017). A LIC cell fabricated using the N-doped defective graphene aerogel (N-DGA) anode and DGA/AC cathode exhibited a maximum energy and power densities of 39 Wh kg^{-1} and 1.2 kW kg^{-1} with a capacitance retention of 71% at 0.05 A g^{-1} after 2000 cycles (Wang et al., 2017a).

Graphdiyne (GDY) is a new two-dimensional (2D) carbon allotrope, which exist as a lattice of benzene rings connected by acetylene bonds comprising both sp- and sp^2-hybridized carbon atoms. GDY possesses high electrical conductivity and excellent chemical stability. Furthermore, GDY consists of a large number of triangle-like pores creating a unique triangular occupation pattern for lithium, leading to a high lithium storage capacity and excellent lithium mobility (Ivanovskii, 2013). A hybrid LIC featuring a bulk GDY anode and an AC cathode delivered energy densities of 112.2 and 95.1 Wh kg^{-1} at power densities of 400.1 and 1000.4 W kg^{-1}, respectively, in an operating voltage window of 2~4 V (Du et al., 2016). Hierarchical porous GDY nanowall based anode material delivered a capacitance more than 189 F g^{-1} over 10000 cycles at 1 A g^{-1} for LIC (Wang et al., 2017b).

Generally, transition metal oxide (TMO)-based anodes offer more capacity than that of graphite and other carbonaceous materials, which gained them much attention as potential anode candidate for LICs (Mohd Abdah et al., 2020). The electrochemical reaction of TMOs with lithium follows three different mechanisms: lithium intercalation/de-intercalation reaction, redox (conversion) reaction, and alloying/de-alloying reaction (Cui et al., 2018). Typical intercalation-type TMOs are compounds with a three-dimensional (3D) network structure that can reversibly intercalate/de-intercalate lithium ions in/out of the lattice sites without any crystallographic phase change (Tomaszewska et al., 2019). A LIC assembled with $Li_4Ti_5O_{12}$/graphene anode and AC cathode delivered energy densities of 44.0 and 11.4 Wh kg^{-1} at power densities of 45 and 7200 W kg^{-1}, respectively. The cell also exhibited a capacitance retention of 80% at 3.2 A g^{-1} after 10000 cycles with nearly 100% coulombic efficiency (Zhang et al., 2017a). A high energy and power LIC based on a TiO_2 nanobelt array anode and a graphene hydrogel cathode was designed to deliver an energy density of 82 Wh kg^{-1} at a power density of 570 W kg^{-1} with an operating voltage range of 0.0-3.8 V (Wang et al., 2015a). The utilization of $TiNb_2O_7$ as an anode along with an AC cathode in LIC results in good cyclability over 3000 cycles and the cell delivered high energy and power densities of 43 Wh kg^{-1} and 3 kW kg^{-1}, respectively (Aravindan et al., 2014b). A flexible LIC was designed with an in-plane assembled orthorhombic Nb_2O_5 nanorod film anode and AC cathode to deliver high gravimetric and volumetric energy/power densities (~95.55 Wh kg^{-1}/5350.9 W kg^{-1}; 6.7 mWh cm^{-3}/374.63 mW cm^{-3}) (Deng et al., 2018). A maximum energy density of 136.4 Wh kg^{-1} at a power density of 532 W kg^{-1} was obtained from a LIC device based on Li_3VO_4/N-doped carbon nanowire anode and AC cathode (Shen et al., 2017). An asymmetric supercapacitor with a maximum energy and power density of 90 Wh kg^{-1} and 11000 W kg^{-1} was developed using $H_2Ti_6O_{13}$-nanowires as a negative electrode and ordered mesoporous carbon (CMK-3) as a positive electrode (Wang et al., 2012a). A hybrid LIC was fabricated with $LiMnBO_3$ nanobead anode and polyaniline nanofiber cathode exhibited an excellent electrochemical performance; discharge capacitance of 125 F g^{-1} at 1 A g^{-1} in a potential range of 0-3 V with maximum energy and power densities of 42 Wh kg^{-1} and 5350 W kg^{-1}, respectively (Kaliyappan et al., 2014).

Conversion-type anodes usually deliver a high theoretical specific capacity than intercalation-type anodes because the reduction reaction of TMOs to their metallic state involves multiple electron transfer (Ulaganathan et al., 2016). One of the major issues observed for conversion-type TMOs are drastic volume changes during lithiation process leading to pulverization of electrode upon extended cycles (Yu et al., 2018a). The high voltage (4 V) LIC cell with mesocrystal MnO cubes as anode and AC as cathode demonstrated excellent cycling performance with the degradation rate of 0.002% per cycle and the maximum achieved energy density reached 227 Wh kg^{-1} (Liu et al., 2016b). Graphene decorated MoO_2 nanoparticles-based anode materials were developed for LIC to provide a high specific energy density of 33.2 W h kg^{-1} at a power density of 3000 W kg^{-1} with a capacitance retention of 91% over 500 cycles (Han et al., 2013). A LIC composed of Fe_3O_4-graphene anode and AC cathode delivered a high energy density of 120.0 Wh kg^{-1}, a power density of 45.4 kW kg^{-1} at 60.5 Wh kg^{-1}, and an excellent capacity retention of up to 81.4% after 10000 cycles (Zhang et al., 2017b). A high-performance LIC fabricated using $ZnMn_2O_4$-graphene hybrid nanosheets anode and N-doped carbon nanosheets cathode presented specific energy values of 202.8 and 98 Wh kg^{-1} at specific power values of 180 and 21000 W kg^{-1}, respectively (Li et al., 2017d). A 4 V LIC assembled with $MnFe_2O_4$/carbon as negative electrode and 3D AMC as positive electrode exhibited a capacity retention of 86.5% after 6000 cycles at 2 A g^{-1}, while achieving high energy density of 157 Wh kg^{-1} at power density of 200 W kg^{-1} (Lee et al., 2016).

The electrochemical alloying reaction of lithium with metals like Sn, In, Cd, etc., or semimetals like Si, Sb, Ge, etc., offer a high theoretical capacity for lithium storage (Han et al., 2018a). Since MOs are cheaper and easier to fabricate, their corresponding oxides are also investigated as potential candidates for LIC anode. A LIC designed with Si/C anode material and rice husk derived AC (RAC) cathode material offered a high energy density of 227 Wh kg^{-1} at a power density of 1146 W kg^{-1}, and 181 Wh kg^{-1} at a power density of 32595 W kg^{-1}. Moreover, the Si/C//RAC LIC exhibited a long-term cyclability over 16000 cycles at 16800 W kg^{-1} (Li et al., 2017e). A rationally designed Sn/C anode with a biomass-derived AC cathode constitute a LIC system and the assembled cell delivers high energy densities of 195.7 and 84.6 Wh kg^{-1} at power densities of 731.25 and 24375 W kg^{-1}, respectively (Sun et al., 2017a). A LIC developed by coupling B-doped Si/SiO_2/C anode with porous spherical carbon displayed an operating voltage window between 2.0-4.5 V with energy densities of 128 and 89 Wh kg^{-1} at 1229 and 9704 W kg^{-1}. Furthermore, the hybrid LIC exhibited good capacity retention of 70% after 6000 cycles at 1.6 A g^{-1} (Yi et al., 2014). A SnO_2-C hybrid anode was coupled with tubular mesoporous carbon cathode to obtain a LIC configuration, which achieved a maximum energy density of 110 Wh kg^{-1} and a maximum power density of 2960 W kg^{-1} (Qu et al., 2014).

Another family of 2D material called MXenes has also found application as anode material in LICs. A LIC fabricated with lithiated Nb_2CT_x-CNT anode and $LiFePO_4$ cathode provide a potential window between 0.3-3.3 V with maximum gravimetric energy density of 43 Wh kg^{-1} (Byeon et al., 2016). Another LIC assembled using the $Ti_3C_2T_x$/CNTs film as anode and AC as cathode exhibited a high energy density of 67 Wh kg^{-1} and a good capacity retention of 81.3% after 5000 cycles (Yu et al., 2018b). Recently, transitional metal sulfides have received increasing interest as electrode materials in LIC research. A novel hybrid LIC was fabricated employing MoS_2/rGO composite as the anode and AC as the cathode, which exhibited specific energy densities of 188 and 45.3 Wh kg^{-1} at 200 and 40000 W kg^{-1}, respectively, as well as long cycle life (Wang et al., 2017c). A CNF@$CoNi_2S_4$ nanoparticle-based anode material and AC cathode material constitute a LIC to deliver an energy density of 85.4 Wh kg^{-1} at a power density of 150 W kg^{-1}. Also, even at the high power density of 15 kW kg^{-1}, the LIC provided the energy density of 35 Wh kg^{-1} (Jagadale et al., 2018). Similarly, transition metal nitrides also proved suitable for LIC applications. Employing 3D VN-rGO composite and porous carbon nanorods with a high surface area of 3343 m^2 g^{-1} as the anode and cathode, respectively, a LIC was fabricated with a maximum energy density of 162 Wh kg^{-1} and a maximum power density of 10 kW kg^{-1} (Wang et al., 2015b). A novel LIC device was assembled using porous NbN as the anode and AC as the cathode. The fabricated device exhibited a wide potential window of 4.0 V with a high energy density of 149 Wh kg^{-1} and a high power density of 45 kW kg^{-1} as well as a superior capacity retention of 95% after 15000 cycles at 1.0 A g^{-1} (Wang et al., 2016b).

1.9.2. Cathode

To attain a high energy and a high power LIC, it is essential to have a cathode material with high operating potential and good electrical conductivity (Guangchao Li et al., 2019). The commonly used cathode materials for LICs can be classified into carbon materials, lithium-intercalated compounds, and composite materials.

Presently, PC is mainly used as the cathode material in LICs. The preponderance of PC usage in ECs mainly arises from its porous structure with large surface area (> 1000 m^2 g^{-1}), which can house large number of charged species and provide fast charge transfer. Other advantages of PC that contribute to its widespread application in ECs include low cost, easy electrolyte accessibility, and chemical inertness (Niu et al., 2018). The common carbon materials used as cathode materials in LIC research includes AC, graphene, and CNTs (Wang et al., 2019b).

The best known and only commercialized cathode material in LICs is AC which is also the extensively studied electrode material in traditional EDLCs. A LIC fabricated based on AC cathode and pre-lithiated graphite anode deliver a discharge energy density of 55 Wh kg^{-1} over the potential range of 3.1-4.1V and 100 Wh kg^{-1} in the extended cut-off potential of 2.0-4.1 V (Sivakkumar et al., 2012). However, AC face problems such as low specific capacitance and low electrical conductivity. As a solution to the above problems, researchers came up with the idea of graphitization and combination of AC with other materials having a high conductivity. The partially graphitic AC cathode coupled with microspherical porous $Li_4Ti_5O_{12}$ anode form a LIC, which delivered a specific capacitances up to 77 F g^{-1} and 62 F cm^{-3} (Cho et al., 2014). Recently, many researchers have shifted their interest towards various biomass-derived AC due to the abundance and renewability of raw materials. Besides, biomass-derived AC other possess favourable properties like good chemical stability, tunable microstructures, and surface functional groups, which makes it suitable for electrode materials (Bi et al., 2019). The hybrid LIC assembled using the egg white-derived AC as the cathode and Si/C nanocomposites as the anode delivered energy densities of 257-147 Wh kg^{-1} at power density from 867 to 29893 W kg^{-1} with a capacity retention 79.2% after 15000 cycles (Li et al., 2016). A porous AC derived from chinese-chive based cathode coupled with Si/flake graphite/C nanocomposite anode form a hybrid LIC with high energy density (159 Wh kg^{-1} at 945 W kg^{-1}) and outstanding cycle stability (80% capacity retention after 8000 cycles at 1 A g^{-1}) (Lu et al., 2018).

Graphene and rGO have been reported as cathode materials for LICs because of its interesting properties such as excellent electrical conductivity, high surface area and high mechanical strength (Zhang et al., 2019b). A LIC composed of graphene@hierarchical meso-/microporous carbon cathode and pre-lithiated graphite anode demonstrated high energy densities of 233.3-143.8 Wh kg^{-1} at power densities from 450.4 to 15686 W kg^{-1} (Li et al., 2018d). A flexible quasi-solid-LIC was developed based on holey rGO film cathode and rGO@Fe_3O_4 film anode to deliver a maximum energy density of 148 Wh kg^{-1}, a maximum power density of 25 kW kg^{-1}, and an excellent capacity retention of 82% after 2000 cycles (Liang et al., 2018). CNTs are considered as another suitable cathode material for LICs due to their unique hollow structure, excellent electrical conductivity, appropriate pore size, and ability to form nanoscale network structures. A flexible nanostructured hybrid LIC based on thin film MWCNT cathode and α-Fe_2O_3/MWNT composite anode provided a specific energy density of 50 Wh kg^{-1} at a specific power density of 1000 W kg^{-1} over the potential range of 0-2.8 V (Zhao et al., 2009).

In addition to graphene and CNT-based cathode materials, some other forms of carbon materials were also investigated. A novel “core-shell” porous graphitic carbon (PGC) was prepared from mesocarbon microbead to replace conventional AC cathode. The LIC assembled with PGC cathode and $Li_4Ti_5O_{12}$ anode delivered a high energy density of 55 Wh kg^{-1} and a high power density of 6474.7 W kg^{-1} (Lei et al., 2013). A N-rich nanotube (NRT) with internal compartments and open mesopores on the surface was prepared from Melamine-Formaldehyde resin. The LIC with NRT cathode and Sn@NRT anode was assembled and tested in a wide potential window of 1.75-4.35 V to deliver high energy densities of 274 and 127 Wh kg^{-1} in the power density range of 153 and 22800 W kg^{-1} (Won et al., 2017).

On the other hand, lithium metal oxides (LMOs) show relatively higher operating potentials. Most of the known LMOs were investigated as cathode materials for LIBs, which undergo intercalation/de-intercalation reactions. Unlike the non-Faradaic carbon-based electrodes, intercalation-type cathodes hold relatively constant working potentials, despite the state of charge of a cell (Desilvestro and Haas, 1990; An et al., 2019). Proper mass balance between the insertion-type cathodes and carbon-based anodes can be considered as an effective strategy to achieve high energy LICs (Madabattula et al., 2020). $LiCoO_2$ was the first explored cathode material in commercial LIBs. It was the same group who introduced a LIC configuration with $LiCoO_2$ as the cathode and nanostructured $Li_4Ti_5O_{12}$ as the anode in 2003. The assembled LIC delivered maximum energy densities of 47 Wh kg-1 and 64.5 Wh L^{-1} (Pasquier et al., 2003). An aqueous LIC was fabricated using $LiMn_2O_4$ and sonochemically reduced graphene as the cathode and anode, respectively, and the fabricated device delivered a high specific capacitance of 59.45 F g^{-1} at 0.4 A g^{-1}, a high specific energy of 39.96 Wh kg^{-1} at a power of 440 W kg^{-1} with better capacitance retention of 90.24 % even after 1000 cycles (Pazhamalai et al., 2017). A $LiFePO_4$-AC cathode and a pre-lithiated hard carbon anode form an internal hybrid LIC and the cell exhibited an excellent capacity retention of 92% over 100,000 cycles at 60C (Shellikeri et al., 2018). The LIC cell including Li_2MoO_3 cathode and hard carbon anode exhibited much higher capacitance than that of the conventional LIC, without significant capacity degradation (Park et al., 2011). A LIC coupled with Li_2MnSiO_4 cathode and AC anode exhibited a high discharge capacitance and energy density of 43.2 Fg^{-1} and 54 Wh kg^{-1}, respectively, at 1.0 mA cm^{-2} with excellent cycling stability over 1000 cycles and coulombic efficiency over > 99% (Karthikeyan et al., 2012). A hybrid asymmetric LIC with lithium-ion intercalated compound $LiNi_{0.5}Mn_{1.5}O_4$ as cathode and AC as anode exhibited a sloping voltage profile from 1.0-3.0 V, a specific energy of 56 Wh kg^{-1} and excellent cyclability with less than 5% capacity loss over 1000 cycles (Wu et al., 2009).

Conducting polymers have been considered as a promising candidate for pseudocapacitive applications. Pseudocapacitor electrodes based on conducting polymers possess certain advantages, like good conductivity, reasonable flexibility, and low cost (Bryan et al., 2016). However, their practical application is still impeded in pure form due to some obstacles. To enhance the electrochemical performance, pure conducting polymers are often mixed with metal oxides and carbon (Fu et al., 2019). A flexible all-solid state asymmetric LIC was fabricated employing $NiMoO_4$/PANi and commercial AC as the positive and negative electrodes, respectively, and the cell delivered a maximum specific energy of 99.26 Wh kg^{-1} and a maximum specific power of 10667 W kg^{-1} (Chen et al., 2015a). $LiNi_{1/3}Mn_{1/3}Fe_{1/3}O_2$-PANi composite cathode together with AC anode based LIC delivered maximum energy and power densities of 49 Wh kg^{-1} and 3 kW kg^{-1}, respectively (Karthikeyan et al., 2013). Other conducting polymer based binary composite electrode materials investigated in the literature include PANi-MnO_2 (Prathap et al., 2013), PANi-CuO (Ates et al., 2015), PPy-V_2O_5 (Sun et al., 2015a), PANi-rGO (Sun et al., 2015b), etc. Recently, many research groups have focused their attention on conducting polymer/metal oxide/carbon ternary composites, such as CNT/PPy/MnO_2 (Zhou et al., 2015), Ni/PPy/MnO2 (Chen et al., 2015b), etc.

1.10. Scope and Objectives

Electrochemical energy storage is a swiftly progressing domain building on a continuous flow of inventive ideas. Driven by rapid development of portable electronic devices, EVs and large-scale energy storage, the need for high-energy and high-power electrochemical devices with long service life is imperative. LIBs and ECs are considered as two of the most promising energy storage devices, owing to their advantages such as excellent electrochemical performance, environmental friendliness, and low cost. Current LIB technology can deliver a gravimetric energy density of 200~250 Wh kg^{-1} based on the Faradic redox reaction with lithium, but are confined by their low power density (<1000 W kg^{-1}) due to sluggish lithium ion diffusion within the electrode. Furthermore, the repeated lithium intercalation /de-intercalation causes structural damage to the electrode material and thus leads to limited cycle life (<1000 cycles). In brief, the power density (>10 kW kg-^{1}) and cycle life (>10000 cycles) of EDLCs far exceeds that of LIB, but with insufficient energy density (~10 Wh kg^{-1}) due to physical adsorption/desorption ions.

In this scenario, LSBs emerged as one of the most promising candidates to satisfy emerging market demands due to its remarkably high theoretical capacity of 1675 mAh g^{-1} and energy density of 2600 Wh kg^{-1}. However, its commercialization is still at bottleneck due to the several technical challenges such as insulating nature of sulfur, irreversible loss of active material due to polysulfide shuttle effect and degradation of lithium-metal anode. Current researches are primarily targeted on resolving the above-mentioned issues, of which polysulfide shuttling is crucial. LICs came out as another promising energy storage technology overcoming the pitfalls of EDLCs, constructed with battery-type anode and capacitor-type cathode, which enables the direct integration of the high energy from LIBs and high power from ECs. Many researchers have put their effort in the search of suitable battery-type anode materials with enhanced Faradaic reaction kinetics matching with the fast non-Faradaic reaction rate of the capacitor-type cathode materials. This doctoral research has been focused on the design and development of materials for the LSB and LIC systems, addressing few of the above-mentioned challenges. The following are the main objectives of the research work:

- To develop ion selective separators coated with conducting polymers for high-performance LSBs
    - To alleviate the polysulfide shuttle effect via an "electrostatic repulsion" approach
    - To investigate the impact of hydrophilic polar functional groups on the electrochemical performance of LSB
    - To evaluate the interfacial properties and Li^+ transporting capability of permselective separator coating
    - To evaluate the self-discharge behaviour of LSB cells with permselective separator
- To develop asymmetric LIC with ultrahigh energy density and long-term cycling
    - To synthesize and characterize phase-pure lithium metal vanadates
    - Electrochemical evaluation of lithium metal vanadate-based electrode in aqueous electrolyte
    - Fabrication and electrochemical evaluation of asymmetric LIC with lithium metal vanadate-based anode and MWCNT based cathode in non-aqueous electrolyte

1.11. Organization of the Thesis

This thesis describes the research work on the development of various materials for lithium storage in LSBs and LICs, material characterization, electrode fabrication and electrochemical evaluation. The focus of our research is on identifying/selecting suitable materials with excellent lithium storage properties. The first part of the thesis explores the ion selective separators coated with various lithiated polymers for high-performance LSBs. The next part of the thesis deals with various intercalation pseudocapacitive lithium metal vanadate-based anode material for LICs. The thesis is organized in eight chapters and a brief description of each chapter is outlined as follows:

Chapter 1 provides a general introduction to the basics and fundamental concepts of various energy storage technologies, and explains the background and basics of LSB and LIC systems. It provides a state-of-the-art literature survey on functional separators for LSBs and electrode materials for LICs. Further, it describes objectives and outline of the thesis.

Chapter 2 presents a permselective lithiated polyelectrolyte coated separator as potential PS cross-over barrier layer for LSB. The chapter focuses on the "electrostatic repulsion" approach imparted by $–SO_3^-$ groups present in the coating layer to alleviate the PS shuttle effect.

Chapter 3 discusses a novel approach of decorating commercial separator by bifunctional lithiated PEDOT:PSS. The dual PS shielding effect through electrostatic shielding ($–SO_3^-$groups in PSS) and chemical interactions (O and S in PEDOT) are investigated in this chapter.

Chapter 4 focuses on inhibiting the PS shuttle effect in LSBs using a carboxylate anchored permselective separator. The effect $–COO^-$ group on confinement of PS and electrochemical performances of LSB is evaluated in detail.

In ***Chapter 5***, micro and nanocrystalline inverse spinel $LiCoVO_4$ is introduced as a new lithium ion intercalation pseudocapacitive electrode material, and the effect of crystallite size on the fundamental lithium storage properties are investigated. In addition to that, the electrochemical performance of asymmetric LIC assembled with nanocrystalline $LiCoVO_4$ anode is evaluated.

Chapter 6 investigates the intercalation pseudocapacitive lithium storage properties of nanocrystalline inverse spinel $LiNiVO_4$ electrode. Further, electrochemical performance evaluation of asymmetric LIC cell assembled with $LiNiVO_4$ anode is discussed.

Chapter 7 presents nanoscale $LiMnVO_4$-based electrode materials for intercalation pseudocapacitive lithium storage with ultrahigh energy density and long-term cycling. The electrochemical performance of asymmetric LIC fabricated with $LiMnVO_4$ anode is investigated.

Chapter 8 summarizes the highlights of the output of the research work and the future perspectives based on this doctoral work.

CHAPTER 2

PERMSELECTIVE LITHIATED POLYELECTROLYTE DECORATED SEPARATOR AS POTENTIAL POLYSULFIDE CROSS-OVER BARRIER LAYER FOR LITHIUM-SULFUR BATTERY

Lithiation of poly(2-acrylamido-2-methyl-1-propanesulfonic acid) (PAMPS) was carried out by a simple ion-exchange method and the obtained lithiated PAMPS (LPAMPS) has been utilized as a functional coating on commercial Celgard separator (CG). Lithiation leads to proton exchange in sulfonic acid group of PAMPS, and the resulted LPAMPS possesses lithium ion transporting capability and functions as a single-ion conductor. The negatively charged sulfonic acid groups present on the LPAMPS coated Celgard (LPAMPS@CG) impart selective diffusion of lithium ions, at the same time repelling polysulfide anions via coulombic interactions. Besides, the LPAMPS@CG separator possesses excellent electrolyte wettability, interfacial contact and ionic conductivity. The Li-S cell containing LPAMPS@CG separator exhibited significant improvement in the battery performance, with a high initial capacity of 1486 mAh g^{-1} *and coulombic efficiency of ~99%. It is noted that the LPAMPS@CG separator impedes shuttle effect by inhibiting polysulfide crossover towards lithium anode, resulting a stable discharge capacity of 1060 mAh* g^{-1} *even after 200 cycles. To further evaluate the role of LPAMPS@CG separator in suppressing the polysulfide shuttle mechanism, post-mortem analysis on cycled cells were carried out using SEM (EDS) and XPS analysis.*

2.1. Introduction

LSB with high theoretical specific capacity and high energy density are considered as one of the potential candidates for next-generation rechargeable batteries. The intrinsic characteristics of the active material sulfur, such as low cost, low toxicity and natural abundance are added benefits for realizing LSB technology (Li et al., 2018e; Liu et al., 2017). Despite these advantages, commercialization of LSBs is still impeded due to several technical challenges discussed in the introduction chapter. Broad in scope, PS shuttling effect is one of the crucial problems leading to low charging efficiency, poor cyclability and high self-discharge rate. Therefore, it is indispensable to quench the shuttling of PSs (Berger et al., 2018; Li et al., 2018a).

Hitherto, various strategies have been dedicated to alleviate the shuttle effect by modifying the sulphur cathode, separator, electrolyte or lithium metal anode (Eftekhari and Kim, 2017; He et al., 2018a; Gupta et al., 2019). Much recent reports focus on confining PSs within the cathode compartment by inserting a chemical/physical barrier between cathode and separator. As an imperative battery component, separator functions as an electrical insulator for preventing internal short circuit and diffusion channels for ion transport. In Li-S system, separator permits the selective passage of lithium ions obstructing the transport of other ions, especially PSs. The transport selectivity of lithium ions and PS anions are crucial for mitigating PS shuttle (Fan et al., 2018; Jeong et al., 2018). Thus, modifying the commercial separator (polyolefin membranes) with functionalized barrier coatings (carbon materials, metal oxides, metal-organic frameworks, conducting polymers, 2D nanomaterials) attract much attention (Deng et al., 2016; Abbas et al., 2016; He et al., 2018a; He et al., 2018b; Rana et al., 2019). Among the various barrier layers, conducting polymers are smart as they can concurrently increase the electrolyte uptake and interfacial conductivity together with alleviating the PS crossover owing to the presence of polar functional groups. The polymers which possess polar negatively charged groups like $–SO_3^-$ and $–COO^-$ can effectively restrain the migration of soluble PSs via coulombic repulsion (Freitag et al., 2017; Huang et al., 2018; Zhu et al., 2019a). Besides, the separator modified with negatively charged groups will function as cation-selective membranes providing transport channels for lithium ions through the coulombic interactions, thereby improving electrochemical performance of LSBs. The polymers containing negatively charged groups like Nafion (Bauer et al., 2014), sulfonated polystyrene (Guo et al., 2018), polyacrylic acid (Song et al., 2018b), PEDOT:PSS (Abbas et al., 2016), sulfonated poly(styrene-ethylene-butylene-styrene) (Yang et al., 2018a), polyamide acid (Luo et al., 2018), sulfonated poly(ether ether ketone) (Babu et al., 2018), carboxylate anchored polyvinyl alcohol (Jiang et al., 2018), etc., have been explored to modify the polyolefin separator. It has been reported that the presence of negatively charged groups selectively permits the ion hopping of positively charged lithium ions and subsides the passage of negatively charged ions (PS anion) (Yang et al., 2018a; Luo et al., 2018; Babu et al., 2018).

As an anionic polyelectrolyte with high molecular weight, poly(2-acrylamido-2-methyl-1-propanesulfonic acid) (PAMPS) has been utilized as an ion conductive binder in lithium ion batteries (Kim et al., 2015), mixed ionic-electronic conductive cathode matrix in LSB (Fu and Manthiram, 2012) and proton conducting membranes in fuel cells (Qiao et al., 2005). PAMPS was reported to show higher proton conductivity due to the sulfonic acid groups in its chemical structure (Randin, 1982). In this chapter, we propose an “electrostatic repulsion” approach using a functional separator composed of lithiated PAMPS (LPAMPS) to effectively alleviate the shuttling of PS anions. Lithiation leads to proton exchange in sulfonic acid group of PAMPS, and the resulted LPAMPS possesses lithium ion transporting capability and functions as a single-ion conductor. The LPAMPS coating on commercial Celgard separator (LPAMPS@CG) effectively reduces interfacial resistance and the $–SO_3^-$ groups inhibits the migration of PSs by “electrostatic repulsion” effect. Subsequently, the Li-S cell employing LPAMPS@CG exhibits excellent electrochemical performance and anti-self-discharge characteristics compared to the uncoated Celgard separator.

2.2. Materials and Methods

2.2.1. Materials

Poly(2-acrylamido-2-methyl-1-propanesulfonate) solution (PAMPS, average M_w 2000000, 15 wt. % in water, Sigma Aldrich), lithium hydroxide (LiOH, 99.995% purity, Sigma Aldrich), lithium sulfide (Li_2S, 99.98%, Sigma Aldrich), sulfur (S, 99.998%, Sigma Aldrich), MWCNT (95% purity, Sigma Aldrich), super P carbon (Alfa Aesar), 1,3-dioxolane (DOL, 99.8% purity, Sigma Aldrich), 1,2-dimethoxyethane (DME, 99.5% purity, Sigma Aldrich), polyvinylidene difluoride (PVDF, M_w ~534000, Sigma-Aldrich), N-methyl pyrrolidone (NMP, 99.5% purity, Sigma-Aldrich), lithium metal foil (99.9% purity, 0.6 mm thickness, Sigma

Aldrich), bis(trifluoromethane)sulfonimide lithium salt (LiTFSI, 99.95% purity, Sigma Aldrich), Aluminium foil (15 µm thickness, MTI Corporation), 2032 type coin cell case, polypropylene membrane (25µm thickness, Celgard 2400).

2.2.2. Synthesis of Lithiated PAMPS (LPAMPS)

Lithiation of PAMPS was carried out by a simple ion-exchange method. 1 mmol LiOH was dissolved in 10 mL distilled water and added to 1 g PAMPS solution. The solution was stirred for 2 h at room temperature followed by vacuum drying at 80 °C for 24 h to obtain LPAMPS. The chemical formula and synthetic scheme of LPAMPS was given in Figure 2.1.

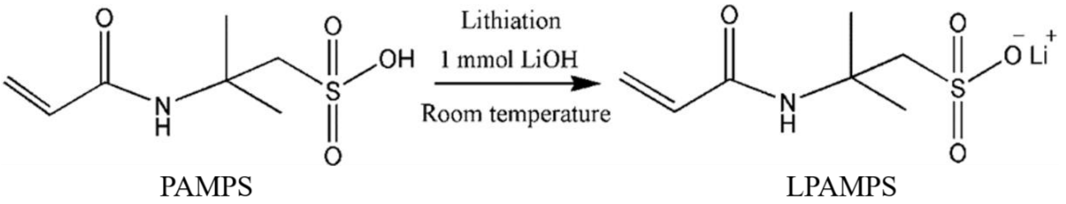

Figure 2.1. Synthesis scheme of LPAMPS

2.2.3. Preparation of LPAMPS Modified Celgard Separator (LPAMPS@CG)

The LPAMPS modified Celgard separator was prepared by doctor blade coating technique. Briefly, 0.033 g of PVDF as binder was dissolved in 2 mL NMP. To this solution, 0.033 g of LPAMPS and 0.033 g of super P carbon was added and the mixture was stirred for 5 h to obtain uniform slurry. The slurry obtained was coated onto one side of commercial Celgard 2320 separator (CG) and dried in vacuum oven at 60 °C for 12 h. The coated membranes were then punched into circular discs with a diameter of 19 mm. The presence of super P carbon can enhance electronic conductivity and adsorb the intermediate PSs suppressing its shuttling mechanism. The overall thickness of PAMPS@CG separator was about 38 µm. Membranes

2.2.4. Preparation of Lithium Polysulfide Solution (Li_2S_6)

1 M Li_2S_6 solution for visual PS diffusion test was prepared by mixing Li_2S and elemental sulfur (molar ratio of 4:3) in a solvent of DOL:DME (v/v= 1:1) in an Argon (Ar)-filled glove box. The mixture was stirred at 50 °C for 12 h giving rise to brownish red solution, corresponds to the average composition of Li_2S_6.

2.2.5. Fabrication of MWCNT@S Composite Cathode

MWCNT@S composite was prepared via melt-diffusion of sulfur on the MWCNT matrix. Typically, elemental sulfur powder and MWCNT were taken in a weight ratio of 7:3 and homogeneously mixed by ball mixer. The mixture was then transferred into a sealed vessel and heated at 155 ℃ in N_2 atmosphere for 12 h. In the course of this process, sulfur melts and diffuses into the 3D conductive network of MWCNT to obtain the MWCNT@S composite. The composite cathode was fabricated by doctor blade coating method. A slurry consisting of 70 wt.% MWCNT@S composite (containing 66 wt.% of sulfur), 20 wt.% super P and 10 wt.% PVDF dispersed in NMP solvent on an aluminium foil, and dried in air oven at 80 °C for 12 h. Finally, the MWCNT@S cathode was roll-pressed and punched into circular disks with a diameter of 16 mm.

2.2.6. Coin Cell Assembly

A standard 2032 type coin cell was assembled in an Ar-filled glove box (M Braun, Germany) employing MWCNT@S electrode with an areal sulfur loading of 0.9 mg cm^{-2}, LPAMPS@CG separator, and lithium metal as the counter electrode. The electrolyte employed was 1M LiTFSI in a mixture of DOL:DME (v/v = 1:1). To standardize the measurement procedure, the quantity of electrolyte added to each cell was fixed to 25 µL. After assembly, coin cell should be kept within glove box for 24 h prior to electrochemical studies to make sure that the separator was soaked well in the electrolyte. The control cell was assembled by the same way employing CG membrane as separator. In order to increase the sulfur loading level, we increased the coating gap between the doctor blade and aluminium foil and obtained higher areal sulfur loadings of 2.5 and 4.2 mg cm^{-2}. Further, coin cells were assembled with higher sulfur loading cathodes using LPAMPS@CG separator. All capacity values were calculated based on the mass of sulfur loaded.

2.2.7. Material and Electrochemical Characterization

The Fourier transform infrared spectra (FT-IR; PerkinElmer Spectrum 100) were recorded over a range of 2000-800 cm^{-1} to confirm the lithiation of PAMPS. The surface morphology of the CG and LPAMPS@CG was observed by field emission scanning electron microscopy (FE-SEM; FEI Quanta FEG 200) equipped with energy dispersive X-ray spectroscopy (EDS) and elemental mapping. The wettability of the separators in non-aqueous liquid electrolyte used for cycling studies was estimated by the contact angle measurement using a goniometer (ramé-hart Model 210 Goniometer, USA) at room temperature. The thermal stability and decomposition profile of the membranes were examined using thermogravimetric analysis (TGA; Hitachi STA7300 thermal analysis system) under inert atmosphere up to 800 °C with a heating rate of 10 °C min^{-1}.

The ionic conductivities of CG and LPAMPS@CG membranes at different temperatures (0, 10, 20, 30, 40, 50, 60 and 70 °C) were evaluated by assembling blocking cells comprised of stainless steel (SS)/membrane/SS using electrochemical impedance spectroscopy (EIS, Metrohm Autolab, Netherlands) in the frequency range of 1 MHz to 50 mHz with a perturbation amplitude of 10 mV.

The symmetric cells (Li/uncoated and coated Celgard/Li) were assembled and lithium ion transference number, t_{Li^+} was calculated by the method originally proposed by Vincent and Bruce using an electrochemical workstation (PGSTAT302N, Metrohm Autolab, Netherlands). The symmetric cells were first polarized by a DC pulse of 10 mV (ΔV) at 25 °C. The current values were recorded before DC polarization (I_o) and in steady state (I_{ss}). The resistances were also measured before (R_o) and after polarization (R_{ss}) from EIS measurements. t_{Li^+} was calculated according to the following equation (Evans et al., 1987; Bruce et al., 1992):

$$t_{Li^+} = \frac{I_{ss}\,(\Delta V - I_o R_o)}{I_o\,(\Delta V - I_{ss} R_{ss})} \tag{2.1}$$

To determine the interfacial stability of membranes with lithium electrodes, a symmetric cell consisted of Li/CG and LPAMPS@CG/Li was assembled and impedance response was monitored as a function of time at 25 °C under open circuit condition. The lithium ion diffusion coefficient, D_{Li^+} was calculated from cyclic voltammogram according to the Randles-Sevcik equation (Wang et al., 2019c; Kim et al., 2019).

$$I_p = 2.69 \times 10^5\, n^{1.5}\, A\, {D_{Li^+}}^{0.5}\, C_{Li}\, \vartheta^{0.5} \tag{2.2}$$

Here, $I_p, n,\ A, C_{Li}$ and ϑ represents the peak current, the number of electrons transferred, area of the electrodes, concentration of lithium ions in the electrolyte and sweep rate, respectively. In order to verify the interaction between LPAMPS and PSs, the zeta potential (Zetasizer Nano ZS, Malvern ZEN3600) of LPAMPS was measured in non-aqueous liquid electrolyte used for electrochemical evaluation.

The cyclic voltammetric (CV) and electrochemical impedance spectroscopic (EIS) studies were performed with PGSTAT302N electrochemical workstation (Metrohm Autolab, Netherlands). The CV curves were recorded at a sweep rate of 0.1 mV s^{-1} in the potential range of 1.6 to 3.0 V. The galvanostatic charge-discharge studies (BTS-4000, Newarelab) were performed between 1.6 to 3.0V at various currents. The EIS measurements were conducted before and after cycling studies at the open circuit voltage (OCV) with a perturbation potential of 10 mV in a frequency range of 0.1 to 10^5 Hz. PS shuttle current was measured for LSB cells with uncoated and LPAMPS coated Celgard at 2.3 V as described by Moy et al. (Moy et al., 2015). After charge-discharge cycling tests, the LSB cells with CG and LPAMPS@CG were carefully disassembled in a dry Ar-filled glove box for the post-mortem analysis of the separator and lithium anode. The morphology and composition of separator and lithium anode from the cycled cells were analyzed by performing FE-SEM (EDS) and X-ray photoelectron spectroscopy (XPS, Physical Electronics, USA, with a monochromatic Al-Kα-X-ray source) anlaysis.

2.3. Results and Discussion

2.3.1. Material Characterization

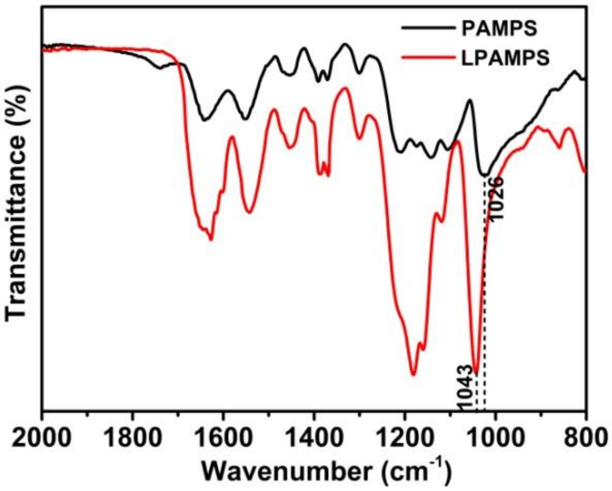

Figure 2.2. FT-IR spectra of PAMPS and LPAMPS

The FT-IR spectra can be used to verify the lithiation of PAMPS i.e., conversion from –SO_3H to –SO_3Li form. Figure 2.2 shows the FT-IR spectra of PAMPS (in protonated form) and LPAMPS (in lithiated form). The absorption band at 1026 cm^{-1} is ascribed to the symmetric stretching vibrations of S-O bond (from –SO_3H group). After lithiation, the vibration mode of -SO_3H shifts to 1043 cm^{-1} indicating the formation of -SO_3Li (Jin et al., 2012).

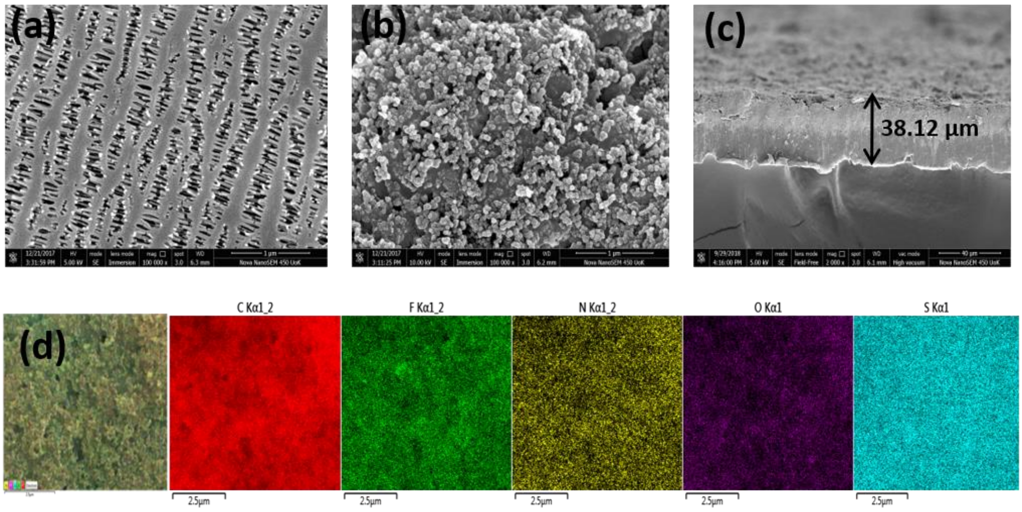

Figure 2.3. SEM micrographs of (a) CG and (b) LPAMPS@CG, (c) cross-section of LPAMPS@CG separator, (d) elemental mapping of the LPAMPS@CG

The surface morphology (SEM micrographs) of the Celgard and LPAMPS@CG membranes are depicted in Figure 2.3a-b. The cross-sectional morphology of LPAMPS@CG reveals a dense structure and the measured thickness was ~38 μm (Figure 2.3c). Elemental mapping of the LPAMPS@CG (Figure 2.3d) shows uniform distribution of carbon, fluorine, sulfur, nitrogen and oxygen, which verifies fine dispersion of LPAMPS with super P and PVDF on the surface of CG.

The electrolyte wettability of membranes plays a key role in determining the performance of LSB (Suriyakumar et al., 2019). As depicted in Fig. 2.4a-b, the contact angle of pristine CG and LPAMPS@CG membranes were found to be 52.6 and 15.7°, respectively. The increased wettability of LPAMPS@CG is attributed to the $–SO_3^-$ group present on LPAMPS polymer. The hydrophilic $–SO_3^-$ group immediately takes up the polar electrolyte droplet to form large clusters in the polymer domain, therefore enhances the wettability of the separator and gives lesser value of contact angle (Blake et al., 2005). The good wetting of the LPAMPS@CG with the non-aqueous electrolyte is likely to reduce the internal resistance and consequently improves the rate capability (Zhang et al., 2018c).

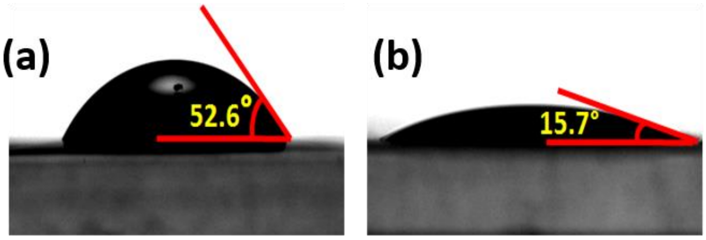

Figure 2.4. Contact angle shots of (a) CG and (b) LPAMPS@CG

For authenticating the “electrostatic repulsion” mechanism rendered by LPAMPS@CG separator towards the PS anions, zeta potential was measured for LPAMPS using non-aqueous electrolyte used in the cycling studies (Suriyakumar et al., 2019). The zeta potential of LPAMPS was found to be -47.4 mV as shown in the Figure 2.5, confirming the driving force between LPAMPS and PSs. Since the PSs remain anionic in the electrolyte and LPAMPS exists as negatively charged, a repulsive force arises between LPAMPS coating on CG and PS anions.

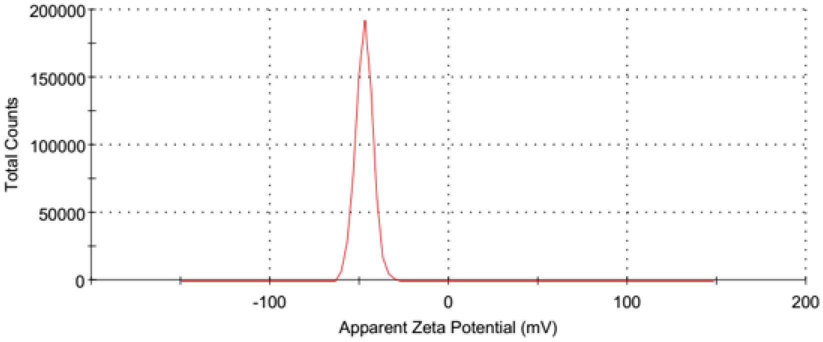

Figure 2.5. Zeta potential distribution of LPAMPS in non-aqueous electrolyte

2.3.2. Electrochemical Evaluation

To verify the effect of $–SO_3^-$ groups on the lithium ion transport properties, both the ionic conductivity and lithium ion transference number were measured. The lithium ion conductivities of CG and LPAMPS@CG were evaluated at different temperatures using EIS measurements and shown in Figure 2.6. Irrespective of the membrane analysed, the ionic conductivity increases with increasing temperature. The increased ionic conductivity of LPAMPS@CG is credited to the higher electrolyte uptake by LPAMPS coating.

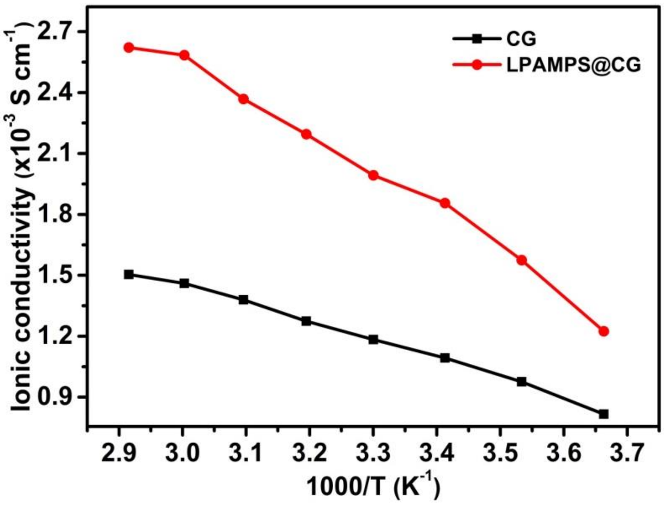

Figure 2.6. Ionic conductivity of CG and LPAMPS@CG separator

The lithium ion transference number (t_{Li^+}) is calculated using equation (2.1) and the calculated values are found to be 0.38 and 0.70 for CG and LPAMPS@CG, respectively according to the chronoamperometric profiles and EIS (Figure 2.7).

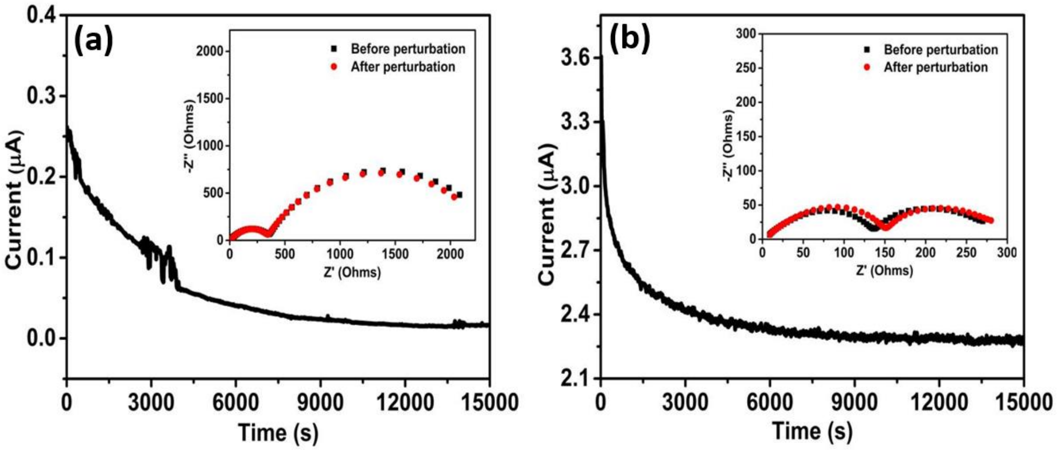

Figure 2.7. Chronoamperometric curves of (a) CG and (b) LPAMPS@CG membranes. Inset: EIS Nyquist plots of symmetric Li/membrane/Li cells before and after perturbation

It is remarkable that t_{Li^+} of LPAMPS@CG is almost twofold the CG. In the ether-based electrolytes, lithium ions usually exist as solvated Li$^+$-ether molecules which are much larger than TFSI$^-$ anions, this suppress the lithium ion transport thereby relatively lower t_{Li^+}value (Zhou et al., 2018; Callsen et al., 2017). On contrary, the high t_{Li^+} for cells with LPAMPS@CG membrane is possibly due to the presence of sulfonate groups along the LPAMPS chain, which could simultaneously speed up the de-solvation of Li$^+$-ether molecules supplying lithium ion coordination sites (–SO$_3^-$) and facilitate the transport of lithium ions (Jiang et al., 2018).

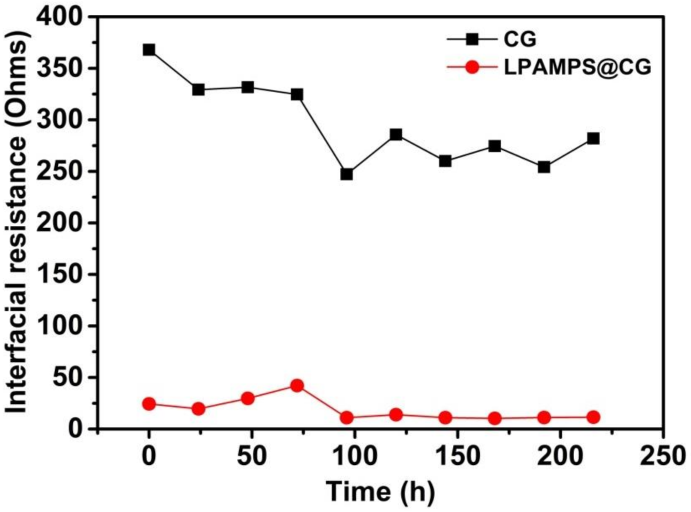

Figure 2.8. Interfacial resistance *vs*. time measurements of (a) CG and (b) LPAMPS@CG separator

To assess the stability of separator/lithium interface, a symmetrical Li/membrane/Li cell was assembled and its interfacial resistance, R_i was measured as a function of time at 25 °C (Suriyakumar et al., 2019). Figure 2.8 displays the variation of R_i with time for Li/CG or LPAMPS@CG/Li cells and the symmetric cell with LPAMPS@CG exhibit lowest R_i. This result further substantiates the observations described *previously* for the ionic conductivity studies.

2.3.3. Cell Performance Evaluation

In order to investigate the electrochemical performance of Li-S cells (areal sulfur loading 0.9 mg cm^{-2}) with CG and LPAMPS@CG membranes, CV, charge-discharge and EIS measurements has been carried out. CV curves of the Li-S cells with CG and LPAMPS@CG membranes are shown in Figure 2.9. Both Li-S cells display two cathodic peaks and one anodic peak regardless of the membrane employed. The two remarkable cathodic peaks are observed around 2.3 V (peak 1) and 2.0 V (peak 2) correspond to the stepwise reduction of sulfur. Peak 1 stands for the conversion of cyclo-S_8 into soluble higher order PSs (Li_2S_x, where $4 \leq x \leq 8$). On the other hand, peak 2 arise from the reduction of higher order PSs formed at high voltage into lower order lithium sulphides, i.e, the end products (Li_2S_2/Li_2S) (Song et al., 2018b; Yang et al., 2018a). This peak is the main peak in cathodic sweep which can deliver significant part of cell's capacity. During anodic scan a single oxidation peak is observed around 2.4 V (Peak 3) and is due to the combined transformation of lithium sulfide to PSs and ultimately to elemental sulfur (Wild et al., 2015). The cell with the CG separator exhibited two broad cathodic peaks and an anodic peak because of the sluggish kinetic process (Elgrishi et al., 2018). In comparison, the incorporation of PMAMPS@CG separator resulted in well-defined redox peaks with an increase in the current density, suggesting the improved redox reaction kinetics and utilization of the active materials in the cells (Lee et al., 2018b). From the second cycle onwards, the Li-S cell with LPAMPS@CG separator exhibit negligible current or potential shifts and the CV curves are found to be almost overlapped. Meanwhile, the Li-S cells with CG separator present a slight shift in peak position. This observation reveals the enhancement in electrochemical reversibility of Li-S cell with LPAMPS@CG membrane (Lee et al., 2018b).

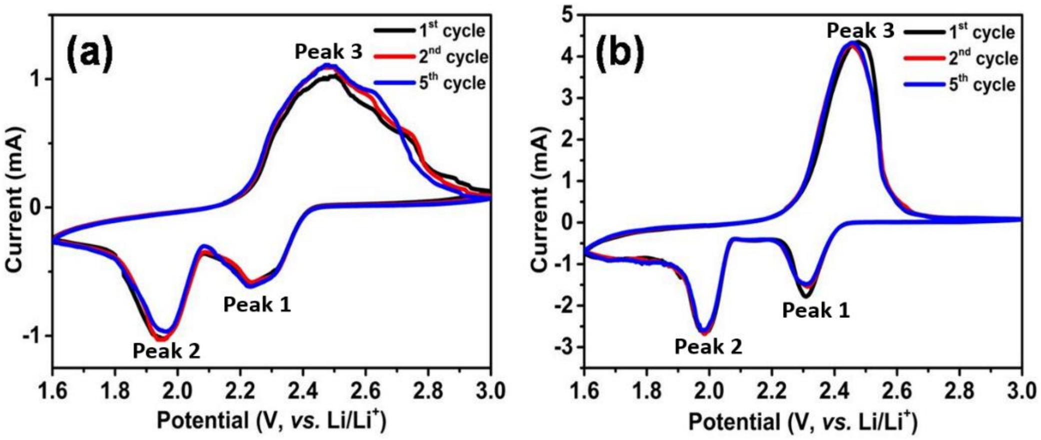

Figure 2.9. CV curves of Li-S cells containing (a) CG and (b) LPAMPS@CG separators

Further, diffusion coefficient of lithium ions was calculated from CV data using Randles-Sevcik equation. In the CV curve of Li-S cell, the two cathodic and the anodic stages were sited. The calculated values of chemical diffusion coefficient of lithium ions are respectively 1.09 x 10^{-7}, 4.71 x 10^{-7}, 4.84 x 10^{-7} cm^{2} s^{-1} for CG and 1.33 x 10^{-6}, 3.00 x 10^{-6}, 8.16 x 10^{-6} cm^{2} s^{-1} for LPAMPS@CG membrane. It is obvious from the calculated values that diffusion coefficients for LPAMPS@CG separator are at least an order of magnitude larger than CG. It is inferred from above result that the LPAMPS@CG separator offer an enhanced lithium ion mobility compared to CG, thereby expecting significant improvement in the specific capacity and rate capability.

Figure 2.10a represents the initial galvanostatic charge-discharge profiles of Li-S cells with CG and LPAMPS@CG separators at 0.1C rate and the plateaus of charge-discharge processes closely match with the peak positions in CV curves. The first plateau in the discharge profile (2.30-2.36 V) corresponds to the reduction of S_8 to higher order Li_2S_x ($4 \leq x \leq 8$), while the second plateau (2.0-2.08 V) results from the transformation of higher order PSs to lower order Li_2S_2/Li_2S. Noticeably, the Li-S cell with LPAMPS@CG exhibits a lesser voltage hysteresis (ΔE) than CG membrane ($\Delta E_{LPAMPS@CG}$ = 164 mV; ΔE_{CG} = 332 mV). The lower value of ΔE for Li-S cells with LPAMPS@CG is ascribed to low electrochemical polarization originated from the good electronic and ionic conductivity of separator coating. These high ionic conducting channels were rendered by the presence of sulfonate group in LPAMPS polymer (Moorthy et al., 2019). The absence of such ion conducting functional groups in CG leads to higher polarization, which in turn results in lower discharge capacity. The cell with LPAMPS@CG separators delivers an initial discharge capacity of 1486 mAh g^{-1} with 88.8% sulfur utilization. At the same time, the cell with CG separator delivers a discharge capacity of 873 mAh g^{-1} corresponding to 52.2% utilization of sulfur. The high initial discharge capacity of the cells with LPAMPS@CG is attributed to good ionic conductivity of LPAMPS coating, which provide a larger conductive surface for the transformation of PS to solid Li_2S_n ($n \leq 2$) (Yao et al., 2014).

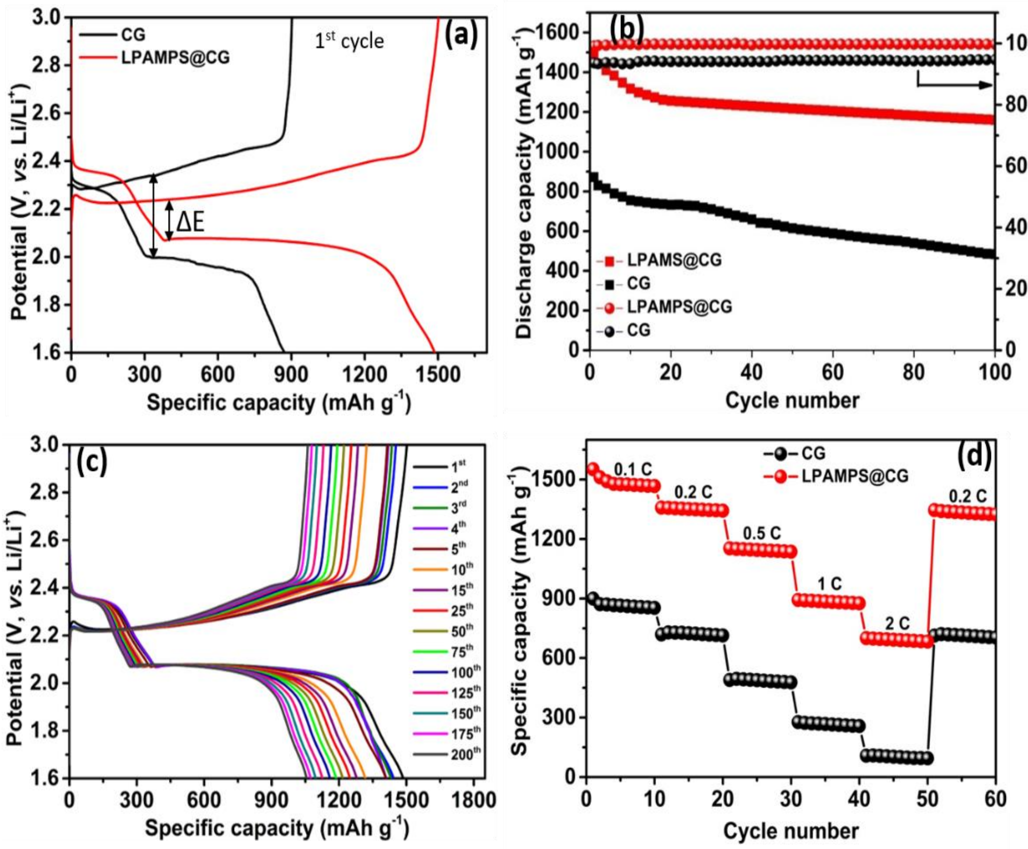

Figure 2.10. (a) Initial charge-discharge profiles of Li-S cell with CG and LPAMPS@CG at 0.1C (b) cycling performance (c) cycling profile of Li-S cell with LPAMPS@CG up to 200 cycles and (d) rate capability studies of Li-S cell with CG and LPAMPS@CG

Figure 2.10b depicts the cycling performances and coulombic efficiencies at 0.1C rate for the cells with CG and LPAMPS@CG separators. It is obvious from

Fig. 2.9b that the Li-S cells with LPAMPS@CG deliver higher discharge capacity and coulombic efficiency than the cells with CG separator. The cell assembled with CG exhibits rapid capacity decay (55.5% capacity retained after 100 cycles) as a consequence of PS shuttling mechanism, which arises from the easy migration of higher order PSs (size range: 1-1.8 nm) through the CG membrane towards lithium metal anode (Xiong et al., 2019). Whereas the cell with LPAMPS@CG exhibits a capacity retention of 79.2% calculated with respect to the initial cycle. However, by 10th cycle the capacity degrades from 1486 to 1311 mAh g^{-1} and after that point capacity degradation dropped to certain degree. Even after 200 continuous charge-discharge cycles, the cell with LPAMPS@CG retained 71.3% capacity with respect to the initial cycle (Figure 2.10c). The improved capacity retention observed in the case of LPAMPS@CG is credited to the presence of sulfonic acid groups which render better PS repulsion coupled with high ionic conductivity (Babu et al., 2018). Besides, the coulombic efficiency of the Li-S cells with LPAMPS@CG is ~99% which is superior to the cell with CG membrane (~93%). Therefore, LPAMPS coating on CG function as a good lithium ion conducting channel as well as efficient shield towards PS diffusion.

The rate capability of the Li-S cells with CG and LPAMPS@CG separators were evaluated at different current densities from 0.1 to 2C. As illustrated in Figure 2.10d, the cell with LPAMPS@CG demonstrates excellent rate performance. With LPAMPS@CG, the cells exhibit discharge capacities of 1495, 1357, 1150, 897 and 704 mAh g^{-1} at the current rates of 0.1, 0.2, 0.5, 1 and 2C, respectively. When the C-rate was taken back from 2 C to 0.2C, a reversible capacity of 1340 mAh g^{-1} was retrieved, attesting an excellent rate performance.

Further, glavanostatic charge-discharge studies were carried out for Li-S cells with higher sulfur loadings of 2.5 and 4.2 mg cm^{-2} at 0.1C rate and their initial profiles were displayed in Figure 2.11a. The initial discharge capacities of the Li-S cells with mass loadings of 2.5 and 4.2 mg cm^{-2} were calculated to be 1274 and 1115 mAh g^{-1}, respectively, approaching a sulfur utilization of 76.0 and 66.5%. After 50 continuous charge/discharge cycles, the three cells exhibit reversible discharge capacities of 1189 and 1068 mAh g^{-1}, respectively, indicating high capacity retention of 93.3 and 95.7%, respectively (Figure 2.11b). In the case of cells with higher sulfur mass loading, especially 4.2 mg cm^{-2}, the discharge capacity slightly increased during the charge-discharge cycles; possibly due to the longer activation process of the larger amount of sulfur used (He et al., 2016). In this sense, it can be concluded that the electrochemical performance of the Li-S cell was found to be improved after increasing the mass loading. Therefore Li/LPAMPS@CG/MWCNT@S cell configuration can be considered for realizing a long cycle life LSB.

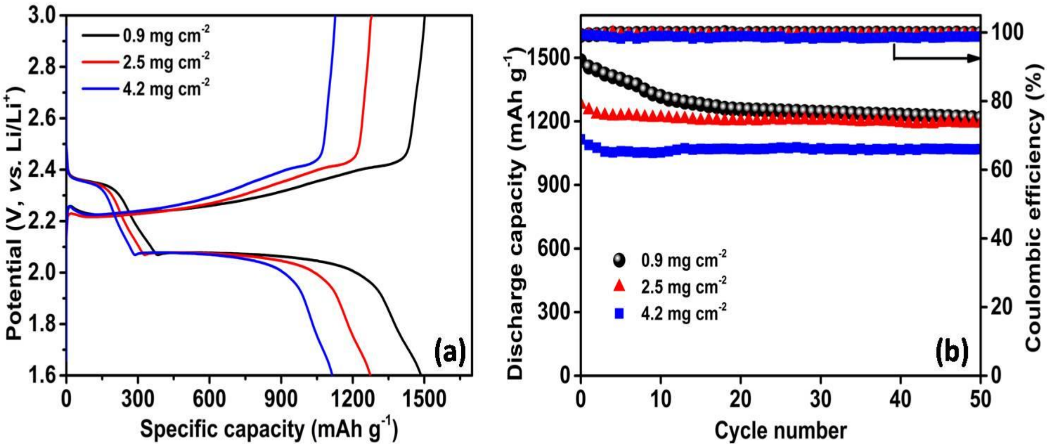

Figure 2.11. (a) Initial charge-discharge profiles and (b) cycling performance of Li-S cell with LPAMPS@CG separator with higher sulfur loading of 0.9, 2.5 and 4.2 mg cm^{-2}

In order to further investigate the influence of LPAMPS coating on cell performance, EIS measurements of Li-S cells were performed with CG and LPAMPS@CG separator before cycling and after 100 cycles (Figure 2.12). As shown in Figure 2.12, the Nyquist plots presented one or two semicircles in the high-medium frequency region and an inclined line in the low frequency region. The starting point of Nyquist plot represents bulk or solution resistance (R_e), which arises from the resistance for ion transport in the electrolyte and cell components. The Li-S cell with CG membrane (Figure 2.12a) exhibits a single semicircle in the high-to-medium frequency region corresponding to the charge-transfer resistance (R_{ct}). On the other hand, the cell with LPAMPS@CG (Figure 2.12b) presented two discrete semicircles; first semicircle in the high frequency region is associated with the interface contact resistance (R_{int}) offered by the coating layer and electrode bulk, while the second semicircle in the medium frequency region is related to the charge-transfer resistance (Lai et al., 2016). Based on the above discussion, we proposed an equivalent circuit model using ZSimpWin software as shown in the inset of Figure 2.12a-b. In the proposed circuit model, R_e is the resistance of electrolyte. R_{int}//CPE_{int} is the interphase contact resistance and its related capacitance (Y_1 and n_1 are CPE_{int} elements). R_{ct}//CPE_{dl} is the charge-transfer resistance and its related capacitance (Y_2 and n_2 are CPE_{dl} elements), which reflects the charge-transfer process at the interface between the conductive coating and the electrolyte. CPE_{dif} is the diffusion impedance (Y_3 and n_3 are CPE_{dif} elements), which represents lithium ion diffusion process (Deng et al., 2013).

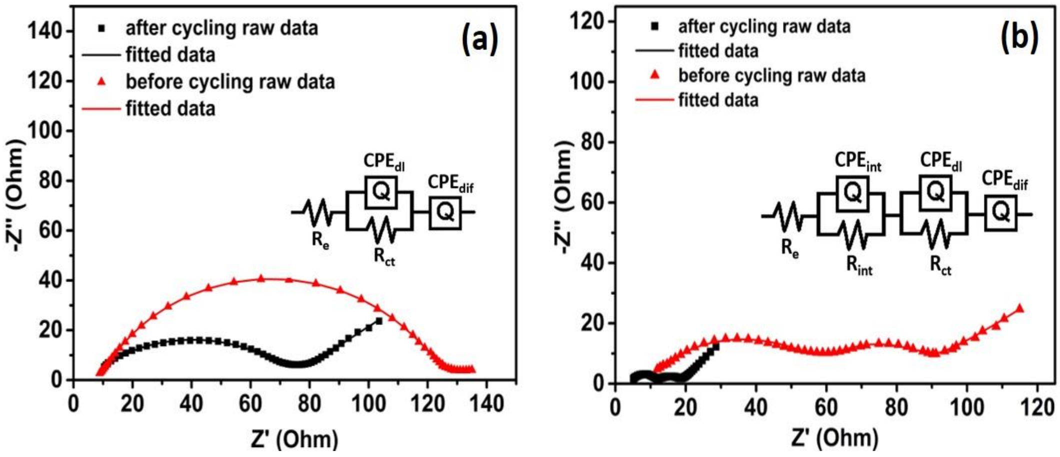

Figure 2.12. Electrochemical impedance spectra of Li-S cells with (a) CG and (b) LPAMPS@CG separators before and after cycling

Table 2.1. Fitted values for the equivalent circuit elements by simulation of impedance spectra in Figure 2.12a-b

		CPE_{int}			CPE_{dl}			CPE_{dif}	
	R_e (Ω)	Y_1 (Ω^{-1} s^n)	n_1	R_{int} (Ω)	Y_2 (Ω^{-1} s^n)	n_2	R_{ct} (Ω)	Y_3 (Ω^{-1} s^5)	n_3
CG before cycling	9.53	-	-	-	9.09E-5	0.85	120.3	3.64E-2	0.61
CG after cycling	4.39	-	-	-	2.68E-5	0.80	72.14	3.45E-2	0.56
LPAMPS@CG before cycling	8.47	3.65E-5	0.84	58.8	8.21E-4	0.84	21.97	3.01E-2	0.56
LPAMPS@CG after cycling	4.20	6.15E-6	0.8	7.67	1.84E-4	0.8	7.36	1.72E-2	0.40

Table 2.1 lists the fitted values for all of the equivalent circuit elements. The R_{ct} value provides an insight into electrode reaction kinetics. It can be clearly seen from table 2.1 that the Li-S cell with LPAMPS@CG separator presented lower R_{ct} values than the cells with CG separator. The significantly reduced R_{ct} value of the

cell with LPAMPS@CG is associated with the improved electrolyte retention capacity and lithium ion conductivity, which originates from the negatively charged $–SO_3^-$ groups present in LPAMPS (Zhang et al., 2018c). Moreover, the lower R_{ct} value contributed to the improved electrode reaction kinetics (Yang et al., 2018a). Further, a considerable reduction is observed in R_{int} and CPE_{dif} elements of the cycled cells with LPAMPS@CG separator, which indicates better lithium ion diffusion ability. This is due to the reason that the LPAMPS coated separator can hold much more electrolyte within the separator facilitating fast ion transport (Zhang et al., 2018c). The above EIS results can be considered as an additional support for the better cycling and rate performance offered by the cell with LPAMPS@CG separator.

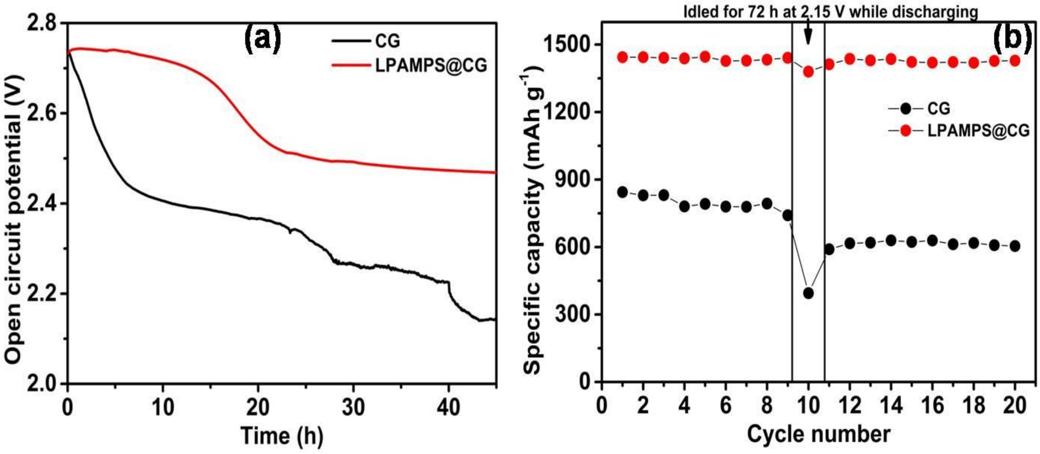

Figure 2.13. (a) Self discharge behaviour of Li-S cells with CG and LPAMPS@CG separators and (b) cycling performance of the cells idled at 2.15 V at the 10th discharging cycle

Identifying the cell's self-discharge characteristics is important for both laboratory scale testing and practical applications (Wang et al., 2016c). For practical applications, shelf life of fresh cell is noteworthy. A fully charged cell at rest always causes rapid capacity decay mainly due to the PS shuttling phenomena. Therefore, alleviating self-discharge of a fully charged cell is a challenge for a practical LSB. To evaluate the self-discharge behaviour of CG and LPAMPS@CG separators, the OCV of the cells were measured as a function of time and shown in Figure 2.13a. The OCV of Li-S cell with CG quickly degrades to 2.14 V within 45 h (capacity retention of 78.3%), which indicates the reduction from higher to lower-order PSs during self-discharge (Suriyakumar et al., 2019). At the same time, the self-discharge is considerably prevented in the cell with LPAMPS@CG membrane, and an OCV of 2.47 V is maintained with 90.4% capacity retention.

To further understand the influence of self-discharge on cell performance, the galvanostatic charge-discharge studies were carried out. After continuous 10 charge-discharge cycles, the cells were rested for 72 h, and then cycled further (Yang et al., 2018a). During the first discharge after rest (11th cycle), the capacity decreases drastically for the cell with CG separator (Figure 2.13b), indicating obvious self-discharge. On the second discharge after rest (12th cycle), the cells restore partial capacity. Even on further cycles, the capacity lost during rest could not be recovered completely. On the other hand, the cell with LPAMPS@CG membrane exhibits no apparent loss of discharge capacity even after rest time, indicating weak self-discharge (Wang et al., 2016c).

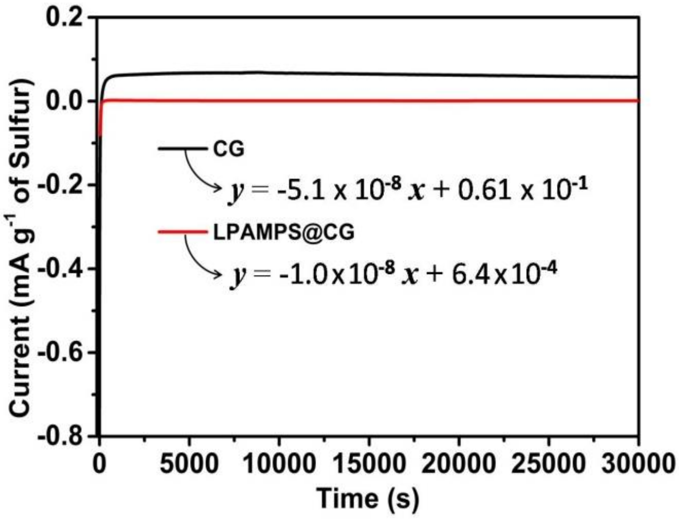

Figure 2.14. Shuttle current measurements of cells containing CG and LPAMPS@CG membranes

The rate of the redox shuttle process can be estimated by quantifying the current passing through the cell under potentiostatic control, as proposed by Moy et al. (Moy et al., 2015). Normally, the potential of a cell decreased steadily at rest because of the PS shuttling process. To retain a constant cell potential, a Faradaic current was supplied in order to balance the PS flow, which is measured as the “shuttle current”. As shown in Figure 2.14, the variation of shuttle current for Li-S cells with CG and LPAMPS@CG separator was measured at 2.3 V as a function of time. The current-time profile exhibited an initial transient arising from a small disagreement between the OCV and hold voltage, and then immediately approached a steady-state that was directly related to the shuttle current (Hu et al., 2017). The rate of decrease of shuttle current was obtained by linearly fitting the region of steady state current using the equation (Moy et al., 2015):

$$y = mx + C \tag{2.3}$$

where y, x, C and m represents current, time, y-intercept and slope, respectively. Usually, a linear decay of shuttle current is observed for Li-S cells and the value of slope (m) denotes the fade in shuttle current. It is evident from Figure 2.14 that the cell with PAMPS@CG separator presented the minimal current decay with time compared to the cell with CG separator. The magnitude of the shuttle current also follows the similar trend. The Li-S cell with LPAMPS@CG exhibits significantly smaller shuttle current than the cell with the CG, which implies significant elimination PS shuttling. The reduction in the rate of shuttle current decay as well as the magnitude of shuttle current directly reflects in the Li-S cell performance, as observed in charge-discharge behaviour and self-discharges.

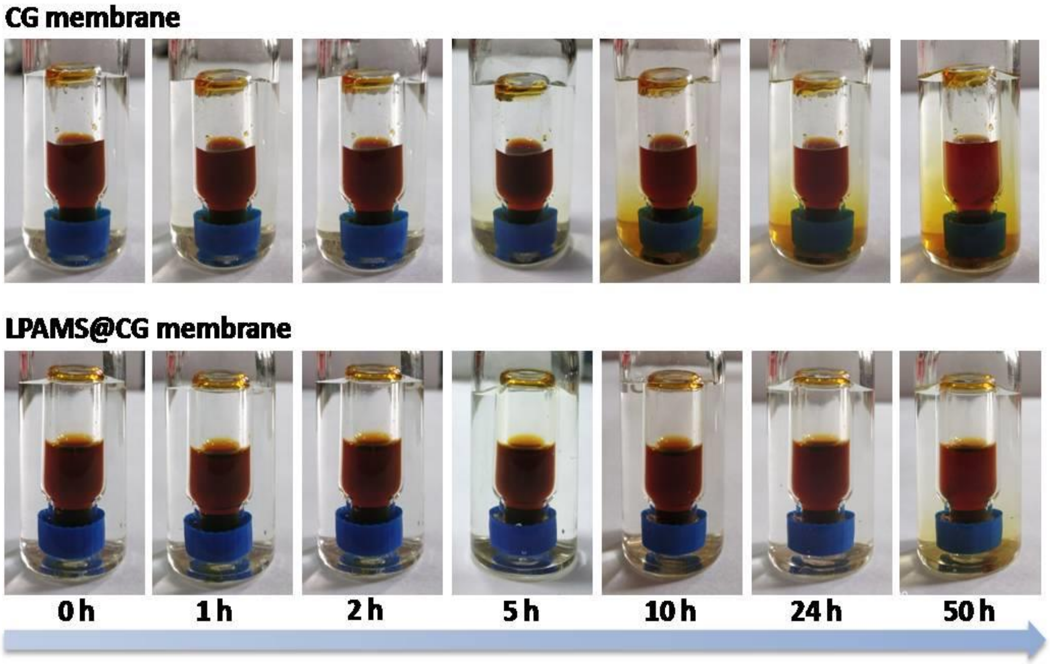

Figure 2.15. Digital photographs of PS crossover across the CG and LPAMPS@CG membranes

In order to assess the PS rejection ability of LPAMPS@CG over CG separator, we conducted a simple visible test. As shown in Figure 2.15, the large outer vial contains 1:1 v% DME:DOL blank electrolyte solution and the small inner vial contains 0.5M Li_2S_6 in blank electrolyte (Yang et al., 2018a). The separators were kept as a septum beneath the small vial's cap and PS crossover was recorded with time using a digital camera. As time passes, Li_2S_6 in the small vial diffuses across the separator into the large vial containing blank electrolyte. As expected, the pristine CG could not block the PS within the small vial due to its porous nature, as a consequence colourless electrolyte in the large vial turned to yellow within 10 h. Interestingly, LPAMPS@CG separator effectively hinder the PS diffusion, as we spot only slight yellow coloration in blank electrolyte even after 50 h. The excellent PS rejection capacity of LPAMPS@CG could be attributed to the coulombic repulsion offered by negatively charged sulfonic acid group in LPAMPS polymer.

2.3.4. Post-Mortem Analysis of Cycled Cells

To further evaluate the role of LPAMPS@CG separator in suppressing the PS shuttle mechanism, the Li-S cells were disassembled after 100 cycles. The CG and LPAMPS@CG separators obtained from the disassembled cells were utilized directly without any washing process.

The surface morphology of the LPAMPS@CG and CG separator facing cathode and anode were observed from SEM micrographs, and corresponding EDS spectra were also recorded. Compared to the fresh separators (Figure 2.3a-b), the cycled one exhibits a denser structure with surface deposits which arises from the accumulation of PSs and electrolyte salts (Figure 2.16a-b). The EDS spectrum (Figure 2.16e-f) further confirms the distribution of sulfur species and the electrolyte on the separator. The PSs deposited on the separator will hardly take part in the redox reactions, which eventually leads to rapid capacity fading of Li-S cell. Moreover, this 'dead sulfur' got trapped in the pores and the surface of CG and ultimately blocks lithium ion diffusion pathways (Kong et al., 2017). Figure 2.16c-d presented SEM micrographs of CG and LPAMPS@CG separators in anodic side, respectively. The effective blocking of PSs in cathodic compartment by LPAMPS assured a comparatively clean surface of separator in contact with lithium anode (Figure 2.16g-h).

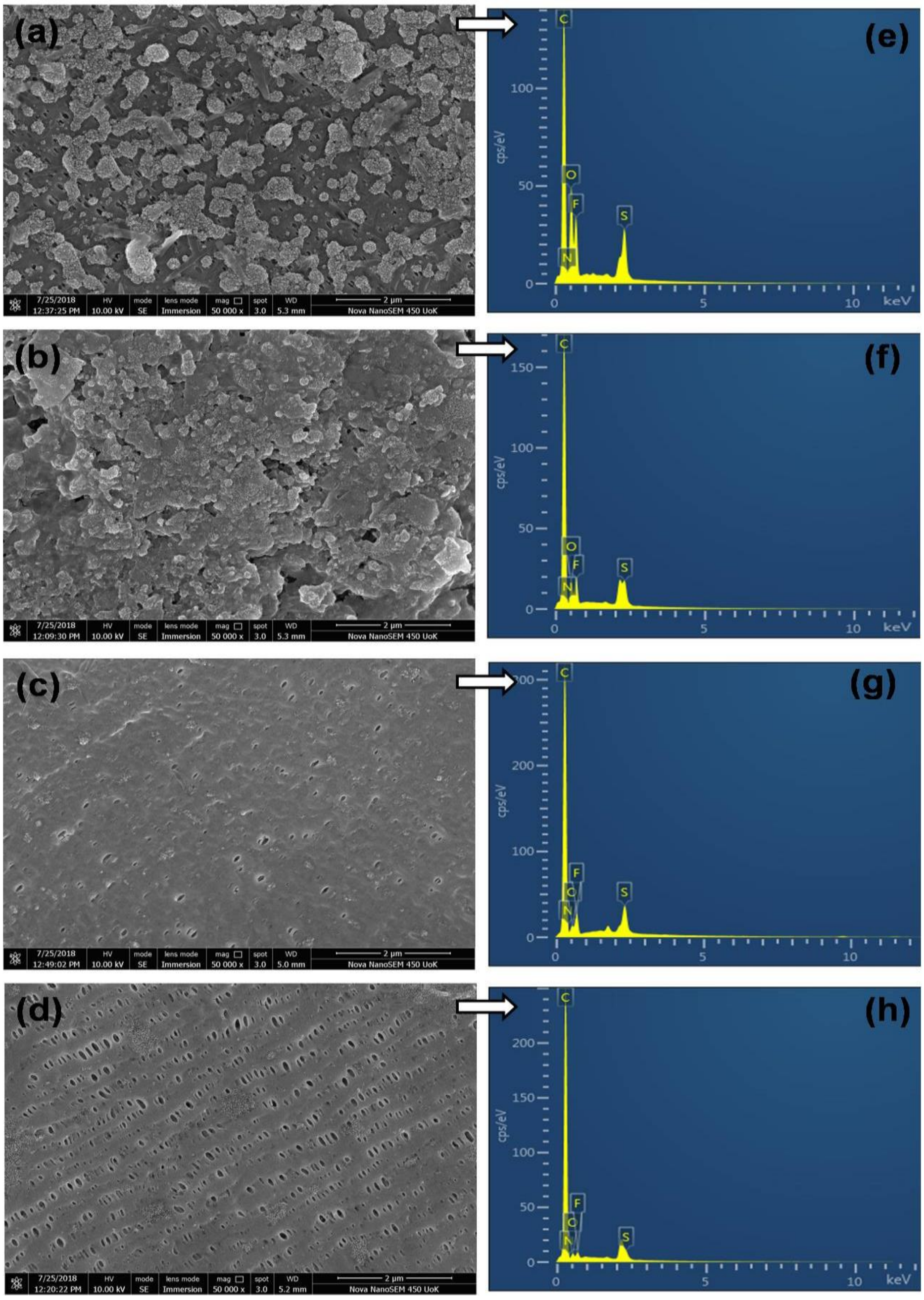

Figure 2.16. Morphology and composition of cycled separators after 100 cycles. SEM images of (a) CG (b) LPAMPS@CG separators on cathode sides and (c) CG (d) LPAMPS@CG separators on anode sides and (e, f, g, h) are the corresponding EDS spectra

Figure 2.17 shows the deconvoluted spectrum of S2p for lithium anodes in the discharged state separated from the cells with CG (Figure 2.17a) and LPAMPS@CG

(Figure 2.17b) membranes after 100 cycles. A broad peak around 168 eV is common for both cells, which could be attributed to the aerobic oxidation of sulfur species upon decrimping the cell (Lang et al., 2015). The relatively small intensity of peaks around 163.5 and 164.1 eV for LPAMPS@CG indicate lower abundance of PSs and Li_2S, respectively (Suriyakumar et al., 2019). This observation clearly supports the proposed mechanism of PS retention within cathode compartment for the cell containing LPAMPS@CG separator.

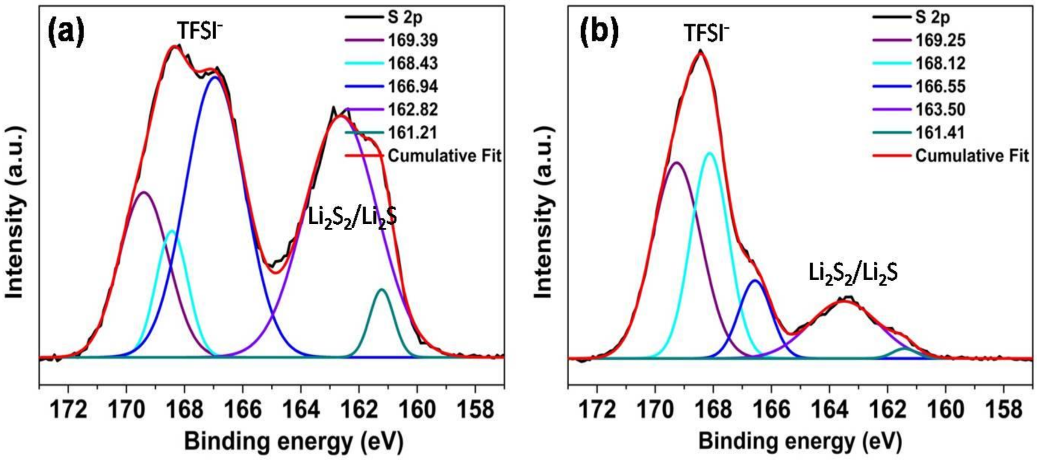

Figure 2.17. Deconvoluted S2p spectra for lithium anodes in the discharged state separated from the cells with (a) CG and (b) LPAMPS@CG membranes

2.4. Conclusion

In summary, a highly permselective LPAMPS modified separator (LPAMPS@CG) was prepared to improve capacity and cycling stability of Li-S cell. The negatively charged sulfonic acid groups present on the LPAMPS impart selective diffusion of lithium ions, at the same time repelling PS anions via coulombic interactions. Besides, the LPAMPS@CG separator possesses excellent electrolyte wettability, interfacial contact and ionic conductivity. The Li-S cell (areal sulfur loading of 0.9 mg cm^{-2}) containing LPAMPS@CG separator exhibited significant improvement in the battery performance, with a high initial capacity of 1486 mAh g^{-1} and coulombic efficiency of ~99%. It is noted that the LPAMPS@CG separator impedes shuttle effect by inhibiting PS crossover towards lithium anode, resulting a stable discharge capacity of 1060 mAh g^{-1} even after 200 cycles. In general, the

LPAMPS coating on commercial separator serves as a facile and effective strategy for future LSB technology, mitigating self-discharge behaviour.

CHAPTER 3

SUPPRESSING SHUTTLE EFFECT USING LITHIATED PEDOT:PSS DECORATED SEPARATOR FOR HIGH-PERFORMANCE LITHIUM-SULFUR BATTERY

Poly(3,4-ethylenedioxythiophene):poly(styrene sulfonate) (PEDOT:PSS) is one of the most investigated and extensively used conducting polymers with wide applications. In this chapter, we present lithiated PEDOT:PSS coated Celgard (Li^+*-PEDOT:PSS@CG) separator with dual role to concurrently inhibit polysulfide shuttling and promote *Li^+* selective diffusion. The proton of the sulfonic acid group in PEDOT:PSS is exchanged with *Li^+* during lithiation and the resulted lithiated PEDOT:PSS possesses *Li^+* transporting capability and functions as a single-ion conductor. The negatively charged sulfonic acid groups present in PSS act as an electrostatic shield for soluble lithium polysulfides through coulombic repulsion, whereas PEDOT provides chemical interactions and form a chelated coordination structure with insoluble polysulfides (*Li_2S/Li_2S_2*) due to the presence of strong electronegative atoms (O and S). The dual shielding effect can effectively suppress the polysulfide shuttling process by confining lithium polysulfides within the cathode compartment of the cell. Moreover, the *Li^+*-PEDOT:PSS@CG membrane possesses excellent electrolyte wettability, interfacial properties and ionic conductivity. The Li-S cell containing *Li^+*-PEDOT:PSS@CG separator exhibited significant improvement in the electrochemical performance and anti-self-discharge characteristics. The cell shows initial capacity of 1360 mAh *g^{-1}* and capacity retention of 1049 mAh *g^{-1}* over 300 cycles with 3.9 mg *cm^{-2}* sulfur loading.*

3.1. Introduction

Recently, researchers adopted various strategies to hinder the so-called “shuttle effect” in LSB. The major strategies can be categorized into two aspects: cathode functionalization and separator modification (He et al., 2018a; Zhang et al., 2018c). Currently, modification of separator attained greater attention because of its ability to restrain the S_x^{2-} within the cathode compartment either by physical hindrance and/or chemical bonding without affecting the utilization of active material (Yu et al., 2015). Therefore, modification of separator (polyolefin membranes like

Celgard) with functionalized coatings (carbon, inorganic oxides and polymers) can be considered as a reliable approach to achieve “shuttle-free” high energy LSBs (Kim et al., 2016b; He et al., 2019). Among various functional coatings on separator, conducting polymers with functional groups are beneficial to reduce the interfacial resistance along with alleviating the polysulfide diffusion towards anode compartment (Rana et al., 2019). Moreover, the commercial Celgard separators have a hydrophobic surface, which severely affects their electrolyte retention ability. Polymer coating on separator makes its surface hydrophilic, thereby improve the electrolyte uptake (Li et al., 2015a). The presence of polar negative groups like $–SO_3^{−}$ and $–COO^{−}$ in the polymer chains not only suppresses S_x^{2-} crossover by Coulombic repulsion, but also renders lithium ion permselectivity via coulombic attraction. In addition, the presence of polar heteroatoms in the polymer shells imparts strong interactions with S_x^{2-} to build chemical bonds, thereby subdue the polysulfide dissolution (Fang et al., 2017). The separators modified with the polymers containing polar functional groups like Nafion (Bauer et al., 2014), PDA (Zhang et al., 2015b), PEG (Luo et al., 2016), PEO (Rana et al., 2019), PAA (Song et al., 2018b), PANi (Chang et al., 2015b), PAN (Zhu et al., 2016b), sulfonated polystyrene (Guo et al., 2018), SSEBS (Yang et al., 2018a), polyamide acid (Luo et al., 2018), PEDOT:PSS (Lee et al., 2018b), SPEEK (Babu et al., 2018) and carboxylate anchored polyvinyl alcohol (Jiang et al., 2018) have proven efficient in improving electrochemical performance of LSB. The separator coated with lithiated polymer act as a single ion conductor providing transport channels for lithium ions, which further contribute to the performance of LSB. The lithiated polymers like lithiated nafion (Jin et al., 2012), lithiated perfluorinated sulfonic acid (Shi et al., 2017), lithiated SSEBS (Yang et al., 2018a) and lithiated SPEEK (Babu et al., 2018) have been explored to modify the polyolefin separator. It has been reported that the lithiated polymers with polar negatively charged groups selectively permits the ion hopping of positively charged lithium ions and subsides the passage of negatively charged ions (S_x^{2-}) (Lu et al., 2017b).

PEDOT:PSS is one of the most investigated and extensively used conducting polymers with wide applications, especially as electrode material in various energy conversion and storage devices such as solar cells, supercapacitors, fuel cells, batteries and thermoelectric devices because it possesses a number of unique properties, such as solution-processability, high electrical conductivity (up to 4600 S cm^{-1}) and good chemical stability (Sun et al., 2015c; Ghosh et al., 2016). PEDOT: PSS has been reported as conducting coating on sulfur cathode, functional separator coating and conductive binder to obtain improved electrochemical properties in LSB (Lee et al., 2015; Pan et al., 2016; Lee et al., 2018b). In this chapter, we present lithiated PEDOT:PSS (Li^+-PEDOT:PSS) coated Celgard separator with dual role to concurrently inhibit polysulfide shuttling and promote lithium ion selective diffusion. The proton of the sulfonic acid group in PEDOT:PSS is exchanged with lithium ions during lithiation and the resulted lithiated PEDOT:PSS possesses lithium ion transporting capability and functions as a single-ion conductor. The Li^+-PEDOT:PSS coating on commercial Celgard separator (Li^+-PEDOT:PSS@CG) effectively reduces interfacial resistance and the $–SO_3^-$ groups inhibits the migration of polysulfides by “electrostatic repulsion” effect. Consequently, the Li-S cell employing Li^+-PEDOT:PSS@CG exhibits excellent electrochemical performance and anti-self-discharge characteristics compared to the uncoated Celgard separator (CG).

3.2. Materials and Methods

3.2.1. Materials

Poly(3,4-ethylenedioxythiophene)-poly(styrenesulfonate) solution (PEDOT:PSS, 3.0-4.0% in water, high-conductivity grade, Sigma Aldrich), all other chemicals are as mentioned in section 2.2.1.

3.2.2. Synthesis of Lithiated PEDOT:PSS (Li^+-PEDOT:PSS)

Lithiation of PEDOT:PSS was carried out using a simple ion-exchange process. 1 g of PEDOT:PSS solution was added to a solution of 0.1M LiOH in distilled water. The resulted solution was stirred for 2 h at room temperature followed by vacuum drying at 80 °C for 24 h to obtain Li^+-PEDOT:PSS. The chemical formula and synthetic scheme of Li^+-PEDOT:PSS was given in Figure 3.1.

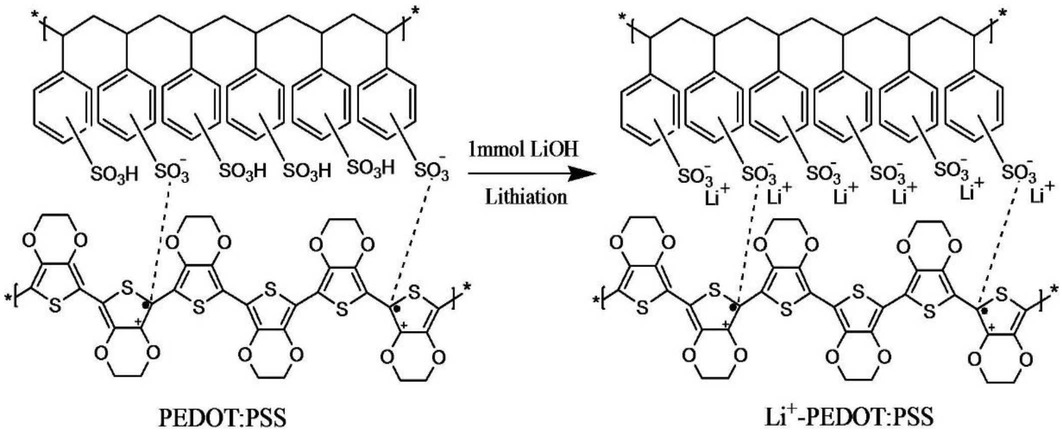

Figure 3.1. Synthetic scheme of Li$^+$-PEDOT:PSS

3.2.3. Preparation of Li$^+$-PEDOT:PSS Coated Celgard Separator (Li$^+$-PEDOT:PSS@CG)

The Li$^+$-PEDOT:PSS coated Celgard separator was prepared by doctor blade coating technique. Briefly, 33 mg of poly(vinylidene fluoride) (PVDF) as binder was dissolved in 2 mL of N-methyl-2-pyrrolidone (NMP). 33 mg of Li$^+$-PEDOT:PSS and 33 mg of super P carbon was added to this solution and the mixture was stirred at room temperature for 5 h to obtain uniform slurry. The obtained slurry was coated onto one side of commercial Celgard 2320 separator (CG) and dried in vacuum oven at 60 °C for 12 h. The presence of super P carbon helps to enhance electronic conductivity and favour the adsorption of intermediate polysulfides, thereby hamper the serious shuttling mechanism in Li-S cell. The overall thickness of Li$^+$-PEDOT:PSS@CG separator was around 34 µm.

3.2.4. Coin Cell Assembly

A standard 2032 type coin cell was assembled by the procedure described in the section 2.2.6, employing MWCNT@S electrode with an areal sulfur loading of 3.9 mg cm^{-2}, Li$^+$-PEDOT:PSS@CG separator, and Li metal as the counter electrode.

3.2.5. Material and Electrochemical Characterization

All characterizations were done by the techniques described in section 2.2.7

3.2.6. PS Diffusion Studies

Li_2S_6 solution was prepared as described in the section 2.2.4. The schematic representation of experimental setup used for visual PS diffusion test is presented in Figure 3.2. As illustrated in the Figure 3.2, the large outer vial contains 1:1 v% DME:DOL blank electrolyte solution and the small inner vial contains 1 M Li_2S_6 in DME:DOL (1:1 v%). The separators were kept as a septum beneath the small vial's cap. The diffusion of the yellowish-brown Li_2S_6 through the separators was visually examined by comparing the colour change of the transparent blank electrolyte and recorded using a digital camera.

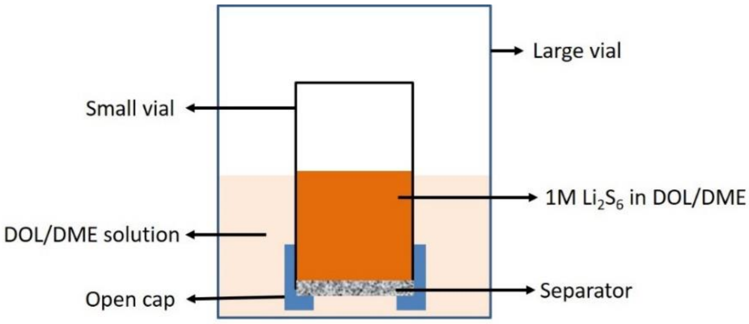

Figure 3.2. Schematic representation of experimental setup used for visual PS diffusion test

3.3. Results and Discussion

3.3.1. Material Characterization

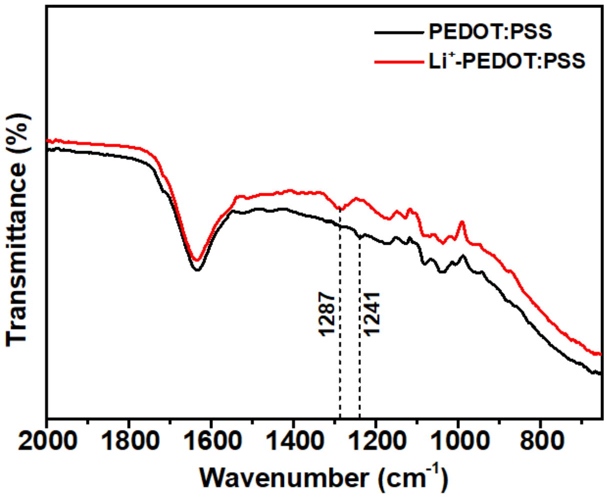

Figure 3.3. FT-IR spectra of PEDOT:PSS and Li^+-PEDOT:PSS

To impart the property of lithium ion selectivity to PEDOT:PSS, the -SO_3H (from PSS) are lithiated using a simple ion-exchange procedure. FT-IR spectra was recorded to confirm the lithiation of PEDOT:PSS. Figure 3.3 presents the FT-IR spectra of pristine PEDOT:PSS and Li^+-PEDOT:PSS. Li^+-PEDOT:PSS exhibits similar FT-IR bands to those of the pristine PEDOT:PSS. However, lithiation of PEDOT:PSS results in a shift of the absorption band corresponding to the -SO_3H group of PSS towards the higher wavenumber (from 1241 cm^{-1} for PEDOT:PSS to 1287 cm^{-1} for Li^+-PEDOT:PSS). Such a shift in the absorption band mostly originate from the disruption of the -SO_3H bond, resulting in the formation of -SO_3Li (Jin et al., 2012).

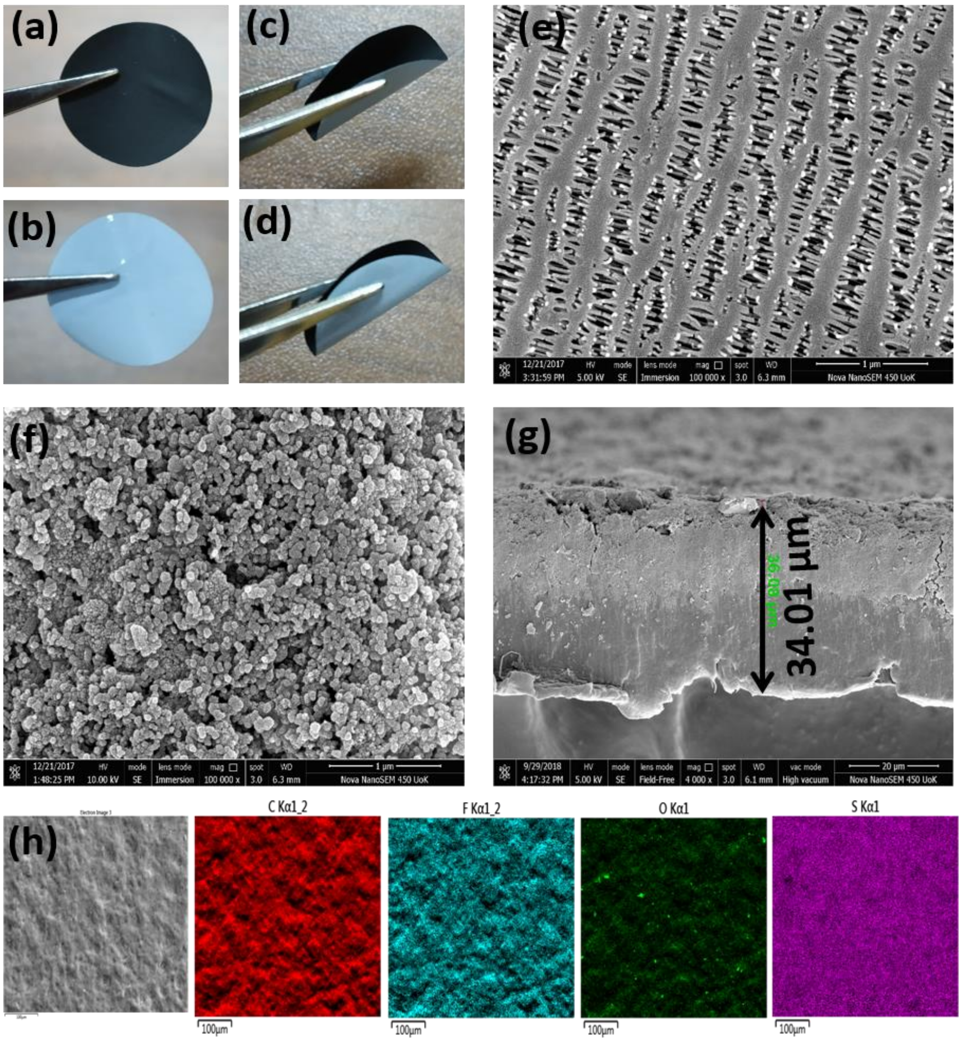

Figure 3.4. Digital photographs of Li^+-PEDOT:PSS@CG membrane (a) coated side (b) uncoated side (c-d) folding test. SEM micrographs of (e) CG (f) Li^+-PEDOT:PSS@CG. (g) Cross-section SEM micrograph of Li^+-PEDOT:PSS@CG. (h) Elemental mapping of the Li^+-PEDOT:PSS@CG

The digital photographs of Li$^+$-PEDOT:PSS-coated commercial CG membrane is given in Figure 3.4a-b. The excellent adhesion property of Li$^+$-PEDOT:PSS onto the CG membrane is illustrated by the folding test, as shown in the Figure 3.4c-d. The surface morphology of CG and Li$^+$-PEDOT:PSS@CG membranes was observed by SEM micrographs (Figure 3.4 e-f). As depicted in Figure 3.4f, a dense coating of Li$^+$-PEDOT:PSS was wrapping the nanopores on the surface of CG. The conducting Li$^+$-PEDOT:PSS coating on the cathodic surface of the CG could physically obstruct the migration of polysulfide anions towards the anodic compartment and simultaneously augment the transport of lithium ions (Zeng et al., 2016; Lee et al., 2018b). Elemental mapping of the Li$^+$-PEDOT:PSS@CG (Figure 3.4h) shows the uniform distribution of carbon, oxygen, fluorine and sulfur, which further confirms the fine dispersion of Li$^+$-PEDOT:PSS with super P and PVDF binder on the surface of CG. The cross-section SEM micrograph of Li$^+$-PEDOT:PSS@CG further expose a dense structure with a thickness of ~36 µm (Figure 3.4g).

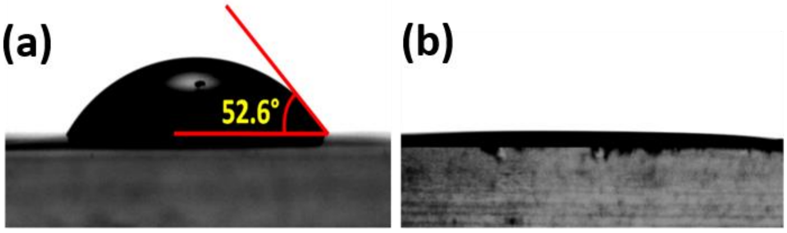

Figure 3.5. Contact angle shots of (a) CG and (b) Li$^+$-PEDOT:PSS@CG

The wettability of membranes with the electrolyte generally plays a vital role in determining the electrochemical performance of the Li-S cell such as interface resistance, lithium ion transportability, etc. Figure 3.5 shows the static contact angle measurements with the sessile drop method. The CG membrane exhibits a contact angle of 52.6° whereas the Li$^+$-PEDOT:PSS@CG membrane exhibits a contact angle close to zero indicating high wettability of the membrane with non-aqueous liquid electrolyte. The increased wettability of the Li$^+$-PEDOT:PSS@CG results from the presence of hydrophilic -SO_3^- group on Li$^+$-PEDOT:PSS. The polar electrolyte droplet is immediately absorbed by the hydrophilic group (-SO_3^-) to form large clusters in the polymer domain, thereby increases the wettability of the separator (Blake et al., 2005; Long et al., 2016). The wettability study affirms that the Li$^+$-PEDOT:PSS coating can tune the surface characteristics of CG and can lend hydrophilic nature.

For authenticating the “electrostatic repulsion” mechanism rendered by Li$^+$-PEDOT:PSS@CG separator towards the polysulfide anions, zeta potential was measured for Li$^+$-PEDOT:PSS using non-aqueous electrolyte used in the cycling studies. The zeta potential of Li$^+$-PEDOT:PSS was found to be -43.5 mV as shown in the Figure 3.6, confirming the driving force between Li$^+$-PEDOT:PSS and polysulfides. Since the polysulfides remain anionic in the electrolyte and Li$^+$-PEDOT:PSS exists as negatively charged, a repulsive force arises between Li$^+$-PEDOT:PSS coating on CG and polysulfide anions (Lei et al., 2018).

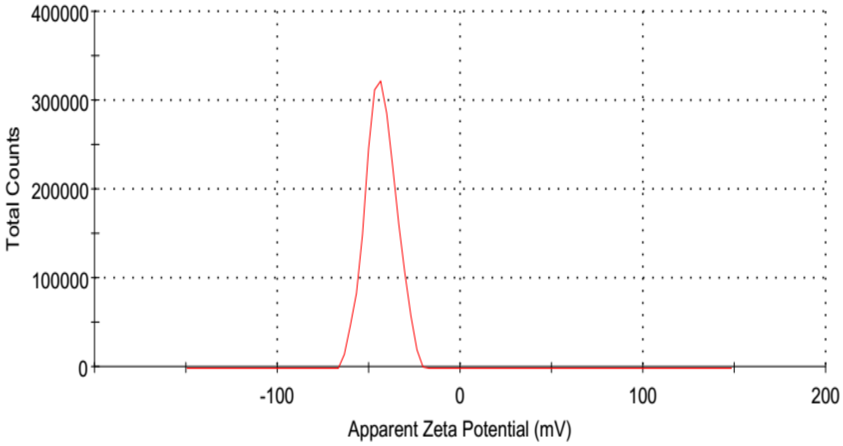

Figure 3.6. Zeta potential distribution of Li$^+$-PEDOT:PSS in non-aqueous electrolyte

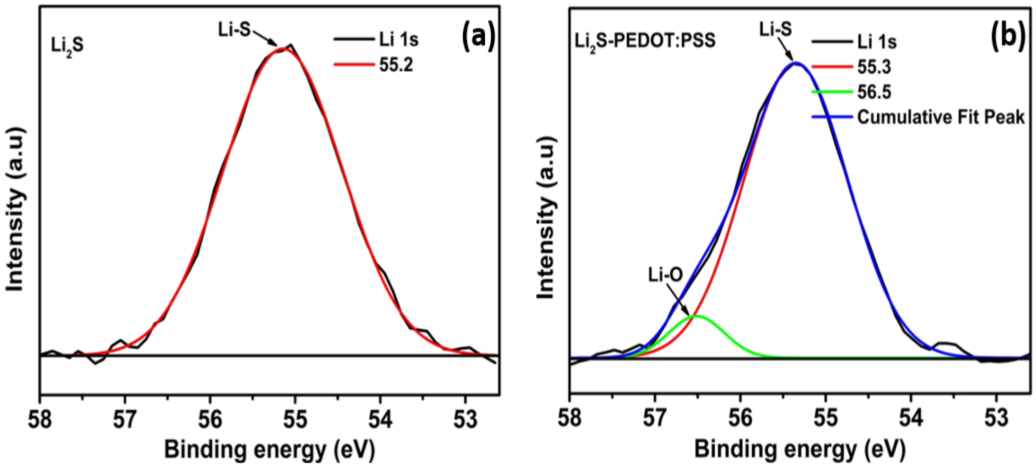

Figure 3.7. XPS spectra of the Li1s peak in (a) pristine Li$_2$S and (b) Li$_2$S-PEDOT:PSS, together with their respective fitted peaks.

The PEDOT:PSS with abundant -SO_3^- groups (from PSS) can effectively restrain the soluble lithium PSs (Li_2S_n, $4 \leq n \leq 8$) through mutual coulombic repulsion. On the contrary, the strong electronegative atoms (S and O) present in the PEDOT can bind strongly with insoluble lithium PSs (Li_2S_2 and Li_2S) through coordination-like interactions between the lone pairs on electronegative atoms and the lithium in Li_2S_2/Li_2S (Abbas et al., 2016). The presence of such Li-O and Li-S interactions are confirmed by using XPS measurements, which is known to be very sensitive to the chemical environment (Seh et al., 2014). We see that the Li1s XPS spectrum of pristine Li_2S can be fitted with a single peak with a binding energy of 55.2 eV (Figure 3.7a), which corresponds to Li in the Li-S bond. In contrast, the Li1s spectrum of the Li_2S-PEDOT:PSS shows asymmetric broadening towards a higher binding energy (Figure 3.7b), which indicates a change in the chemical environment experienced by Li. This spectrum can be fitted using two peaks: the peak at 55.3 eV corresponds to Li in the Li-S bond, while the additional peak at 56.5 eV can be attributed to Li-O interaction in the Li_2S-PEDOT:PSS (Liu et al., 2020a).

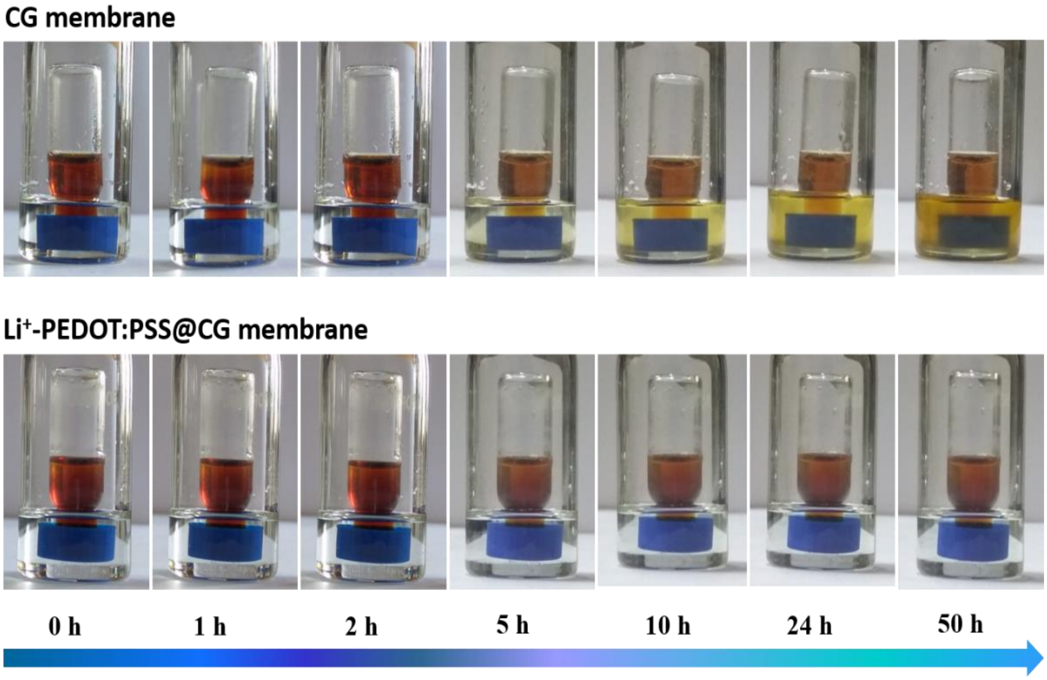

Figure 3.8. Digital photographs of polysulfide crossover across the CG and Li^+-PEDOT:PSS @CG membranes

To visually confirm the PS rejection ability of CG and Li^+-PEDOT:PSS@CG membranes, PS diffusion tests were conducted (Figure 3.8). As time passes, Li_2S_6 in the small vial diffuses across the membrane into the large vial containing blank electrolyte (Yang et al., 2018a). As expected, the pristine CG could not block the polysulfide within the small vial due to its porous nature, as a consequence colourless electrolyte in the large vial turned to yellow within 10 h. On the other hand, Li^+-PEDOT:PSS@CG separator effectively hinder the polysulfide diffusion, as we spot only slight yellow coloration in blank electrolyte even after 50 h. The excellent polysulfide rejection capacity of Li^+-PEDOT:PSS@CG could be attributed to the coulombic repulsion offered by the negatively charged $–SO_3^-$ group in Li^+-PEDOT:PSS (Ahn et al., 2019).

3.3.2. Electrochemical Evaluation

The lithium ion conductivity as a function of inverse temperature for CG and Li^+-PEDOT:PSS@CG were measured and shown in Figure 3.9. Irrespective of the membrane used, the ionic conductivity increases with increasing temperature. The increase in ionic conductivity of Li^+-PEDOT:PSS@CG membrane was credited to the higher uptake of electrolyte by the hydrophilic $-SO_3^-$ group present in the Li^+-PEDOT:PSS coating (Hencz et al., 2019).

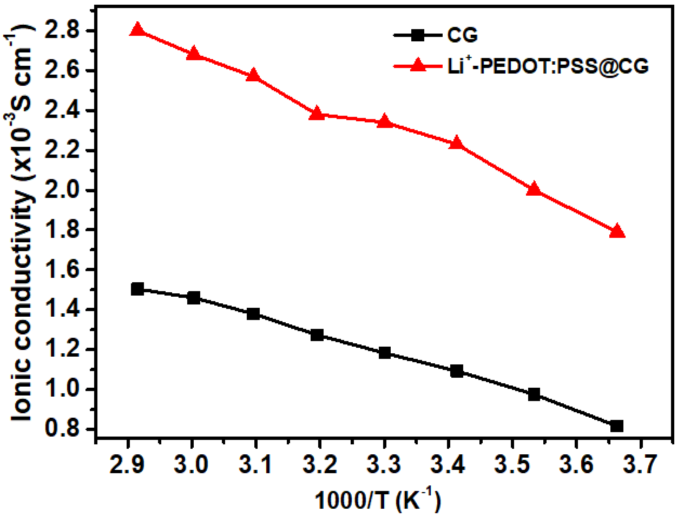

Figure 3.9. Ionic conductivity of CG and Li^+-PEDOT:PSS@CG separator

The lithium ion transference number (t_{Li^+}) was calculated from chronoamperometry and EIS analysis, employing equation (2.1). The chronoamperometric curves of Li/membrane/Li symmetric cells were recorded till it reached steady state and presented in Figure 3.10. Inset: EIS spectra of the cells before and after DC polarization with a bias voltage of 10 mV (Zhao et al., 2008; Karuppasamy et al., 2017).

For Li$^+$-PEDOT:PSS@CG separator, the obtained t_{Li^+} value is 0.72, which is almost twofold higher than the CG separator (0.38). Lithium ions usually exists as solvated Li$^+$-ether molecules in the ether-based electrolytes, which is much larger than TFSI$^-$ ions. These larger solvated molecules suppress the transport of lithium ions, thereby relatively lower t_{Li^+} values (Zhou et al., 2018; Callsen et al., 2017). Meanwhile, the high t_{Li^+} for the cells with Li$^+$-PEDOT:PSS@CG can be attributed to the -SO_3^- group present along the Li$^+$-PEDOT:PSS chain, which is well-known for its ether coordination sites to promote the dissociation of Li$^+$-ether molecules facilitating the transport of lithium ions (Yamada et al., 2013; Wang et al., 2016d; Jiang et al., 2018).

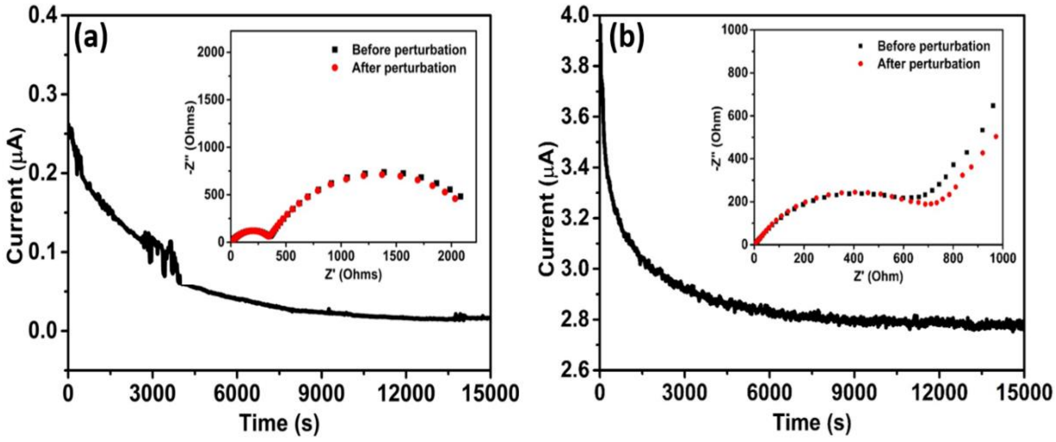

Figure 3.10. Chronoamperometric curves of (a) CG and (b) Li$^+$-PEDOT:PSS@CG membranes. Inset: EIS Nyquist plots of symmetric Li/membrane/Li cells before and after perturbation

In order to determine the interfacial stability of CG and Li$^+$-PEDOT:PSS@CG membranes with lithium metal, a symmetrical cell consisting of Li/membrane/Li was assembled and its interfacial resistance, R_i was measured as a function of time at 25 °C and illustrated in Figure 3.11. The symmetric cell assembled with PEDOT:PSS@CG membrane demonstrated lowest R_i. This observation further supports the earlier observations for ionic conductivity studies and t_{Li^+} calculations (Raja and Stephan, 2014).

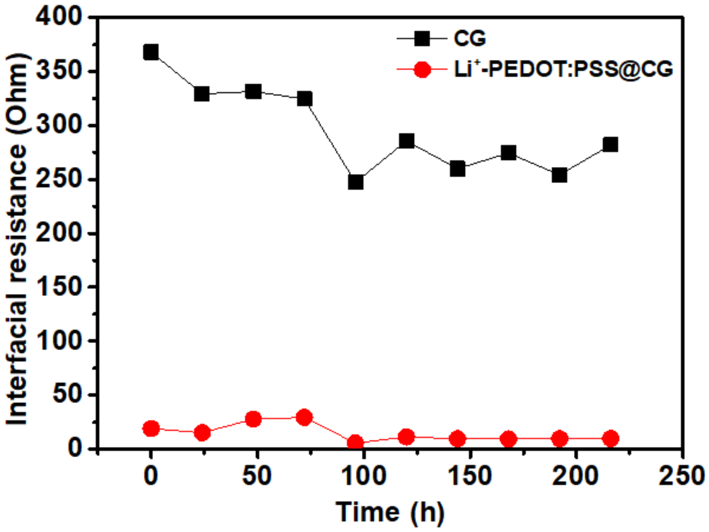

Figure 3.11. Interfacial resistance vs time measurements of (a) CG and (b) Li^+-PEDOT:PSS@CG separator

3.3.3. Cell Performance Evaluation

The electrochemical performance of Li-S cells with CG and Li^+-PEDOT:PSS@CG separators was investigated by CV, galvanostatic charge-discharge and EIS measurements. Cyclic voltammograms of Li-S cells with CG and Li^+-PEDOT:PSS@CG are shown in the Figure 3.12. The cathodic sweep presents two peaks, one around 2.3 V (peak 1) and another around 2 V (peak 2). Peak 1 arises from the conversion of cyclo-S_8 to soluble higher order PSs (Li_2S_n, $4 \leq n \leq 8$). Peak-2 is the main peak in the cathodic sweep corresponding to the reduction of higher order PSs into lower order lithium sulphides (Li_2S_2/Li_2S), which will deliver significant part of cell's capacity. During anodic sweep, a splitted oxidation peak is observed around 2.4V (peak 3), the first peak is due to conversion of Li_2S_2/Li_2S to Li_2S_n (where $4 \leq n \leq 8$) and the next peak is due to further oxidation of Li_2S_n (where $4 \leq n \leq 8$) to elemental sulfur (S_8) (Song et al., 2018b; Yang et al., 2018a; Wild et al., 2015). The cell with CG membrane exhibited broad cathodic and anodic peaks due to the sluggish nature of the conversion kinetics (Elgrishi et al., 2018). In contrast, the cells with Li^+-PEDOT:PSS@CG membrane presented well-defined redox peaks with an increased current density compared to the cells with CG membrane, indicating an improved conversion reaction kinetics and active material utilization (Ghosh and Basu, 2018).

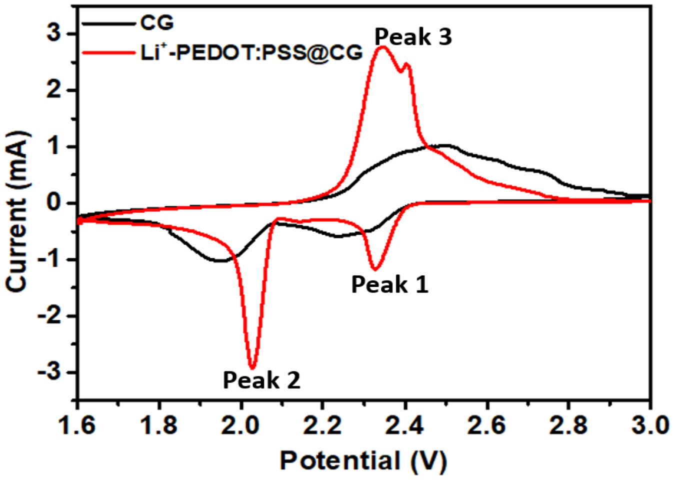

Figure 3.12. CV curves of Li-S cells containing CG and Li$^+$-PEDOT:PSS@CG separators

Further, diffusion coefficient of lithium ions (D_{Li^+}) was calculated from cyclic voltammogram using Randles-Sevcik equation. The calculated values are tabulated in Table 3.1 and it is obvious from the calculated values that diffusion coefficients for Li$^+$-PEDOT:PSS@CG separator are at least an order of magnitude larger than CG. The above result suggests that the Li$^+$-PEDOT:PSS@CG separator render an improved lithium ion mobility compared to CG, thereby expecting significant improvement in the specific capacity and rate capability.

Table 3.1. Diffusion coefficient of lithium ions calculated for Li-S cells with CG and Li$^+$-PEDOT:PSS@CG separator

D_{Li^+} (cm^2 s^{-1})	CG	Li$^+$-PEDOT:PSS@CG
Peak 1	4.84×10^{-7}	3.30×10^{-6}
Peak 2	1.09×10^{-7}	9.10×10^{-6}
Peak 3	4.71×10^{-7}	3.68×10^{-6}

The initial galvanostatic charge-discharge profiles for Li-S cells containing CG and Li$^+$-PEDOT:PSS@CG separator at 0.1C rate are shown in Figure 3.13a. The plateaus observed in the charge-discharge profiles correlates closely with the peak positions in the cyclic voltammogram. Two distinct plateaus are identified in the discharge profile, first one with upper plateau voltage corresponds to the reduction of cyclo-S_8 to soluble higher order PSs (Li_2S_n, $4 \leq n \leq 8$), which is a kinetically fast process. The second plateau at lower voltage results from the conversion of higher order PSs to Li_2S_2/Li_2S, which is a kinetically sluggish process contributing to nearly 75% of cell's capacity. The voltage hysteresis (ΔE) between the discharging and charging curve (at the second discharge plateau) for Li-S cells with CG and Li^+-PEDOT:PSS@CG are 0.34 and 0.18 V, respectively, for the first cycle. The lower ΔE value for Li-S cell with Li^+-PEDOT:PSS@CG indicate lower electrochemical polarization originated from the good electronic and ionic conductivity of the Li^+-PEDOT:PSS coating layer. The high ionic conducting pathway of Li^+-PEDOT:PSS was imparted by the presence of sulfonate groups in its chemical structure (Moorthy et al., 2019). The absence of such ion conducting functional groups in the case of CG causes higher polarization, which in turn results in lower discharge capacity (Puthirath et al., 2019). The Li-S cells with CG and Li^+-PEDOT:PSS@CG separator delivered an initial discharge capacity of 697 and 1360 mAh g^{-1} with 81.3 and 41.6% sulfur utilization, respectively. The high initial discharge capacity of cells with Li^+-PEDOT:PSS@CG is ascribed to good ionic conductivity of Li^+-PEDOT:PSS coating, which provide a larger conductive surface for the conversion of soluble PSs to insoluble Li_2S_n ($n \leq 2$) (Yao et al., 2014).

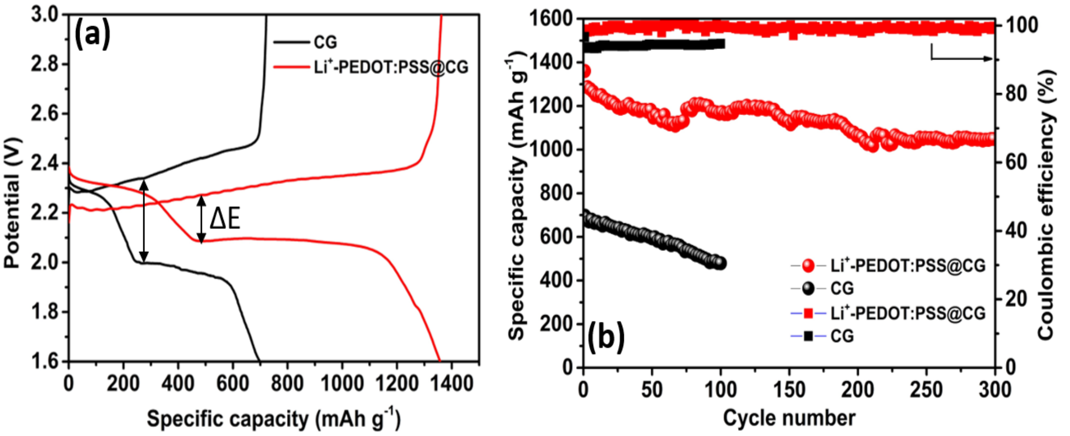

Figure 3.13. (a) Initial charge-discharge profiles of Li-S cell with CG and Li^+-PEDOT:PSS@CG at 0.1C. (b) Cycling performance and coulombic efficiencies at 0.1C rate for Li-S cell with CG and Li^+-PEDOT:PSS@CG

Figure 3.13b compares the cycling performance and coulombic efficiency of Li-S cells containing CG and Li^+-PEDOT:PSS@CG separators at a current density of 0.1C. It is clear from Figure 3.13b that the Li-S cell with Li^+-PEDOT:PSS@CG deliver higher discharge capacity and coulombic efficiency than the cell with CG. The poor capacity retention exhibited by the Li-S cell assembled with CG (68% capacity retained after 100 cycles) might be due to the PS shuttle effect, which occurs as a result of easy migration of higher order PSs in the size range of 1-1.8 nm through the micropores of pristine CG separator towards the lithium metal anode. At the same time, the cell made of Li^+-PEDOT:PSS@CG separator exhibits a capacity retention of 86% (1172 mAh g^{-1}) and 77% (1047 mAh g^{-1}) at 100th and 300th cycles, respectively. The high capacity retention observed in the case of Li^+-PEDOT:PSS@CG is attributed to the presence of $-SO_3^-$ groups (from PSS) which impart PS repulsion ability together with the polar interaction of electronegative atoms (from PEDOT) with lower order lithium PS (Lee et al., 2018b; Babu et al., 2018). Besides, Figure 3.12b shows an improvement in coulombic efficiency of Li-S cell when Li^+-PEDOT:PSS@CG separator is employed. The high coulombic efficiency is an indirect indication of high ionic selectivity and low capacity loss (Wang et al., 2019d). The observed high coulombic efficiency arise from the permselectivity of Li^+-PEDOT:PSS coating, which selectively permeates lithium ions and effectively blocks the PS anions.

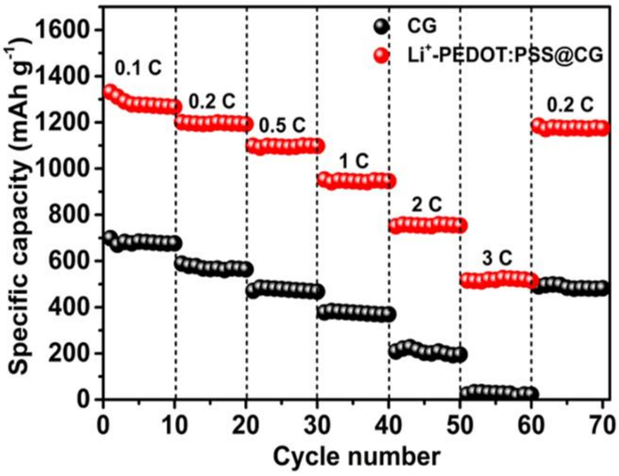

Figure 3.14. Rate capability studies of Li-S cell with CG and Li^+-PEDOT:PSS@CG

The rate capability studies were conducted to compare the performance of Li-S cells with CG and Li^+-PEDOT:PSS@CG separators at different current densities from 0.1 to 3C (Figure 3.14). Consequent cycles at 0.1, 0.2, 0.5, 1, 2, and

3C rates delivered capacities of 1336, 1196, 1099, 952, 750, and 520 mAh g^{-1}, respectively, for Li^+-PEDOT:PSS@CG separator. When the C-rate was reverted back from 3C to 0.2C, a reversible capacity of 1170 mAh g^{-1}, i.e., 97.8% of the original capacity was achieved. On the other hand, pristine CG separator provided discharge capacities of 699, 578, 485, 377, 199, and 36 mAh g^{-1}, respectively, at 0.1, 0.2, 0.5, 1, 2 and 3C. When the discharge current was switched back from 3 to 0.2C, a reversible capacity of 490 mAh g^{-1}, i.e., only 84.7% of the original capacity was recovered. The excellent stability at different C-rates for Li-S cells with Li^+-PEDOT:PSS@CG can be attributed to the effective confinement of PS within the cathode compartment (Lee et al., 2018b).

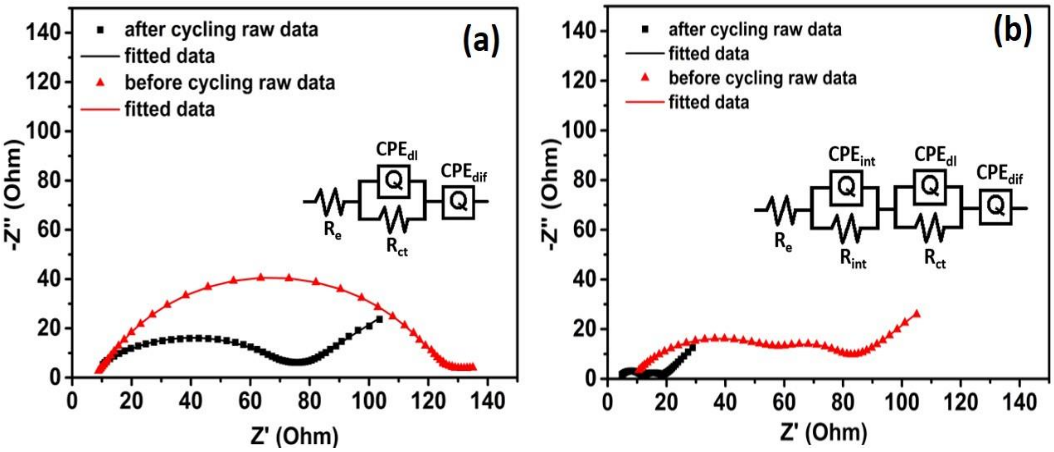

Figure 3.15. Electrochemical impedance spectra of Li-S cells with (a) CG and (b) Li^+-PEDOT:PSS@CG separators before and after cycling

To gain additional insight into the influence of the Li^+-PEDOT:PSS coating on the separator, EIS measurements were carried out for Li-S cells with CG and PEDOT:PSS@CG separator. These measurements were conducted for freshly prepared cells and cycled cells (after 100 cycles). The Nyquist plots displayed one or two semicircles in the high-to-medium frequency range and an inclined line in the lower frequency range (Figure 3.15a-b). The high frequency intercept represents the bulk or solution resistance (R_e) of the cell, which includes resistance for ion transport in the electrolyte and cell components. A single semicircle displayed by Li-S cell with CG corresponds to the charge-transfer resistance (R_{ct}). At the same time, two discreate semicircles are presented by Li-S cell with Li^+-PEDOT:PSS@CG; the first semicircle in the high frequency range is associated with the interface contact resistance (R_{int}) offered by the coating layer and electrode bulk, while the second semicircle in the medium frequency range corresponds to the R_{ct} (Lai et al., 2016). Based on the above discussion, we proposed an equivalent circuit model using ZSimpWin software as shown in the inset of Figure 3.15a-b. In the proposed circuit model, $R_{int}//CPE_{int}$ is the interphase contact resistance and its related capacitance (Y_1 and n_1 are CPE_{int} elements). $R_{ct}//CPE_{dl}$ is the charge-transfer resistance and its related capacitance (Y_2 and n_2 are CPE_{dl} elements), which reflects the charge-transfer process at the interface between the conductive coating and the electrolyte. CPE_{dif} is the diffusion impedance (Y_3 and n_3 are CPE_{dif} elements), which represents lithium ion diffusion process (Deng et al., 2013).

Table 3.2. Fitted values for the equivalent circuit elements by simulation of impedance spectra in Figure 3.12a-b.

		CPE_{int}			CPE_{dl}			CPE_{dif}	
	R_e (Ω)	Y_1 (Ω^{-1} s^n)	n_1	R_{int} (Ω)	Y_2 (Ω^{-1} s^n)	n_2	R_{ct} (Ω)	Y_3 (Ω^{-1} s^5)	n_3
CG before cycling	9.53	-	-	-	9.09E-5	0.85	120.3	3.64E-2	0.61
CG after cycling	4.39	-	-	-	2.68E-5	0.80	72.14	3.45E-2	0.56
Li^+-PEDOT:PSS@CG before cycling	8.18	2.26E-5	0.87	53.48	4.04E-5	0.74	15.54	8.14E-2	0.56
Li^+-PEDOT:PSS@CG after cycling	3.97	6.31E-6	0.84	7.42	1.77 E-5	0.65	6.43	1.70E-2	0.49

Table 3.2 lists the fitted values for all of the equivalent circuit elements. It is evident from the fitted values for the equivalent circuit elements that the Li-S cell with PEDOT:PSS@CG presented lower R_e and R_{ct} values than the cell with CG separator. The significantly reduced R_{ct} value for the Li-S cell with Li^+-PEDOT:PSS@CG is associated with the improved lithium ion conductivity and electrolyte retention ability, which stem from the presence of -SO_3^- groups in the Li^+-PEDOT:PSS coating (Zhang et al., 2018c; Yang et al., 2018a).

The static electrochemical stability of LSBs described in terms of their self-discharge properties is an important parameter to be considered for both laboratory scale testing and commercial applications (Wang et al., 2016c). In the case of LSB, the self-discharge rate is much higher than in conventional LIBs and it leads to rapid capacity fading. The diffusion and side reactions of PSs with lithium metal anode is believed to be the major cause for high self-discharge rate in LSB (Shen et al., 2019). To evaluate self-discharge characteristics of Li-S cells with CG and Li^+-PEDOT:PSS@CG, the OCV of the cells was measured as a function of time and displayed in Figure 3.16a. The OCV of CG-based cell quickly drops to 2.14 V within 45 h, i.e.,78.3% capacity retention, while Li^+-PEDOT:PSS@CG-based cell maintained an OCV of 2.46 V with 87.2% capacity retention.

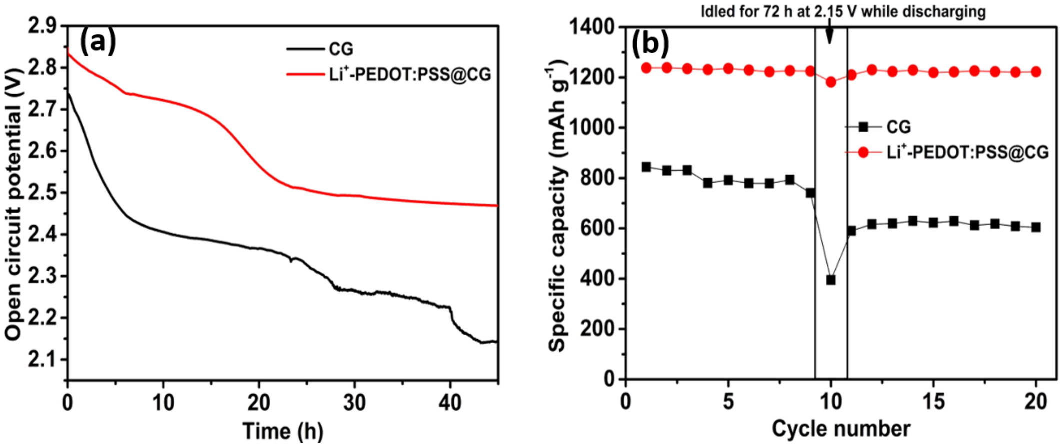

Figure 3.16. (a) Self discharge behaviour of Li-S cells with CG and Li^+-PEDOT:PSS@CG separators and (b) cycling performance of the cells idled at 2.15 V at the 10th discharging cycle

To better understand the effect of self-discharge on cell performance, the galavanostatic charge-discharge testing were conducted (Yang et al., 2018a). After 10 continuous charge-discharge cycles, the cells were kept in rest for 72 h, and then cycled further. During the first discharge after rest (11^{th} cycle), the cell with CG separator exhibited a drastic decrease in capacity (Figure 3.16b), indicating obvious self-discharge. On the second discharge after rest (12^{th} cycle), the cells restore only partial capacity. Even on further cycles, the capacity loss occurred during rest could not be recovered completely. On the other hand, the cell with Li^+-PEDOT:PSS@CG displays no apparent loss in discharge capacity even after the rest time, indicating lower self-discharge.

Moy et al. have proposed a simple and direct method to quantify the rate of shuttling process in LSBs (termed as "shuttle current") by measuring the current passing through the cell under potentiostatic control (Moy et al., 2015). Usually, the potential of a cell gradually decreases when at rest due to the PS shuttling mechanism. In order to maintain a constant cell potential, a Faradaic current was supplied to balance the migration of PSs, which is measured as the shuttle current. The variation of shuttle current for Li-S cells with CG and Li$^+$-PEDOT:PSS@CG membranes was measured at 2.3 V as a function of time (Figure 3.17). The rate of decrease of shuttle current was obtained by linearly fitting the region of steady state current using the equation $y = mx + C$, where y, x, C and m represents current, time, y-intercept and slope, respectively. The slope, m is an important parameter as it is a direct indication of the fade in shuttle current (Hu et al., 2017). It is clear from the Figure 3.16 that the cell with Li$^+$-PEDOT:PSS@CG membrane produced the minimal current fade with time compared to the cell with CG membrane. The magnitude of shuttle current also follows the similar trend, i.e., the Li-S cell with Li$^+$-PEDOT:PSS@CG exhibits lower shuttle current than the cell with CG. The reduction in shuttle current affirms the extensive elimination of PS shuttling process, which further accord with the improved electrochemical performance and self-discharge characteristics of Li-S cells with Li$^+$-PEDOT:PSS@CG.

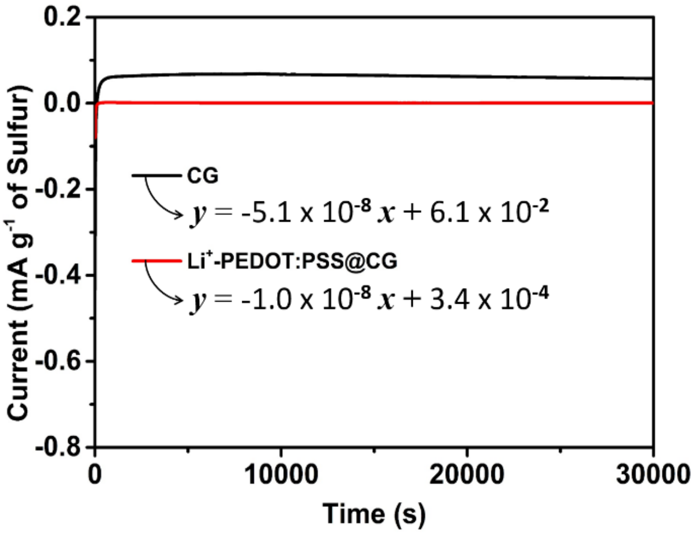

Figure 3.17. Shuttle current measurements of cells containing CG and Li$^+$-PEDOT:PSS @CG membranes

3.3.4. Post-Mortem Analysis of Cycled Cells

To further investigate the influence of Li$^+$-PEDOT:PSS@CG separator in mitigating the shuttle effect, the Li-S cells were disassembled after 100 cycles. The

CG and Li$^+$-PEDOT:PSS@CG separators collected after decrimping the cells were used directly without any washing treatment (Lei et al., 2018).

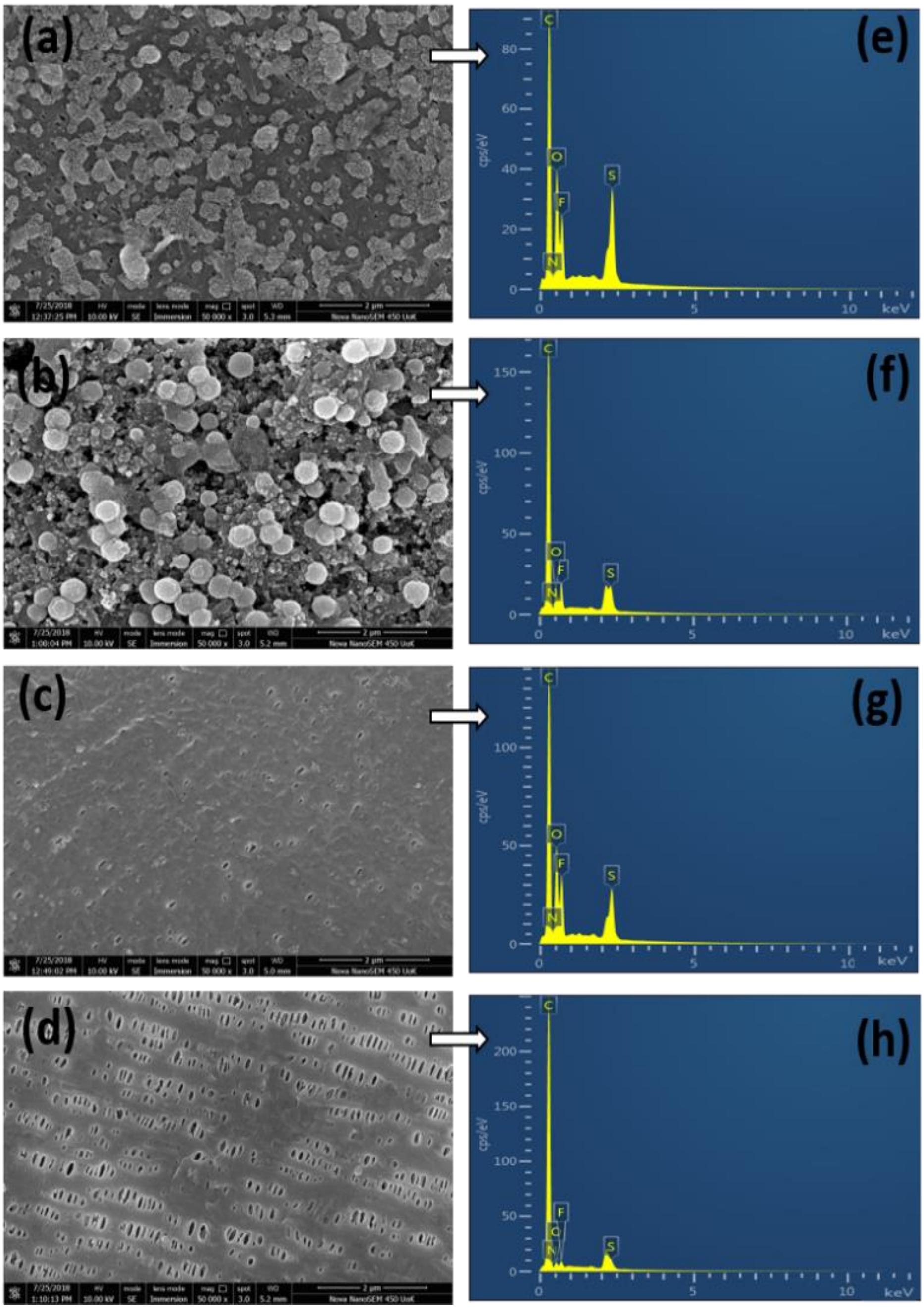

Figure 3.18. Morphology and composition of cycled separators after 100 cycles. SEM images of (a) CG (b) Li$^+$-PEDOT:PSS@CG separators on cathode sides and (c) CG (d) Li$^+$-PEDOT:PSS@CG separators on anode sides and (e, f, g, h) are the corresponding EDS spectra

The surface morphology and elemental composition of cathode and anode side of cycled separators were observed by SEM and EDS measurements.

Compared with fresh separators (Figure 3.4e-f), the cycled ones (cathode side) exhibit a denser structure with surface deposits (Figure 3.18 a-b) result from the accumulation of the PSs and electrolyte salts. The EDS results (Figure 3.18e-f) further confirms above observation. The PSs deposited on the separator will hardly take part in the redox reactions, which eventually leads to rapid capacity fading of Li-S cell. Moreover, this ‘dead sulfur’ got trapped in the pores and the surface of CG and ultimately blocks the lithium ion diffusion pathways (Kong et al., 2017). Figure 3.18c-d displayed the anode side SEM micrographs of CG and Li^+-PEDOT:PSS@CG separators. The effective blocking of PSs in cathode compartment by Li^+-PEDOT:PSS provide a comparatively clean anode side surface of the separator (Figure 3.18g-h).

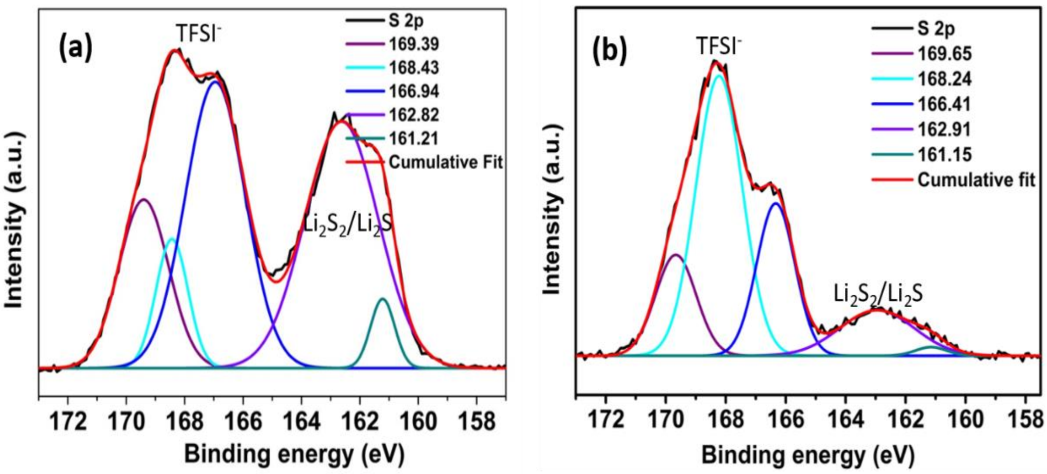

Figure 3.19. Deconvoluted S2p spectra for lithium anodes in the discharged state separated from the cells with (a) CG and (b) Li^+-PEDOT:PSS@CG membranes

The XPS analysis were conducted for lithium metal anodes peeled off from the two cells after 100 cycles. Figure 3.19 shows the deconvoluted S2p spectra for lithium anode obtained from Li-S cells with CG (Figure 3.19a) and Li^+-PEDOT:PSS@CG (Figure 3.19b). Both spectra presents a broad peak around 168 eV, which could be attributed to the aerobic oxidation of sulfur species upon dis-assembling the cell (Lang et al., 2015). The relatively small intensity of peaks around 163 and 161 eV for Li^+-PEDOT:PSS@CG indicate lower abundance of polysulfides and Li_2S, respectively (Cao et al., 2019). This observation clearly supports the proposed mechanism of polysulfide retention within cathode compartment for the cell containing Li$^+$-PEDOT:PSS@CG separator.

3.4. Conclusion

In this chapter, we propose a novel approach of decorating commercial separator by bifunctional lithiated PEDOT:PSS (Li$^+$-PEDOT:PSS@CG). Owing to strong chemical interactions of PEDOT with insoluble PSs and the electrostatic repulsion between the negatively charged –SO_3^-groups present in PSS and PS anions, the Li-S cell (areal sulfur loading of 3.9 mg cm^{-2}) with Li$^+$-PEDOT:PSS@CG separator demonstrated a high initial discharge capacity of 1360 mAh g^{-1} and coulombic efficiency of ~99%. It is notable that the Li$^+$-PEDOT:PSS@CG separator possesses excellent electrolyte wettability, interfacial properties and ionic conductivity, resulting in a stable discharge capacity of 1047 mAh g^{-1} even after 300 cycles at 0.1 C with 77% capacity retention. The excellent cycling stability exemplify this facile approach can effectively constrain the shuttle effect of polysulfides and make further progress to the practical application of LSBs.

CHAPTER 4

EFFECTIVE SUPPRESSION OF POLYSULFIDE SHUTTLE EFFECT IN LITHIUM-SULFUR BATTERY USING LITHIATED POLY(ACRYLIC ACID-CO-MALEIC ACID) DECORATED SEPARATOR

In this chapter, we propose a carboxyl functional lithiated poly(acrylic acid-co-maleic acid) (LPAM) coated onto Celgard (LPAM@CG) separator for LSBs. The LPAM@CG separator can not only effectively inhibit the shuttle effect of polysulfides, but also promote the diffusion of lithium ions. Particularly, the –COO$^-$ groups present in the LPAM allow the rapid transfer of positively charged lithium ions while preventing the diffusion of negatively charged PS anions through coulombic interactions. Besides, the LPAM@CG membrane possesses good interfacial properties, ionic conductivity, excellent electrolyte wettability and remarkable electrolyte uptake. In order to investigate the electrochemical performance of Li-S cells (areal sulfur loading 4.1 mg cm^{-2}) with LPAM@CG membranes, cyclic voltammetry, galvanostatic charge-discharge and EIS measurements has been carried out. The Li-S cell with LPAM@CG separator exhibit significant improvement in the electrochemical performances, with a high initial discharge capacity of 1213 mAh g^{-1}, an excellent rate capability of 637 mAh g^{-1} at 3 C, and a good capacity retention of 957 mAh g^{-1} (~79% over 300 cycles).

4.1. Introduction

The PS shuttle mechanism caused by the diffusion, dissolution and side reaction soluble lithium PSs is considered as a roadblock for the commercialization of LSBs (Deng et al., 2019). In order to repress the detrimental effects caused by the shuttle effect, significant amount of research works focused on hindering the shuttle of soluble PSs have been reported. The major strategies can be categorized into two aspects: (i) cathode functionalization, using materials such as carbonaceous materials, inorganic materials, and polymers to absorb PSs physically and/or chemically; (ii) separator modification, employing carbon materials, inorganic materials and conducting polymers to physically and/or chemically wrap PSs within the cathode compartment (Deng et al., 2016; Kang et al., 2016; He et al., 2018b; Rana et al., 2019).

As a key component of battery, the separator serves two major roles: (i) electrical insulator for preventing internal short circuit, and (ii) diffusion channels for lithium ion transport (Arora and Zhang, 2004). In the case of LSB, separator allows the selective transport of lithium ions blocking the passage of PSs (Li et al., 2015b). An ion selective separator is an efficient and reliable strategy for mitigating PS shuttle (Gu et al., 2014; Luo et al., 2018). Thus, modifying the commercial separator (polyolefin membranes) with functionalized barrier coatings attracted much attention. Among the various separator coatings, conducting polymers are considered efficient as they can simultaneously increase the electrolyte uptake ability and interfacial conductivity together with suppressing the PS crossover owing to the presence of polar functional groups (Ma et al., 2016; Zhu et al., 2019). The polymers containing polar negatively charged groups can perform two functions: (i) effectively restrain the migration of soluble PSs via coulombic repulsion, and (ii) provide transport pathways for lithium ions through the coulombic interactions, thereby improving electrochemical performance of LSBs (Abbas et al., 2016; Hencz et al., 2019). The polymers containing negatively charged groups like Nafion (Bauer et al., 2014; Yu et al., 2015), sulfonated polystyrene (Guo et al., 2018), polyacrylic acid (Song et al., 2018b), PEDOT:PSS (Abbas et al., 2016; Lee et al., 2018b) , sulfonated poly(styrene-ethylene-butylene-styrene) (Yang et al., 2018a), polyamide acid (Luo et al., 2018), sulfonated poly(ether ether ketone) (Babu et al., 2018), carboxylate anchored polyvinyl alcohol (Jiang et al., 2018), etc., have been explored to modify the polyolefin separator.

Poly (acrylic acid-co-maleic acid) (PAM) is a hydrophilic polymer, which has been used as an electrocatalytic electrode for methanol oxidation and dispersant to improve the stability of electrodes slurries for large scale processing (Yang et al., 2011; Kasinathan et al., 2018; Joshi et al., 2018). In this chapter, we propose an “electrostatic repulsion” approach using a functional separator composed of lithiated PAM (LPAM) to effectively alleviate the shuttling of PS anions. Lithiation leads to proton exchange in carboxylic acid group of PAM, and the resulted LPAM possesses lithium ion transporting capability and functions as a single-ion conductor. The LPAM coating on commercial Celgard separator (LPAM@CG) effectively reduces interfacial resistance and the $–COO^{-}$ groups inhibits the migration of PSs by mutual coulombic repulsion. Subsequently, the Li-S cell employing LPAM@CG separator exhibits excellent electrochemical performance and anti-self-discharge characteristics compared to the pristine Celgard separator (CG).

4.2. Materials and Methods

4.2.1. Materials

Poly (acrylic acid-co-maleic acid) solution (PAM, 50 wt% in water, average M_w 3000, Sigma Aldrich), all other chemicals are as mentioned in section 2.2.1.

4.2.2. Synthesis of Lithiated PAM (LPAM)

Lithiation of PAM was carried out using a simple ion-exchange process. 1 g PAM solution was added to a solution of 0.1M LiOH in distilled water. The resulted solution was stirred for 2 h at room temperature followed by vacuum drying at 80 °C for 24 h to obtain LPAM. The chemical formula and synthetic scheme of LPAM was given in Figure 4.1.

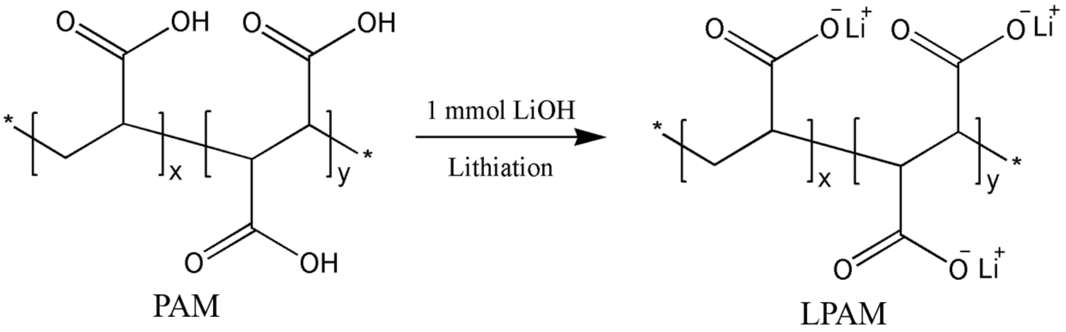

Figure 4.1. Synthesis scheme of LPAM

4.2.3. Preparation of LPAM Coated Celgard Separator (LPAM@CG)

The LPAM coated Celgard separator was prepared by doctor blade coating technique. Briefly, 33 mg of PVDF as binder was dissolved in 2 mL of NMP. 33 mg of LPAM and 33 mg of super P carbon was added to this solution and the mixture was stirred at room temperature for 5 h to obtain uniform slurry. The obtained slurry was coated onto one side of commercial Celgard 2320 separator (CG) and dried in vacuum oven at 60 °C for 12 h. The presence of super P carbon helps to enhance electronic conductivity and favour the adsorption of intermediate polysulfides, thereby hamper the serious shuttling mechanism in Li-S cell. The overall thickness of LPAM@CG separator was around 28 μm.

4.2.4. Coin Cell Assembly

A standard 2032 type coin cell was assembled by the procedure described in the section 2.2.6, employing MWCNT@S electrode with an areal sulfur loading of 4.1 mg cm^{-2}, LPAM@CG separator, and Li metal as the counter electrode.

4.2.5. Material and Electrochemical Characterization

All characterizations were done by the techniques described in section 2.2.7 and 3.2.6.

4.3. Results and Discussion

4.3.1. Material Characterization

The FT-IR spectra can be used to verify the conversion of the PAM from the H$^+$ form to the Li$^+$ form. Results of FT-IR are shown in Figure 4.2. The adsorption band at 1623 cm^{-1} is ascribed to the unreacted carboxyl –COOH group. After the lithiation procedure, the vibration mode of carboxyl shifts to 1567 cm^{-1}, owing to the formation of –COOLi (Jiang et al., 2018).

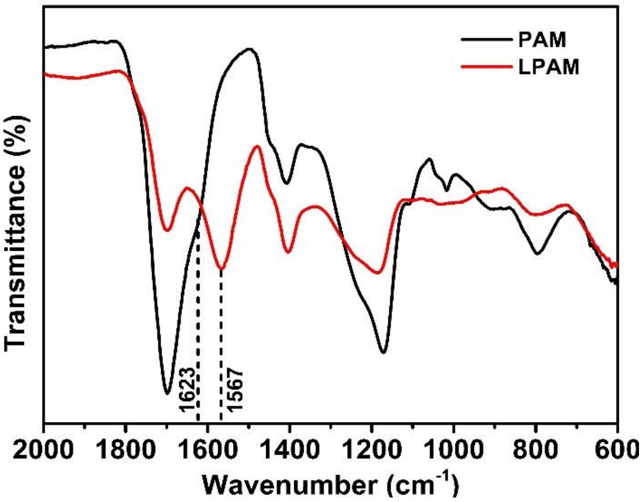

Figure 4.2. FT-IR spectra of PAM and LPAM

The surface morphology (SEM micrographs) of the CG and LPAM@CG separators are depicted in Figure 4.3a-b. The cross-sectional morphology of LPAM@CG reveals a dense coating of LPAM covering the surface of CG and the measured thickness was ~28 µm (Figure 4.3c). Elemental mapping of the LPAM@CG (Figure 4.3d) shows the uniform distribution of carbon, fluorine, and oxygen, which verifies the fine dispersion of LPAM with super P and PVDF on the surface of CG.

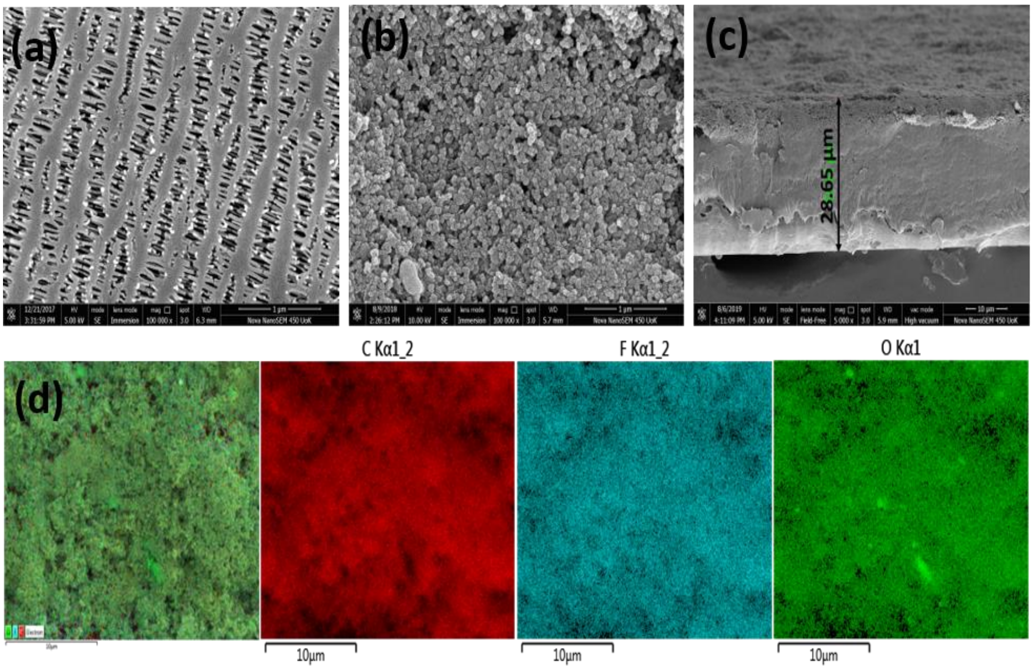

Figure 4.3. SEM micrographs of (a) CG and (b) LPAM@CG, (c) cross-section of LPAM@CG separator, (d) elemental mapping of the LPAM@CG

The wetting behaviour of the separators was investigated using a liquid electrolyte absorption test and the corresponding static electrolyte contact angle is shown in Figure 4.4c-d. As can be seen in Figure 4.4a-b, the CG separator gets hardly wetted by the liquid electrolyte due to its strong hydrophobicity. In contrast, the LPAM@CG separator soaked up the electrolyte immediately, where the electrolyte droplet could easily spread over surface. The static electrolyte contact angle test results were similar to the electrolyte absorption test. As depicted in Fig. 4.3a-b, the contact angle of pristine CG and LPAM@CG membranes were found to be 48.2 and 8.8°, respectively. The increased wettability of LPAM@CG is attributed to the $-COO^{-}$ group present on LPAM polymer. The hydrophilic $-COO^{-}$ group immediately takes up the polar electrolyte droplet to form large clusters in the polymer domain, therefore enhances the wettability of the separator and gives lesser value of contact angle (Zhang et al., 2015c; Lu et al., 2017b). The good wetting of the LPAM@CG with the non-aqueous electrolyte is likely to reduce the internal resistance and consequently improves the rate capability (Zhang et al., 2018c; Chen et al., 2019).

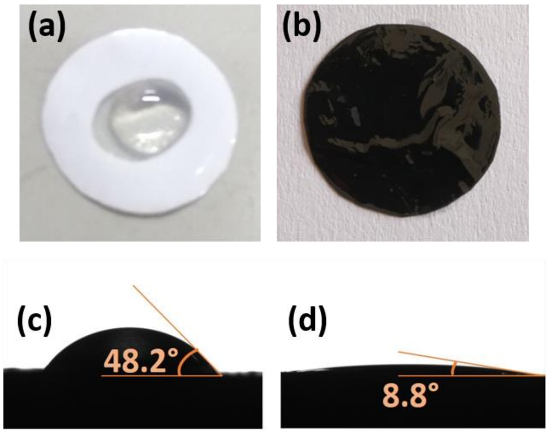

Figure 4.4. Liquid electrolyte wettability of (a) CG and (b) LPAM@CG, and the corresponding contact angles (c and d)

To determine the charge state of the LPAM, zeta potential measurement was carried out in non-aqueous electrolyte used for cycling studies. As seen, the zeta potential of LPAM is approximately -45.6 mV (Figure 4.5), confirming the electronegative nature of the LPAM in non-aqueous electrolyte. Since the PSs remain anionic in the electrolyte and LPAM is negatively charged, a repulsive force arises between LPAM coating on CG and PS anions, authenticating the “electrostatic repulsion” mechanism rendered by LPAM@CG separator towards the PS anions (Lei et al., 2018).

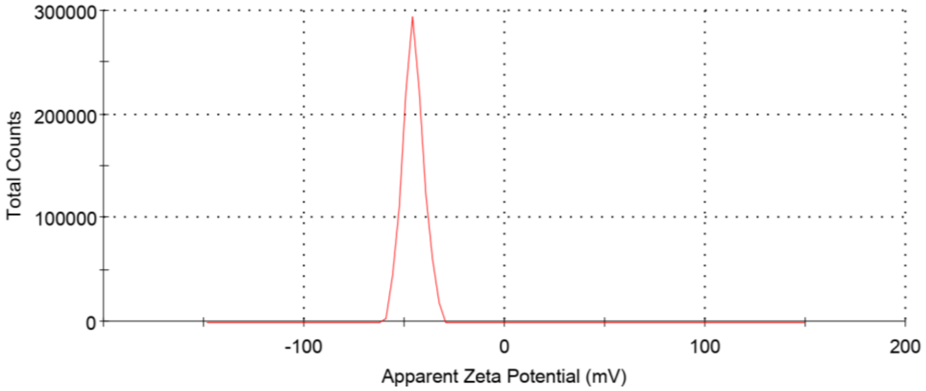

Figure 4.5. Zeta potential distribution of LPAM in non-aqueous electrolyte

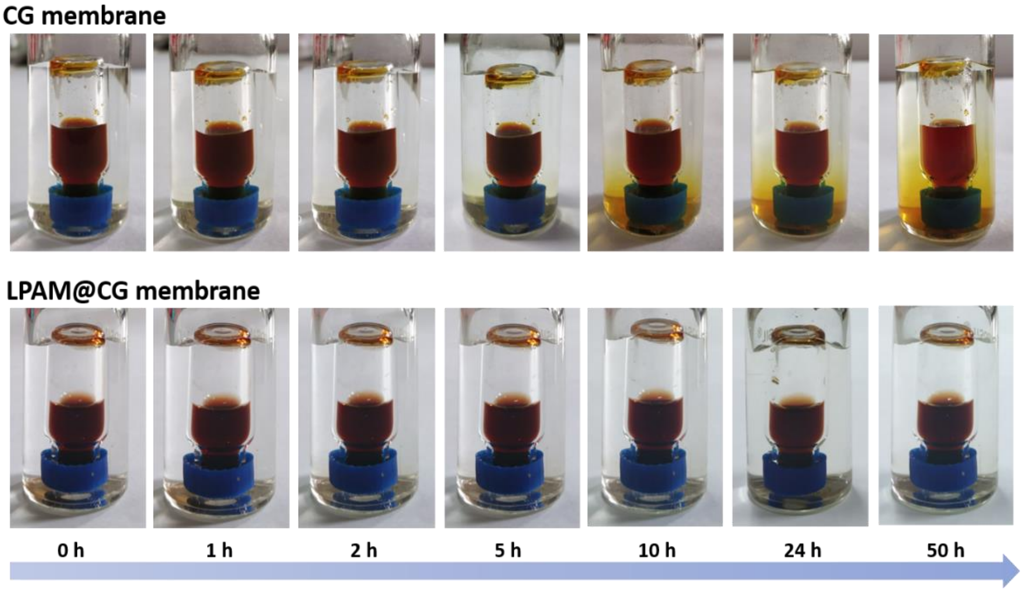

Figure 4.6. Digital photographs of visual PS diffusion test for CG and LPAM@CG membranes

The physical blocking of PS by CG and LPAM@CG membranes is verified by visual PS diffusion test (Figure 4.6). Driven by concentration gradient, the Li_2S_6 diffuse from inner vial to outer vial (Yang et al., 2018a). As expected, the pristine CG membrane could not block the PS within the small vial due to its porous nature, as a consequence colourless blank electrolyte in the large vial turned to yellow within 10 h. While, the blank electrolyte in the large vial remains colourless in the case of LPAM@CG separator even after 50 h, suggesting effective suppression of

PS diffusion. The excellent PS blocking ability of LPAM@CG membrane could be ascribed to the coulombic repulsion offered by negatively charged –COO¯ group in LPAM polymer (Ahn et al., 2019).

4.3.2. Electrochemical Evaluation

To evaluate the influence of –COO¯ groups on the lithium ion transport properties, both the ionic conductivity and lithium ion transference number were measured (Zhu et al., 2013). The lithium ion conductivities of CG and LPAM@CG were evaluated at different temperatures using EIS measurements and shown in Figure 4.7. Irrespective of the membrane analysed, the ionic conductivity increases with increasing temperature. The increased ionic conductivity of LPAM@CG is credited to the higher electrolyte uptake by LPAM coating.

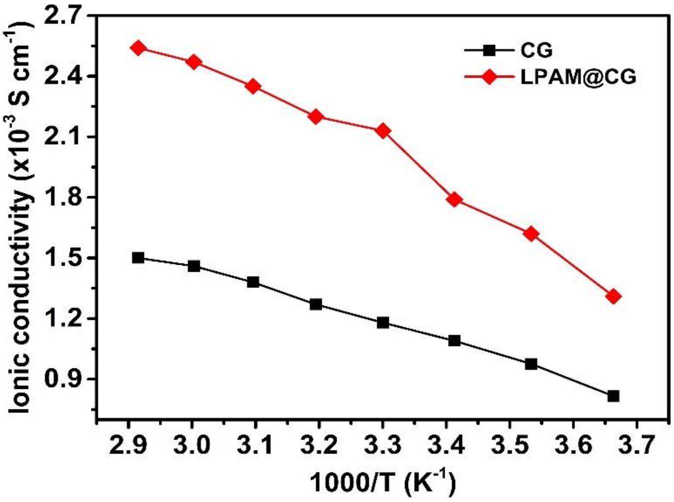

Figure 4.7. Ionic conductivity of CG and LPAM@CG membrane

The lithium ion transference number (t_{Li^+}) is calculated using equation (2.1) and the calculated values are found to be 0.38 and 0.74 for CG and LPAM@CG membranes, respectively, according to the chronoamperometric profiles and EIS measurements (Figure 4.8). It is remarkable that t_{Li^+} of LPAM@CG is almost twofold the CG. In the ether-based electrolytes, lithium ions usually exist as solvated Li^+-ether molecules which are much larger than TFSI¯anions, this suppress the lithium ion transport thereby relatively lower t_{Li^+}value (Zhou et al., 2018; Callsen et al., 2017). On contrary, the high t_{Li^+} for cells with LPAM@CG membrane is possibly due to the presence of fixated carboxylate groups along the LPAM chain, which could accelerate the de-solvation of Li^+-ether molecules supplying lithium ion coordination sites (–COO^-) to promote the transport of lithium ions (Yamada et al., 2013; Ueno et al., 2016; Wang et al., 2016d).

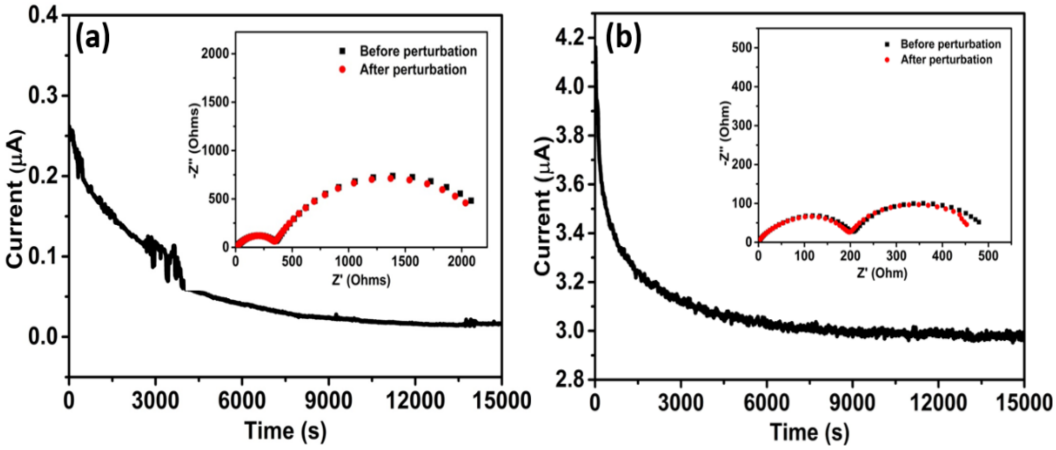

Figure 4.8. Chronoamperometric curves of (a) CG and (b) LPAM@CG membranes. Inset: EIS Nyquist plots of symmetric Li/membrane/Li cells before and after perturbation

To determine the stability of membrane/lithium interface, a symmetrical Li/membrane/Li cells was assembled and its interfacial resistance, R_i was measured as a function of time at 25 °C. Figure 4.9 displays the variation of R_i with time for Li/CG or LPAM@CG/Li cells and the symmetric cell with LPAM@CG exhibit lowest R_i. This result further substantiates the observations described *previously* for the ionic conductivity studies (Suriyakumar et al., 2019).

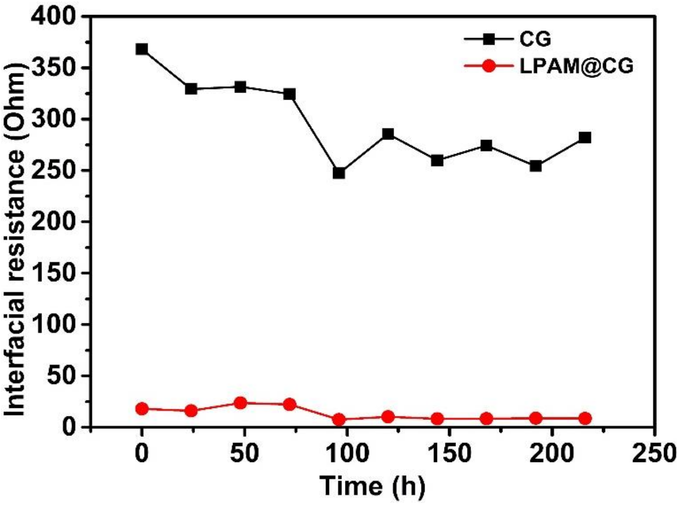

Figure 4.9. Interfacial resistance vs time measurements of (a) CG and (b) LPAM@CG separator

4.3.3. Cell Performance Evaluation

To evaluate the benefits of the functional separator in LSBs, CR2025-type coin cells were assembled. A comparative study was conducted with the control cell employing an unmodified CG separator. The cyclic voltammetric studies of the cell with CG and LPAM@CG membranes was carried out at a scan rate of 0.1 mV s^{-1} in the voltage window of 1.6-3 V (Figure 4.10). The cathodic scan presents two peaks, one around 2.3 V (peak 1) and another around 2 V (peak 2). Peak 1 arises from the conversion of cyclo-S_8 to soluble higher order PSs (Li_2S_n, $4 \leq n \leq 8$). Peak-2 is the main peak in the cathodic scan corresponding to the reduction of higher order PSs into lower order lithium sulphides (Li_2S_2/Li_2S), which will deliver significant part of cell's capacity. During anodic sweep, a splitted oxidation peak is observed around 2.4V (peak 3), the first peak is due to conversion of Li_2S_2/Li_2S to Li_2S_n (where $4 \leq n \leq 8$) and the next peak is due to further oxidation of Li_2S_n (where $4 \leq n \leq 8$) to elemental sulfur (S_8) (Song et al., 2018b; Yang et al., 2018a; Wild et al., 2015). The cell with CG membrane exhibited broad cathodic and anodic peaks due to the sluggish nature of the conversion kinetics. In contrast, the cells with LPAM@CG membrane presented well-defined redox peaks with an increased current density compared to the cells with CG membrane, indicating an improved active material utilization and conversion reaction kinetics (Elgrishi et al., 2018; Ghosh and Basu, 2018).

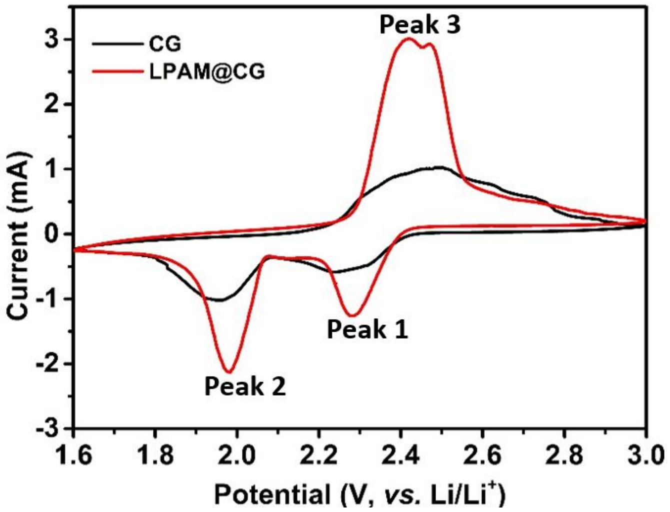

Figure 4.10. CV profiles of Li-S cells containing CG and LPAM@CG separators

Further, diffusion coefficient of lithium ions (D_{Li^+}) was calculated from CV curves using Randles-Sevcik equation. The calculated values of chemical diffusion coefficient of lithium ions are respectively 4.84 x 10^{-7}, 1.09 x 10^{-7}, 4.71 x 10^{-7} cm^2 s^{-1} for CG and 3.93 x 10^{-6}, 7.02 x 10^{-7}, 9.95 x 10^{-6} cm^2 s^{-1} for LPAM@CG membrane. It is obvious from the calculated values that the diffusion coefficients for LPAM@CG separator are at least an order of magnitude greater than CG. The above result suggests that the LPAM@CG separator provide an improved lithium ion mobility compared to CG, thereby expecting significant improvement in the specific capacity and rate capability (Lee and Ryu, 2017).

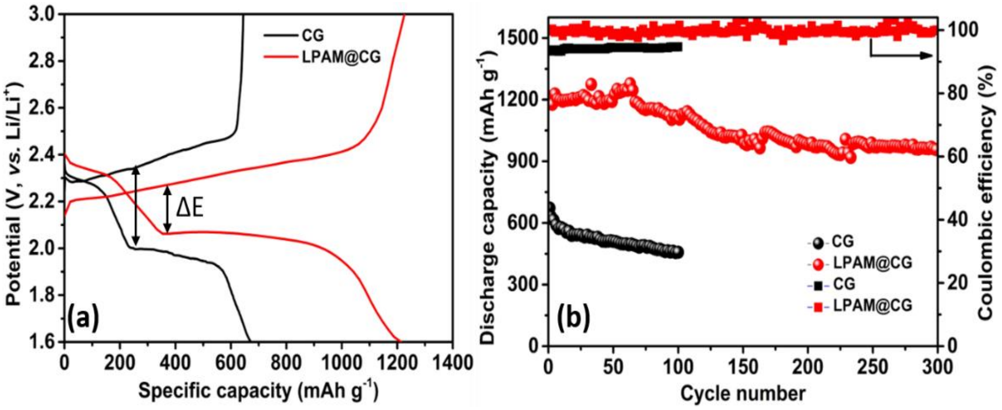

Figure 4.11. (a) Initial charge-discharge profiles of Li-S cell with CG and LPAM@CG at 0.1C (b) cycling performance and coulombic efficiencies at 0.1C rate for Li-S cell with CG and LPAM@CG

Figure 4.11a shows the initial galvanostatic charge-discharge profile of Li-S cells with CG and LPAM@CG membranes. As displayed in the Figure 4.11a, both cells exhibited two typical discharge plateaus, indicating multi-electron redox reactions, which is in agreement with the CV curves. The upper discharge plateau corresponds to cyclo-S_8 reduction to soluble long-chain lithium PSs, and the lower discharge plateau pertains to the formation of insoluble short-chain lithium sulfide (Li_2S_2/Li_2S) (Zhang, 2013; Wild et al., 2015). The discharge plateaus for the cell with the LPAM@CG separator were found to be longer and flatter than the cell with CG separator. Notably, the cell with LPAM@CG exhibits a lesser voltage hysteresis (ΔE) than CG membrane ($\Delta E_{LPAM@CG}$ = 194 mV; ΔE_{CG} = 345 mV). The lower value of ΔE for the cells with LPAM@CG is due to low electrochemical polarization, which originate from the good ion conducting pathways provided by the carboxylate group in LPAM polymer (Long et al., 2016; Zhang et al., 2017c; Moorthy et al., 2019). The absence of such ion conducting functional groups in uncoated CG leads to higher polarization, which in turn results in lower discharge capacity. The cell with LPAM@CG separator delivers an initial discharge capacity of 1213 mAh g^{-1} with 73.5% sulfur utilization. At the same time, the cell with CG separator delivers a discharge capacity of 672 mAh g^{-1} corresponding to 40.1% utilization of sulfur. The high initial discharge capacity of the cells with LPAM@CG is ascribed to good ionic conductivity of LPAM coating, which provide a larger conductive surface for the conversion of soluble PSs to solid Li_2S_n ($n \leq 2$) (Yao et al., 2014; Pan et al., 2016).

The cycling performance of the Li-S cells with CG and LPAM@CG were evaluated at the current density of 0.1C, as shown in the Figure 4.11b. It is obvious that the cell with LPAM@CG deliver higher discharge capacity than the cell with CG membrane. The cell assembled with CG membrane exhibits drastic capacity fading in 100 cycles (68% capacity retention) as a consequence of PS crossover mechanism, which arises from the easy migration of long-chain PSs (size range: 1-1.8 nm) through the porous CG membrane towards lithium metal anode. Whereas the cell with LPAM@CG exhibits a capacity retention of 78.8% (956 mAh g^{-1}) even after 300 continuous charge-discharge cycles. The improved cycling stability for Li-S cell with LPAM@CG separator is supposed to be derived from the presence of $–COO^{-}$ groups in the LPAM polymer, which can effectively restrict the migration of soluble PSs through coulombic repulsion (Lee et al., 2018b; Jiang et al., 2018). Again, the cell with CG exhibits a low coulombic efficiency (~94%), and the inferior performance is attributed to the severe shuttle effect stemming from porous structure of CG (Zhu et al., 2019b). The coulombic efficiency of LPAM@CG-based Li-S cell remains stable at about 99% over the entire cycles, which is mainly credited to the effective confinement of PS anions by the LPAM coating layer, as proved by the visual PS diffusion test.

The rate performances of Li-S cell with CG and LPAM@CG are shown in the Figure 4.12. Similar to the cycling performances, the cell with LPAM@CG exhibits better discharge capacities than the cell with CG at different C-rates from 0.1 to 3C. Consequent cycles at 0.1, 0.2, 0.5, 1, 2, and 3C-rates delivered capacities of 1221, 1120, 1048, 957, 820, and 633 mAh g^{-1}, respectively, for LPAM@CG separator. When the C-rate was reverted back from 3C to 0.2C, a reversible capacity of 1109 mAh g^{-1} was achieved. On the other hand, pristine CG separator provided discharge capacities of 669, 579, 475, 384, 228, and 46 mAh g^{-1}, respectively, at 0.1, 0.2, 0.5, 1, 2 and 3C. When the discharge current was switched back from 3 to 0.2C, a reversible capacity of 518 mAh g^{-1} was recovered. The excellent rate performance of Li-S cell with LPAM@CG can be attributed to the higher ionic conductivity offered by the LPAM coating (Lee et al., 2018b). Lower ionic conductivity leads to greater concentration polarization, which causes increase in the charging potential and decrease in the discharging potential. The charge-discharge potential reaches the cut-off voltage quickly for cells with high concentration polarization, resulting in poor rate performance (Jin et al., 2013). Thus, the electrochemical performance of the cell with LPAM separator could effectively improve compared to the cell with CG separator at even at higher C-rates, where high transport rate of lithium ion through the separator is required.

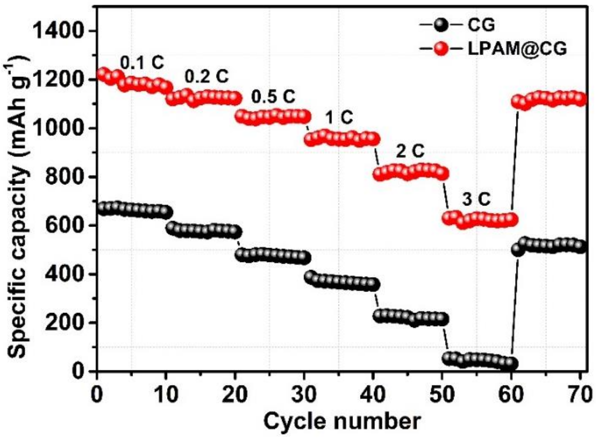

Figure 4.12. Rate capability studies of Li-S cell with CG and LPAM@CG

We carried out EIS measurements to gain additional insight into the influence of the LPAM coating on the CG separator. These measurements were conducted using freshly prepared cells and cycled cells (after 100 cycles) incorporating the CG and LPAM@CG separators. The Nyquist plots displayed one or two semicircles in the high-to-medium frequency range and an inclined line in the lower frequency range (Figure 4.13a-b). The high frequency intercept represents the bulk or solution resistance (R_e) of the cell, which includes resistance for ion transport in the electrolyte and cell components. A single semicircle displayed by Li-S cell with CG corresponds to the charge-transfer resistance (R_{ct}) (Yan et al., 2016). At the same time, two discreate semicircles are presented by Li-S cell with LPAM@CG; the first semicircle in the high frequency range is associated with the interface contact resistance (R_{int}) offered by the coating layer and electrode bulk, while the second semicircle in the medium frequency range corresponds to the R_{ct} (Lai et al., 2016). Based on the above discussion, we proposed an equivalent circuit model using ZSimpWin software as shown in the inset of Figure 4.13a-b. In the proposed circuit model, R_{int}//CPE_{int} is the interphase contact resistance and its related capacitance (Y_1 and n_1 are CPE_{int} elements). R_{ct}//CPE_{dl} is the charge-transfer resistance and its related capacitance (Y_2 and n_2 are CPE_{dl} elements), which reflects the charge-transfer process at the interface between the conductive coating and the electrolyte. CPE_{dif} is the diffusion impedance (Y_3 and n_3 are CPE_{dif} elements), which represents lithium ion diffusion process (Deng et al., 2013).

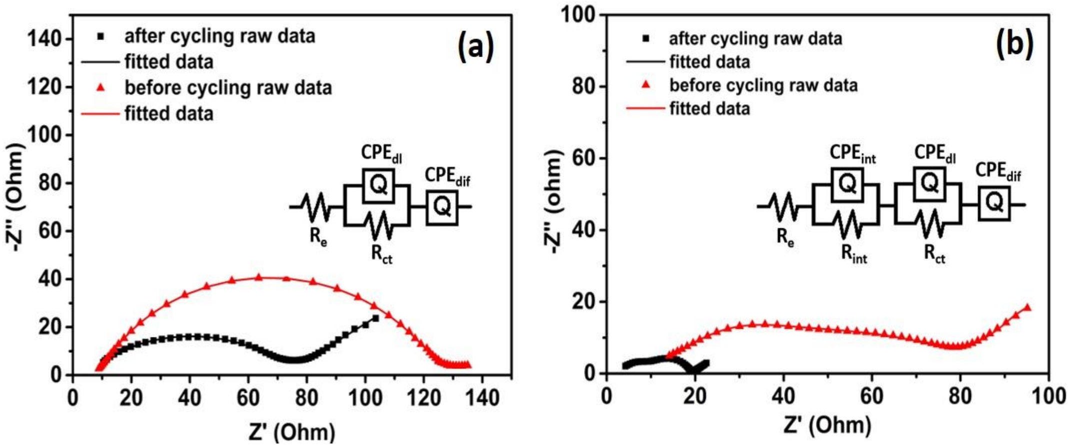

Figure 4.13. Electrochemical impedance spectra of Li-S cells with (a) CG and (b) LPAM@CG separators before and after 100 cycles

Table 4.1. Fitted values for the equivalent circuit elements by simulation of impedance spectra in Figure 4.13a-b.

		CPE_{int}			CPE_{dl}			CPE_{dif}	
	R_e (Ω)	Y_1 (Ω^{-1} s^n)	n_1	R_{int} (Ω)	Y_2 (Ω^{-1} s^n)	n_2	R_{ct} (Ω)	Y_3 (Ω^{-1} s^5)	n_3
CG before cycling	9.53	-	-	-	9.09E-5	0.85	120.3	3.64E-2	0.61
CG after cycling	4.39	-	-	-	2.68E-5	0.8	72.14	3.45E-2	0.56
LPAM@CG before cycling	6.74	4.52E-5	0.84	54.89	5.38E-4	0.7	12.08	3.33E-2	0.6
LPAM@CG after cycling	2.86	3.62E-6	0.83	7.16	4.51 E-5	0.8	6.43	1.25 E-2	0.49

Table 4.1 presents the fitted values for all of the equivalent circuit elements. It is evident from the fitted values for the equivalent circuit elements that the Li-S cell with LPAM@CG exhibited lower R_e and R_{ct} values than the cell with CG separator. The significantly reduced R_{ct} value for the Li-S cell with LPAM@CG is associated with the improved lithium ion conductivity and electrolyte retention ability, which stem from the presence of $-COO^-$ groups in the LPAM coating. The above EIS results can be considered as an additional support for the better cycling and rate performance offered by the cell with LPAM@CG separator (Zhang et al., 2018c; Yang et al., 2018a; Jiang et al., 2018).

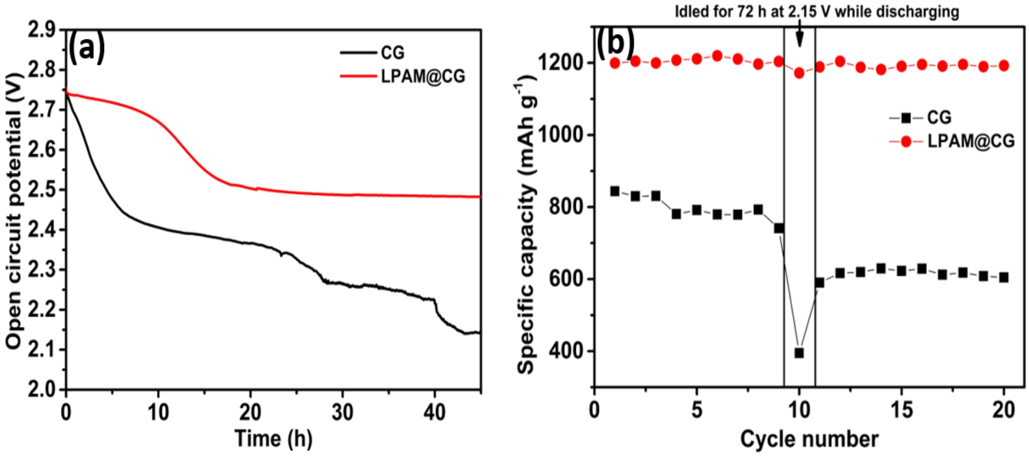

Figure 4.14. (a) Self discharge behaviour of Li-S cells with CG and LPAM@CG separators and (b) cycling performance of the cells idled at 2.15 V at the 10th discharging cycle

Self-discharge is a critical parameter to assess batteries, which has largely been neglected. Self-discharge easily occurs under storage of Li–S cells, especially after a full charge (Wang et al., 2016c). The robust chemical reactions of PSs with metallic lithium, stemming from the continuous migration and diffusion of Li_2S_n (where $4 \leq n \leq 8$) due to a concentration gradient, leads to the degradation of cell's OCV and capacity (Shen et al., 2019). Therefore, alleviating self-discharge of a fully charged cell is a challenge for a practical LSB. To evaluate the self-discharge behaviour of Li-S cells with CG and LPAM@CG separators, the OCV of the cells was measured as a function of time and shown in Figure 4.14a. The OCV of Li-S cell with CG quickly degrades to 2.14 V within 45 h. Whereas, the self-discharge is considerably prevented for the cell with LPAM@CG membrane, and an OCV of 2.48 V is maintained. To further understand the influence of LPAM@CG on self-discharge behaviour, the galvanostatic charge-discharge studies were carried out. After continuous 10 charge-discharge cycles, the cells were rested for 72 h, and then cycled further (Yang et al., 2018a). During the first discharge after rest (11th cycle), the capacity decreases drastically for the cell with CG separator (Figure 4.14b), indicating obvious self-discharge. On the second discharge after rest (12th cycle), the cells restore only partial capacity. Even on further cycles, the capacity lost during rest could not be recovered completely. At the same time, the cell with LPAM@CG membrane exhibits no apparent loss of discharge capacity even after rest time, reduced self-discharge.

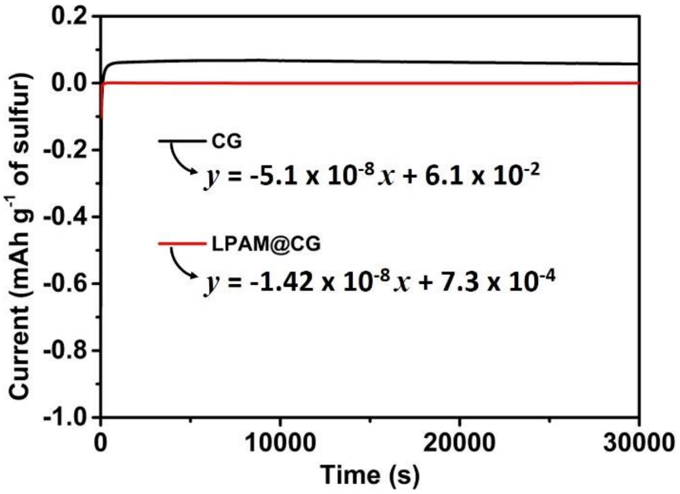

Figure 4.15. Shuttle current measurements of cells containing CG and LPAM@CG membranes

Generally, measurement of coulombic efficiency is widely employed to quantify the shuttle process. Moy et al., have proposed a direct method to quantify the rate of shuttling phenomenon also termed ‘‘shuttle current’’ by measuring and observing its change with time (Moy et al., 2015). The variation of the shuttle current for the Li-S cell with CG and LPAM@CG membranes was measured at 2.3 V, as shown in the Figure 4.15. The rate of decrease of shuttle current was obtained from the slope of algebraic equation: $y = mx + C$, where y, x, C and m represents current, time, y-intercept and slope, respectively. The slope, m is an important parameter as it is a direct indication of the fade in shuttle current. Typically, a linear decay in shuttle current is usually observed for Li-S cells. The decay in shuttle current can be related to the amount of PSs converted to insoluble lower-order PSs at the anode. In other words, reducing the extent of deposition of insoluble species at the anode is expected to favourably impact the retention of capacity for the Li-S cell, through its implications on the shuttle current (Hu et al., 2017). It is clear from Figure 4.15 that the Li-S cell with LPAM@CG separator produced the least current decay with time, as compared to the Li-S cell with CG separator. A similar trend has been observed in the magnitude of the shuttle current. The Li-S cell with CG membrane exhibits higher shuttle current than the Li-S cell with LPAM@CG membranes, which implies the fact that a large amount of higher order PSs is converted into lower order PSs at the anode in the case of CG membrane (Suriyakumar et al., 2019). Obviously, the reduction in the shuttle current in the case of Li-S cell with LPAM@CG directly reflects the charge-discharge behaviour.

4.3.4. Post-Mortem Analysis of Cycled Cells

To better understand the advantageous effects of the LPAM coated CG separator on the electrochemical performance, a post-mortem analysis of the Li-S cells was conducted. After 100 charge-discharge cycles, the cells were disassembled in a fully discharged state, and the CG and LPAM@CG separators were retrieved without being washed (Lei et al., 2018).

The surface morphology of the CG and LPAM@CG separators facing cathode and anode were observed from SEM micrographs, and corresponding EDS spectra were also recorded. Compared to the fresh separators (Figure 4.3a-b), the cycled one exhibits a denser structure with surface deposits which arises from the accumulation of PSs and electrolyte salts (Figure 4.16a-b). The EDS spectrum (Figure 4.16e-f) further confirms the distribution of sulfur species and the electrolyte on the separator. The PSs deposited on the separator will hardly take part in the redox reactions, which eventually leads to rapid capacity fading of Li-S cell. Moreover, this ‘dead sulfur’ got trapped in the pores and the surface of CG and ultimately blocks lithium ion diffusion pathways (Kong et al., 2017). Figure 4.16c-d presented SEM micrographs of CG and LPAM@CG separators in anodic side, respectively. The effective blocking of PSs in cathodic compartment by LPAM assured a comparatively clean surface of separator in contact with lithium anode (Figure 4.16g-h).

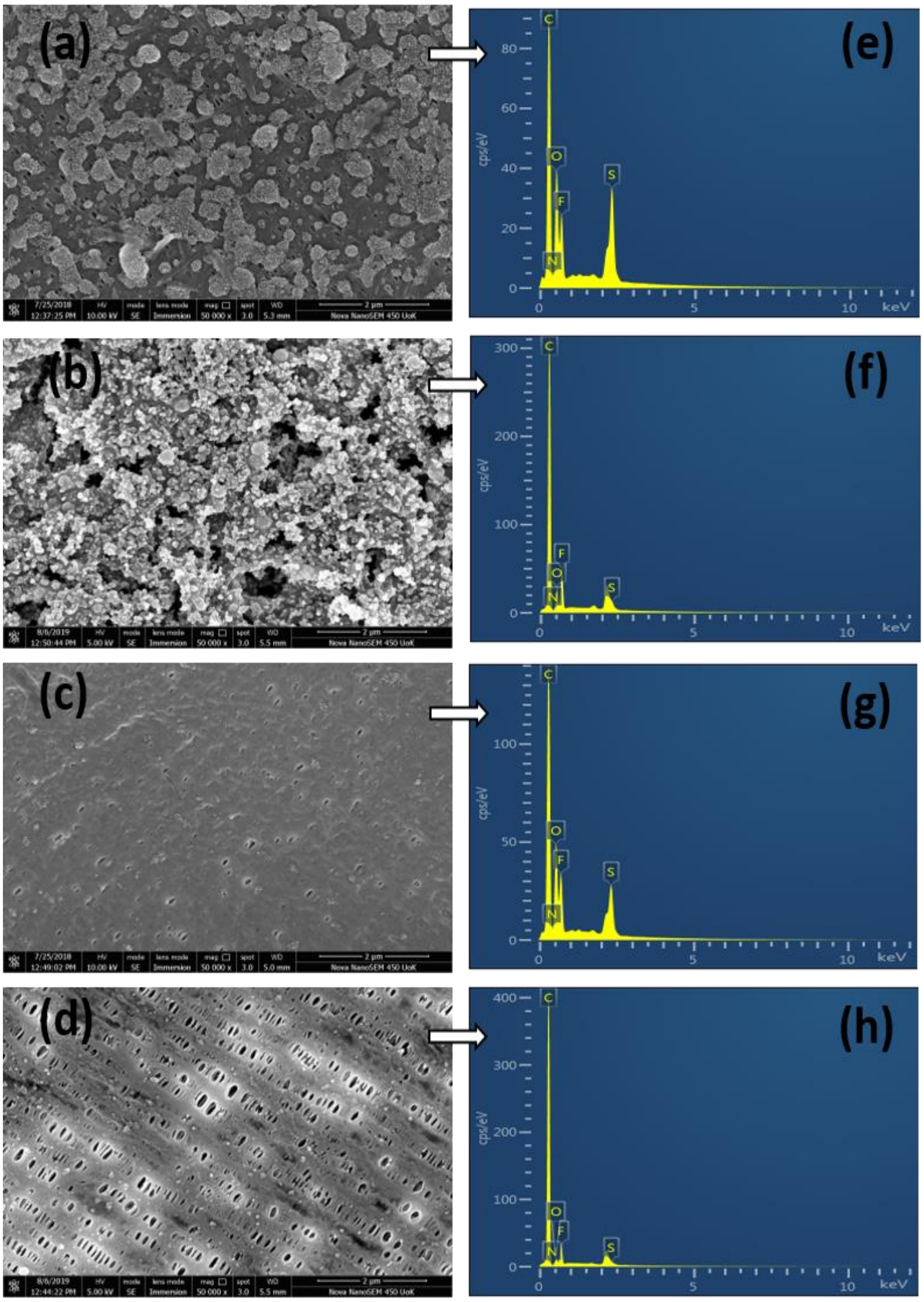

Figure 4.16. Morphology and composition of cycled separators after 100 cycles. SEM images of (a) CG (b) LPAM@CG separators on cathode sides and (c) CG (d) LPAM@CG separators on anode sides and (e, f, g, h) are the corresponding EDS spectra.

The lithium metal anodes were peeled off from the cells after 100 cycles, and investigated by conducting the ex-situ XPS analysis. The characteristic S2p peaks at ~166 eV (for polythionate complexes, a kind of transfer mediator that converts from long-chain PSs to short-chain PSs) and ~161 eV (assigned to insoluble Li_2S_2/Li_2S) and were considerably weakened at the lithium metal surface of Li-S cell containing LPAM@CG separator (Figure 4.17b) compared to the results of the control cell (Figure 4.17a). This post-mortem analysis verifies that the LPAM coating on the CG separator effectively prevented the shuttle effect, thus contributing to the superior cycling performance (Lang et al., 2015; Cao et al., 2019).

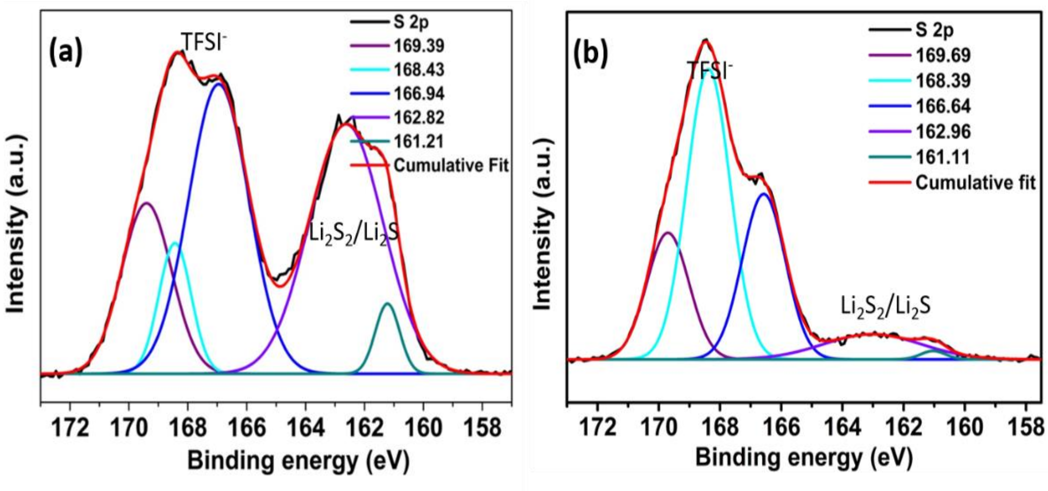

Figure 4.17. Deconvoluted S2p spectra for lithium anodes in the discharged state separated from the cells with (a) CG and (b) LPAM@CG membranes

4.4. Conclusion

In summary, a multi-functional permselective LPAM coated CG membranes was prepared by simple bar coating technique and applied as separators for Li-S cells. The LPAM@CG separator not only blocks the migration of PS anions, but also allows the free transportation of lithium cations. The presence of negatively charged -COO^{-} groups on the LPAM coating impart the selective diffusion of lithium ions while preventing the diffusion of negatively charged PS ions through the coulombic interactions. Besides, the LPAMP@CG separator possesses excellent electrolyte wettability, interfacial contact and ionic conductivity. These advantages bring significant improvement in the performance of cell (areal sulfur loading 4.1 mg cm^{-2}) with LPAM@CG separator, with a high initial capacity of 1213 mAh g^{-1}, an excellent rate capability of 633 mAh g^{-1} at 3C, and a good capacity retention of 956 mAh g^{-1} (78.8%) after 300 cycles at 0.1C. It is suggested here that the functional physical barrier (LPAM coating) layer on separator effectively suppress the PS crossover and improve the performance of LSB.

CHAPTER 5

MICRO AND NANOCRYSTALLINE INVERSE SPINEL $LiCoVO_4$ AS ELECTRODE MATERIALS FOR HIGH-PERFORMANCE LITHIUM-ION CAPACITOR

Intercalation pseudocapacitance has been recognized as a new type of charge storage mechanism in crystalline metal oxides, wherein intercalation of lithium-ions is not limited to surface structures, instead extended to the bulk crystalline framework of the material. This may narrow the performance gap between pseudocapacitors and battery materials. Hitherto, only a few crystalline materials have been found to exhibit such an intrinsic capacitive property. In this chapter, we introduce the intercalation pseudocapacitive lithium storage property of inverse spinel $LiCoVO_4$*. Micro and nanocrystalline* $LiCoVO_4$ *were synthesized via conventional solid-state reaction and hydrothermal reaction followed by calcination, respectively. In particular, nanocrystalline* $LiCoVO_4$ *demonstrated better lithium-ion intercalation benefited from its small crystallite size with highly exposed lithium-ion selective crystallographic pathways towards electrolyte. The* $LiCoVO_4$ *nanocrystals demonstrated excellent capacitive performance, including high specific capacitance (929.58 F* g^{-1} *at 1 A* g^{-1}*) and cycling stability in aqueous electrolyte. Moreover, asymmetric hybrid LICs were assembled using nanocrystalline* $LiCoVO_4$ *and MWCNT as the negative and positive electrode, respectively, in non-aqueous electrolyte. The hybrid LIC exhibited an unprecedented energy density (315.7 Wh* kg^{-1} *at a power density of 399.6 W* kg^{-1}*) and superior cycling stability (93% capacitance retention after 10000 cycles).*

5.1. Introduction

Both rechargeable batteries and pseudocapacitors store charges by means of a Faradaic redox reaction of the metal ions in electrode materials (Wang et al., 2016a; Liu et al., 2018b). The charge storage in batteries is controlled by cation diffusion within the crystalline framework of electrode material; while the pseudocapacitor is not controlled by diffusion, instead a surface-controlled process (Conway et al., 1997). Transition metal oxides with layered or tunnel crystalline structures are interesting electrode materials for lithium storage because of their capability to intercalate/de-intercalate lithium ions in the lattice sites (Augustyn et al., 2014; Brousse et al., 2015). Recently, lithium storage via intercalation pseudocapacitance received significant attention considering its ability to overcome the slow intrinsic lithium solid-state diffusion limited battery kinetics with surface process (Liu et al., 2018b; Liu et al., 2020b). However, intercalation pseudocapacitive lithium storage is hardly observed in most metal oxides. To date, only a few transition metal oxides such as Nb_2O_5 (Deng et al., 2018), α-MoO_3 (Brezesinski et al., 2010), TiO_2 (Han et al., 2018b), $H_3Ti_6O_{13}$ (Wang et al., 2012a), $LiFePO_4$ (Xie et al., 2015), LiV_3O_8 (Zheng et al., 2016), $LiFeTiO_4$ (Chen et al., 2015c), etc. exhibited lithium storage through intercalation pseudocapacitance mechanism. The significance of this new class of pseudocapacitance is that lithium storage in battery materials can be attained at rapid rates comparable to that of electrochemical capacitors (Wang et al., 2016a; Jiang and Liu, 2019).

Among a variety of intercalation host materials for LIB, spinel and inverse spinel-type structures earned a special interest as lithium hosts permitting three dimensional pathways for rapid lithium diffusion accompanying a low energy barrier (Haetge et al., 2011; Goodenough and Park, 2013). Nanocrystalline structure contributes increased number of lattice sites for accommodation of lithium-ions with expanded solid-solution limits. The combination of ion-selective channels and nanocrystalline structure exhibited a possible way for high rate lithium storage (Kim et al., 2011). The search of new lithium-ion intercalation pseudocapacitive electrode materials capable of delivering high energy density and long cycle life found great interest in the research of electrochemical capacitors. $LiCoVO_4$ was investigated as a LIB electrode material due to their capability of lithium storage through intercalation/extraction mechanism, providing a theoretical capacity 148 mAh g^{-1} (Chen et al., 2003). $LiCoVO_4$ possess an inverse spinel structure in which Li^+ and Co^{2+} ion equally reside in octahedral sites, and V^{5+} ions occupy the tetrahedral sites. The lithium ions present in the octahedral site take part in the intercalation process (Prakash et al., 2013a). Despite these investigations, the application of $LiCoVO_4$ for lithium storage via intercalation pseudocapacitance has not been studied.

In this chapter, we introduce inverse spinel $LiCoVO_4$ as a new lithium-ion intercalation pseudocapacitive electrode material operated in aqueous electrolyte and the effect of crystallite size on the fundamental lithium storage properties has been investigated. The micro and nanocrystalline $LiCoVO_4$ was synthesized by conventional solid-state reaction (S-LCVO) and hydrothermal method followed by calcination (H-LCVO), respectively. The electrochemical studies reveal that nanocrystalline inverse spinel $LiCoVO_4$ exhibits a high specific capacitance of 929.6 F g^{-1} at a current density of 1 A g^{-1} with excellent cycling stability in 1 M LiOH aqueous electrolyte. The kinetic information gained from cyclic voltammetric response, i.e., the so-called b-value defining the power law evolution of the measured current at a fixed potential with respect to potential sweep rate confirms the proposed lithium-ion intercalation mechanism. Furthermore, the as-assembled asymmetric hybrid LIC comprised of H-LCVO as negative electrode and MWCNT as positive electrode demonstrated excellent capacitive performances in aqueous and non-aqueous electrolyte. The LIC cells assembled in non-aqueous system exhibited a wide voltage window of 3V, superior energy density of 315.7 Wh kg^{-1} and excellent capacitance retention of 93% after 10000 cycles.

5.2. Materials and Methods

5.2.1. Materials

The precursors employed for synthesizing $LiCoVO_4$ active electrode material includes lithium nitrate ($LiNO_3$, 99.99% purity), cobalt nitrate ($Co(NO_3)_2.6H_2O$, 99.99% purity), and ammonium metavanadate (NH_4VO_3, 99.99% purity) were purchased from Sigma Aldrich. The chemicals used for electrochemical evaluation consists of PVDF, NMP, super P carbon, MWCNT, LiTFSI, DOL, DME, Celgard 2400 membrane, 2032 type coin cell case (details are given in section 2.2.1), nickel foam (1.6 mm thickness, MTI Corporation). All chemicals were used as received without further purification.

5.2.2. Synthesis of Micro and Nanocrystalline $LiCoVO_4$

The microsized $LiCoVO_4$ (S-LCVO) was synthesized by the solid-state reaction. The stoichiometric amounts of $LiNO_3$, $Co(NO_3)_2$, and NH_4VO_3 in a molar ratio of 1:1:1were pulverised for 6 h, using yttrium stabilized zirconia balls and then pressed into pellets. The pellets were sintered at 600 °C for 6 h in a muffle furnace. After cooling in air to room temperature, grinded using an agate mortar and sintered at 800 °C for 8 h to obtain a highly crystalline $LiCoVO_4$ powder.

The nanosized $LiCoVO_4$ (H-LCVO) was synthesized via hydrothermal reaction. The stoichiometric amounts of $LiNO_3$, $Co(NO_3)_2$, and NH_4VO_3 in a molar ratio of 1:1:1 were dissolved in distilled water to form a homogeneous solution. This precursor solution was then transferred into a 100 mL Teflon-lined stainless steel autoclave and maintained at 200 °C for 12 h. The light brown precipitate obtained was thoroughly washed with de-ionized water and ethanol to remove ions possibly remaining in the final hydrothermal products, dried at 80 °C in the air. The obtained powder was further calcined at 400 °C for 6 h to increase the crystallinity.

5.2.3. Material Characterization

The crystallographic structure and average crystallite size of the samples were determined by powder X-ray diffraction (XRD, PANalytical X'pert Pro diffractometer) patterns using a Cu-Kα radiation ($\lambda = 0.15406$ nm) in the range from 10° to 80°. The functional groups were detected using Fourier-transform infrared (FT-IR, PerkinElmer Spectrum 100) spectra recorded employing KBr pellet method. The thermal stability of the samples were evaluated using thermogravimetric analysis (TGA, Hitachi STA7300 Thermal analysis system) under inert atmosphere up to 800 °C with a heating rate of 10 °C min^{-1}. The morphology and microstructure of the samples were observed by scanning electron microscopy (SEM, FEI Quanta FEG 200) and transmission electron microscopy (TEM, JEOL JEM 2100, at 200 kV). The elemental composition was identified using energy dispersive X-ray spectrometry (EDS). The X-ray photoelectron spectroscopy (XPS, Kratos-Analytical Axis Ultra spectrometer) with a monochromatic Al-Kα X-ray source was performed to estimate the various chemical states of bonded atoms in the sample.

5.2.4. Electrode Preparation and Fabrication of Coin Cells

The individual electrodes were fabricated for both S-LCVO and H-LCVO. The slurry of pseudocapacitive $LiCoVO_4$ electrodes were prepared by mixing active material, Super P, and PVDF binder in a weight ratio of 8:1:1 in NMP solvent. Then the slurry was cast onto nickel foam current collector and dried at 80 °C in a vacuum oven. A 1 cm × 1 cm square electrodes were used for three-electrode system.

The negative electrode of LIC cell was prepared by coating H-LCVO slurry on nickel foam and dried. Then, it was roll-pressed and punched into circular disks with a diameter of 15 mm. The positive electrode was prepared comprising MWCNT, super P and PVDF binder in a weight ratio of 8:1:1. The materials were grinded in NMP to form slurry, which was then coated on the nickel foam and dried for 12 h at 120 °C. Then roll-pressed and punched into circular disks with a diameter of 15 mm. A standard 2032 type coin cell was assembled with aqueous (1M LiOH) and non-aqueous electrolyte (1M LiTFSI in the mixture solvent of DOL and DME in a volume ratio of 1:1). The coin cell using non-aqueous electrolyte was assembled in an Ar-filled glove box (M Braun, Germany).

5.2.5. Electrochemical Evaluation

The effect of crystallite size on pseudocapacitive lithium storage of the fabricated electrodes was evaluated using a three-electrode setup in 1 M LiOH aqueous solution as electrolyte. Cyclic voltammetry (CV), electrochemical impedance spectroscopy (EIS), and galvanostatic charge-discharge measurements were conducted by using PGSTAT302N electrochemical workstation (Metrohm Autolab, Netherlands). The micro and nanocrystalline $LiCoVO_4$ acted as the working electrodes, platinum mesh and Ag/AgCl electrodes were used as counter and reference electrodes, respectively. The CV curves were measured in a potential range of -0.2 to 0.6 V at various sweep rates (range from 1 to 100 mV s^{-1}). The EIS was measured at the working electrode potential of 0 V with a perturbation potential of 5 mV in a frequency range of 0.1 to 10^5 Hz. The hybrid cells were assembled in order to investigate the capacitive performance in non-aqueous electrolyte. The full-cell was fabricated using nanocrystalline $LiCoVO_4$ as the negative electrode and MWCNT as the positive electrode. The mass loading ratio between positive and negative electrodes was optimized according to the specific capacitance calculated from their discharge curves, and can be expressed as follows (Tang et al., 2013; Madabattula et al., 2020):

$$\frac{m_+}{m_-} = \frac{C_- \times V_-}{C_+ \times V_+} \tag{5.1}$$

where m (g) is the mass of active material in electrode, C (F g^{-1}) is the specific capacitance calculated using equation (1.12), and ΔV (V) is the operating potential of each electrodes. The specific capacitance can be calculated from the discharge curves according to the equation (1.12), where m (g) is the mass of active material coated on the individual electrode for 3-electrode setup or the total mass of active materials on the two electrodes for full-cell setup. Energy density (Wh kg^{-1}) and power density (W kg^{-1}) were calculated according to the equations (1.10) and (1.11).

5.3. Results and Discussion

5.3.1. Material Characterization

The crystal structure and phase purity of $LiCoVO_4$ active material synthesized via solid-state and hydrothermal reaction were characterized by powder XRD. XRD patterns for both S-LCVO and H-LCVO samples are shown in Figure 5.1a, which can be indexed on the basis of the standard PDF card (JCPDS 01-073-1635). The diffraction peaks at 2θ = 21.04°, 30.59°, 36.44°, 43.89°, 54.23°, 58.02°, 63.81°, 72.92° and 75.98° corresponds to the crystal planes (111), (220), (311), (400), (422), (511), (440), (620) and (533). It is clear that all intense diffraction peaks correspond to a cubic phase and $Fd\bar{3}m$ (227) space group, in which Li and Co ions partially occupy 16d sites, V is located in 8a site, and O occupy 32e site (Prakash et al., 2013b). The peaks indexed as (311) and (111) planes are characteristics of an inverse spinel structure (Li et al., 2009). Diffraction peak broadness was observed for H-LCVO, implying smaller crystallite size.

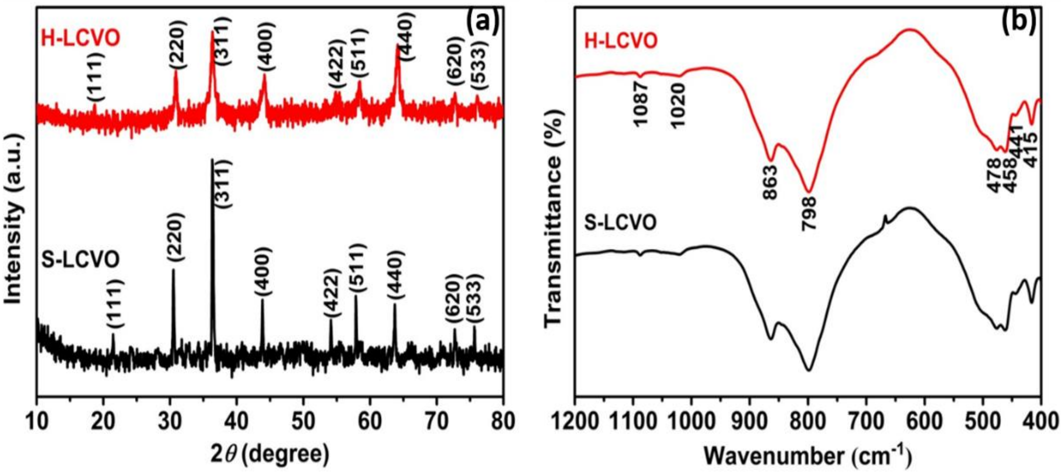

Figure 5.1. (a) XRD patterns and (b) FT-IR spectrum of S-LCVO and H-LCVO

Figure 5.1b shows the FT-IR spectra of S-LCVO and H-LCVO, which provides further insight into the structural information. The absorption band observed at 863 and 798 cm^{-1} are assigned to the stretching vibrations of VO$_4$ tetrahedrons. The bands sited around 600 to 450 cm^{-1} range are associated with the vibrations of Co-O bonds in CoO$_6$ and Li-O bonds in LiO$_6$ octahedral units or bending vibrations of VO$_4$ tetrahedron. The two weak absorption bands observed at 1087 and 1020 cm^{-1} corresponds to the asymmetric stretching vibration mode of Co-O bonds in CoO$_6$ octahedron. The two weak bands around 441 and 415 cm^{-1} refer to asymmetric stretching vibrations of Li-O bonds in LiO$_6$ octahedron (Bhuvaneswari et al., 2005).

The morphologies of S-LCVO and H-LCVO were observed by SEM and TEM, as shown in Figure 5.2. The SEM micrograph of S-LCVO (Figure 5.2a) reveals the formation of an irregular cube-like structure with a dimension ranging from 800 to 1000 nm. In contrast, Figure 5.2b depicts SEM image of H-LCVO, which consists of roughly spherical grains with grain size ranging from 45 to 60 nm. The elemental composition was confirmed using EDS analysis (Figure 5.2c-d). EDS analysis revealed the presence of Co, V, and O with an average ratio of 1:1 for Co: V.

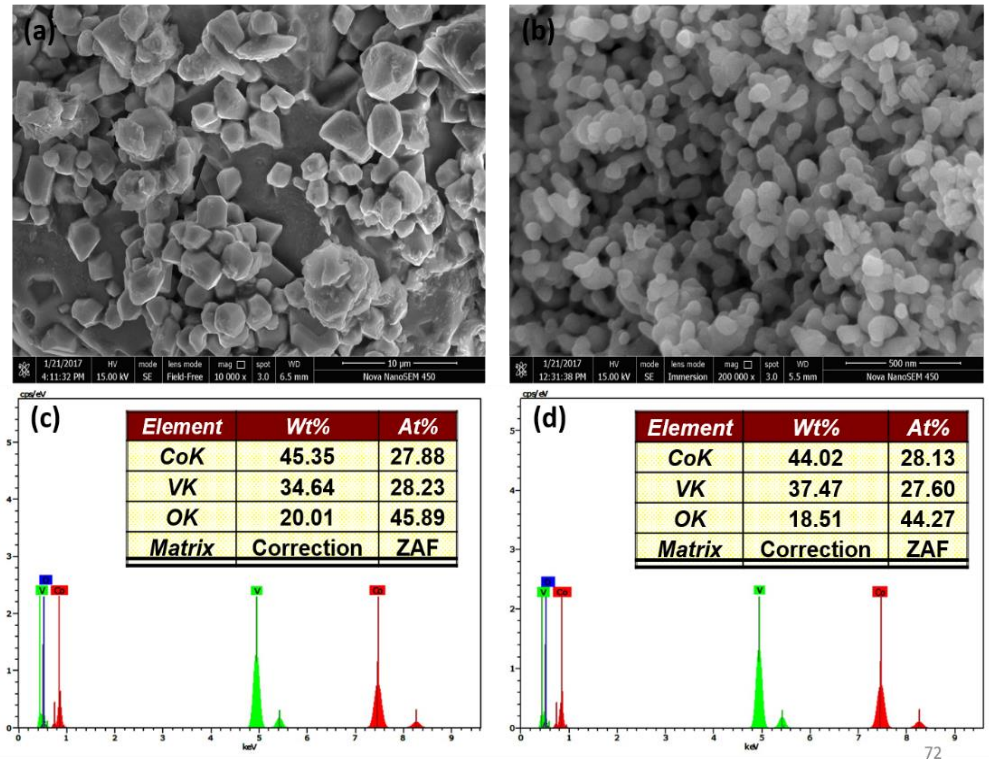

(c)

Element	Wt%	At%
CoK	45.35	27.88
VK	34.64	28.23
OK	20.01	45.89
Matrix	Correction	ZAF

(d)

Element	Wt%	At%
CoK	44.02	28.13
VK	37.47	27.60
OK	18.51	44.27
Matrix	Correction	ZAF

Figure 5.2. FESEM images of (a) S-LCVO (b) H-LCVO, and EDS spectrum of (c) S-LCVO (d) H-LCVO

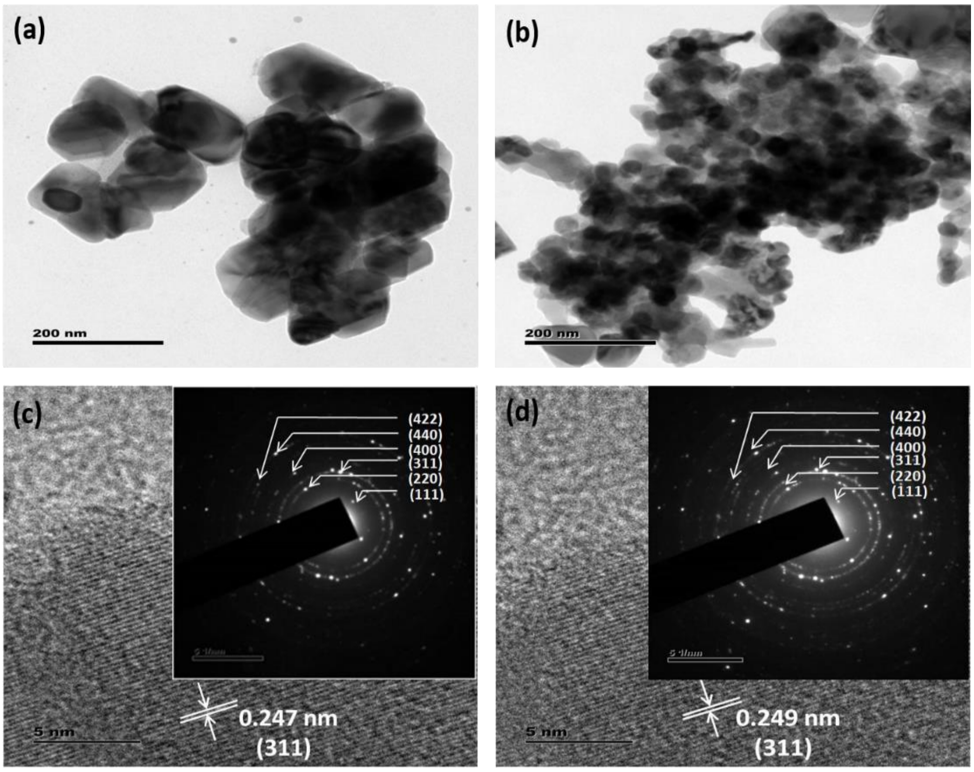

Figure 5.3. TEM images of (a) S-LCVO (b) H-LCVO, high-resolution TEM and indexed SAED patterns of (c) S-LCVO (d) H-LCVO

Further, the TEM imaging was carried out to gather insight on $LiCoVO_4$ crystal structure. TEM images of S-LCVO (Figure 5.3a) and H-LCVO (Figure 5.3b) expose well defined crystal faces. High resolution TEM images shown in Figure 5.3c-d shows lattice fringes from the crystallites. The lattice spacing of 0.247 and 0.249 nm corresponds to the (311) plane of S-LCVO and H-LCVO, respectively. The selected area electron diffraction (SAED) pattern shown in the inset of Figure 5.3c-d demonstrates crystalline nature of the sample and the diffraction spots can be clearly indexed to the inverse spinel $LiCoVO_4$ phase.

The surface electronic sates of each elements present in $LiCoVO_4$ was obtained from XPS measurements. Figure 5.4 shows the Li, Co, V and O XPS core level spectra for S-LCVO and H-LCVO. It can be clearly seen in Figure 5.4, that the XPS peak positions for both samples are analogous. The binding energy of the Li1s core level emission peak (Figure 5.4a) was located at 54.6 eV and appeared as a broadened signal (Kanamura et al., 1995). The Co2p core spectrum (Figure 5.4b) consists of $Co2p_{3/2}$ and $Co2p_{1/2}$ peaks at 779 and 794.8 eV, respectively and corresponding weak shake up satellite peaks of Co^{2+}. The V2p core spectrum (Figure 5.4c) splits to $V2p_{3/2}$ and $V2p_{1/2}$ peaks located at 516.9 and 524.2 eV, characteristics of V^{5+}. The XPS O1s peak (Figure 5.4d) shows a peak around 529.6 eV assigned to Co-O bonds, and a shoulder peak at 531.2 eV associated with oxygen in low coordination sites at the surface (Prakash et al., 2013a).

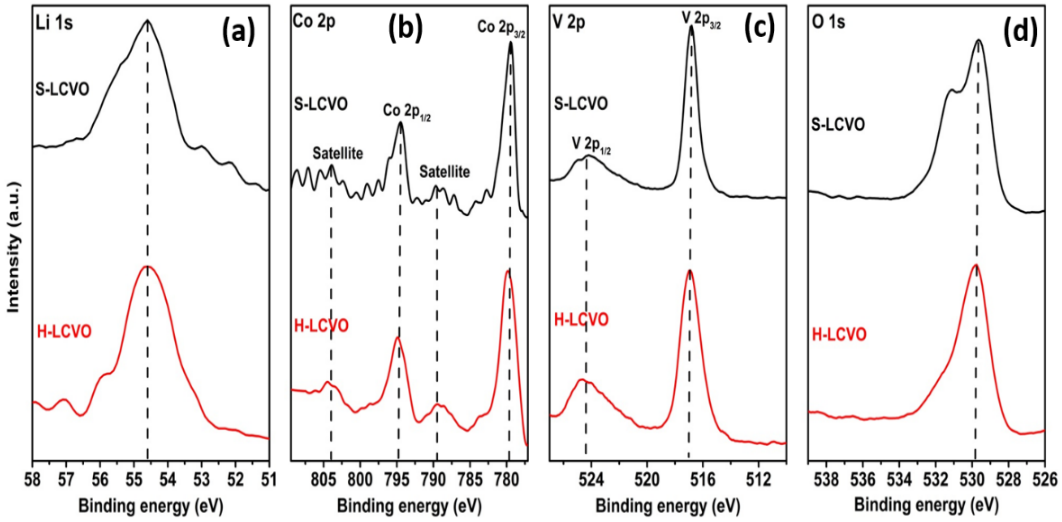

Figure 5.4. XPS core level spectra of both S-LCVO and H-LCVO (a) Li1s (b) Co2p (c) V2p (d) O1s

TGA analysis was carried out in order to determine thermal stability and decomposition profile of the samples. Figure 5.5 shows the thermal decomposition profile of S-LCVO and H-LCVO in a temperature range of 25 to 800 °C. The initial weight loss below 100 °C is attributed to the evaporation of residual water. The next weight loss observed in the temperature range of 200 to 300 °C is due to the decomposition of residual precursor materials, which takes place at its melting points. After 300 °C, both S-LCVO and H-LCVO gives a stable decomposition curve. The percentage weight loss until the weight stabilizes is 14.6% for S-LCVO and 8.5% for H-LCVO. From the TGA curve, it is clear that the microcrystalline S-LCVO exhibited greater degree of weight loss compared to nanocrystalline H-LCVO. The greater weight loss observed in S-LCVO can be ascribed to the enthalpic gain due to weak bonding between constituent atoms as well as entropic gain obtained by liberating more number of left over water molecules (Kim et al., 2013).

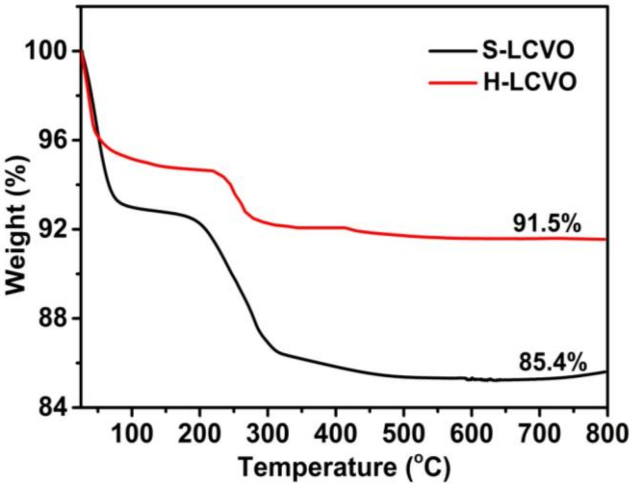

Figure 5.5. TGA curves of S-LCVO and H-LCVO

5.3.2. Electrochemical Lithium Storage Performance of Micro and Nanocrystalline $LiCoVO_4$

The pseudocapacitive lithium storage of $LiCoVO_4$ electrodes in 1 M LiOH aqueous electrolyte was evaluated on the basis of its response to a potential sweep (CV), alternating current (EIS), and constant current (galvanostatic charge-discharge measurements).

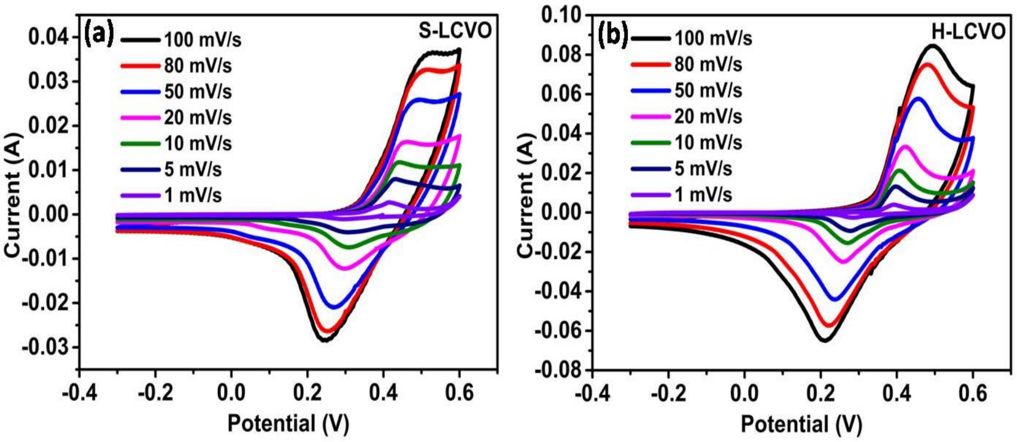

Figure 5.6. CV curves of (a) S-LCVO and (b) H-LCVO at different sweep rates

The electrochemical performance of micro and nanocrystalline $LiCoVO_4$ electrodes was firstly examined by CV using a 3-electrode setup (Figure 5.6a,b). The CV curves exhibited symmetric cathodic and anodic peaks with a slight voltage separation in the sweep rates ranging from 20 to 1 mV s^{-1}. This feature is one of the indicatives of pseudocapacitive behaviour. Beyond the sweep rates of 20 mV s^{-1}, there is an evident peak shift owing to ohmic contribution (Wang et al., 2015c).

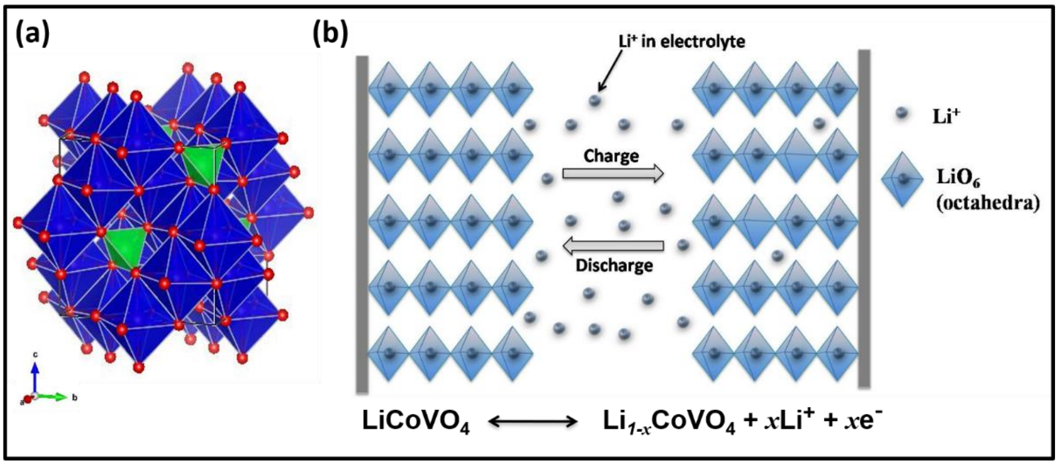

Figure 5.7. (a) The 3D visualization of $LiCoVO_4$ crystal using VESTA 3, where Li and Co equally occupies MO_6 (M = Li, Co) octahedra indicated in blue colour and VO_4 tetrahedra in green colour (b) schematic illustration of the Li^+ intercalation and de-intercalation process in $LiCoVO_4$ electrode during charge-discharge process. CoO_6 octahedra and VO_4 tetrahedra in the $LiCoVO_4$ crystal structure are not represented.

The cathodic and anodic peaks observed in the potential range of 0.2 to 0.6 V can be attributed to the reversible electrochemical lithium-ion intercalation and extraction process represented by the following reaction:

$$LiCoVO_4 \leftrightarrow Li_{1-x}CoVO_4 + xLi^+ + xe^- \qquad (5.2)$$

where x is the mole fraction of inserted lithium given by x = QM/mF, where Q is the stored charge, M is the molecular weight, m is the mass and F is the Faraday constant (Brezesinski et al., 2010). In this reaction, lithium ions can intercalate and de-intercalate during the charge-discharge process (as shown in Figure 5.7), which is similar to that of the LIB. The electrochemical insertion of lithium ions into $LiCoVO_4$ was expected to occur with concomitant oxidation of Co^{2+} to Co^{3+}.

Comparative CV curves of S-LCVO and H-LCVO at the sweep rate of 100 mV s^{-1} was represented in Figure 5.8a. The current density and area of the CV curve were much larger for H-LCVO compared to S-LCVO, because of the nanocrystalline nature of H-LCVO. The nanocrystalline structure offer more number of 3D lithium-ion diffusion pathways within the unit area of electrode surface, thereby providing fast ion transport path and enhanced electrolyte accessibility (Xia et al., 2018).

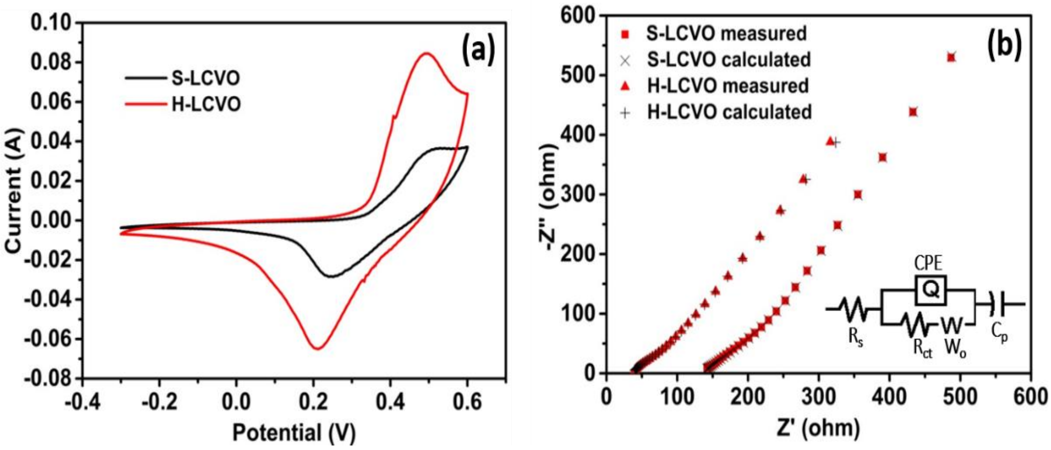

Figure 5.8. (a) CV curves of S-LCVO and H-LCVO at the same sweep rate of 100 mV s^{-1} (b) EIS spectra of both S-LCVO and H-LCVO. Inset: corresponding equivalent circuit

The electrochemical behaviour of microsized S-LCVO and nanosized H-LCVO was further analysed using EIS analysis. Figure 5.8b shows the EIS Nyquist plots and its calculated curve by the ZSimpWin software. An equivalent circuit used to fit the impedance curve is given in the inset of Figure 5.8b, which includes elements of bulk solution resistance (R_s), charge-transfer resistance (R_{ct}), constant phase element (CPE) to account for the double layer capacitance, Warburg diffusion element (W) and a pseudocapacitive element (C_p) from the lithium-ion diffusion associated with intercalation/extraction process of electrode materials. The equivalent series resistance (R_s) of the electrodes can be obtained from the high frequency intersection of Nyquist plot in the x-axis (Li et al., 2014c; Eskandari et al., 2020). It is found that H-LCVO has reduced R_s value compared to S-LCVO electrode in 1 M LiOH aqueous electrolyte. The reduced R_s value of H-LCVO electrode could be attributed to the small crystallite size of the active material, which shortens the lithium-ion diffusion path length and thereby boost the lithium-ion movement in the electrolyte. In addition, the absence of semicircle in the high frequency region of Nyquist plot implies negligible charge-transfer resistance for both electrodes. The slopes of straight lines in the low frequency region of both S-LCVO and H-LCVO electrodes were larger than that of 45° straight line, indicating characteristic capacitor behaviour (Ates et al., 2015; Gupta et al., 2015; Mei et al., 2018).

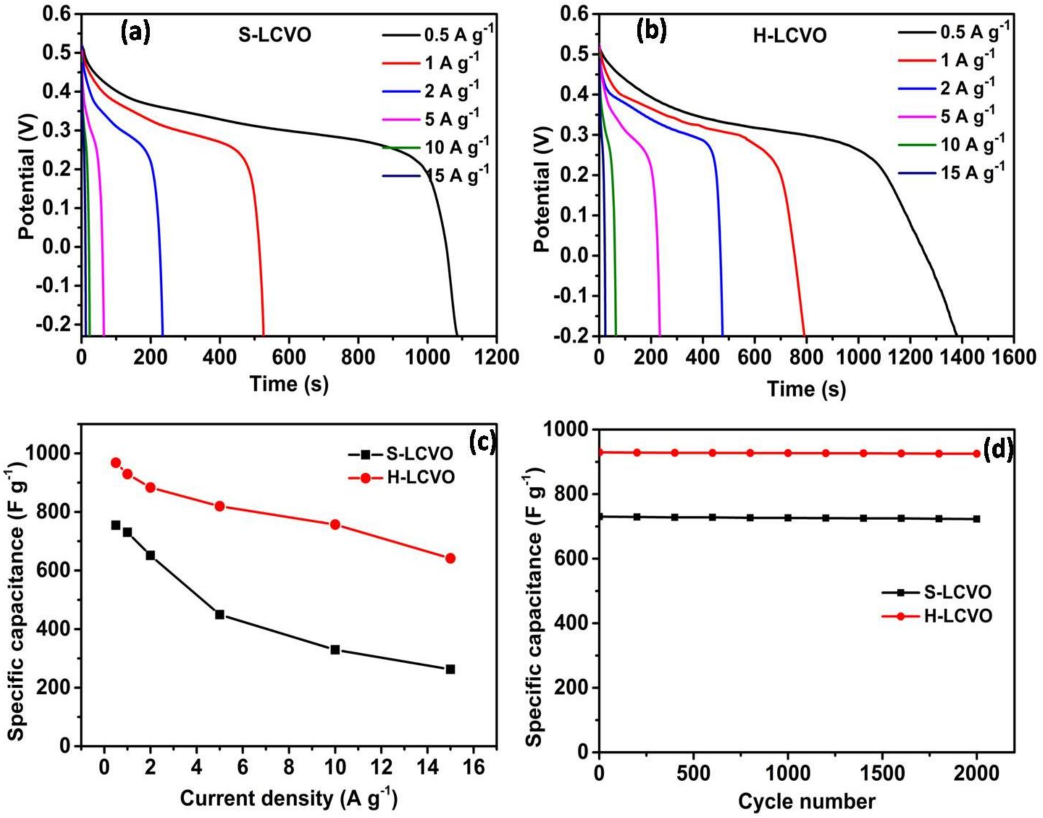

Figure 5.9. Galvanostatic discharge curves of (a) S-LCVO and (b) H-LCVO at various current densities (c) specific capacitance of S-LCVO and H-LCVO at different current densities (d) long-term cycling stability of S-LCVO and H-LCVO

The lithium storage capacity of micro and nanocrystalline $LiCoVO_4$ electrodes were investigated using galvanostatic charge-discharge studies in the potential range of -0.2 to 0.52 V to avoid IR drop. Figure 5.9a-b show the discharge curves of S-LCVO and H-LCVO at various current densities between 0.5 A g^{-1} to 15 A g^{-1}. Correspondingly, a discharge plateau was observed, which is consistent with CV results. The discharge time of H-LCVO electrode is higher than of S-LCVO electrode, implying a higher specific capacitance for H-LCVO.

The specific capacitance calculated from the discharge curves at various current densities is shown in Figure 5.9c. At different current densities of 0.5, 1, 2, 5, 10, and 15 A g^{-1}, the specific capacitance was estimated to be 754.5, 730.4, 651.6, 449.3, 329.1 and 262.5 F g^{-1} for S-LCVO and 967.9, 929.5, 883.3, 819.4, 756.9 and 641.6 F g^{-1} for H-LCVO electrode. The specific capacitance of H-LCVO was apparently larger than that of S-LCVO. The higher electrochemical capacitance of H-LCVO electrode can be ascribed to its nanocrystalline structure which possibly exposes a large active surface to enhance the electrolyte accessibility, and thereby provides a large number of active sites for rapid lithium-ion transport (Lukatskaya et al., 2016). The continuous charge-discharge measurements were carried out to evaluate the long term cyclability of the micro and nanocrystalline $LiCoVO_4$ electrodes. Figure 5.9d shows the variation of specific capacitance versus cycle number at a current density of 1 A g^{-1}. The capacitance loss was merely 1.05% for S-LCVO and 0.48% for H-LCVO after 2000 continuous charge-discharge cycles. The excellent cycle stability exhibited by S-LCVO and H-LCVO electrodes can be endorsed to its unique structural feature which provides facile lithium-ion migration pathways with negligible crystallographic phase change during lithiation/delithiation process (Lubimtsev et al., 2013; Mohd Abdah et al., 2020). Moreover, H-LCVO demonstrated the improved electrochemical performance (specific capacitance as well as cycle stability) compared to S-LCVO. It is believed that the nanocrystalline structure could provide large number of ion conducting channels per unit area and favour fast lithium-ion transport for H-LCVO (Tomaszewska et al., 2019; Kim et al., 2019). The capacitive charge storage observed in both micro and nanosized $LiCoVO_4$ crystals with negligible phase transformation further confirms the intrinsic pseudocapacitive behavior of $LiCoVO_4$.

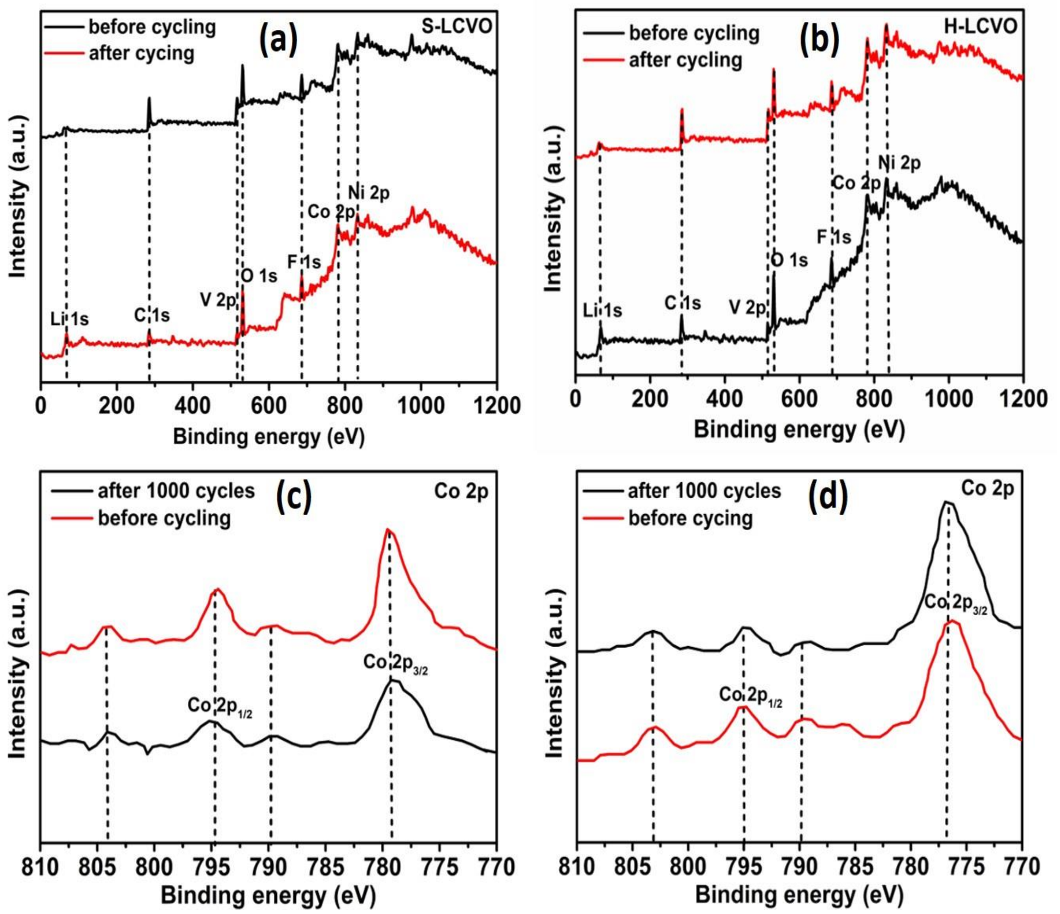

Figure 5.10. XPS survey spectrum of (a) S-LCVO electrode before and after cycling (b) H-LCVO electrode before and after cycling. Comparative XPS core level spectrum of Co 2p (c) S-LCVO electrode before and after cycling (d) H-LCVO electrode before and after cycling

XPS analysis of S-LCVO and H-LCVO electrode materials were carried out to further confirm the proposed lithium-ion intercalation mechanism and excellent cycling stability. It can be clearly seen from the survey spectra (Figure 5.10a-b) that S-LCVO and H-LCVO electrode before and after charge-discharge cycles primarily composed of Li1s, Co2p, V2p, and O1s peaks. The additional XPS peaks C1s and F1s were originated from Super P and PVDF employed during electrode coating process and Ni2p peak from the nickel foam substrate. No apparent shift in peak position was observed for both S-LCVO and H-LCVO electrodes after repeated 2000 charge-discharge cycles, which validate the conclusion that there is no perceptible phase transformation after cycling. The comparative Co2p core level spectra of S-LCVO and H-LCVO electrode before and after cycling were evaluated (Figure5.10c-d), which comprises of two major peaks, centered around 776.65 eV for Co2p$_{3/2}$ and 795.03 eV for Co2p$_{1/2}$ with shake-up satellite peaks (Prakash et al., 2013a). It is obvious that the core level Co2p peaks hardly shift even after continuous charge-discharge cycles. This observation substantiates the fact that capacitance performance in $LiCoVO_4$ electrode is exclusively lithium-ion intercalation/extraction process without any crystallographic phase change.

SEM micrographs of S-LCVO and H-LCVO electrodes before and after cycling further provide evidence for the lithium-ion intercalation mechanism with negligible structural changes (Figure 5.11a-d), affirming XPS results.

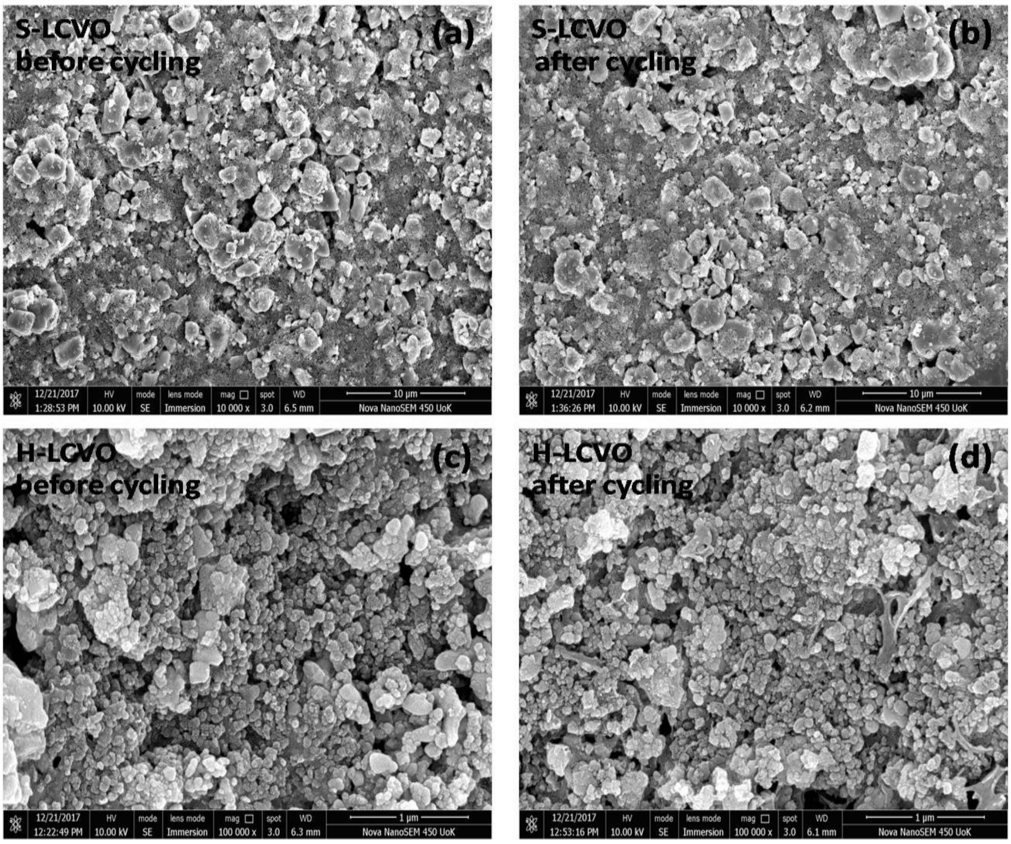

Figure 5.11. FESEM images: S-LCVO (a) before cycling (b) after cycling and H-LCVO (c) before cycling (d) after cycling

Further insight regarding kinetics of charge storage in micro and nanocrystalline $LiCoVO_4$ can be obtained from detailed evaluation of CV data. The relationship between the redox peak current (i) and sweep rate (v) should obey the power law: $i = av^b$. The calculated b-value can be used to distinguish the charge storage behaviour, whether it originates from battery-type (controlled by cation diffusion in the crystalline framework of electrode material) or capacitive (not limited by the diffusion of cations within the crystalline framework of electroactive materials) processes. The b-value of 0.5 represents battery-type semi-infinite diffusion- process, whereas b-value of 1 indicates capacitor-type behaviour via a fast Faradaic reaction (Augustyn et al., 2014; Wang et al., 2016a). Figure 5.12 shows the b-value determination of cathodic peaks by plotting log(i) versus log(v). The b-values close to 1 is obtained for both micro and nanocrystalline $LiCoVO_4$ in the potential sweep rate ranges from 1 to 20 mV s^{-1}, and deviates severely when the sweep rate is beyond 20 mV s^{-1}. The deviation observed in the faster sweep rates can be ascribed to poor electronic conductivity of the active electrode materials resulting in the lethargic electron transportation (Augustyn et al., 2013; Elgrishi et al., 2018). Thus, it can be concluded that total stored energy in the $LiCoVO_4$ arises from the intercalation/de-intercalation of lithium-ion that is not limited by solid-state diffusion.

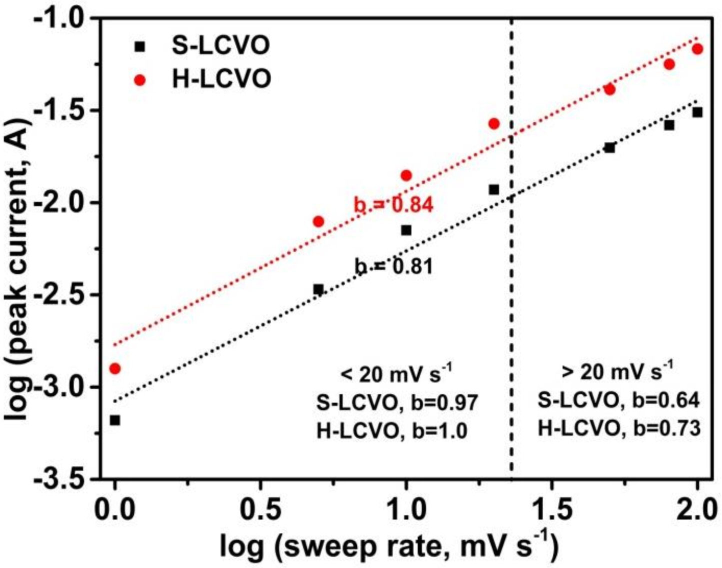

Figure 5.12. b-value determination of cathodic peak currents

In the case of cation-intercalation pseudocapacitance, the advantage of batteries is integrated with that of supercapacitors. Therefore, overall capacity of the material can be considered as a contribution from capacitive charge storage and bulk charge storage. However, the capacitive component contributes more. For such materials exhibiting hybrid charge storage, the *b*-value is only close to and slightly less than 1. The calculated *b*- values for S-LCVO and H-LCVO electrodes in the wide range of sweep rate (1 to 100 mV s^{-1}) are 0.81 and 0.84, respectively. In other words, the $LiCoVO_4$ electrodes possess hybrid charge storage behaviour, which can be described as a combination of surface-controlled capacitive and diffusion-controlled lithium-ion intercalation mechanism (Augustyn et al., 2014; Wang et al., 2016a; Jiang and Liu, 2019).

5.3.3. Electrochemical Lithium Storage Performance of Nanocrystalline $LiCoVO_4$ Hybrid LIC in Aqueous Electrolyte

For asymmetric LICs, it is crucial that the capacities of cathode and anode should match with each other to fully utilize the electrochemical properties of both electrodes (Cericola and Kötz, 2012; Wang et al., 2019e). Generally, the capacity of anode is much higher than that of cathode, which requires a higher mass loading of cathode according to the equation (5.1).

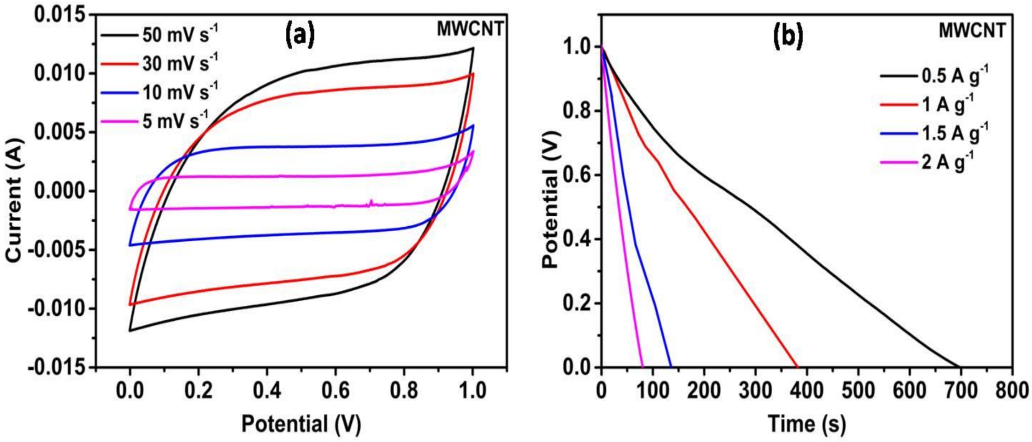

Figure 5.13. Electrochemical evaluation of MWCNT electrode in 1 M LiOH electrolyte: (a) CV curves at different potential sweep rates (b) galvanostatic discharge curves at different applied current densities

The hybrid cells were fabricated using H-LCVO as negative electrode and MWCNT as the positive electrode. The MWCNT based positive electrode provide accessible mesopores due to its central canal and entangled structure, which possibly facilitate the lithium-ion intercalation process. In addition, the presence of multiple rolled layers in MWCNT enhances lithium-ion insertion in a way similar to graphite (Landi et al., 2009; Xiong et al., 2013). The electrochemical evaluation of MWCNT electrode in 1 M LiOH electrolyte is represented in Figure 5.13a-b.

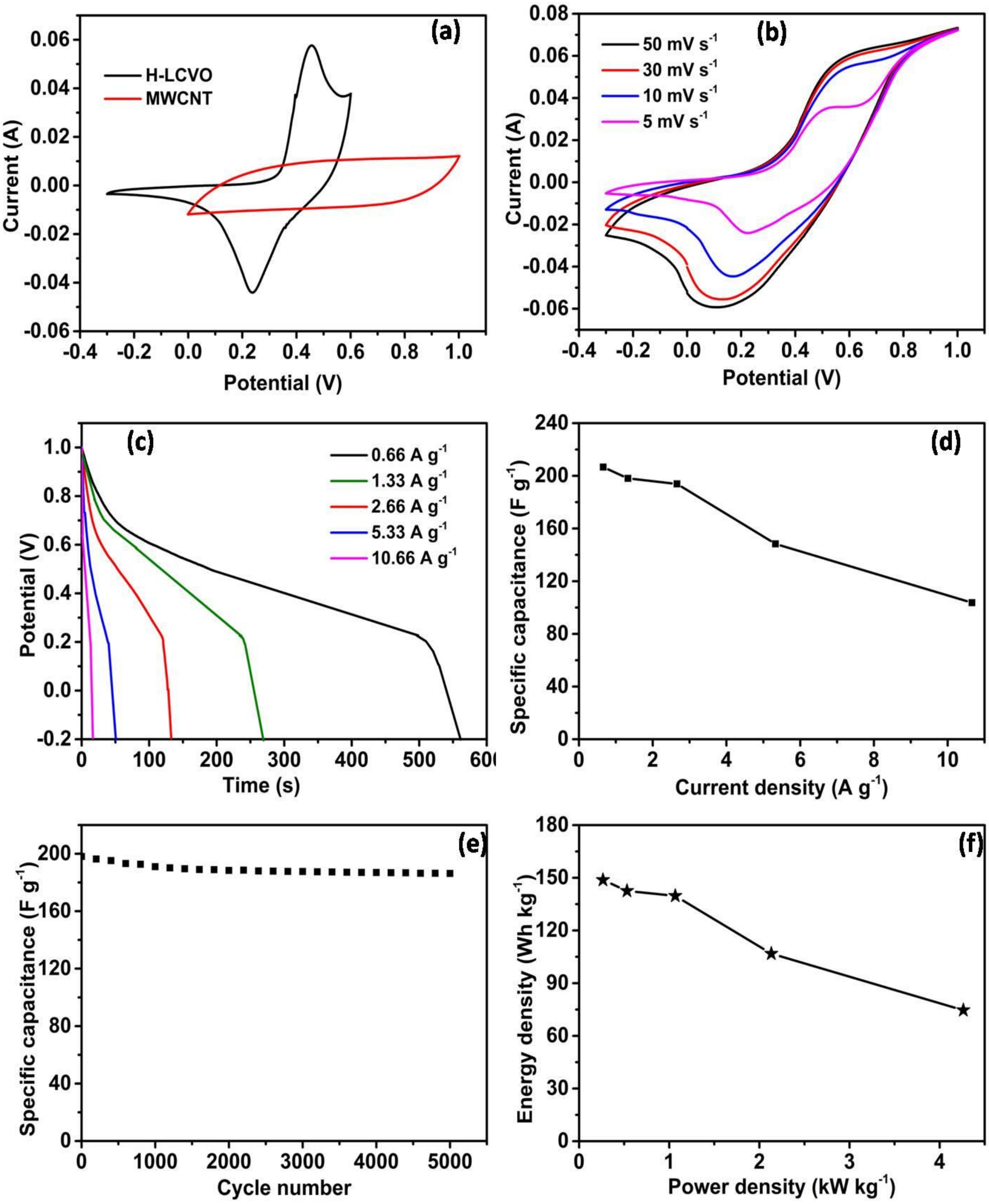

Figure 5.14. (a) CV profiles of H-LCVO and MWCNT electrodes. Electrochemical performance of assembled hybrid cells: (b) CV curves at various sweep rates and (c) galvanostatic charge-discharge at various current densities (d) Specific capacitance at various current densities (e) Cycling stability at 1.33 A g^{-1} (f) Ragone plot

As shown in Figure 5.14a, H-LCVO and MWCNT electrode exhibited a stable voltage window of -0.2 to 0.6 V and 0 to 1 V (vs. Ag/AgCl) at 50 mV s^{-1}, respectively. Thus, an extended operating voltage window from -0.2 to 1 V can be expected for assembled cell. The specific capacitance of individual H-LCVO and MWCNT was calculated from their discharge curves, and found to be 968 and 158.5 F g^{-1}, respectively, at 0.5 A g^{-1}. Here, the mass ratio of active material coated on the negative to positive electrode was set to 0.227 to maintain charge balance across the electrodes (Dsoke et al., 2015).

Figure 5.14b demonstrates the CV curves of the H-LCVO//MWCNT hybrid cell cycled at various sweep rates (from -0.2 to 1 V). The presence of redox peaks observed in the CV curve suggests the pseudocapacitive behaviour of the assembled supercapacitor due to fast lithium-ion transport through intercalation process (Wang et al., 2016a). The galvanostatic discharge curves of hybrid cell were shown in Figure 5.14c. Lithium-ion intercalation into the crystalline framework of $LiCoVO_4$ takes place during charging and lithium-ion extraction into the electrolyte occur during discharging. Based on total mass of active material in both electrodes, specific capacitance of the cell at various current densities were calculated from the discharge curves and represented in Figure 5.14d. The cell displays a capacitance of 206 F g^{-1} at 0.66 A g^{-1} and decrease to 103.6 F g^{-1} at 10.66 A g^{-1}. Further, the long-term cycle performance of the fabricated H-LCVO//MWCNT hybrid cell was evaluated from continuous charge-discharge cycling at 1.33 A g^{-1} for 5000 cycles (Figure 5.14e). Capacitance retention of nearly 94% is observed even after 5000 continuous charge-discharge cycles indicating excellent electrochemical stability. The energy density and power density of the hybrid supercapacitors were calculated using (1.10) and (1.11), and given in the Ragone plot (Figure 5.14f).The H-LCVO//MWCNT cell exhibited a maximum energy density of 148.7 Wh kg^{-1} at a power density of 260 W kg^{-1}, and a maximum power density of 4260 W kg^{-1} at an energy density of 74.6 Wh kg^{-1}. The maximum value of energy density delivered by fabricated hybrid cell is better than that of supercapacitor electrodes previously reported in aqueous electrolyte (Sun et al., 2017b; Pan et al., 2019).

5.3.4. Electrochemical Lithium Storage Performance of Nanocrystalline $LiCoVO_4$ Hybrid LIC in Non-Aqueous Electrolyte

In order to achieve better energy density, we developed an asymmetric LIC which is based on a negative electrode of H-LCVO and a positive electrode of MWCNT in an organic electrolyte containing lithium-ions. On charge process, anions from electrolyte are absorbed in porous structure of MWCNT (positive electrode). At the same time, lithium-ions from electrolyte are intercalated into the H-LCVO (negative electrode). Discharge reverses the charge process.

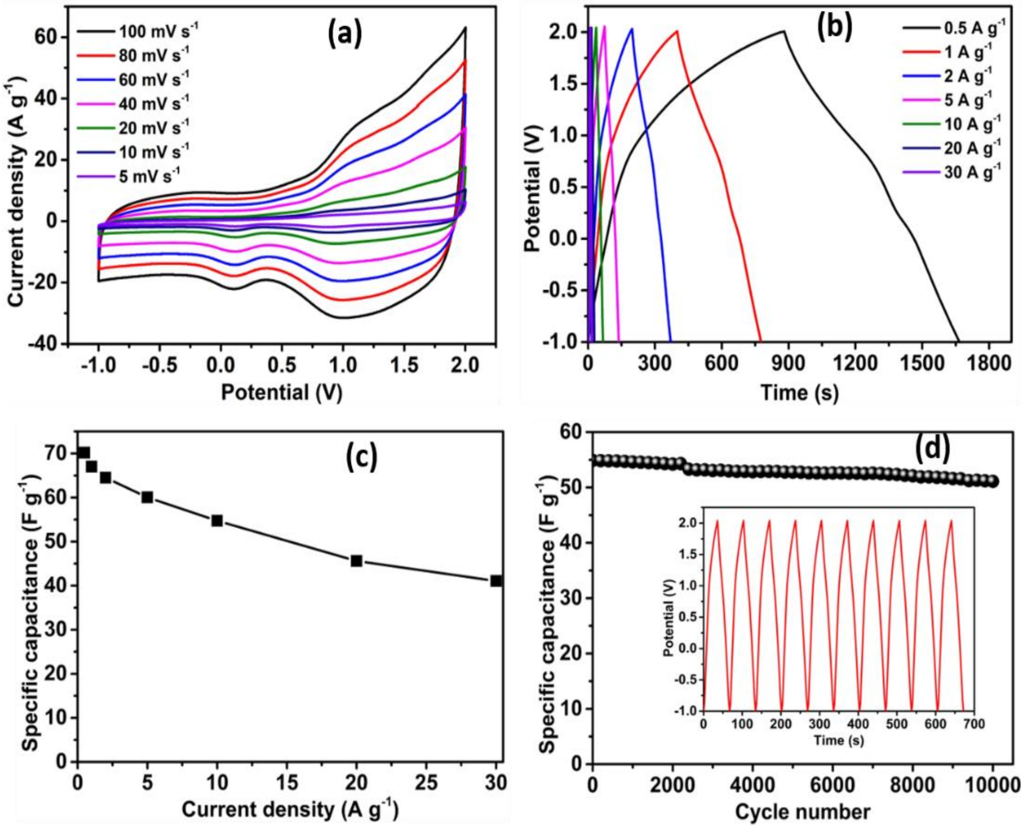

Figure 5.15. Electrochemical performance of H-LCVO//MWCNT LIC: (a) CV curves at various scan rates, (b) galvanostatic charge-discharge curves at different current densities, (c) specific capacitance values calculated from galvanostatic charge/discharge curves under different current densities, (d) cycle stability for 10000 cycles at a current density of 5 A g^{-1}, Inset: charge-discharge profiles for 10 continuous charge-discharge cycles

The CV curves and charge-discharge curves of the H-LCVO//MWCNT hybrid LICs are displayed in Figure 5.15a-b. The CV curves are different from those of the conventional symmetric capacitors, gradually deviate from the ideal rectangular shape with increasing scan rates, which is due to the insertion-type energy storage mechanism of H-LCVO (Wang et al., 2016a; Shao et al., 2018b). However, the curve profiles reveal the rectangular part from 0.75-2 V, indicating the co-existence of the EDLC-type and battery-type charge storing features. The charge-discharge curves in Figure 5.15b exhibit a great linear relation especially at large current densities and show some bending at low current densities, corresponding to the redox peak in CV curves (Huang and Niederberger, 2019; Huang et al., 2020). The specific capacitance values of H-LCVO//MWCNT hybrid LIC (based on total mass of cathodic and anodic active materials) were 70.1, 67, 64.5, 60, 54.7, 45.6, 41 F g^{-1} at the current densities of 0.5, 1, 2, 5, 10, 20, 30 A g^{-1}, respectively (Figure 5.15c).Furthermore, H-LCVO//MWCNT based LIC also exhibits a good cycle stability (Figure 5.15d) with the capacity retention of ~93% after 10000 cycles at a high current density of 5 A g^{-1}.

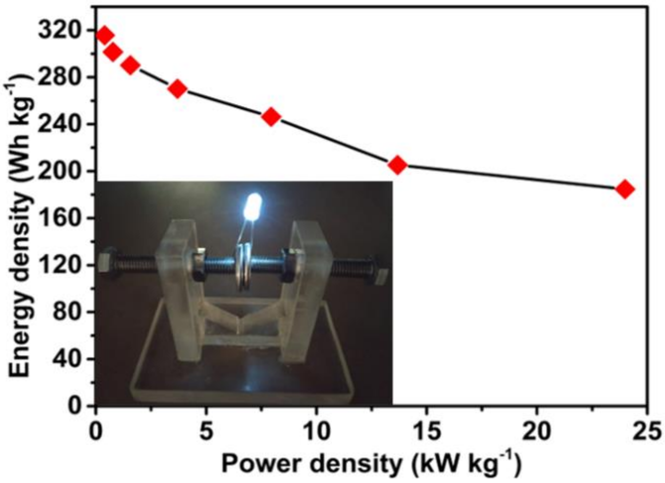

Figure 5.16. Ragone plot of LIC cell (inset shows a white LED powered by two LIC devices in series)

The Ragone plot (energy density *vs.* power density) of H-LCVO//MWCNT hybrid LIC is shown in Figure 5.16. It can be seen from Figure 5.16 that the H-LCVO//MWCNT can attain high energy density of 315.7 Wh kg^{-1} at power density of 399.6 W kg^{-1}, even at a relatively higher power density of 23990.2 W kg^{-1}, the energy density can retain 184.7 Wh kg^{-1}, which is calculated from the active material mass of both the electrodes. Finally, in order to reveal the potential of H-

LCVO//MWCNT in practical applications, we use a light-emitting diode (LED) system for measurement (inset of Figure 5.16). After charging for 20s, the LIC system could glow a white LED for over 2 minutes.

Table 5.1. Comparison of the electrochemical performance of LIC fabricated using aqueous and non-aqueous electrolyte

	Current density ($A\ g^{-1}$)	Specific capacitance ($F\ g^{-1}$)	Energy density ($Wh\ kg^{-1}$)	Power density ($W\ kg^{-1}$)
Aqueous electrolyte	0.66	206.6	148.7	264.4
	10.66	103.6	74.6	4263.6
Non-aqueous electrolyte	0.5	70.1	315.7	399.6
	10	54.7	246.2	7944.6

The extraordinary electrochemical performance observed for H-LCVO//MWCNT can be attributed to the nanocrystalline structure of $LiCoVO_4$, which renders rapid lithium-ion transport pathway within the crystal lattice. On the other hand, the unique coupling with MWCNT electrode also contributes to the excellent performance of assembled capacitor. Together with lithium-ion intercalation type (H-LCVO) electrode, EDLC-type (MWCNT) counter electrode boost up the energy density, but at a cost of power density. Our studies reveal an excellent pseudocapacitive lithium storage performance with an exceptionally high energy density, in the meantime retaining reasonable power density.

5.4. Conclusion

In summary, the pseudocapacitive lithium storage capability of micro and nanocrystalline $LiCoVO_4$ have been investigated in aqueous electrolyte. The $LiCoVO_4$ nanocrystals demonstrated better lithium-ion intercalation/de-intercalation properties benefited from its small crystallite size with highly exposed crystallographic framework towards electrolyte. On the grounds, we fabricated a hybrid asymmetric capacitor (nanocrystalline $LiCoVO_4$//MWCNT) using aqueous and non-aqueous electrolyte. The LIC cell in non-aqueous electrolyte displays a specific capacitance of 67 F g^{-1} at a current density of 1 A g^{-1}, and good reversibility with a capacitance retention of ~93% after 10000 cycles. The energy performance of the hybrid LIC cell reported here reaches 315.7 Wh kg^{-1} (at a power density of 399.6 W kg^{-1}). Therefore, the designed hybrid LIC with exceptionally high energy density and excellent cycling stability, offer a promising approach to develop advanced supercapacitor devices for both commercial and consumer applications.

CHAPTER 6

NANOCRYSTALLINE INVERSE SPINEL $LiNiVO_4$ AS AN INSERTION ANODE FOR LITHIUM-ION CAPACITOR

The nanocrystalline $LiNiVO_4$ was synthesized via hydrothermal reaction followed by calcination. The phase purity, surface morphology and microstructure of the $LiNiVO_4$ synthesized were analysed by XRD, FT-IR, SEM (EDS), TEM and XPS analysis. The lithium ion intercalation-extraction behaviour of the $LiNiVO_4$ electrode material was investigated in aqueous (1M LiOH) and non-aqueous (1M LiTFSI in 1:1 v/v DOL:DME) electrolyte systems. The electrochemical evaluation of $LiNiVO_4$ electrode in aqueous electrolyte demonstrated good capacitive performance with a specific capacitance of 406 F g^{-1} at a current density of 1 A g^{-1}. The cycle stability test reveals exceptional capacitance retention of ~99% even after 1000 cycles owing to the unique structural feature which permit intercalation mechanism. The lithium storage through intercalation pseudocapacitance was confirmed by CV kinetics studies. Further, asymmetric supercapacitor cell has been assembled with $LiNiVO_4$ as negative electrode and MWCNT as positive electrode in non-aqueous (1M LiTFSI in 1:1 v/v DOL:DME) electrolyte. The assembled hybrid cells exhibited a high energy density of 255 Wh kg^{-1} with maximum power density of 22325 W kg^{-1} and excellent capacitance retention of ~92% after 10000 cycles. These findings demonstrate the significance of lithium transition metal vanadate based electrode material in the development of lithium ion intercalation pseudocapacitors.

6.1. Introduction

Lithium-ion capacitors (LICs), combination of a Faradaic LIB anode and a capacitive EC cathode, are emerging as a highly promising energy storage technology (Cabán-Huertas et al., 2017; Li et al., 2019f). These two electrodes with different storage mechanisms can operate reversibly in different potential ranges in LIC device, thus providing an opportunity to effectively improve the energy and power densities as well as cycle life (Yoo et al., 2014; Dubal et al., 2018). However, the full energy utilization of the Faradaic LIB anode is hindered due to the kinetic imbalance between the Faradaic anode and capacitive cathode (Shen et al., 2017). According to their reaction mechanisms, the proposed LIB anode materials can be divided into three main categories. Materials relying on alloying/dealloying and conversion reactions have a large volume variation and poor kinetics, causing large electrode polarization and capacity loss during prolonged cycling. These two types of materials are not suitable as Faradaic anode for LICs (Wang et al., 2016a; Shao et al., 2018b). Therefore, high performance lithium intercalation type anodes are desired that deliver high energy densities without sacrificing the cycle life. Several different types of lithium insertion anode materials, including $Li_4Ti_5O_{12}$ (Dsoke et al., 2015; Zhang et al., 2017a), TiO_2 (Han et al., 2018b), TiO_2-B (Zukalová et al., 2005), $H_2Ti_6O_{13}$ (Wang et al., 2012a), $TiNb_2O_7$ (Aravindan et al., 2014b), Nb_2O_5 (Wang et al., 2015c; Deng et al., 2018), etc., have been explored as insertion anode materials for LIC applications.

Between a variety of insertion-type host materials for LIB, spinel and inverse spinel-type structures gained a special interest as lithium hosts, owing to the availability of 3D pathways for rapid lithium-ion diffusion accompanying a low energy barrier (Xiao et al., 2018). Nanoscale structure contributes increased number of lattice sites for accommodation of lithium-ions with expanded solid-solution limits (Han et al., 2018a). The combination of ion-selective diffusion channels and nanoscale structure exhibited a possible way for high rate lithium storage (Xu et al., 2017; Panda et al., 2020). The search of new lithium-ion intercalation pseudocapacitive electrode materials capable of delivering high energy density and long cycle life found great interest in the research of ECs. Lithium nickel vanadate ($LiNiVO_4$) has been recognized as a promising cathode material for LIBs (Lu et al., 1999). $LiNiVO_4$ possess an AB_2O_4 inverse spinel structure in which Li^+ ions and Ni^{2+} ions equally reside in octahedral sites, and V^{5+} ions occupy the tetrahedrally coordinated sites. Lithium ion present in the octahedral site exhibits a reversible electrochemical intercalation-extraction process (Prakash et al., 2013b; Kazakopoulos et al., 2008). However, the exploitation of $LiNiVO_4$ as electrode material for lithium-ion intercalation pseudocapacitors has not yet been investigated.

In this chapter, the lithium ion intercalation pseudocapacitive behaviour of nanocrystalline inverse spinel $LiNiVO_4$ electrode has been investigated in aqueous electrolyte. Here, we prepared $LiNiVO_4$ particles of nanoscale range by hydrothermal synthesis followed by calcination. The electrochemical studies reveal that nanocrystalline inverse spinel $LiNiVO_4$ exhibits a high specific capacitance of 406.2 F g^{-1} at a current density of 1 A g^{-1} with excellent cycling stability in 1 M LiOH aqueous electrolyte. We demonstrated that the pseudocapacitance dominates the charge storage process in the $LiNiVO_4$ electrode material by kinetic analysis. Furthermore, the as-assembled asymmetric hybrid LIC comprised of $LiNiVO_4$ as negative electrode and MWCNT as positive electrode in non-aqueous electrolyte demonstrated excellent capacitive performances in non-aqueous electrolyte. The LIC cells exhibited a superior energy density 255.2 Wh kg^{-1} and excellent capacitance retention of 92% after 10000 cycles.

6.2. Materials and Methods

6.2.1. Materials

Nickel nitrate ($Ni(NO_3)_2.6H_2O$, 99.999% purity, Sigma Aldrich), all other chemicals are as mentioned in section 5.2.1.

6.2.2. Synthesis of Nanocrystalline $LiNiVO_4$

The nanocrystalline $LiNiVO_4$ was synthesized via hydrothermal reaction. The stoichiometric amounts of $LiNO_3$, $Ni(NO_3)_2$, and NH_4VO_3 in a molar ratio of 1:1:1 were dissolved in distilled water to form a homogeneous solution. This precursor solution was then transferred into a 100 mL Teflon-lined stainless steel autoclave and maintained at 200 °C for 12 h. The light brown precipitate obtained was thoroughly washed with de-ionized water and ethanol to remove ions possibly remaining in the final hydrothermal products, dried at 80 °C in the air. The obtained powder was further calcined at 400 °C for 6 h to increase the crystallinity.

6.2.3. Electrode Preparation and Fabrication of Coin Cells

The slurry of pseudocapacitive $LiNiVO_4$ electrodes were prepared by mixing $LiNiVO_4$, Super P, and PVDF binder in a weight ratio of 8:1:1 in NMP solvent.

Then the slurry was cast onto nickel foam current collector and dried at 80 °C in a vacuum oven. A 1 cm × 1 cm square electrodes were used for three-electrode system.

The negative electrode for LIC cell was prepared by coating $LiNiVO_4$ slurry onto nickel foam and dried. The positive electrode was prepared comprising MWCNT, super P and PVDF binder in a weight ratio of 8:1:1. The materials were grinded in NMP to form slurry, which was then coated on the nickel foam and dried for 12 h at 120 °C. Then, both the electrodes were roll-pressed and punched into circular disks with a diameter of 15 mm. A standard 2032 type coin cell was assembled with non-aqueous electrolyte (1M LiTFSI in the mixture solvent of DOL and DME in a volume ratio of 1:1). The coin cell using non-aqueous electrolyte was assembled in an Ar-filled glove box (M Braun, Germany).

6.2.4. Material and Electrochemical Characterization

All characterizations were done by the techniques described in section 5.2.3 and 5.2.5.

6.3. Results and Discussion

6.3.1. Material Characterization

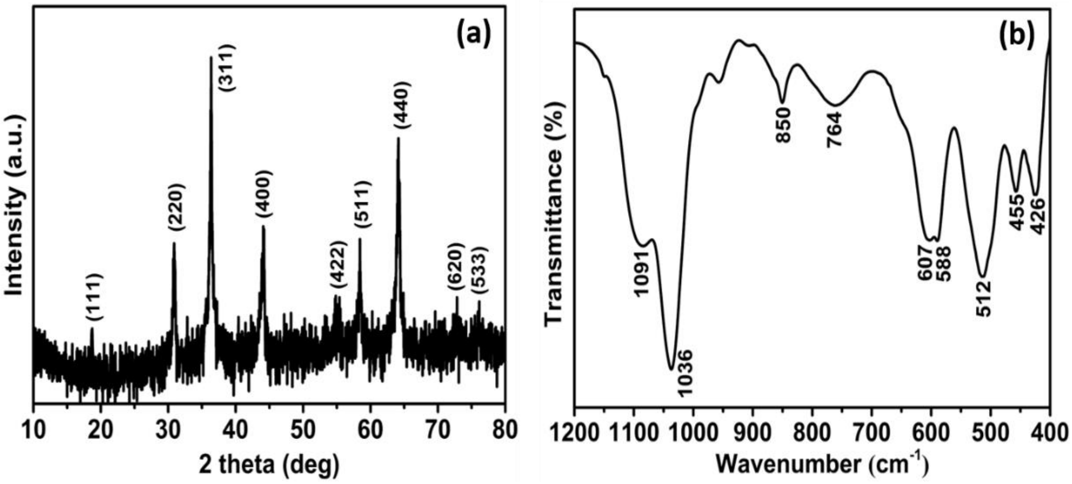

Figure 6.1. (a) XRD patterns and (b) FT-IR spectrum of $LiNiVO_4$

The crystal structure and phase purity of $LiNiVO_4$ were characterized by powder XRD, as shown in Figure 6.1a. $LiNiVO_4$ exhibited characteristic diffraction peaks at 2θ = 18.60º, 30.90º, 36.44º, 44.14º, 54.84º, 58.42º, 64.09º, 73.04º and 76.80º, corresponding to the crystal planes of (111), (220), (311), (400), (422), (511), (440), (620) and (533), respectively. It is clear that all intense diffraction peaks corresponds to cubic phase of $LiNiVO_4$ and $Fd\overline{3}m$ (227) space group (JCPDS No. 38-1395), without any collateral peaks. The diffraction peaks indexed as (311) and (111) planes are characteristics of an inverse spinel structure (Lu et al., 1999; Li et al., 2009). The presence of sharp diffraction peaks indicates high degree of crystallinity of the prepared sample (Holder and Schaak, 2019).

FT-IR spectrum of $LiNiVO_4$ in the wave number range of 400 to 1200 cm^{-1} is presented in Figure 6.1b. The absorption band observed at 850, 764, and 607 cm^{-1} are assigned to stretching vibrations of VO_4 tetrahedrons. The bands at 750 to 400 cm^{-1} region are largely associated with the vibrations of NiO_6 and LiO_6 octahedral units or the bending vibrations of VO_4 tetrahedron. The two absorption band sited around 1091 and 1036 cm^{-1} belongs to an asymmetric stretching vibrational mode of Ni-O bonds in NiO_6 octahedron. The two weak bands around 455 and 426 cm^{-1} are assigned to asymmetric stretching vibrations caused by Li-O bond of LiO_6 octahedron (Lu et al., 1999; Bhuvaneswari et al., 2005).

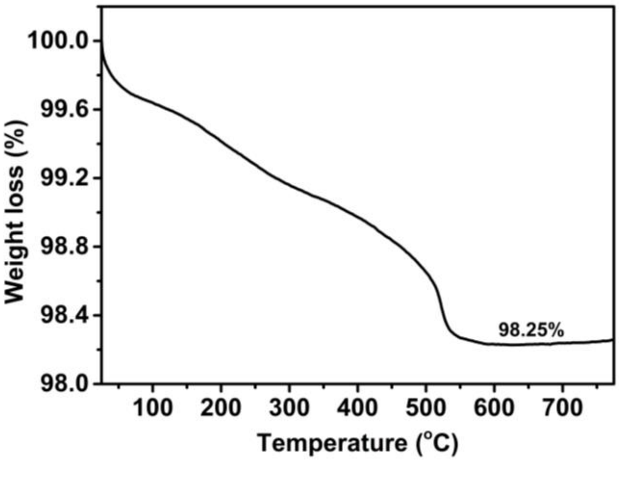

Figure 6.2. TGA curve of $LiNiVO_4$

Thermal studies were carried out in order to determine the thermal stability and decomposition profile of the sample. We examined TGA under argon atmosphere in a temperature range from 25 to 750 °C with a heating rate of 10 °C min^{-1} (Figure 6.2). The observed initial weight loss below 100 ºC is attributed to the evaporation of residual water. The next weight loss noticed in the wide temperature range is due to the decomposition of lithium nitrate and ammonium metavanadate, which takes place at the melting point of both raw materials (Fey and Chen, 1999). The decomposition process stops at 500 ºC. The percentage of weight loss until the weight stabilizes in nanosized $LiNiVO_4$ is 1.75%.

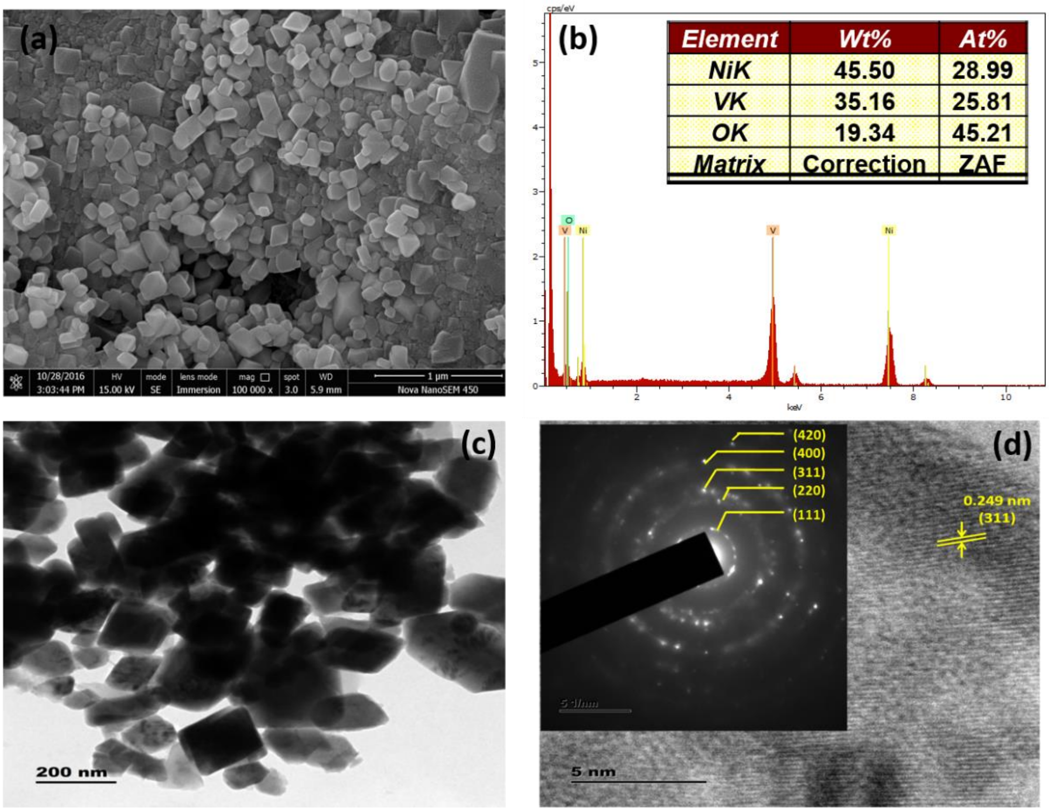

Element	Wt%	At%
NiK	45.50	28.99
VK	35.16	25.81
OK	19.34	45.21
Matrix	Correction	ZAF

Figure 6.3. (a) FESEM image and (b) EDS spectrum of $LiNiVO_4$. (c) TEM images of $LiNiVO_4$, (d) high-resolution TEM and indexed SAED patterns of $LiNiVO_4$

The surface morphology of $LiNiVO_4$ was observed by SEM analysis, as shown in Figure 6.3. The SEM micrograph of $LiNiVO_4$ (Figure 6.3a) reveals the formation of an irregular cube-like structure with a size ranging from 90 to 120 nm. Elemental composition of $LiNiVO_4$ is confirmed by EDS analysis, which is shown in Figure 6.3b. EDS analysis demonstrated the presence of Ni, V, and O with an average ratio of 1:1 for Ni:V. Further, the TEM imaging was carried out to gather insight on $LiNiVO_4$ crystal structure. TEM images of $LiNiVO_4$ (Figure 6.3c) expose well defined crystal faces. High resolution TEM images shown in Figure 6.3d shows lattice fringes from the crystallites. The lattice spacing of 0.249 nm corresponds to the (311) plane of $LiNiVO_4$. The SAED pattern shown in the inset of Figure 6.3d demonstrates crystalline nature of the sample and the diffraction spots can be clearly indexed to the inverse spinel $LiNiVO_4$ phase (Zhou and Greer, 2016).

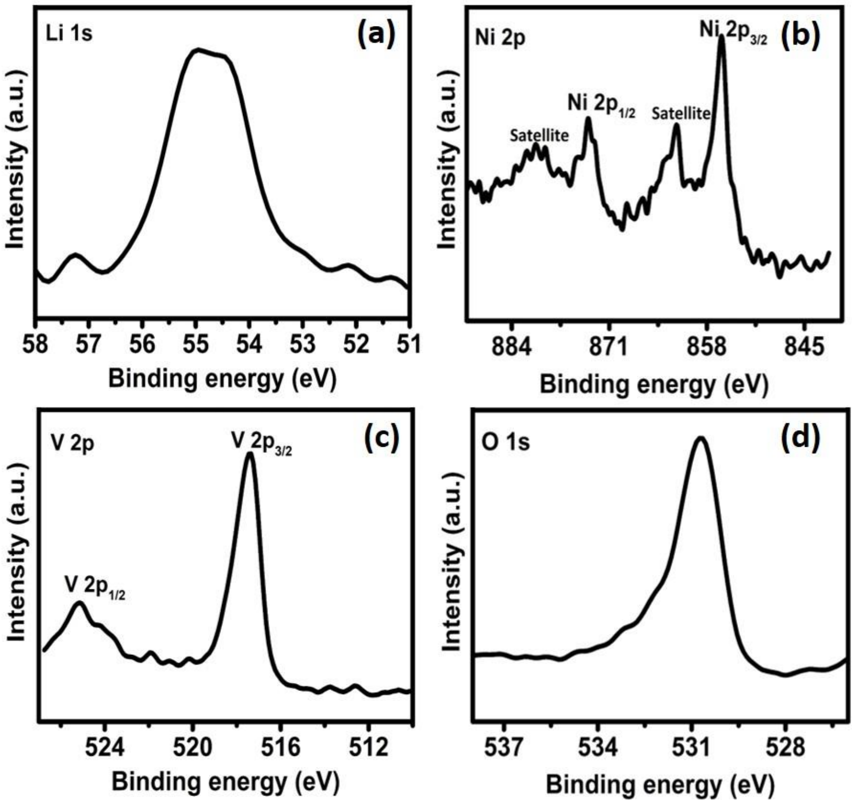

Figure 6.4. XPS core level spectra of $LiNiVO_4$ (a) Li 1s (b) Ni 2p (c) V 2p (d) O 1s

XPS analysis have been extensively used to study the electronic structure of materials. The XPS binding energy provides useful information on the surface electronic sates of each elements present in $LiNiVO_4$ (Shard, 2020). Figure 6.4 shows the Li, Ni, V and O XPS core level spectra for $LiNiVO_4$. The binding energy of the Li1s core level emission peak (Figure 6.4a) was located at 54.6 eV and appeared as a broadened signal. The Ni2p core spectrum (Figure 6.4b) consists of $Ni2p_{3/2}$ and $Ni2p_{1/2}$ peaks at 855.3 and 872.9 eV, respectively and corresponding weak shake up satellite peaks of Co^{2+}. The V2p core spectrum (Figure 6.4c) splits to $V2p_{3/2}$ and $V2p_{1/2}$ peaks located at 516.7 and 524.2 eV, characteristics of V^{5+}.

The XPS O1s peak (Figure 6.4d) shows a peak around 529.6 eV assigned to Ni-O bonds, and a shoulder peak at 530 eV associated with oxygen in low coordination sites at the surface (Fey and Chen, 1999; Lu et al., 1999).

6.3.2. Electrochemical Lithium Storage Performance of Nanocrystalline $LiNiVO_4$

Figure. 6.5 shows the current-voltage (CV) curves of nanocrystalline $LiNiVO_4$ electrode material in 1M LiOH electrolyte at various potential sweep rate. Two strong redox peaks suggest the reversible electrochemical oxidation (lithium extraction) and reduction (lithium insertion) of $LiNiVO_4$ electrode material. The large redox peaks arising due to Faradaic redox reactions indicate that the capacitance characteristic of $LiNiVO_4$ electrode is of typical pseudocapacitance (Wang et al., 2016a). The peak current rises with increase in the potential sweep rate, indicating rapid Faradaic redox reactions and increased rates of electronic and ionic transport (Augustyn et al., 2014; Elgrishi et al., 2018).

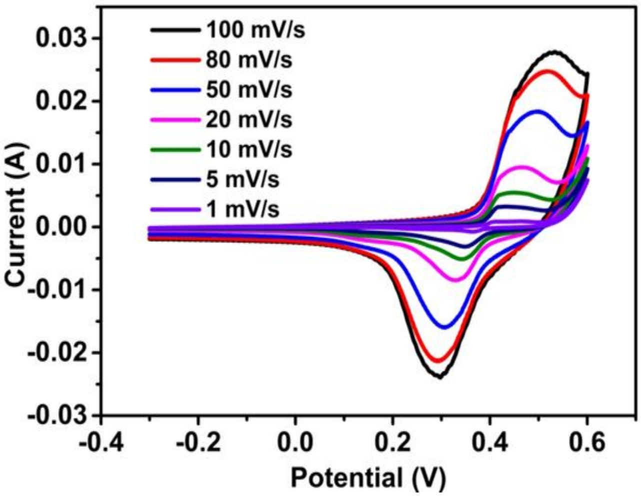

Figure 6.5. CV curves of $LiNiVO_4$ at different scan rates

Investigation of CV can be further considered as an efficient tool to explain electrode kinetics in nano-structured $LiNiVO_4$ (Sandford et al., 2019). A slight shift in the redox peak position is observed with increased potential sweep rate. This can be described by the existence of two capacitive processes, namely interface-related pseudocapacitive contribution arising from the large active surface area of nanocrystalline structure and diffusion-controlled lithium-ion intercalation reaction (Wang et al., 2007; Shao et al., 2018b).

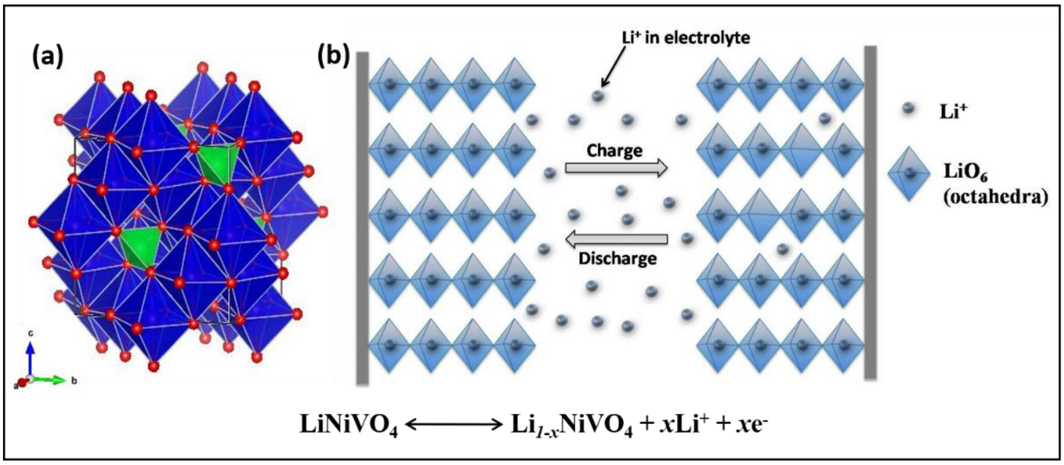

Figure 6.6. (a) The 3D visualization of $LiNiVO_4$ crystal using VESTA 3, where Li and Ni equally occupies MO_6 (M = Li, Ni) octahedra indicated in blue colour and VO_4 tetrahedra in green colour (b) schematic illustration of the lithium-ion intercalation and de-intercalation process in $LiNiVO_4$ electrode during charge-discharge process. NiO_6 octahedra and VO_4 tetrahedra in the $LiNiVO_4$ crystal structure are not represented

The pseudocapacitive charge storage mechanism of $LiNiVO_4$ via the intercalation of lithium ions in an aqueous electrolyte is proposed as follows:

$$LiNiVO_4 \quad \leftrightarrow \quad Li_{1-x}NiVO_4 + xLi^+ + xe^- \qquad (6.1)$$

where x is the mole fraction of inserted lithium given by x = QM/mF, where Q is the stored charge, M is the molecular weight, m is the mass and F is the Faraday constant (Brezesinski et al., 2010). In this reaction, lithium ions can intercalate and de-intercalate during the charge-discharge process (as shown in Figure 6.6), which is similar to that of the LIB. The electrochemical insertion of lithium ions into $LiNiVO_4$ was expected to occur with simultaneous oxidation of Ni^{2+} to Ni^{3+}.

In order to substantiate the CV results, the EIS analysis was carried out for $LiNiVO_4$ electrode. Nyquist plot of nanosized $LiNiVO_4$ electrode is shown in Figure 6.7. The straight line at low-frequency region represents Warburg impedance, which results from the ion diffusion at the electrode-electrolyte interface. The line at lower frequencies which is parallel to imaginary axis, indicate the desired pseudocapacitive behaviour Inset of Figure 6.7 shows the equivalent circuit of the impedance curve obtained using the ZSimpWin software. The fitted

EIS data contains elements of bulk solution resistance (R_s), charge-transfer resistance (R_{ct}), constant phase element (CPE) to account for double layer capacitance, Warburg diffusion element (W_o) and a pseudocapacitive element (C_p) from the redox processes at the electrode. The equivalent series resistance (R_s) of the electrode can be obtained from the high frequency intersection of EIS Nyquist plot in the real axis (Li et al., 2014c; Eskandari et al., 2020).

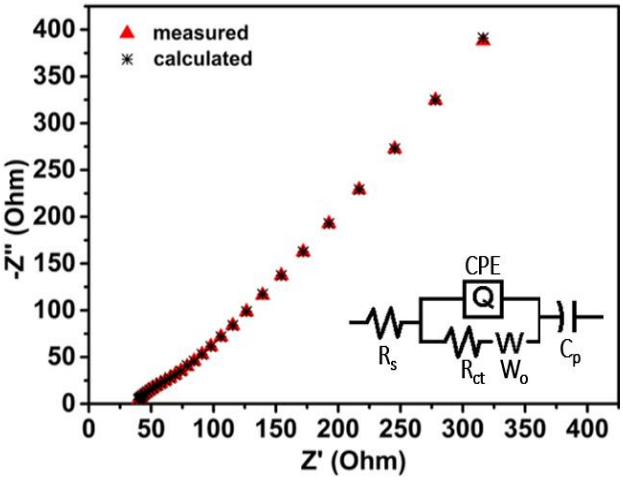

Figure 6.7. EIS Nyquist plot of $LiNiVO_4$ electrode. Inset: corresponding equivalent circuit

The charge storage capacity of $LiNiVO_4$ electrode was further investigated using galvanostatic charge-discharge measurements in the potential range of -0.2 to 0.52 V. Figure 6.8a displays the discharge behaviour of nanosized $LiNiVO_4$ electrode at different current densities. The maximum specific capacitance reaches 456 F g^{-1} at a current density of 0.5 A g^{-1}. The high capacitance of $LiNiVO_4$ can be mainly ascribed to the nano size of $LiNiVO_4$. The nanocrystalline structure of $LiNiVO_4$ not only provide a fast ion transport path and a large active surface area, but also enhances the accessibility of LiOH electrolyte and therefore, promotes the ion transport within the electrode (Lukatskaya et al., 2016). Figure 6.8b shows the variation of specific capacitance with applied current. At different current densities of 0.5, 1, 2, 5, and 10 A g^{-1}, the specific capacitance was estimated to be 456.5, 406.2, 312.7, 203.5, and 124.6 F g^{-1} for nanocrystalline $LiNiVO_4$ electrode. The decrease in the specific capacitance with increasing discharge current could be attributed to the increase in potential drop as well as insufficient Faradaic redox reactions at higher currents (Shao et al., 2018b).

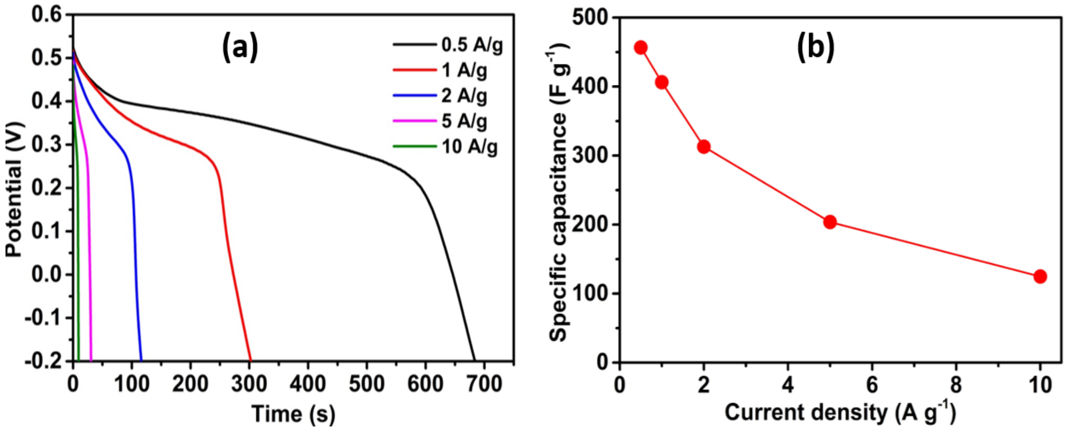

Figure 6.8. (a) Galvanostatic discharge curves of $LiNiVO_4$ at various current densities (b) specific capacitance of $LiNiVO_4$ at different current densities

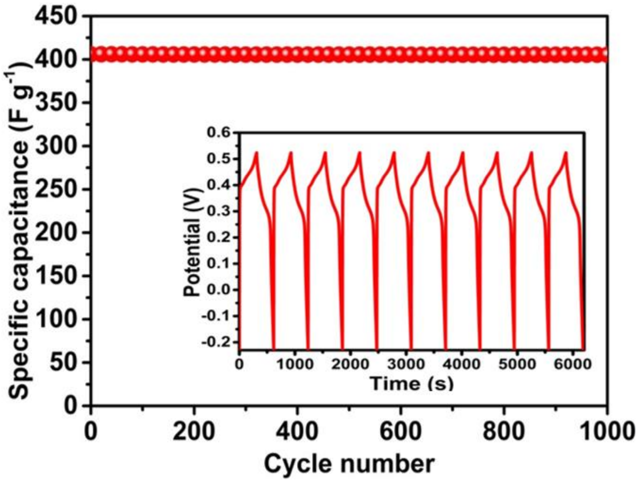

Figure 6.9. Long-term cycling stability of $LiNiVO_4$ at a current density of 1 A g^{-1} (Inset: charge-discharge curves for first 10 cycles).

Further, the long-term cycling stability of the electrode material were investigated at the current density of 1 A g^{-1} (Figure 6.9). After 1000 continuous charge-discharge cycles, $LiNiVO_4$ electrodes exhibited excellent cycling stability with no sign of capacitance degradation. Capacitance retention of ~99% was obtained for $LiNiVO_4$ electrode, which is better than those of other lithium-based and nickel-based vanadates, such as LiV_3O_8 nanosheet (34.12% retention after 100 cycles) (Zheng et al., 2016), $Ni_3V_2O_8$ nanoflakes (73.0 % after 1000 cycles) (Liu et al., 2014). The excellent cycle stability of the electrodes may be attributed to the morphological and structural stability of $LiNiVO_4$. The inverse spinel structure of $LiNiVO_4$ electrode, which enables ion intercalation/extraction between electrode and electrolyte leads to Faradic reaction, resulting in better electrochemical performance (Lubimtsev et al., 2013; Mohd Abdah et al., 2020).

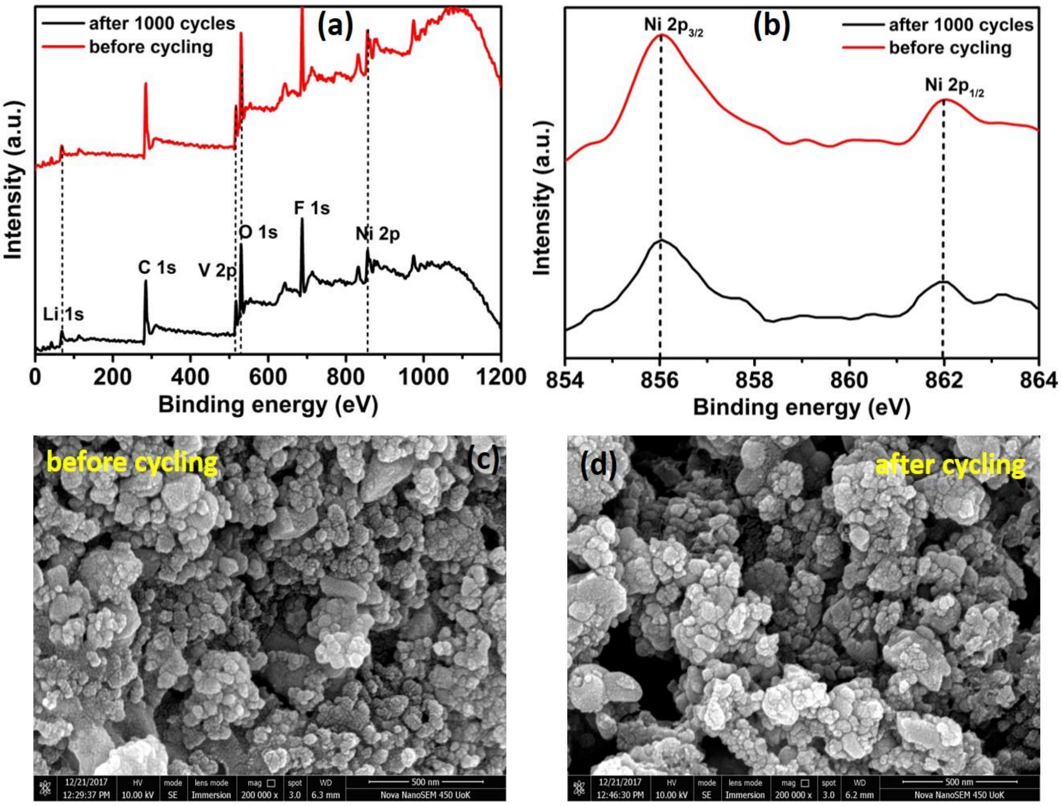

Figure 6.10. (a) XPS survey spectrum of $LiNiVO_4$ electrode before and after cycling (b) comparative XPS core level spectrum of Ni 2p of $LiNiVO_4$ electrode before and after cycling. FESEM images of $LiNiVO_4$ electrodes (a) before cycling (b) after cycling

XPS measurements of $LiNiVO_4$ electrode material were carried out before and after cycling, which provide critical evidence about the excellent electrochemical performance. The XPS survey spectra of $LiNiVO_4$ before and after cycling (Figure 6.10a) confirm the distinct peaks of Li1s, Ni2p, V2p, O1s. The XPS peaks C1s and F1s originated from Super P and PVDF employed during electrode coating process. The XPS peaks in survey spectra of nano-structured $LiNiVO_4$ electrode before cycling is in good agreement with the electrode after 1000 cycles, which leads to the conclusion that there is no change in the oxidation states of $LiNiVO_4$ constituents after cycling. Figure 6.10b shows the comparative XPS core level spectrum of Ni 2p, which contain two major peaks with binding energies at 856.9 and 863.1 eV correspond to Ni $2p_{3/2}$ and Ni $2p_{1/2}$, respectively (Fey and Chen, 1999; Lu et al., 1999). It is obvious that the Ni 2p peaks hardly change even after cycling. This realization verifies that pseudocapacitance behaviour in $LiNiVO_4$ electrode is purely lithium-ion intercalation/de-intercalation, which further confirms the proposed intercalation mechanism. SEM micrographs of $LiNiVO_4$ electrode before and after cycling further provide evidence for the lithium-ion intercalation mechanism with negligible structural changes (Figure 6.10c-d), confirming the XPS results.

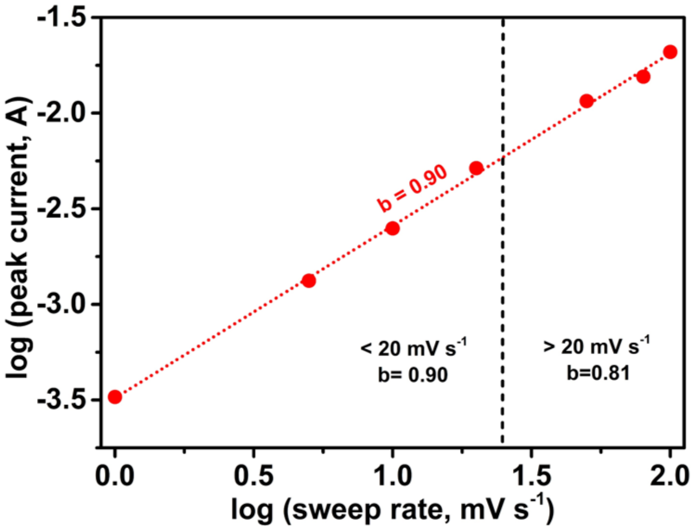

Figure 6.11. *b*-value determination of cathodic peak currents

The kinetic characterization is studied by plotting log(i) versus log(v) for cathodic current peak with varied sweep rates, which can be used to distinguish the charge storage whether arises diffusion-controlled or capacitive processes. This relation is expressed as $i = av^b$ with the value of b providing insights regarding the charge storage mechanism. Whereas a *b*-value of 0.5 indicates that the current is controlled by semi-infinite linear diffusion, and a value of 1 indicates that the current is capacitive process (Augustyn et al., 2014; Wang et al., 2016a). In sweep rate range of 1-20 mV s^{-1}, the *b*-value of nanocrystalline $LiNiVO_4$ is very close to 1 but deviates slightly at high rates (20-100 mV s^{-1}), as shown in Figure 6.11. The deviation observed in the faster sweep rates can be ascribed to poor electronic conductivity of the active electrode materials resulting in the sluggish electron transportation (Augustyn et al., 2013; Elgrishi et al., 2018). Thus, it can be concluded that total stored energy in the $LiNiVO_4$ electrode arises from the intercalation/de-intercalation of lithium-ion that is not limited by solid-state diffusion.

6.3.3. Electrochemical Lithium Storage Performance of Nanocrystalline $LiNiVO_4$ hybrid LIC in Non-Aqueous Electrolyte

A hybrid LIC was fabricated with nanocrystalline $LiNiVO_4$ as the anode and MWCNT as the cathode in an organic electrolyte containing lithium-ions. In the electrode materials involving a different reaction mechanism, the applied current will split into the capacity of the individual electrodes. Therefore, the charge balance ($q^+ = q^-$) between the two electrodes is necessary to achieve higher energy density in LIC configuration. The stored charge is related to the specific capacity (C) and the mass of the electrode (m), which follows the equation: $q = C \text{ x } m$ (Tang et al., 2013; Dsoke et al., 2015; Madabattula et al., 2020). On the basis of the individual specific capacitance value for the $LiNiVO_4$ (Figure 6.8a) and MWCNT (Figure 5.11b), the optimal mass ratio between the two electrodes is fixed to be anode/cathode = 0.482 (calculated from equation 5.1) in the LIC. During the discharge process, lithium-ions are deintercalated from $LiNiVO_4$ electrode, while $TFSI^-$ is desorbed from the accessible mesopores originate from the central canal and entangled structure of MWCNT.

Figure 6.12a shows the CV studies of LIC recorded at different scan rates between -1.0 and 2.0 V. The CV curves of LIC clearly depicts the combined charge storage mechanism i.e. both (de-)intercalation and EDLC behaviour. Appearance of distorted CV profiles signifies the involvement of two different charge storage mechanism in LIC (Byeon et al., 2016; Sun et al., 2017a), for example, adsorption of $TFSI^-$ in cathode and de-intercalation reaction on counter electrode. Intercalation and $TFSI^-$ desorption are noted during discharge process. Galvanostatic charge-discharge studies for $LiNiVO_4$//MWCNT LIC is performed at different current rates between -1.0 and 2.0 V and illustrated in Figure 6.12b. The applied current densities are based on the total mass loading of both electrodes. Irrespective of current rates, charge/discharge curves showed two voltage stages in the range of 1.4 to 0.9 and 0.4 to -0.15 V, which is consistent with CV profiles. The relationship between specific capacitance and current density is displayed in Figure 6.12c. As expected, the decrease in specific capacitance is noted while increasing the current rate, because at higher current rates only the surface of the active material is involved in the electrochemical reaction (Aljaafari et al., 2019). The specific capacitance values of $LiNiVO_4$//MWCNT hybrid LIC were 56.7, 53.2, 52.2, 49.1, 46.3, 38.5, 34.7 F g^{-1} at the current densities of 0.5, 1, 2, 5, 10, 20, 30 A g^{-1}, respectively. Besides, the hybrid LIC exhibits passable cycle stability (Figure 6.12d) with the capacitance retention of ~92% after 10000 cycling numbers at a high current density of 5 A g^{-1}.

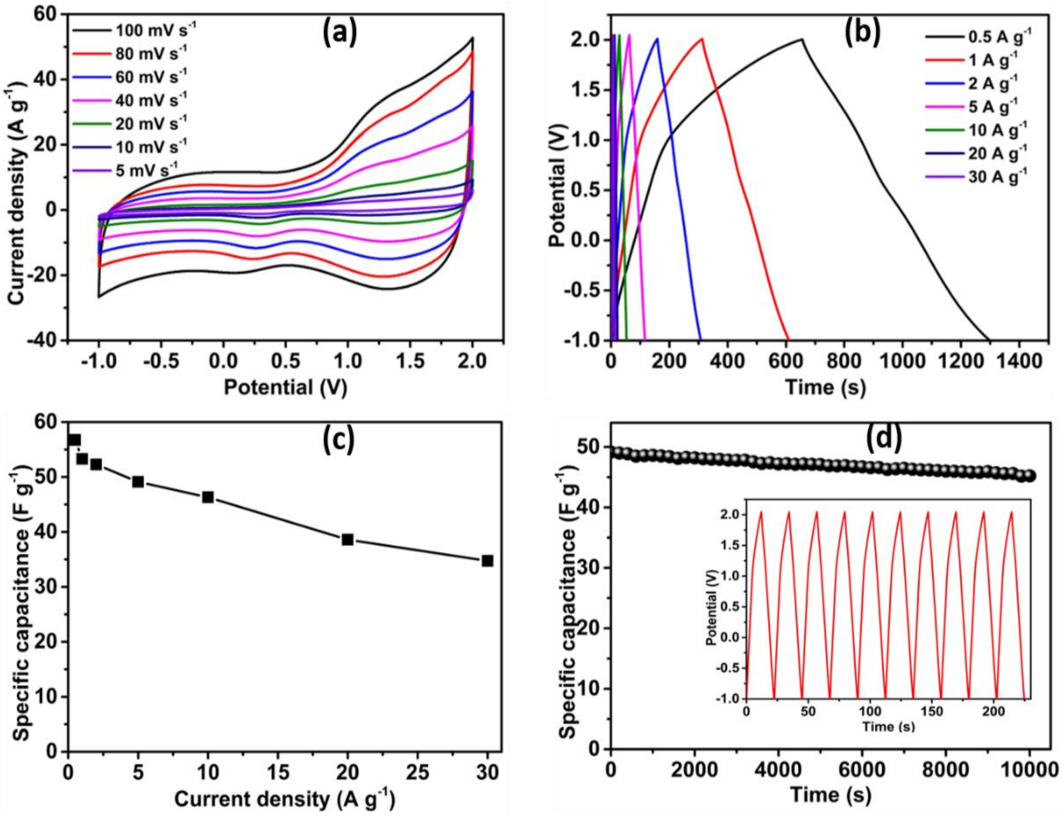

Figure 6.12. Electrochemical performance of $LiNiVO_4$//MWCNT LIC: (a) CV curves at various scan rates, (b) galvanostatic charge-discharge curves at different current densities, (c) specific capacitance values calculated from galvanostatic charge/discharge curves under different current densities, (d) cycle stability for 10000 cycles at a current density of 5 A g^{-1}, Inset: charge-discharge profiles for 10 continuous charge-discharge cycles

Figure 6.13 represents the Ragone plot of the $LiNiVO_4$//MWCNT LIC. The energy density and power density are calculated by using equations (1.10) and (1.11), respectively. As shown in Figure 6.13, the energy density of the LIC decreases from 255.2 to 156.2 Wh kg^{-1} as the power density increases from 0.39 to 22.3 kW kg^{-1}. This energy and power density are much higher than that of other LICs based on $LiTi_2(PO_4)_3$//AC (14 Wh kg^{-1} at 0.18 kW kg^{-1}) (Aravindan et al., 2012), TiO_2-B Nanowire//CNT (12.5 Wh kg^{-1} at a current rate of 10 C) (Wang et al., 2006), V_2O_5 fibers//Bucky paper (18 Wh kg^{-1} and 315 kW kg^{-1}) (Aravindan et al., 2012), TiO_2-B nanotubes//MWCNTs (19.3 Wh kg^{-1} at a rate of 10 C) (Wang et al., 2012b), $Li_4Ti_5O_{12}$//AC system (1000-2000 W kg^{-1} at 10-15 Wh kg^{-1}) (Dsoke et al., 2015), CNT/V_2O_5//AC (6.9 Wh kg^{-1} at 6.3 kW kg^{-1}) (Chen et al., 2011), TiO2 NBA//graphene hydrogel (82 Wh kg^{-1} at 570 W kg^{-1}) (Wang et al., 2015a), etc. Further, the two fabricated LIC devices are serially connected, illuminating the white LED for a duration of 1.5 minutes when fully charged (inset of Figure 6.13). This physical demonstration further validates the great potential of the $LiNiVO_4$//MWCNT LIC for electrochemical energy storage with high energy and power densities.

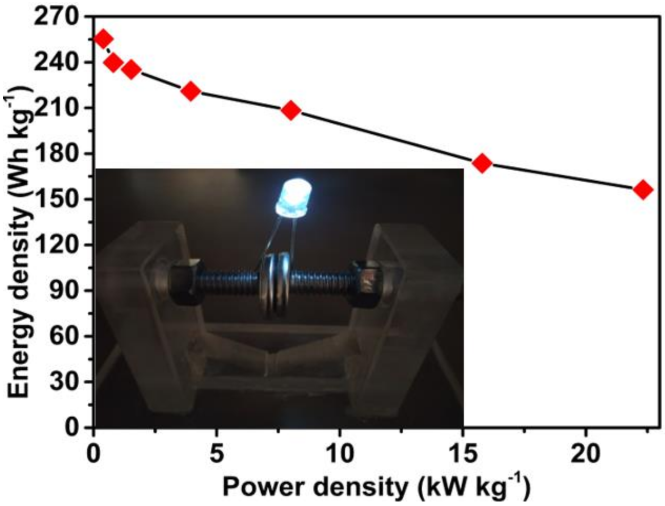

Figure 6.13. Ragone plot of LIC cell (inset shows a white LED powered by two LIC devices in series)

6.4. Conclusion

In summary, we have prepared a nanocrystalline $LiNiVO_4$ through a hydrothermal route followed by calcination and used as a high-performance pseudocapacitive material for lithium storage in aqueous electrolyte. The $LiNiVO_4$ nanocrystals demonstrated better lithium-ion intercalation/de-intercalation properties benefited from its small crystallite size with highly exposed crystallographic framework towards electrolyte. A hybrid LIC based on $LiNiVO_4$ anode and MWCNT cathode has been developed in non-aqueous medium to achieve high energy and power densities. An energy density of 156.2 Wh kg^{-1} has been achieved at a high power density of 22.3 kW kg^{-1}, and the maximum energy density is 255.2 Wh kg^{-1}. The energy and power densities could potentially bridge the gap between conventional LIBs and supercapacitors, and meet the present power demands. Therefore, the $LiNiVO_4$//MWCNT is a good material combination for LIC towards application in hybrid vehicle systems.

CHAPTER 7

NANOSCALE $LiMnVO_4$ AS AN INTERCALATION-TYPE ANODE FOR HIGH-ENERGY LITHIUM-ION CAPACITORS

Capacitive energy storage offers numerous attractive properties in contrary to batteries, including faster charging, higher power, and longer cycle life. A key constraint to this electrochemical energy-storage technique is its low energy density and, for this reason, there is substantial interest in search for new pseudocapacitor materials where faradaic reactions are utilized to attain greater charge storage. Herein, nanoscale $LiMnVO_4$ *was synthesized by a facile hydrothermal approach and subsequent calcination. The intercalation pseudocapacitive lithium storage behaviour of the* $LiMnVO_4$ *electrode material was investigated in aqueous electrolyte, which demonstrated a high specific capacitance of 961 F* g^{-1} *at a current density of 1 A* g^{-1} *with a capacitance retention of ~99% after 1000 cycles. Detailed evaluation of CV data was conducted in order to confirm the proposed lithium-ion intercalation mechanism. Further, an asymmetric LIC device has been fabricated with* $LiMnVO_4$ *as negative electrode and MWCNT as positive electrode in non-aqueous electrolyte. The LIC delivers a specific capacitance of 81 F* g^{-1} *(with a wide voltage window of 3 V), and good rate performance of 47 F* g^{-1} *at 30 A* g^{-1}*. Further, they show an energy density of 368 Wh* kg^{-1} *and a maximum power density of 24781 W* kg^{-1} *in association with superior cycling stability (~97% capacitance retention after 10000 cycles at 5 A* g^{-1}*).*

7.1. Introduction

In the recent past, development of LICs are attractive due to their possible applications to power EVs and HEVs (Khaligh and Li, 2010; Hannan et al., 2017; Li et al., 2019a). LICs exhibit higher energy density than rechargeable battery systems (e.g. LIBs) and higher power density than EDLCs (Cericola and Kötz, 2012). Generally, LICs are constructed with supercapacitor electrodes on one side (cathode) and lithium-ion intercalating type electrodes on the counter side (anode) (Shao et al., 2018b; Madabattula et al., 2020). Supercapacitor electrodes supply necessary power for the system through the reversible non-Faradaic charge storage mechanism, i.e., double layer formation across an electrode-electrolyte interface, whereas the battery-type counter electrode (anode) undergoes a lithium-ion insertion/extraction reaction and obeys a Faradaic reaction in either aqueous or non-aqueous medium (Conway, 1991; Naoi, 2010; Hou et al., 2019). The introduction of battery-type counter electrode not only enhances the theoretical specific capacitance but also augments the operating voltage, thereby offers an energy density 3-4 times higher than conventional symmetric supercapacitors (An et al., 2019; Panda et al., 2020). Despite their potentially high power densities and long term cycleability, aqueous LICs typically deliver much lower energy density (Aravindan et al., 2014a; Li et al., 2018c; Li et al., 2019f). Hence, the research focus is directed towards the development of high energy density non-aqueous LICs.

After the first prototype proposed by Amatucci et al. (Amatucci et al., 2001), various LIC systems using different anodes have been reported with promising performances. Pseudocapacitive materials such as nanostructured Nb_2O_5 (Deng et al., 2018), TiO_2 (Zukalová et al., 2005; Han et al., 2018b), $Li_4Ti_5O_{12}$ (Dsoke et al., 2015; Zhang et al., 2017a), V_2O_5 (Aravindan et al., 2012), Li_3VO_4 (Zheng et al., 2016), and $TiNb_2O_7$ (Aravindan et al., 2014b), etc., have been widely investigated in LICs. They are ideal candidates to bridge the huge gap between the diffusion limited lithium-ion insertion process and the surface-controlled physical adsorption/desorption (Cho et al., 2014; Yang et al., 2015; Han et al., 2018a). The search of new lithium-ion intercalation type anode materials capable of delivering high energy density and long cycle life found great interest in the research of ECs. Lithium manganese vanadate ($LiMnVO_4$) has been explored as a cathode material for LIBs. $LiMnVO_4$ structure contains tetrahedral VO_4 and octahedral LiO_6 and MnO_6 groups. It belongs to the ordered olivine-type structures, since the inversion site is occupied by Li^+ ions and the mirror site is taken by Mn^{2+} ions (Paques-Ledent, 1975; Rui et al., 2013). Lithium ion present in the octahedral site exhibits a reversible electrochemical insertion-extraction process (Liu et al., 2016a). However, the exploitation of $LiMnVO_4$ as electrode material for lithium-ion intercalation pseudocapacitors has not yet been investigated.

This study focuses on exploring the use of $LiMnVO_4$ as a potential battery type anode material for LIC. Here, we prepared $LiMnVO_4$ nanorods by hydrothermal synthesis followed by calcination, and the preliminary electrochemical evaluation of $LiMnVO_4$ electrode material was carried out in aqueous electrolyte. The electrochemical results reveal that the olivine $LiMnVO_4$ nanorod electrode exhibits a high specific capacitance of 961 F g^{-1} at a current density of 1 A g^{-1} with a capacitance retention of ~99% after 1000 cycles. Detailed evaluation of CV data and XPS analysis of cycled electrode materials were carried out to further confirm the lithium-ion intercalation mechanism and excellent cycling stability. Furthermore, an asymmetric hybrid LIC was fabricated by coupling $LiMnVO_4$ as negative electrode and MWCNT as positive electrode under an optimum mass ratio. The assembled hybrid LIC demonstrated an excellent capacitive performance in non-aqueous electrolyte. The LIC cells exhibited a superior energy density of 213 Wh kg^{-1} even at a high power density of 24781 W kg^{-1} and excellent capacitance retention of ~97% after 10000 cycles at a current density of 5 A g^{-1}.

7.2. Materials and Methods

7.2.1. Materials

Lithium acetate ($CH_3COOLi.2H_2O$, 99% purity, Sigma Aldrich), manganese acetate ($(CH_3CO_2)_2Mn$, 98% purity, Sigma Aldrich), vanadyl acetylacetonate ($VO(C_5H_7O_2)_2$, 98% purity, Sigma Aldrich), all other chemicals are as mentioned in section 5.2.1.

7.2.2. Synthesis of $LiMnVO_4$ Nanorods

The $LiMnVO_4$ nanorod was synthesized via hydrothermal reaction. The stoichiometric amounts of $CH_3COOLi.2H_2O$, $(CH_3CO_2)_2Mn$, and $VO (C_5H_7O_2)_2$ in a molar ratio of 1:1:1 were dissolved in distilled water to form a homogeneous solution. This precursor solution was then transferred into a 100 mL Teflon-lined stainless steel autoclave and maintained at 200 °C for 12 h. The light brown precipitate obtained was thoroughly washed with de-ionized water and ethanol to remove ions possibly remaining in the final hydrothermal products, dried at 80 °C in the air. The obtained powder was further calcined at 400 °C for 6 h to increase the crystallinity.

7.2.3. Electrode Preparation and Fabrication of Coin Cells

The fabrication of pseudocapacitive $LiMnVO_4$ electrodes was carried out by a blade-casting method. To prepare electrode slurry, the $LiMnVO_4$ active material was well-mixed with super P and PVDF in weight ratios of 8:1:1 in NMP solvent. The slurry was uniformly coated onto nickel foam current collector and dried in vacuum oven overnight at 120 °C. A 1 cm × 1 cm square electrodes were used for three-electrode system in 1M LiOH aqueous electrolyte.

The nickel foam coated with $LiMnVO_4$ slurry was dried, roll-pressed and punched into circular disks with a diameter of 15 mm (negative electrode). The positive electrode was prepared comprising MWCNT, super P and PVDF binder in a weight ratio of 8:1:1. The materials were grinded in NMP to form slurry, which was then coated on the nickel foam and dried for 12 h at 120 °C. Then roll-pressed and punched into circular disks with a diameter of 15 mm. CR2032-type coin cells were assembled in an argon-filled glove box (MBraun, Germany). Celgard 2400 was used as the separator, 1M LiTFSI in the mixture solvent of DOL and DME (DOL/DME, v/v = 1:1) was used as non-aqueous electrolyte

7.2.4. Material and Electrochemical Characterization

All characterizations were done by the techniques described in section 5.2.3 and 5.2.5.

7.3. Results and Discussion

7.3.1. Material Characterization

Figure 7.1a shows the X-ray pattern of nanocrystalline $LiMnVO_4$, which can be indexed on the basis of the standard data (mp-775199). $LiMnVO_4$ exhibited characteristic diffraction peaks at 2θ = 16.92°, 18.63°, 20.36°, 27.48°, 29.12°, 33.72°, 34.27°, 36.58°, 40.26°, 42.56°, 44.10°, 46.05°, 51.10°, 52.30°, 53.68°, 56.31°, 59.15°, and 64.02°, corresponding to the crystal planes of (200), (101), (210), (020), (301), (311), (121), (410), (112), (321), (302), (022), (412), (610), (331), (430), (620), and (313). It clearly revealed that the $LiMnVO_4$ nanorods were indexed well to a pure orthorhombic system of olivine-type structure with the space group of Pnma (Cabán-Huertas et al., 2017). The obtained $LiMnVO_4$ nanorods was well crystalline, as the diffraction peaks were narrow and sharp (Holder and Schaak, 2019). $LiMnVO_4$ contains pure olivine phase in spite of being synthesized in air.

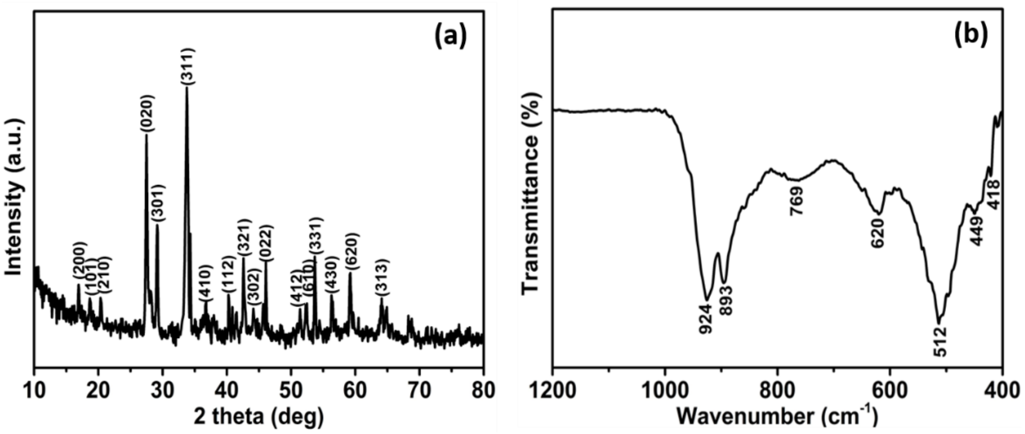

Figure 7.1. (a) XRD patterns and (b) FT-IR spectrum of $LiMnVO_4$

Figure 7.1b shows the FT-IR spectrum of $LiMnVO_4$, which provides further insight into the structural information. The absorption band observed at 924, 893 and 769 cm^{-1} are assigned to the stretching vibrations of VO_4 tetrahedrons. The bands sited around 600 and 500 cm^{-1} range are largely associated with the vibrations of MnO_6 and LiO_6 octahedral units or the bending vibrations of VO_4 tetrahedron. The two weak bands around 449 and 418 cm^{-1} refer to asymmetric stretching vibrations of Li-O bonds in LiO_6 octahedron (Lu et al., 1999; Bhuvaneswari et al., 2005).

TGA analysis is performed from 25 to 700 °C at a ramp rate of 10 °C min^{-1} in air. As shown in Figure 7.2, the TGA curve exhibits two main regions over two temperature ranges, 25-300 °C and 300-620 °C, which involve a total weight loss of 1.74%. The first weight loss at the temperatures below 300 °C may correspond to the evaporation of free water, adsorbed water and coordinated water, while the following weight loss between 300 and 620 °C may be attributed to the decomposition of the Li-Mn-V-based precursor to form the final $LiMnVO_4$ (Manthiram and Kim, 1998; Prakash et al., 2012).

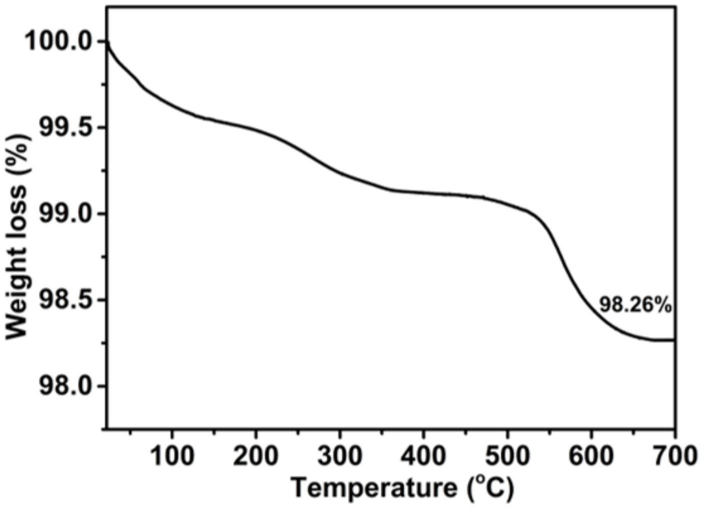

Figure 7.2. TGA curve of $LiMnVO_4$

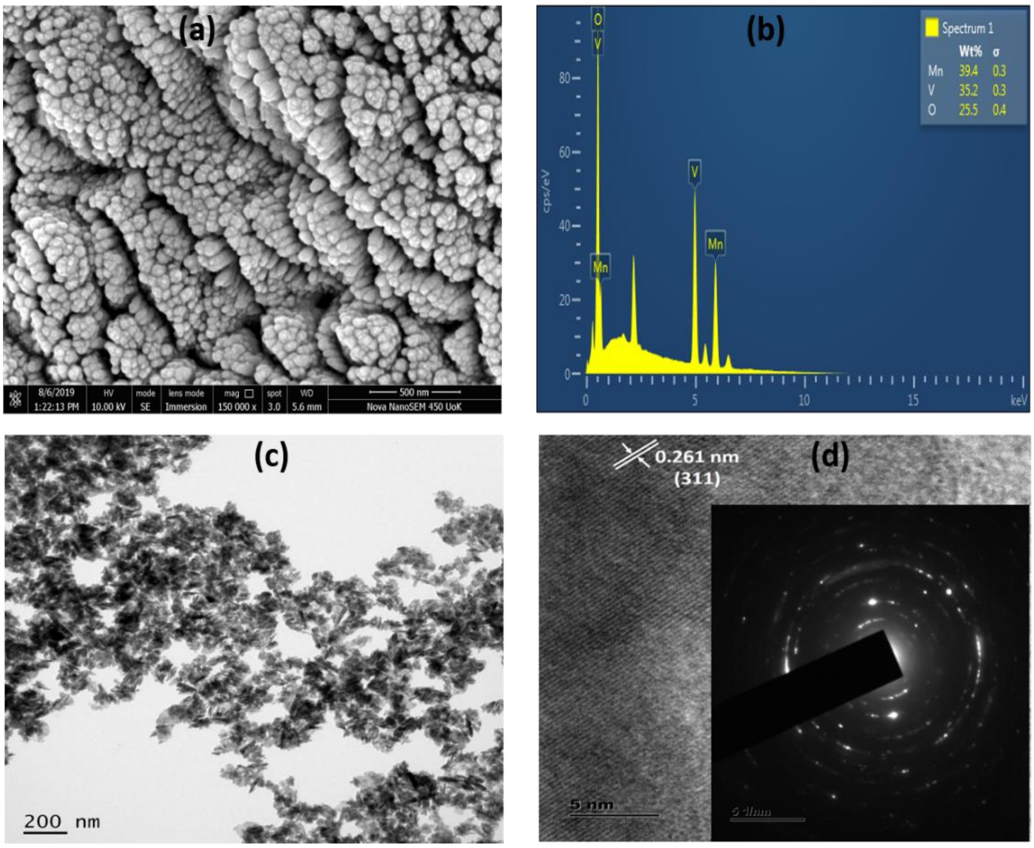

Figure 7.3. (a) FESEM image and (b) EDS spectrum of $LiMnVO_4$. (c) TEM images of $LiMnVO_4$, (d) high-resolution TEM and indexed SAED patterns of $LiMnVO_4$

The surface morphology of $LiMnVO_4$ nanorods were characterized by FESEM analysis, as shown in Figure 7.3a. Figure 7.3a shows that the $LiMnVO_4$ presents nanorod structure with rough surface and diameters around 40-80 nm. Furthermore, the elemental composition of $LiMnVO_4$ is determined by EDS analysis, which is shown in Figure 7.3b. EDS results confirmed the presence of Mn, V and O with average atomic ratio of Mn:V is around 1:1. TEM measurements provide further insight into the morphology and detailed crystal structure of the $LiMnVO_4$ nanorod. As shown in Figure 7.3c, the sample exhibits a nanorod structure, which is consistent with the SEM observation. Figure 7.3d shows the high-resolution TEM image of the sample. The lattice fringes corresponding the interplanar spacing of 0.261 nm can be accurately assigned to the (311) plane of $LiMnVO_4$. The SAED pattern shown in the inset of Figure 7.3d demonstrates crystalline nature of the sample and the diffraction spots corresponds to the orthorhombic olivine phase of $LiMnVO_4$ (Zhou and Greer, 2016).

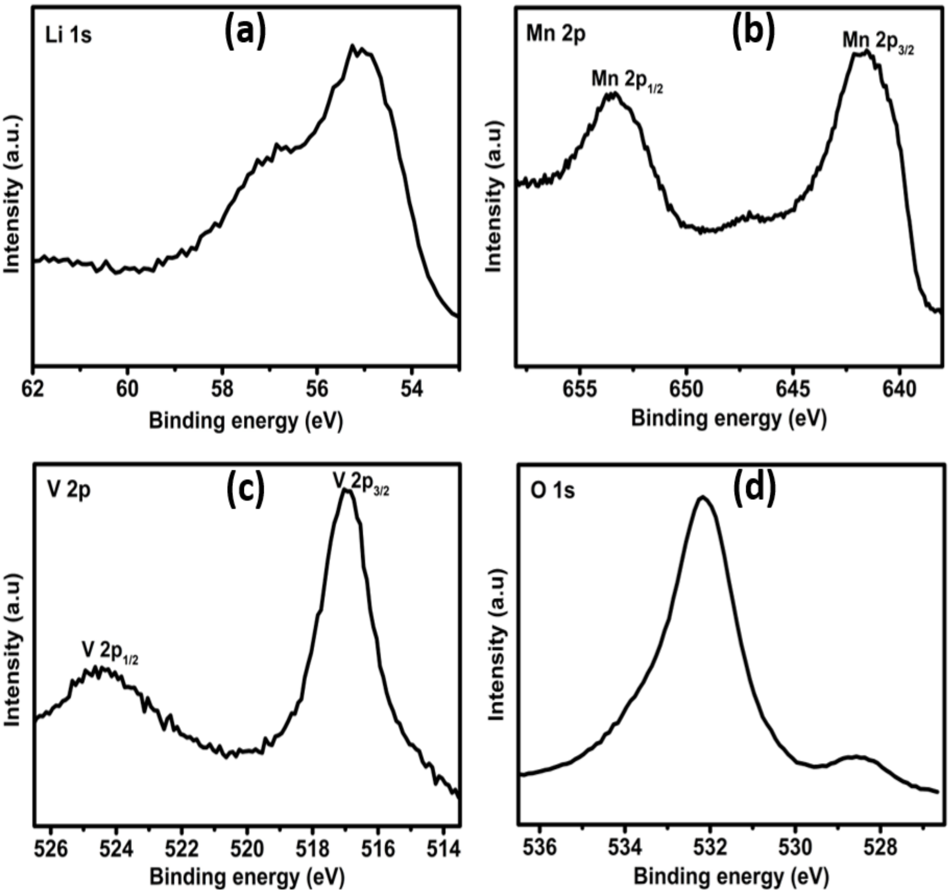

Figure 7.4. XPS core level spectra of $LiMnVO_4$ (a) Li 1s (b) Mn 2p (c) V 2p (d) O 1s

The chemical composition and surface chemical bonding state of the $LiMnVO_4$ nanorods were further determined by XPS analysis. Figure 7.4 shows the Li, Mn, V and O XPS core level spectra for $LiMnVO_4$. The binding energy of the Li1s core level emission peak was located at 55.1 eV and appeared as a broadened signal which is shown in Figure 7.4a. This value is close to that for Li_2O (Prakash et al., 2012). The Mn2p photoemission signals (Figure 7.4b) presents $Mn2p_{3/2}$ and $Mn2p_{1/2}$ peaks at 641.6 and 653.4 eV, respectively with no strong satellite structures typical of Mn(II) compounds (Clemens et al., 2012). The V2p core spectrum (Figure 7.4c) splits to $V2p_{3/2}$ and $V2p_{1/2}$ peaks located at 516.9 and 524.5 eV, characteristics of V^{5+}. Figure 7.4d shows the O1s spectra, which exhibited complex profile including a main peak centered at 529-535 eV. The major peak at 532.2 eV is assigned to Mn-O bonds, and a shoulder peak around 534 eV associated with oxygen in low coordination sites at the surface (Dupin et al., 2000). Based on these results, the compound prepared with Li, Mn, V and O are in +1, +2, +5, and -2 oxidation states, respectively, which confirm the compound $LiMnVO_4$.

7.3.2. Electrochemical Lithium Storage Performance of Nanocrystalline $LiMnVO_4$

The pseudocapacitive lithium storage of $LiMnVO_4$ electrodes in 1 M LiOH aqueous electrolyte was evaluated on the basis of its response to a potential sweep (CV), alternating current (EIS), and constant current (galvanostatic charge-discharge measurements).

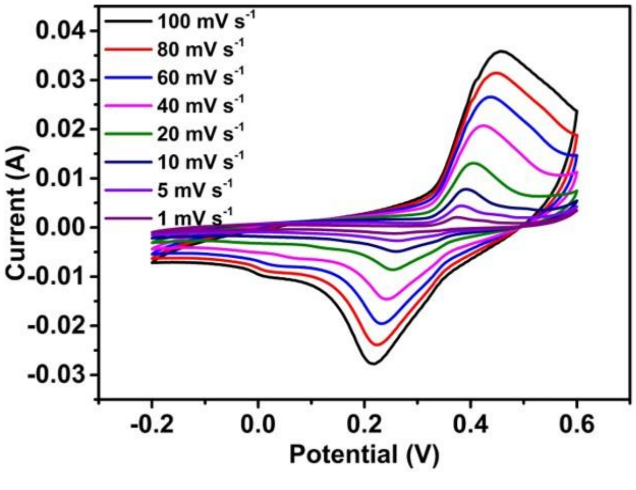

Figure 7.5. CV curves of $LiMnVO_4$ at different scan rates

CV was performed in a lithium ion containing electrolyte to determine the lithium storage performance of $LiMnVO_4$ electrodes using a three-electrode setup at different sweep rates (Figure 7.5). The CV curves exhibited symmetric cathodic and anodic peaks with a slight voltage separation in the sweep rates ranging from 20 to 1 mV s^{-1}. This indicate that the capacitance characteristic of $LiMnVO_4$ electrode is of typical pseudocapacitance (Wang et al., 2015c). Obviously, the current density increases with increasing sweep rate, while the anodic and cathodic peaks slightly shift towards the more positive and negative potentials respectively, which is supposed to be related to the internal resistance of the electrode and limitation of charge transfer kinetics (Du et al., 2016).

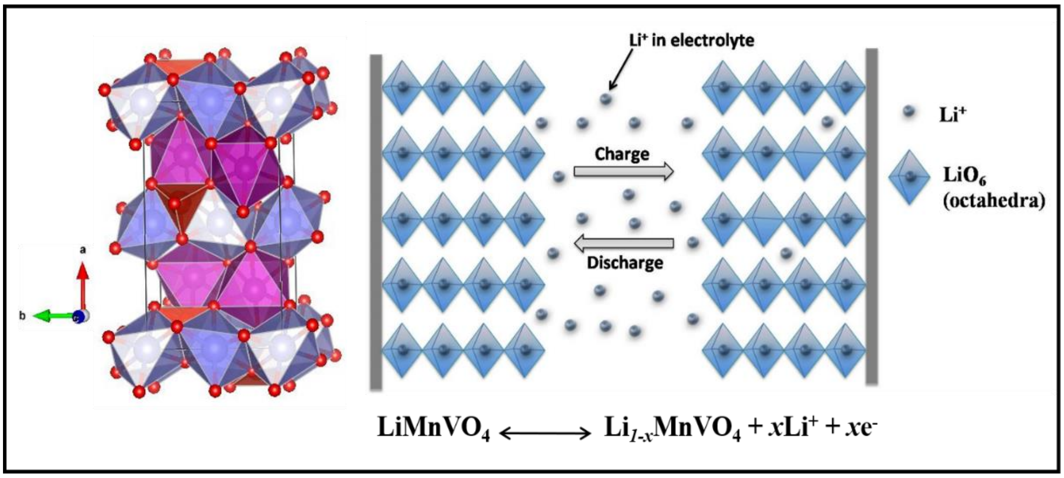

Figure 7.6 (a) The 3D visualization of $LiMnVO_4$ crystal using VESTA 3, where Li and Mn occupies MO_6 octahedra (LiO_6 in blue colour; MnO_6 in violet colour) and VO_4 tetrahedra (red colour) (b) schematic illustration of the lithium-ion intercalation and de-intercalation process in $LiMnVO_4$ electrode during charge-discharge process. MnO_6 octahedra and VO_4 tetrahedra in the $LiMnVO_4$ crystal structure are not represented

For $LiMnVO_4$, the cathodic and anodic peaks observed in the potential range of 0.2 to 0.6 V can be attributed to the reversible electrochemical lithium-ion intercalation and extraction process represented by the following reaction:

$$LiMnVO_4 \leftrightarrow Li_{1-x}MnVO_4 + xLi^+ + xe^- \quad (7.1)$$

where x is the mole fraction of inserted lithium given by $x = QM/mF$, where Q is the stored charge, M is the molecular weight, m is the mass and F is the Faraday constant (Brezesinski et al., 2010). In this reaction, lithium ions can intercalate and de-intercalate during the charge-discharge process (as shown in Figure 6.6), which is similar to that of the LIB. For $LiMnVO_4$ in a lithium ion containing electrolyte, charge storage occurs through the insertion of lithium ions with concomitant oxidation of Mn^{2+} to Mn^{3+}.

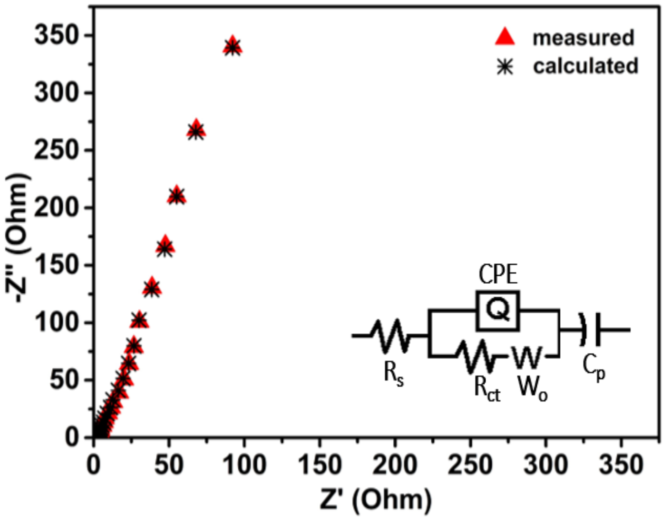

Figure 7.7. EIS Nyquist plot of $LiMnVO_4$ electrode. Inset: corresponding equivalent circuit

EIS measurement was carried out to further investigate the electrochemical behaviour of the $LiMnVO_4$ electrode. Figure 7.7 shows the EIS Nyquist plot of $LiMnVO_4$ electrode and its calculated curve by the ZSimpWin software. An equivalent circuit used to fit the impedance curve is given in the inset of Figure 7.7, which includes elements of bulk solution resistance (R_s), charge-transfer resistance (R_{ct}), constant phase element (CPE) to account for the double layer capacitance, Warburg diffusion element (W) and a pseudocapacitive element (C_p) from the lithium-ion diffusion associated with intercalation/extraction process of electrode materials (Li et al., 2014c; Eskandari et al., 2020). The high frequency intersection of Nyquist plot in the real axis represents the equivalent series resistance (R_s), including the ionic resistance of the electrolyte, intrinsic resistance of active materials and the contact resistance between the active materials and current collector, which is determined to be 2.38 Ω. In addition, the absence of semicircle in the high frequency region of Nyquist plot implies negligible charge-transfer resistance for $LiMnVO_4$ electrode suggesting the easy and rapid charge transfer on the electrode. The straight line in the low frequency region presents the Warburg impedance (Z_W), associated with the diffusion of the electrolyte ions along the

$LiMnVO_4$ electrode. The large slope of the straight line shown in Figure 7.7 demonstrates a very small Z_w of the electrolyte ion diffusion, indicating characteristic capacitor behaviour (Ates et al., 2015; Mei et al., 2018). The small values of R_s, R_{ct} and Z_w suggest that there is a large electro-active surface area and higher electrical conductivity with the $LiMnVO_4$ nanorods, which could extend the reaction zone of the electrode, making more electrode materials available for the charge-discharge process, leading to high capacitance (Du et al., 2016).

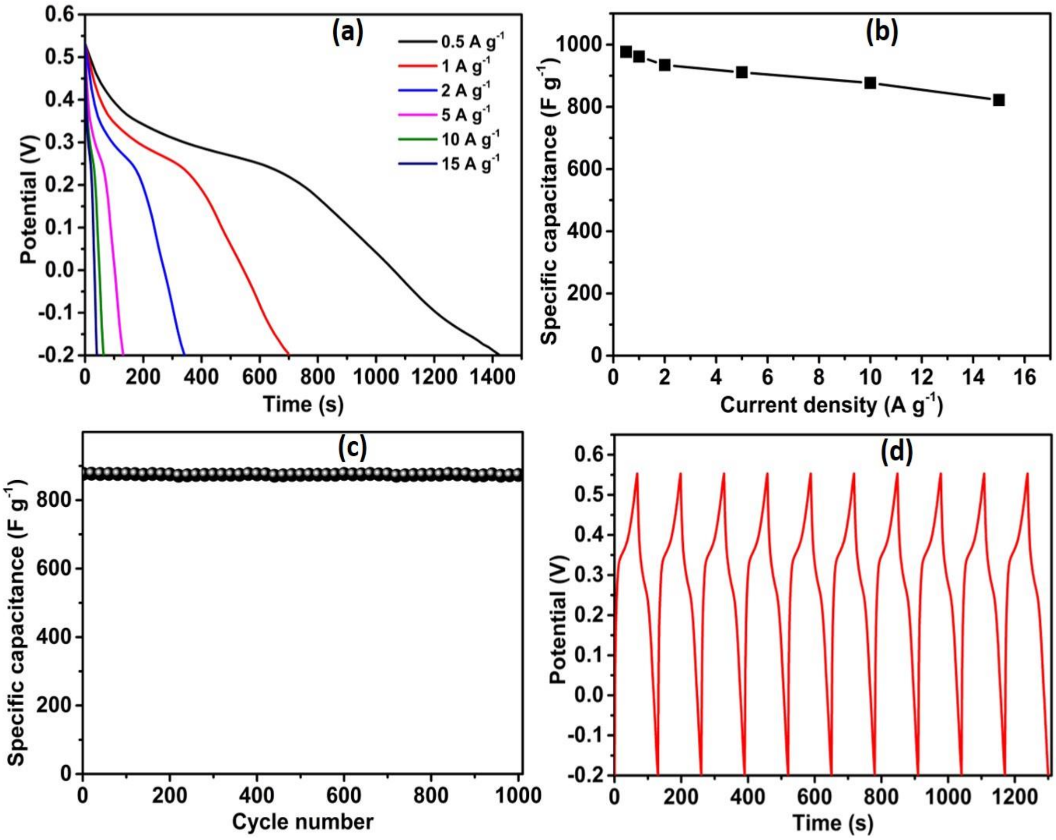

Figure 7.8. (a) Galvanostatic discharge curves of $LiMnVO_4$ electrode at various current densities (b) specific capacitance of $LiMnVO_4$ electrodes at different current densities (c) long-term cycling stability of $LiMnVO_4$ at a current density of 10 A g^{-1} (d) charge-discharge curves for first 10 cycles at 10 A g^{-1}

The lithium storage capacity of nanocrystalline $LiMnVO_4$ electrode was further investigated using galvanostatic charge-discharge studies in the potential range of -0.2 to 0.52 V to avoid IR drop. Figure 7.8a shows the galvanostatic discharge curves of $LiMnVO_4$ electrodes at various current densities from 0.5 to 15 A g^{-1}. The nonlinear discharge profiles further support the pseudocapacitive characteristics of the electrode, which is in good agreement with the CV curves as shown in Figure 7.5 (Du et al., 2016). Based on the discharge curves, the corresponding specific capacitances were calculated. The maximum capacitance was calculated to be 976.7 F g^{-1} at the current density of 0.5 A g^{-1}. The high capacitance of $LiMnVO_4$ can be mainly ascribed to the nano size of $LiMnVO_4$. The nanocrystalline structure of $LiMnVO_4$ not only provide a fast ion transport path and a large active surface area, but also enhances the accessibility of LiOH electrolyte and therefore, promotes the ion transport within the electrode (Lukatskaya et al., 2016).

Figure 7.8b shows the variation of specific capacitance with applied current. At different current densities of 0.5, 1, 2, 5, 10 and 15 A g^{-1}, the specific capacitance was estimated to be 976.7, 961.6, 934.2, 910.9, 876.7, and 821.9 F g^{-1} for nanocrystalline $LiMnVO_4$ electrode. It is believed that the degradation of capacitance with the increase of the current densities is mainly attributed to the incremental IR drop and insufficient active material involved in redox reactions at higher current densities (Du et al., 2016; Shao et al., 2018b). However, the electrode exhibits remarkable rate capability even at high current density, namely, the specific capacitance remained 821.9 F g^{-1} at a current density as high as 15 A g^{-1}. To further investigate the durability of the $LiMnVO_4$ electrode, its cycling performance was recorded at 10 A g^{-1} (Figure 7.8c). The specific capacitance still retains ~99% of the initial value even after 1000 cycles, which demonstrates excellent electrochemical stability. The excellent cycle stability of the electrodes may be attributed to the morphological and structural stability of $LiMnVO_4$.

To probe the stability of the $LiMnVO_4$ electrode, the samples after the cycling stability test was observed by SEM. Figure 7.9a-b presents the SEM of $LiMnVO_4$ electrode before and after 1000 charge-discharge cycles at 10 A g^{-1}; it can be clearly seen that the physical microstructures of the electrode maintain very well. As no notable changes can be found on the electrode before and after the cycling measurements, it proves the good stability of the $LiMnVO_4$ electrode. Further, XPS analysis of $LiMnVO_4$ electrodes were carried out to confirm the proposed lithium-ion intercalation mechanism and excellent cycling stability. It can be clearly seen from the survey spectra (Figure 7.9c) that $LiMnVO_4$ electrode before and after 1000 charge-discharge cycles at 10 A g^{-1} primarily composed of Li

1s, Mn 2p, V 2p, and O 1s peaks. The additional XPS peaks C 1s and F 1s were originated from Super P and PVDF employed during electrode coating process and Ni 2p peak from the nickel foam substrate. No apparent shift in peak position was observed for $LiMnVO_4$ electrodes even after 1000 continuous charge-discharge cycles, which validate the conclusion that there is no traceable phase transformation after cycling. Further, the comparative Mn 2p core level spectra of $LiMnVO_4$ electrode before and after cycling were evaluated (Figure 7.9d), which comprises of two major peaks, centered around 641 eV for Mn $2p_{3/2}$ and 653 eV for Mn $2p_{1/2}$ with no strong satellite peaks characteristic of Mn^{2+} (Prakash et al., 2012). It is obvious that the core level Mn 2p peaks hardly shift even after 1000 continuous charge-discharge cycles. This observation substantiates the fact that capacitance performance in $LiMnVO_4$ electrode is exclusively lithium-ion intercalation/de-intercalation process.

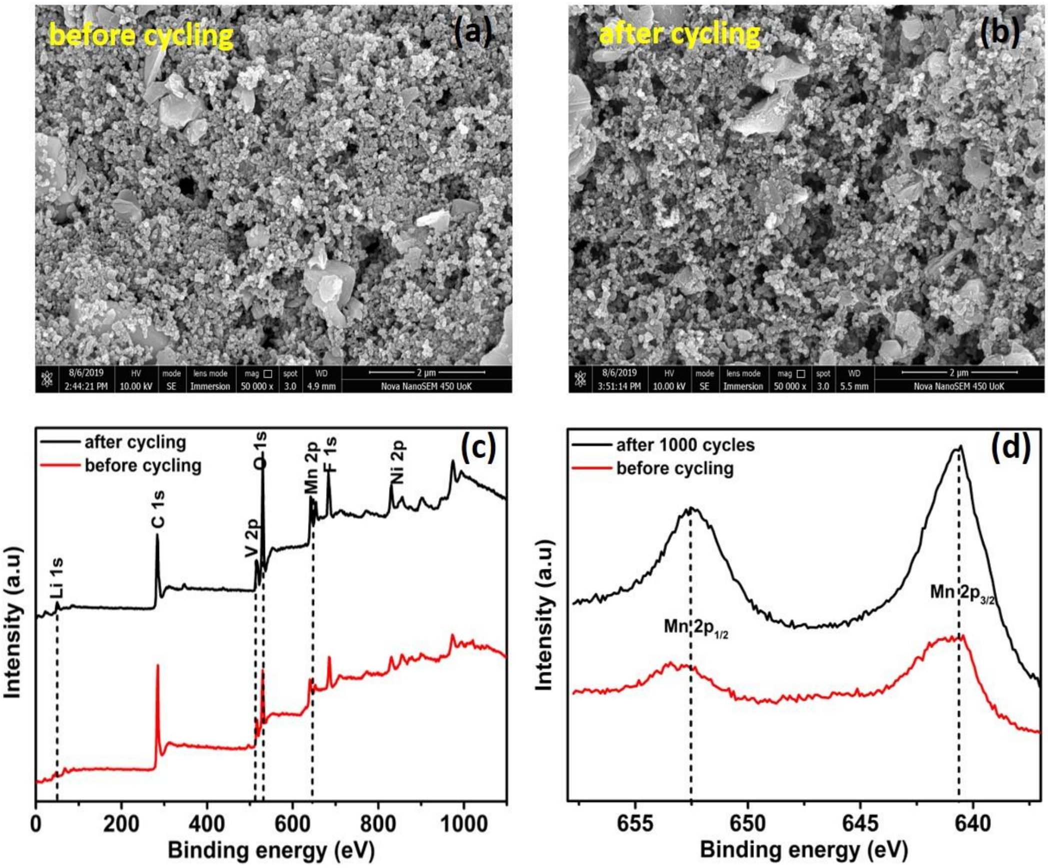

Figure 7.9. FESEM images of $LiMnVO_4$ electrodes (a) before cycling (b) after cycling (c) XPS survey spectrum of $LiMnVO_4$ electrode before and after cycling (d) comparative XPS core level spectrum of Mn 2p of $LiMnVO_4$ electrode before and after cycling

Though the intercalation pseudocapacitance is generated by the battery-type intercalation/de-intercalation of electrolyte ions in the interlayer of crystalline $LiMnVO_4$, which can be proved by the redox peaks in the CV curves, the kinetics of this process is predominantly surface reaction controlled and similar to the pseudocapacitive behaviour. To explore the reaction kinetics towards lithium ions, the charge storage mechanism is analyzed by investigating both coupled redox peaks of CV curves at various scan rates. The relationship between the current i and scan rate v obeys a power law, given by

$$i = av^b \tag{7.2}$$

where, a and b are variable parameters and the measured current density (i) obey to the power law function with scan rate (v) (Augustyn et al., 2014; Wang et al., 2016a).

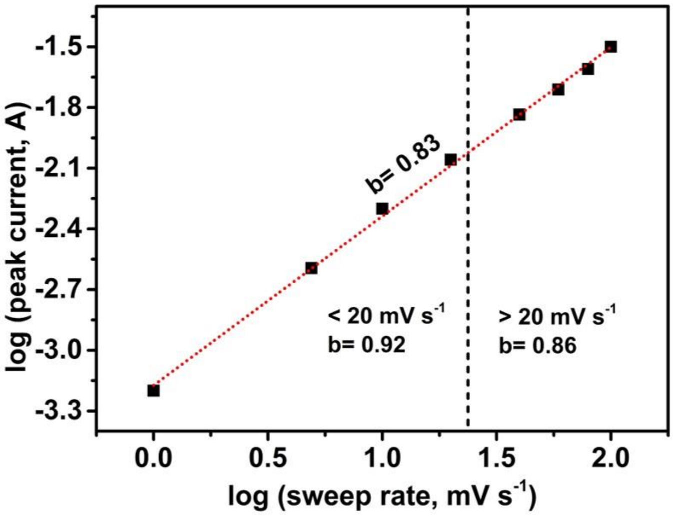

Figure 7.10. *b*-value determination of cathodic peak currents

When b values are close to one, the response is predominantly capacitive in nature. For the diffusion-controlled processes, current density is expected to vary with the square root of the scan rate and in this case, b values are close to 0.5. *b*-values were determined by plotting the log(i) versus log(v). The plotted values, according to equation (7.2), give straight line with slope equal to b. In scan rate range of 1-20 mV s^{-1}, the *b*-value obtained for $LiMnVO_4$ electrode is very close to 1 but deviates slightly at high rates (20-100 mV s^{-1}), as shown in Figure 7.10. The deviation observed in the faster sweep rates can be ascribed to poor electronic conductivity of the active electrode materials resulting in the lethargic electron transportation (Augustyn et al., 2013; Elgrishi et al., 2018). Thus, it can be concluded that total stored energy in the $LiMnVO_4$ electrode arises from the intercalation/de-intercalation of lithium-ion that is not limited by solid-state diffusion.

7.3.3. Electrochemical Lithium Storage Performance of Nanocrystalline $LiMnVO_4$ Hybrid LIC in Non-Aqueous Electrolyte

An asymmetric LIC device was assembled by using MWCNT as the positive electrode and $LiMnVO_4$ as the negative electrode in an organic electrolyte containing lithium-ions. Prior to this LIC assembly, the mass loading of positive (q_+) and negative (q_-) electrodes should be balanced from the charges of each electrode to realize the higher energy density (Tang et al., 2013; Dsoke et al., 2015; Wang et al., 2019e; Madabattula et al., 2020). Accordingly, the single electrode performance of $LiMnVO_4$ (Figure 7.8a) and MWCNT (Figure 5.11b) has been assessed using 1M LiOH electrolyte. Based on the single electrode performance of both electrodes, mass loading ratio between anode and cathode is fixed to be anode/cathode = 0.308 (calculated from equation 5.1) in the LIC.

Figure 7.11a shows the CV curves of $LiMnVO_4$//MWCNT LIC recorded at different scan rates (5, 10, 20, 40, 60, 80 and 100 mV s^{-1}) between -1.0 and 2.0 V.The CV curves exhibited a typical rectangular shape within the voltage range of -1.0-2.0 V, indicating a capacitance-dominated energy storage behavior (Wang et al., 2016a; Shao et al., 2018b). The slight deviation at higher voltage is caused by the different energy harvesting mechanism between capacitive cathode and intercalative anode (Byeon et al., 2016; Sun et al., 2017a). In the charging process, the $TFSI^-$ ions are absorbed in the cathode to elevate the voltage of this capacitor-type electrode. On the anode side, lithium ions are de-intercalated from the $LiMnVO_4$ and the potential of this battery-type electrode declines. The movement of ions is in the reverse direction during the discharge process.

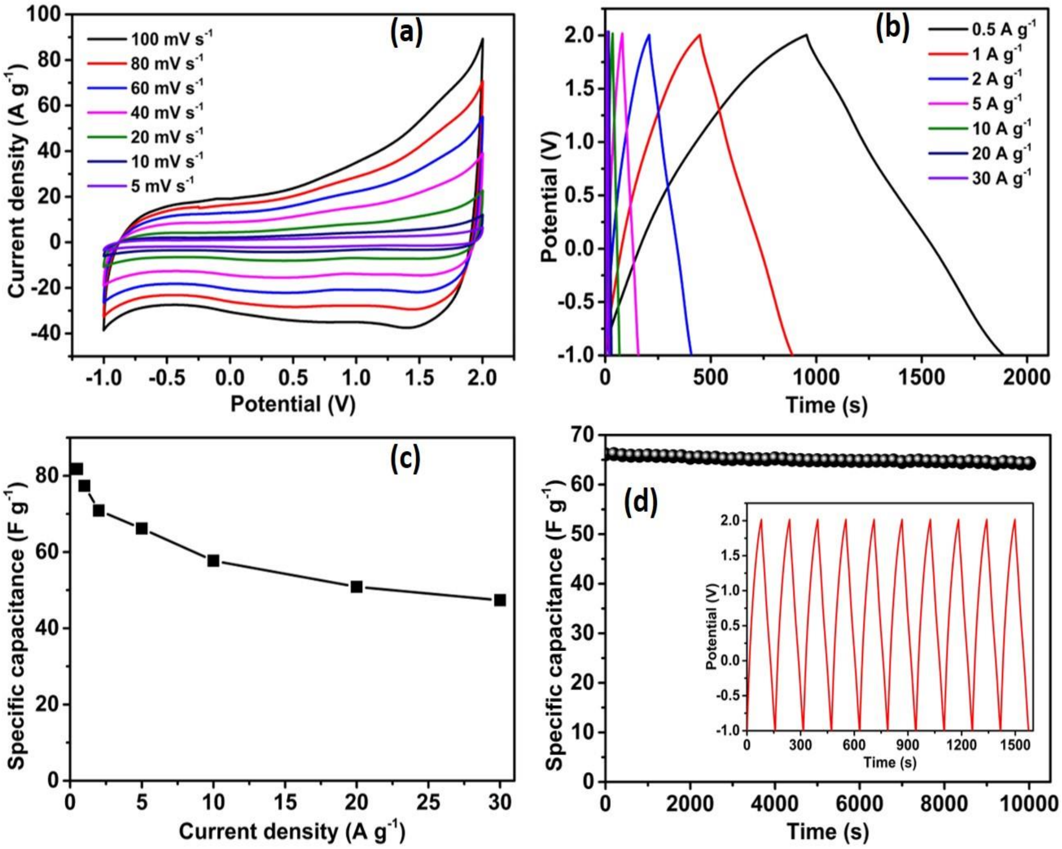

Figure 7.11. Electrochemical performance of $LiMnVO_4$//MWCNT LIC: (a) CV curves at various scan rates, (b) galvanostatic charge-discharge curves at different current densities, (c) specific capacitance values calculated from galvanostatic charge/discharge curves under different current densities, (d) cycle stability for 10000 cycles at a current density of 5 A g^{-1}, Inset: charge-discharge profiles for 10 continuous charge-discharge cycles

The galvanostatic charge-discharge curves of the asymmetric $LiMnVO_4$//MWCNT LIC were recorded at the current densities from 0.5 to 30 A g^{-1} (Figure 7.11b). It can be seen that the discharge curves slightly deviates from the linear behaviour, especially at low current densities, indicating the double contribution of electric double-layer capacitance and pseudocapacitance, which is consistent with the CV results (Huang and Niederberger, 2019; Huang et al., 2020). Based on the total mass of the positive and negative electrodes, the specific capacitance at various current densities is plotted in Figure 7.11c. The calculated capacitances are 81.7, 77.3, 70.8, 66, 57.7, 50.8 and 47.3 F g^{-1} at current densities of 0.5, 1, 2, 5, 10, 20 and 30 A g^{-1}, respectively. As expected, the decrease in specific capacitance is noted while increasing the current rate, because at higher current rates only the surface of the active material is involved in the electrochemical reaction (Aljaafari et al., 2019). To further investigate the durability of the asymmetric LIC, its cycling performance was recorded at 5 A g^{-1} (Figure 7.11d). The specific capacitance retains 97% of the initial value even after 10000 cycles, which demonstrates excellent electrochemical stability.

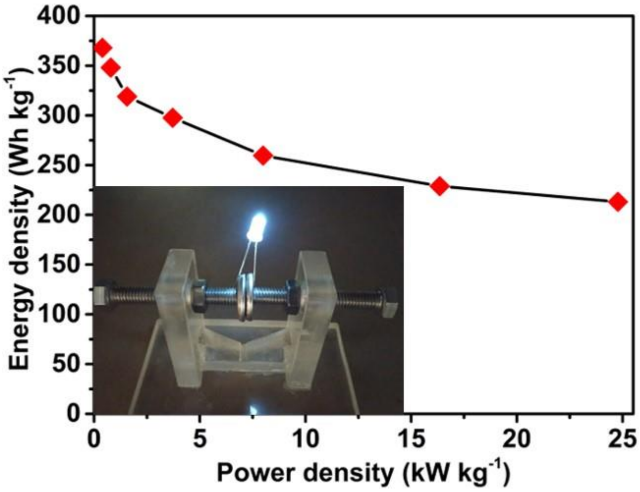

Figure 7.12. Ragone plot of LIC cell (inset shows a white LED powered by two LIC devices in series)

The Ragone plots of the asymmetric supercapacitor derived from the discharge curve based on equations (1.10) and (1.11) are displayed in Figure 7.12. The maximum energy density can be determined to be 368 Wh kg^{-1} at the average power density of 396.5 W kg^{-1}. It can still maintain 213 Wh kg^{-1} even at a high power density of 24781 W kg^{-1}. It is found that the performance of the $LiMnVO_4$//MWCNT asymmetric LIC is better than that of many previously reported systems, such as Mn_3O_4-Graphene//PANI derived AC (97.2 Wh kg^{-1} at power density of 62.5 W kg^{-1}) (Liu et al., 2019), $LiFePO_4$/EG//AC (15.1 Wh kg^{-1} at 129.5 W kg^{-1}) (Lv et al., 2019), $Li_3V_2(PO_4)_3$-C//AC (~25 Wh kg^{-1}) (Satish et al., 2015), $Li_4Ti_5O_{12}$/N-enriched carbon hybrid nanofiber sheet//AC (91 Wh kg^{-1} at 50 W kg^{-1}) (Choi et al., 2011), rGO@Fe_3O_4//holey rGO (148 Wh kg^{-1} and 25 kW kg^{-1}) (Liang eta al., 2018), $TiNb_2O_7$@carbon//CNF (110.4 Wh kg^{-1} at 99.58 W kg^{-1}) (Wang et al., 2015d), $MnFe_2O_4$/carbon//Amorphous carbon (157 Wh kg^{-1} at 200 W kg^{-1}) (Lee et al., 2016). In addition, the two fabricated $LiMnVO_4$//MWCNT LIC devices serially connected can effectively operate a white LED when fully charged (Inset of Figure 7.12). The LED illuminated for more than 180 s, indicating the assembled LICs function well in practical applications.

7.4. Conclusion

In summary, $LiMnVO_4$ nanorods was prepared via a facile hydrothermal method followed by calcination. Electrochemical results reveal that $LiMnVO_4$ has excellent lithium ion intercalation pseudocapacitance in aqueous electrolyte benefited from its small crystallite size with highly exposed crystallographic framework towards electrolyte (961.6 F g^{-1} at 1 A g^{-1}). The assembled asymmetric LIC based on $LiMnVO_4$ anode and MWCNT cathode in non-aqueous electrolyte achieve high energy and power densities. An energy density of 213.1 Wh kg^{-1} has been achieved at a high power density of 24.7 kW kg^{-1}, and the maximum energy density is 368 Wh kg^{-1} at a power density of 0.39 kW kg^{-1}. More interestingly, this $LiMnVO_4$//MWCNT LIC also shows long-term cycling stability up to 99% after 10,000 cycles. These results demonstrate that the $LiMnVO_4$//MWCNT is a good material combination for LIC which can potentially bridge the gap between conventional LIBs and supercapacitors, and meet the present energy and power demands.

CHAPTER 8

CONCLUSIONS AND FUTURE PERSPECTIVES

8.1. Conclusions

LSBs have attracted considerable attention for energy storage owing to its high theoretical capacity, energy density and low cost compared to the state-of-the-art lithium-ion technology. However, their practical applications are greatly limited by rapid capacity degradation because of the unfavourable reaction between soluble intermediate PSs and the lithium anode (Shen et al., 2019). The separator is an important component in a LSB, which acts as an electron insulator to prevent a short circuit (Arora and Zhang, 2004). Commercial separators are generally polymer membranes with a large number of nanoscale pores, which have a much larger size than PSs, so the soluble PSs can diffuse freely through the separator and react with the lithium anode, resulting in the degradation of the lithium anode (Rana et al., 2019). This thesis demonstrates functional modification of separators as an efficient way to inhibit the shuttling of PSs.

Various materials and approaches have been devoted to modifying the commercially available separators, including carbon-based materials, polymer-based materials, inorganic oxide-based materials and other novel functional materials (Deng et al., 2016; He et al., 2018b; Deng et al., 2019). Among them, modification of separator with polymers containing polar negatively charged functional groups and unique chain structure are smart as they can concurrently increase the electrolyte uptake and interfacial conductivity together with mitigating the PS crossover owing to the presence of polar functional groups. Besides, the separator modified with negatively charged groups will function as cation-selective membranes providing transport channels for lithium through the Coulombic interactions, thereby improving electrochemical performance of LSBs (Deng et al., 2019). Hence, in the first part of the thesis, we have investigated the "electrostatic repulsion" approach using functional separators composed of various lithiated polymers to effectively alleviate the shuttling of PS anions. The lithiated polymers utilized in this thesis include lithiated poly(2-acrylamido-2-methyl-1-propanesulfonic acid) (LPAMPS), lithiated poly(3,4-ethylenedioxythiophene): poly(styrene sulfonate) (Li^+-PEDOT:PSS) and lithiated poly(acrylic acid-co-maleic acid) (LPAM). The lithiated polymer modified separators studied here are highly permselective in nature. The negatively charged functional groups present on the lithiated polymers impart selective diffusion of lithium ions, at the same time repelling polysulfide anions via coulombic interactions. Besides, the modified separator possesses excellent electrolyte wettability, interfacial contact and ionic conductivity. The Li-S cell assembled with modified separator exhibited significant improvement in the electrochemical performance compared to the cell with pristine commercially available separator. In general, the lithiated polymer coating on commercial separator serves as a facile and effective strategy for future LSB technology, mitigating self-discharge behaviour. The major results obtained from the study are listed in the table 8.1.

Table 8.1. Comparison of the electrochemical performance of Li-S cells fabricated using lithiated polymer coated separators

Separator coating material	Separator coating thickness (µm)	Cathode S content (wt%)	Cathode S loading (mg cm^{-2})	Initial discharge capacity (mAh g^{-1})	Discharge capacity at n^{th} cycle and C-rate
LPAMPS	13	66	0.9	1486	1056/200/0.1
LPAMPS	13	66	2.5	1274	1189/50/0.1
LPAMPS	13	66	4.2	1115	1068/50/0.1
Li^+-PEDOT:PSS	9	66	3.9	1360	1049/300/0.1
LPAM	3.7	66	4.1	1213	957/300/0.1

Also, it is essential that a separator specimen has uniform thickness and assured contact with both electrodes while not allowing contact between the two electrodes. The separator thickness is a critical property that affects mechanical strength, cell impedance, energy density and rate capability. Thickness values should be minimal to allow increased conductivity of a cell without compromising the mechanical strength. The variations in thickness of the separators influence the performance of the battery, especially in high C-rate applications because of high internal impedance. For lab-scale experiments, it can be assumed that the thickness plays a minimum role in performance because of low C-rate used for the testing.

Capacitive energy storage has attracted great interest due to their numerous attractive properties, including fast charging, long cycle life, and the ability to deliver up to ten times more power compared to conventional batteries (Gür, 2018). Among the various capacitive storage mechanisms, intercalation pseudocapacitance has been recognized as a new type of charge storage mechanism in crystalline metal oxides, in which intercalation is not limited to surface structures, instead extended to the bulk crystalline framework of the material. This may narrow the performance gap between supercapacitors and battery materials (Augustyn et al., 2014). Transition metal oxides with layered or tunnel crystalline structures are interesting electrode materials for lithium storage because of their capability to intercalate/de-intercalate lithium ions in the lattice sites (Aravindan et al., 2014a). The significance of this class of pseudocapacitance is that the lithium storage in battery materials can be attained at rapid rates comparable to that of electrochemical capacitors (Wang et al., 2016a). In the second part of the thesis, we synthesized various lithium metal vanadates and its intercalation pseudocapacitive lithium storage properties have been investigated. The various lithium metal vanadate-based electrode materials explored in this part of the thesis include lithium cobalt vanadate ($LiCoVO_4$), lithium nickel vanadate ($LiNiVO_4$) and lithium manganese vanadate ($LiMnVO_4$). Herein, the intercalation pseudocapacitive lithium storage properties of nanocrystalline $LiMVO_4$ (M = Co, Ni, Mn) electrode materials were evaluated in aqueous electrolyte. In the case of $LiCoVO_4$, micro and nanocrystalline electrode materials has been investigated to study the effect of crystallite size on the fundamental lithium storage properties. The nanocrystalline electrode demonstrated better lithium-ion intercalation/de-intercalation properties benefited from its small crystallite size with highly exposed crystallographic framework towards electrolyte. The electrochemical results reveal that the nanocrystalline $LiMVO_4$ (M = Co, Ni, Mn) electrode materials has high specific capacitance ($LiCoVO_4$, 929.5 F g^{-1} at 1 Ag^{-1}; $LiNiVO_4$, 406.3 F g^{-1} at 1 A g^{-1}; $LiMnVO_4$, 961.6 F g^{-1} at 1 A g^{-1}) and excellent cycling stability (~99% capacitance retention after 1000 cycles). Detailed evaluation of CV data further confirms the proposed lithium-ion intercalation mechanism.

LICs are excellent energy-storage devices that close the gap between LIBs and supercapacitors. The selection and design of the electrode material, the quality of matching between the positive and negative electrodes, and the operation of the potential window directly affect the energy density, power density, and cycle life of LICs. This research focused on exploring the use of nanocrystalline $LiMVO_4$ (M = Co, Ni, Mn) as a potential battery-type anode material for LIC. An asymmetric LIC devices were assembled using MWCNT as the positive electrode and nanocrystalline $LiMVO_4$ (M = Co, Ni, Mn) as the negative electrode in an organic electrolyte containing lithium-ions. The assembled LICs demonstrated an excellent capacitive performance like superior energy density, high power density and excellent capacitance retention. The studies demonstrate that the $LiMVO_4$ (M = Co, Ni, Mn)//MWCNT is a good material combination for LIC which can meet the present energy and power demands. The major findings and contributions of the study are listed below.

- Nanocrystalline $LiMVO_4$ (M = Co, Ni, Mn) demonstrate good Li^+ intercalation pseudocapacitive properties benefited from its small crystallite size with highly exposed Li^+ selective crystallographic pathways towards electrolyte.
- The asymmetric LIC device ($LiCoVO_4$//MWCNT) exhibit high energy density of 315 Wh kg^{-1} (at a power density of 399.6 W kg^{-1}) and superior cycling stability (~93% capacitance retention after 10000 cycles at 5 A g^{-1}).
- The assembled hybrid cells ($LiNiVO_4$//MWCNT) deliver a high energy density of 255 Wh kg^{-1} with maximum power density of 22325 W kg^{-1} and excellent capacitance retention of ~92% after 10000 cycles at 5 A g^{-1}.
- The fabricated device ($LiMnVO_4$//MWCNT) show an energy density of 368 Wh kg^{-1} and a maximum power density of 24781 W kg^{-1} in association with superior cycling stability (~97% capacitance retention after 10000 cycles at 5 A g^{-1}).

8.2. Future Perspectives

This doctoral research work focused on the development of suitable materials with excellent lithium storage properties for LSBs and LICs. Even though, the selected materials could overcome the major shortcomings associated with LSBs and LICs, their commercialization is still impeded due to certain unresolved challenges. LSBs and LICs are considered as the most viable options next-generation energy storage devices, in terms of energy, power, cycle life, safety, cost, and environmental compatibility. In order to achieve this goal, further optimisation of material selection is required in the case of all cell components. The following are the possible future research possibilities based on this thesis.

- Designing LSBs with practically necessary parameters such as high sulfur content and loading, low E/S ratio, long cyclability, etc.
- Application of the modified separators (LPAMPS@CG, Li^+-PEDOT:PSS@CG and LPAM@CG) in the pouch cell. The advantage of the modified separators will be limited when we procced for pouch cells, due to the limited PS adsorption capacity of these separators with high sulfur loading in the electrode (>5 mg cm^{-2}). Increasing the amount of coating material on separators would anchor more lithium polysulfides, but the overall specific capacity reduces, and the cost inevitably increases. There should have a balance between thickness/mass of the separator coating and sulfur content/loading.
- Exploiting lithium metal vanadates, $LiMVO_4$ (M = Co, Ni, Mn) as cathodes to obtain Li-S full-cell architectures with high energy density
- Application of $LiMVO_4$ (M = Co, Ni, Mn) as cathode additives to improve LSB performance
- Exploiting the polyelectrolyte as functional binders for LSB cathode
- Design of polymer electrolytes using poly(ionic liquid)s
- Synthesis, characterization and preliminary evaluation of pseudocapacitive behaviour of nanostructured, mixed transition metal vanadates for electrochemical lithium storage and its application as anode materials for LICs.

REFERENCES

1. Abbas, S. A., Ibrahem, M. A., Hu, L.-H., Lin, C.-N., Fang, J., Boopathi, K. M., Wang, P.-C., Li, L.-J., and Chu, C.-W. (2016). Bifunctional separator as a polysulfide mediator for highly stable Li–S batteries. *Journal of Materials Chemistry A, 4*(24): 9661-9669.

2. Ahn, J. H., Shin, H.-J., Abbas, S., Lee, K.-Y., and Ha, H. Y. (2019). Plasma-functionalized carbon-layered separators for improved performance of lithium sulfur batteries. *Journal of Materials Chemistry A, 7*(8): 3772-3782.

3. Ahn, W., Lim, S. N., Lee, D. U., Kim, K.-B., Chen, Z., and Yeon, S.-H. (2015). Interaction mechanism between a functionalized protective layer and dissolved polysulfide for extended cycle life of lithium sulfur batteries. *Journal of Materials Chemistry A, 3*(18): 9461-9467.

4. Aida, T., Murayama, I., Yamada, K., and Morita, M. (2007). Improvement in Cycle Performance of a High-Voltage Hybrid Electrochemical Capacitor. *Electrochemical and Solid-State Letters, 10*(4): A93-A96.

5. Ajuria, J., Redondo, E., Arnaiz, M., Mysyk, R., Rojo, T., and Goikolea, E. (2017). Lithium and sodium ion capacitors with high energy and power densities based on carbons from recycled olive pits. *Journal of Power Sources, 359*: 17-26.

6. Akridge, J. R., Mikhaylik, Y. V., and White, N. (2004). Li/S fundamental chemistry and application to high-performance rechargeable batteries. *Solid State Ionics, 175*(1): 243-245.

7. Ali, S., Waqas, M., Jing, X., Chen, N., Chen, D., Xiong, J., and He, W. (2018). Carbon–Tungsten Disulfide Composite Bilayer Separator for High-Performance Lithium–Sulfur Batteries. *ACS Applied Materials & Interfaces, 10*(46): 39417-39421.

8. Aljaafari, A., Parveen, N., Ahmad, F., Alam, M. W., and Ansari, S. A. (2019). Self-assembled Cube-like Copper Oxide Derived from a Metal-Organic Framework as a High-Performance Electrochemical Supercapacitive Electrode Material. *Scientific Reports, 9*(1): 9140-9140.

9. Amatucci, G. G., Badway, F., Du Pasquier, A., and Zheng, T. (2001). An Asymmetric Hybrid Nonaqueous Energy Storage Cell. *Journal of The Electrochemical Society, 148*(8): A930-A939.

10. An, C., Zhang, Y., Guo, H., and Wang, Y. (2019). Metal oxide-based supercapacitors: progress and prospectives. *Nanoscale Advances, 1*(12): 4644-4658.

11. Anu Prathap, M. U., Satpati, B., and Srivastava, R. (2013). Facile preparation of polyaniline/MnO2 nanofibers and its electrochemical application in the

simultaneous determination of catechol, hydroquinone, and resorcinol. *Sensors and Actuators B: Chemical, 186*: 67-77.

12. Aravindan, V., Cheah, Y. L., Mak, W. F., Wee, G., Chowdari, B. V. R., and Madhavi, S. (2012). Fabrication of High Energy-Density Hybrid Supercapacitors Using Electrospun V2O5 Nanofibers with a Self-Supported Carbon Nanotube Network. *ChemPlusChem, 77*(7): 570-575.

13. Aravindan, V., Chuiling, W., Reddy, M. V., Rao, G. V. S., Chowdari, B. V. R., and Madhavi, S. (2012). Carbon coated nano-LiTi2(PO4)3 electrodes for non-aqueous hybrid supercapacitors. *Physical Chemistry Chemical Physics, 14*(16): 5808-5814.

14. Aravindan, V., Gnanaraj, J., Lee, Y.-S., and Madhavi, S. (2014a). Insertion-Type Electrodes for Nonaqueous Li-Ion Capacitors. *Chemical Reviews, 114*(23): 11619-11635.

15. Aravindan, V., Sundaramurthy, J., Jain, A., Kumar, P. S., Ling, W. C., Ramakrishna, S., Srinivasan, M. P., and Madhavi, S. (2014b). Unveiling TiNb2O7 as an Insertion Anode for Lithium Ion Capacitors with High Energy and Power Density. *ChemSusChem, 7*(7): 1858-1863.

16. Arora, P., and Zhang, Z. (2004). Battery Separators. *Chemical Reviews, 104*(10): 4419-4462.

17. Ates, M., Serin, M. A., Ekmen, I., and Ertas, Y. N. (2015). Supercapacitor behaviors of polyaniline/CuO, polypyrrole/CuO and PEDOT/CuO nanocomposites. *Polymer Bulletin, 72*(10): 2573-2589.

18. Augustyn, V., Come, J., Lowe, M. A., Kim, J. W., Taberna, P.-L., Tolbert, S. H., Abruña, H. D., Simon, P., and Dunn, B. (2013). High-rate electrochemical energy storage through Li^+ intercalation pseudocapacitance. *Nature Materials, 12*(6): 518-522.

19. Augustyn, V., Simon, P., and Dunn, B. (2014). Pseudocapacitive oxide materials for high-rate electrochemical energy storage. *Energy & Environmental Science, 7*(5): 1597-1614.

20. Aurbach, D., Pollak, E., Elazari, R., Salitra, G., Kelley, C. S., and Affinito, J. (2009). On the Surface Chemical Aspects of Very High Energy Density, Rechargeable Li–Sulfur Batteries. *Journal of The Electrochemical Society, 156*(8): A694-A702.

21. Babu, D. B., Giribabu, K., and Ramesha, K. (2018). Permselective SPEEK/Nafion Composite-Coated Separator as a Potential Polysulfide Crossover Barrier Layer for Li–S Batteries. *ACS Applied Materials & Interfaces, 10*(23): 19721-19729.

22. Bai, S., Liu, X., Zhu, K., Wu, S., and Zhou, H. (2016a). Metal–organic framework-based separator for lithium–sulfur batteries. *Nature Energy, 1*(7): 16094.

23. Bai, S., Zhu, K., Wu, S., Wang, Y., Yi, J., Ishida, M., and Zhou, H. (2016b). A long-life lithium–sulphur battery by integrating zinc–organic framework based separator. *Journal of Materials Chemistry A, 4*(43): 16812-16817.

24. Balach, J., Jaumann, T., Klose, M., Oswald, S., Eckert, J., and Giebeler, L. (2016a). Improved cycling stability of lithium–sulfur batteries using a polypropylene-supported nitrogen-doped mesoporous carbon hybrid separator as polysulfide adsorbent. *Journal of Power Sources, 303*: 317-324.

25. Balach, J., Jaumann, T., Mühlenhoff, S., Eckert, J., and Giebeler, L. (2016b). Enhanced polysulphide redox reaction using a RuO2 nanoparticle-decorated mesoporous carbon as functional separator coating for advanced lithium–sulphur batteries. *Chemical Communications, 52*(52): 8134-8137.

26. Balach, J., Linnemann, J., Jaumann, T., and Giebeler, L. (2018). Metal-based nanostructured materials for advanced lithium–sulfur batteries. *Journal of Materials Chemistry A, 6*(46): 23127-23168.

27. Barghamadi, M., Best, A. S., Bhatt, A. I., Hollenkamp, A. F., Musameh, M., Rees, R. J., and Rüther, T. (2014). Lithium–sulfur batteries—the solution is in the electrolyte, but is the electrolyte a solution? *Energy & Environmental Science, 7*(12): 3902-3920.

28. Bauer, I., Thieme, S., Brückner, J., Althues, H., and Kaskel, S. (2014). Reduced polysulfide shuttle in lithium–sulfur batteries using Nafion-based separators. *Journal of Power Sources, 251*: 417-422.

29. Béguin, F., Presser, V., Balducci, A., and Frackowiak, E. (2014). Carbons and Electrolytes for Advanced Supercapacitors. *Advanced Materials, 26*(14): 2219-2251.

30. Berger, A., Freiberg, A. T. S., Siebel, A., Thomas, R., Patel, M. U. M., Tromp, M., Gasteiger, H. A., and Gorlin, Y. (2018). The Importance of Chemical Reactions in the Charging Process of Lithium-Sulfur Batteries. *Journal of The Electrochemical Society, 165*(7): A1288-A1296.

31. Bhuvaneswari, M. S., Selvasekarapandian, S., Kamishima, O., Kawamura, J., and Hattori, T. (2005). Vibrational analysis of lithium nickel vanadate. *Journal of Power Sources, 139*(1): 279-283.

32. Bi, Z., Kong, Q., Cao, Y., Sun, G., Su, F., Wei, X., Li, X., Ahmad, A., Xie, L., and Chen, C.-M. (2019). Biomass-derived porous carbon materials with different dimensions for supercapacitor electrodes: a review. *Journal of Materials Chemistry A, 7*(27): 16028-16045.

33. Bini, M., Capsoni, D., Ferrari, S., Quartarone, E., and Mustarelli, P. (2015). 1 - Rechargeable lithium batteries: key scientific and technological challenges. In A. A. Franco (Ed.), *Rechargeable Lithium Batteries* (pp. 1-17): Woodhead Publishing.

34. Bizuneh, G. G., Fan, J., Sun, C., Xiangfei, Y., Xue, F., Deng, D., Lei, J., Lin, X., Jia, Y., Yang, J., Yan, H., Wang, X., Zheng, M., and Dong, Q. (2019). LaLiO2-Based Multi-Functional Interlayer for Enhanced Performance of Li-S Batteries. *Journal of The Electrochemical Society, 166*(2): A68-A73.

35. Blake, N. P., Petersen, M. K., Voth, G. A., and Metiu, H. (2005). Structure of Hydrated Na−Nafion Polymer Membranes. *The Journal of Physical Chemistry B, 109*(51): 24244-24253.

36. Borenstein, A., Hanna, O., Attias, R., Luski, S., Brousse, T., and Aurbach, D. (2017). Carbon-based composite materials for supercapacitor electrodes: a review. *Journal of Materials Chemistry A, 5*(25): 12653-12672.

37. Brezesinski, T., Wang, J., Tolbert, S. H., and Dunn, B. (2010). Ordered mesoporous α-MoO3 with iso-oriented nanocrystalline walls for thin-film pseudocapacitors. *Nature Materials, 9*(2): 146-151.

38. Brousse, T., Bélanger, D., and Long, J. W. (2015). To Be or Not To Be Pseudocapacitive? *Journal of The Electrochemical Society, 162*(5): A5185-A5189.

39. Bruce, P. G., Hardgrave, M. T., and Vincent, C. A. (1992). The determination of transference numbers in solid polymer electrolytes using the Hittorf method. *Solid State Ionics, 53-56*: 1087-1094.

40. Bryan, A. M., Santino, L. M., Lu, Y., Acharya, S., and D’Arcy, J. M. (2016). Conducting Polymers for Pseudocapacitive Energy Storage. *Chemistry of Materials, 28*(17): 5989-5998.

41. Burke, A. (2000). Ultracapacitors: why, how, and where is the technology. *Journal of Power Sources, 91*(1): 37-50.

42. Burke, M. J., and Stephens, J. C. (2018). Political power and renewable energy futures: A critical review. *Energy Research & Social Science, 35*: 78-93.

43. Byeon, A., Glushenkov, A. M., Anasori, B., Urbankowski, P., Li, J., Byles, B. W., Blake, B., Van Aken, K. L., Kota, S., Pomerantseva, E., Lee, J. W., Chen, Y., and Gogotsi, Y. (2016). Lithium-ion capacitors with 2D Nb2CTx (MXene) – carbon nanotube electrodes. *Journal of Power Sources, 326*: 686-694.

44. Cabán-Huertas, Z., Dubal, D. P., Ayyad, O., and Gómez-Romero, P. (2017). Capacitive vs Faradaic Energy Storage in a Hybrid Cell with LiFePO4/RGO Positive Electrode and Nanocarbon Negative Electrode. *Journal of The Electrochemical Society, 164*(1): A6140-A6146.

45. Cai, M., Sun, X., Chen, W., Qiu, Z., Chen, L., Li, X., Wang, J., Liu, Z., and Nie, Y. (2018). Performance of lithium-ion capacitors using pre-lithiated multiwalled carbon nanotubes/graphite composite as negative electrode. *Journal of Materials Science, 53*(1): 749-758.

46. Cai, M., Sun, X., Nie, Y., Chen, W., Qiu, Z., Chen, L., Liu, Z., and Tang, H. (2017). Electrochemical Performance of Lithium-Ion Capacitors Using Pre-Lithiated Multiwalled Carbon Nanotubes as Anode. *Nano, 12*(04): 1750051.

47. Callsen, M., Sodeyama, K., Futera, Z., Tateyama, Y., and Hamada, I. (2017). The Solvation Structure of Lithium Ions in an Ether Based Electrolyte Solution from First-Principles Molecular Dynamics. *The Journal of Physical Chemistry B, 121*(1): 180-188.

48. Cano, Z. P., Banham, D., Ye, S., Hintennach, A., Lu, J., Fowler, M., and Chen, Z. (2018). Batteries and fuel cells for emerging electric vehicle markets. *Nature Energy, 3*(4): 279-289.

49. Cao, Y., Zuo, P., Lou, S., Sun, Z., Li, Q., Huo, H., Ma, Y., Du, C., Gao, Y., and Yin, G. (2019). A quasi-solid-state Li–S battery with high energy density, superior stability and safety. *Journal of Materials Chemistry A, 7*(11): 6533-6542.

50. Carenco, S., Portehault, D., Boissière, C., Mézailles, N., and Sanchez, C. (2013). Nanoscaled Metal Borides and Phosphides: Recent Developments and Perspectives. *Chemical Reviews, 113*(10): 7981-8065.

51. Cericola, D., and Kötz, R. (2012). Hybridization of rechargeable batteries and electrochemical capacitors: Principles and limits. *Electrochimica Acta, 72*: 1-17.

52. Chang, C.-H., Chung, S.-H., and Manthiram, A. (2015). Ultra-lightweight PANiNF/MWCNT-functionalized separators with synergistic suppression of polysulfide migration for Li–S batteries with pure sulfur cathodes. *Journal of Materials Chemistry A, 3*(37): 18829-18834.

53. Chang, C.-H., Chung, S.-H., and Manthiram, A. (2016). Effective Stabilization of a High-Loading Sulfur Cathode and a Lithium-Metal Anode in Li-S Batteries Utilizing SWCNT-Modulated Separators. *Small, 12*(2): 174-179.

54. Chen, G.-F., Liu, Z.-Q., Lin, J.-M., Li, N., and Su, Y.-Z. (2015b). Hierarchical polypyrrole based composites for high performance asymmetric supercapacitors. *Journal of Power Sources, 283*: 484-493.

55. Chen, R., Knapp, M., Yavuz, M., Ren, S., Witte, R., Heinzmann, R., Hahn, H., Ehrenberg, H., and Indris, S. (2015c). Nanoscale spinel LiFeTiO4 for intercalation pseudocapacitive Li+ storage. *Physical Chemistry Chemical Physics, 17*(2): 1482-1488.

56. Chen, W., Mai, L. Q., Xu, Q., Zhu, Q. Y., and Yang, H. P. (2003). Novel soft solution synthesis and characterization of submicromic LiCoVO4. *Materials Science and Engineering: B, 100*(3): 221-224.

57. Chen, X., He, W., Ding, L.-X., Wang, S., and Wang, H. (2019). Enhancing interfacial contact in all solid state batteries with a cathode-supported solid electrolyte membrane framework. *Energy & Environmental Science, 12*(3): 938-944.

58. Chen, Y., Liu, B., Liu, Q., Wang, J., Liu, J., Zhang, H., Hu, S., and Jing, X. (2015a). Flexible all-solid-state asymmetric supercapacitor assembled using coaxial NiMoO4 nanowire arrays with chemically integrated conductive coating†. *Electrochimica Acta, 178*: 429-438.

59. Chen, Z., Augustyn, V., Wen, J., Zhang, Y., Shen, M., Dunn, B., and Lu, Y. (2011). High-Performance Supercapacitors Based on Intertwined CNT/V2O5 Nanowire Nanocomposites. *Advanced Materials, 23*(6): 791-795.

60. Cheng, P., Guo, P., Liu, D., Wang, Y., Sun, K., Zhao, Y., and He, D. (2019). Fe3O4/RGO modified separators to suppress the shuttle effect for advanced lithium-sulfur batteries. *Journal of Alloys and Compounds, 784*: 149-156.

61. Cho, M.-Y., Kim, M.-H., Kim, H.-K., Kim, K.-B., Yoon, J. R., and Roh, K. C. (2014). Electrochemical performance of hybrid supercapacitor fabricated using multi-structured activated carbon. *Electrochemistry Communications, 47*: 5-8.

62. Choi, J. W., and Aurbach, D. (2016). Promise and reality of post-lithium-ion batteries with high energy densities. *Nature Reviews Materials, 1*(4): 16013.

63. Chung, S.-H., Han, P., Singhal, R., Kalra, V., and Manthiram, A. (2015). Electrochemically Stable Rechargeable Lithium–Sulfur Batteries with a Microporous Carbon Nanofiber Filter for Polysulfide. *Advanced Energy Materials, 5*(18): 1500738.

64. Chung, S.-H., and Manthiram, A. (2014). High-Performance Li–S Batteries with an Ultra-lightweight MWCNT-Coated Separator. *The Journal of Physical Chemistry Letters, 5*(11): 1978-1983.

65. Clemens, O., Bauer, M., Haberkorn, R., Springborg, M., and Beck, H. P. (2012). Synthesis and Characterization of Vanadium-Doped LiMnPO4-Compounds: LiMn(PO4)x(VO4)1–x (0.8 ≤ x ≤ 1.0). *Chemistry of Materials, 24*(24): 4717-4724.

66. Conway, B. E. (1991). Transition from “Supercapacitor” to “Battery” Behavior in Electrochemical Energy Storage. *Journal of The Electrochemical Society, 138*(6): 1539-1548.

67. Conway, B. E., Birss, V., and Wojtowicz, J. (1997). The role and utilization of pseudocapacitance for energy storage by supercapacitors. *Journal of Power Sources, 66*(1): 1-14.

68. Cui, Q., Zhong, Y., Pan, L., Zhang, H., Yang, Y., Liu, D., Teng, F., Bando, Y., Yao, J., and Wang, X. (2018). Recent Advances in Designing High-Capacity Anode Nanomaterials for Li-Ion Batteries and Their Atomic-Scale Storage Mechanism Studies. *Advanced Science, 5*(7): 1700902.

69. Dehghani-Sanij, A. R., Tharumalingam, E., Dusseault, M. B., and Fraser, R. (2019). Study of energy storage systems and environmental challenges of batteries. *Renewable and Sustainable Energy Reviews, 104*: 192-208.

70. Deng, B., Lei, T., Zhu, W., Xiao, L., and Liu, J. (2018). In-Plane Assembled Orthorhombic Nb2O5 Nanorod Films with High-Rate Li+ Intercalation for High-Performance Flexible Li-Ion Capacitors. *Advanced Functional Materials, 28*(1): 1704330.

71. Deng, C., Wang, Z., Wang, S., and Yu, J. (2019). Inhibition of polysulfide diffusion in lithium–sulfur batteries: mechanism and improvement strategies. *Journal of Materials Chemistry A, 7*(20): 12381-12413.

72. Deng, D. (2015). Li-ion batteries: basics, progress, and challenges. *Energy Science & Engineering, 3*(5): 385-418.

73. Deng, N., Kang, W., Liu, Y., Ju, J., Wu, D., Li, L., Hassan, B. S., and Cheng, B. (2016). A review on separators for lithiumsulfur battery: Progress and prospects. *Journal of Power Sources, 331*: 132-155.

74. Deng, Z., Zhang, Z., Lai, Y., Liu, J., Li, J., and Liu, Y. (2013). Electrochemical Impedance Spectroscopy Study of a Lithium/Sulfur Battery: Modeling and Analysis of Capacity Fading. *Journal of The Electrochemical Society, 160*(4): A553-A558.

75. Desilvestro, J., and Haas, O. (1990). Metal Oxide Cathode Materials for Electrochemical Energy Storage: A Review. *Journal of The Electrochemical Society, 137*(1): 5C-22C.

76. Díez, N., Ferrero, G. A., Sevilla, M., and Fuertes, A. B. (2019). A simple and general approach for in situ synthesis of sulfur–porous carbon composites for lithium–sulfur batteries. *Sustainable Energy & Fuels, 3*(12): 3498-3509.

77. Dong, C., Gao, W., Jin, B., and Jiang, Q. (2018). Advances in Cathode Materials for High-Performance Lithium-Sulfur Batteries. *iScience, 6*: 151-198.

78. Dsoke, S., Fuchs, B., Gucciardi, E., and Wohlfahrt-Mehrens, M. (2015). The importance of the electrode mass ratio in a Li-ion capacitor based on activated carbon and Li4Ti5O12. *Journal of Power Sources, 282*: 385-393.

79. Du, D., Lan, R., Xu, W., Beanland, R., Wang, H., and Tao, S. (2016). Preparation of a hybrid Cu2O/CuMoO4 nanosheet electrode for high-performance asymmetric supercapacitors. *Journal of Materials Chemistry A, 4*(45): 17749-17756.

80. Du, H., Yang, H., Huang, C., He, J., Liu, H., and Li, Y. (2016). Graphdiyne applied for lithium-ion capacitors displaying high power and energy densities. *Nano Energy, 22*: 615-622.

81. Du Pasquier, A., Plitz, I., Menocal, S., and Amatucci, G. (2003). A comparative study of Li-ion battery, supercapacitor and nonaqueous asymmetric hybrid devices for automotive applications. *Journal of Power Sources, 115*(1): 171-178.

82. Dubal, D. P., Jayaramulu, K., Zboril, R., Fischer, R. A., and Gomez-Romero, P. (2018). Unveiling BiVO4 nanorods as a novel anode material for high performance lithium ion capacitors: beyond intercalation strategies. *Journal of Materials Chemistry A, 6*(14): 6096-6106.

83. Dupin, J.-C., Gonbeau, D., Vinatier, P., and Levasseur, A. (2000). Systematic XPS studies of metal oxides, hydroxides and peroxides. *Physical Chemistry Chemical Physics, 2*(6): 1319-1324.

84. Eftekhari, A., and Kim, D.-W. (2017). Cathode materials for lithium–sulfur batteries: a practical perspective. *Journal of Materials Chemistry A, 5*(34): 17734-17776.

85. El Kharbachi, A., Zavorotynska, O., Latroche, M., Cuevas, F., Yartys, V., and Fichtner, M. (2020). Exploits, advances and challenges benefiting beyond Li-ion battery technologies. *Journal of Alloys and Compounds, 817*: 153261.

86. Elgrishi, N., Rountree, K. J., McCarthy, B. D., Rountree, E. S., Eisenhart, T. T., and Dempsey, J. L. (2018). A Practical Beginner's Guide to Cyclic Voltammetry. *Journal of Chemical Education, 95*(2): 197-206.

87. Eskandari, M., Malekfar, R., Buceta, D., and Taboada, P. (2020). NiCo2O4-based nanostructured composites for high-performance pseudocapacitor electrodes. *Colloids and Surfaces A: Physicochemical and Engineering Aspects, 584*: 124039.

88. Evans, J., Vincent, C. A., and Bruce, P. G. (1987). Electrochemical measurement of transference numbers in polymer electrolytes. *Polymer, 28*(13): 2324-2328.

89. Fan, C.-Y., Yuan, H.-Y., Li, H.-H., Wang, H.-F., Li, W.-L., Sun, H.-Z., Wu, X.-L., and Zhang, J.-P. (2016). The Effective Design of a Polysulfide-Trapped Separator at the Molecular Level for High Energy Density Li–S Batteries. *ACS Applied Materials & Interfaces, 8*(25): 16108-16115.

90. Fan, W., Zhang, L., and Liu, T. (2018). Multifunctional second barrier layers for lithium–sulfur batteries. *Materials Chemistry Frontiers, 2*(2): 235-252.

91. Fan, Y., Liu, D., Rahman, M. M., Tao, T., Lei, W., Mateti, S., Yu, B., Wang, J., Yang, C., and Chen, Y. (2019). Repelling Polysulfide Ions by Boron Nitride

Nanosheet Coated Separators in Lithium–Sulfur Batteries. *ACS Applied Energy Materials, 2*(4): 2620-2628.

92. Fang, R., Zhao, S., Sun, Z., Wang, D.-W., Cheng, H.-M., and Li, F. (2017). More Reliable Lithium-Sulfur Batteries: Status, Solutions and Prospects. *Advanced Materials, 29*(48): 1606823.

93. Feng, X., Wang, Q., Li, R., and Li, H. (2019). CoFe2O4 coated carbon fiber paper fabricated via a spray pyrolysis method for trapping lithium polysulfide in Li-S batteries. *Applied Surface Science, 478*: 341-346.

94. Fey, G. T.-K., and Chen, K.-S. (1999). Synthesis, characterization, and cell performance of LiNiVO4 cathode materials prepared by a new solution precipitation method. *Journal of Power Sources, 81-82*: 467-471.

95. Fotouhi, A., Auger, D., O'Neill, L., Cleaver, T., and Walus, S. (2017). Lithium-Sulfur Battery Technology Readiness and Applications—A Review. *Energies, 10*: 1937.

96. Frackowiak, E., and Béguin, F. (2001). Carbon materials for the electrochemical storage of energy in capacitors. *Carbon, 39*(6): 937-950.

97. Freitag, A., Stamm, M., and Ionov, L. (2017). Separator for lithium-sulfur battery based on polymer blend membrane. *Journal of Power Sources, 363*: 384-391.

98. Fu, L., Qu, Q., Holze, R., Kondratiev, V. V., and Wu, Y. (2019). Composites of metal oxides and intrinsically conducting polymers as supercapacitor electrode materials: the best of both worlds? *Journal of Materials Chemistry A, 7*(25): 14937-14970.

99. Fu, Y., and Manthiram, A. (2012). Enhanced Cyclability of Lithium–Sulfur Batteries by a Polymer Acid-Doped Polypyrrole Mixed Ionic–Electronic Conductor. *Chemistry of Materials, 24*(15): 3081-3087.

100. Ghosh, S., and Basu, R. N. (2018). Multifunctional nanostructured electrocatalysts for energy conversion and storage: current status and perspectives. *Nanoscale, 10*(24): 11241-11280.

101. Ghosh, S., Maiyalagan, T., and Basu, R. N. (2016). Nanostructured conducting polymers for energy applications: towards a sustainable platform. *Nanoscale, 8*(13): 6921-6947.

102. Gielen, D., Boshell, F., Saygin, D., Bazilian, M. D., Wagner, N., and Gorini, R. (2019). The role of renewable energy in the global energy transformation. *Energy Strategy Reviews, 24*: 38-50.

103. Goodenough, J. B. (2014). Electrochemical energy storage in a sustainable modern society. *Energy & Environmental Science, 7*(1): 14-18.

104. Goodenough, J. B., and Park, K.-S. (2013). The Li-Ion Rechargeable Battery: A Perspective. *Journal of the American Chemical Society, 135*(4): 1167-1176.

105. Gopalakrishnan, R., Goutam, S., Miguel Oliveira, L., Timmermans, J.-M., Omar, N., Messagie, M., Van den Bossche, P., and van Mierlo, J. (2017). A Comprehensive Study on Rechargeable Energy Storage Technologies. *Journal of Electrochemical Energy Conversion and Storage, 13*(4).

106. Gu, M., Lee, J., Kim, Y., Kim, J. S., Jang, B. Y., Lee, K. T., and Kim, B.-S. (2014). Inhibiting the shuttle effect in lithium–sulfur batteries using a layer-by-layer assembled ion-permselective separator. *RSC Advances, 4*(87): 46940-46946.

107. Gu, W., and Yushin, G. (2014). Review of nanostructured carbon materials for electrochemical capacitor applications: advantages and limitations of activated carbon, carbide-derived carbon, zeolite-templated carbon, carbon aerogels, carbon nanotubes, onion-like carbon, and graphene. *WIREs Energy and Environment, 3*(5): 424-473.

108. Guan, Y., Liu, X., Akhtar, N., Wang, A., Wang, W., Zhang, H., Suntivich, J., and Huang, Y. (2019a). Cr_2O_3 Nanoparticle Decorated Carbon Nanofibers Derived from Solid Leather Wastes for High Performance Lithium-Sulfur Battery Separator Coating. *Journal of The Electrochemical Society, 166*(8): A1671-A1676.

109. Guan, B., Zhang, Y., Fan, L., Wu, X., Wang, M., Qiu, Y., Zhang, N., and Sun, K. (2019b). Blocking Polysulfide with Co_2B@CNT via "Synergetic Adsorptive Effect" toward Ultrahigh-Rate Capability and Robust Lithium–Sulfur Battery. *ACS Nano, 13*(6): 6742-6750.

110. Guo, Y., Sun, M., Liang, H., Ying, W., Zeng, X., Ying, Y., Zhou, S., Liang, C., Lin, Z., and Peng, X. (2018). Blocking Polysulfides and Facilitating Lithium-Ion Transport: Polystyrene Sulfonate@HKUST-1 Membrane for Lithium–Sulfur Batteries. *ACS Applied Materials & Interfaces, 10*(36): 30451-30459.

111. Gupta, A., Bhargav, A., and Manthiram, A. (2019). Highly Solvating Electrolytes for Lithium–Sulfur Batteries. *Advanced Energy Materials, 9*(6): 1803096.

112. Gupta, R., Candler, J., Palchoudhury, S., Ramasamy, K., and Gupta, B. (2015). Flexible and High Performance Supercapacitors Based on NiCo2O4 for Wide Temperature Range Applications. *Scientific Reports, 5*.

113. Gür, T. M. (2018). Review of electrical energy storage technologies, materials and systems: challenges and prospects for large-scale grid storage. *Energy & Environmental Science, 11*(10): 2696-2767.

114. Haetge, J., Hartmann, P., Brezesinski, K., Janek, J., and Brezesinski, T. (2011). Ordered Large-Pore Mesoporous Li4Ti5O12 Spinel Thin Film Electrodes with Nanocrystalline Framework for High Rate Rechargeable Lithium Batteries: Relationships among Charge Storage, Electrical Conductivity, and Nanoscale Structure. *Chemistry of Materials, 23*(19): 4384-4393.

115. Han, C., Li, H., Shi, R., Xu, L., Li, J., Kang, F., and Li, B. (2018a). Nanostructured Anode Materials for Non-aqueous Lithium Ion Hybrid Capacitors. *Energy & Environmental Materials, 1*(2): 75-87.

116. Han, J., Hirata, A., Du, J., Ito, Y., Fujita, T., Kohara, S., Ina, T., and Chen, M. (2018b). Intercalation pseudocapacitance of amorphous titanium dioxide@nanoporous graphene for high-rate and large-capacity energy storage. *Nano Energy, 49*: 354-362.

117. Han, P., Ma, W., Pang, S., Kong, Q., Yao, J., Bi, C., and Cui, G. (2013). Graphene decorated with molybdenum dioxide nanoparticles for use in high energy lithium ion capacitors with an organic electrolyte. *Journal of Materials Chemistry A, 1*(19): 5949-5954.

118. Han, P., and Manthiram, A. (2017). Boron- and nitrogen-doped reduced graphene oxide coated separators for high-performance Li-S batteries. *Journal of Power Sources, 369*: 87-94.

119. Han, X., Han, P., Yao, J., Zhang, S., Cao, X., Xiong, J., Zhang, J., and Cui, G. (2016). Nitrogen-doped carbonized polyimide microsphere as a novel anode material for high performance lithium ion capacitors. *Electrochimica Acta, 196*: 603-610.

120. Hannan, M. A., Hoque, M. M., Mohamed, A., and Ayob, A. (2017). Review of energy storage systems for electric vehicle applications: Issues and challenges. *Renewable and Sustainable Energy Reviews, 69*: 771-789.

121. Hao, Z., Yuan, L., Li, Z., Liu, J., Xiang, J., Wu, C., Zeng, R., and Huang, Y. (2016). High performance lithium-sulfur batteries with a facile and effective dual functional separator. *Electrochimica Acta, 200*: 197-203.

122. He, J., Li, X., Lu, T., Shen, X., Wang, N., and Huang, C. (2019). Graphdiyne applied for electrochemical energy storage. *Dalton Transactions, 48*(39): 14566-14574.

123. He, N., Zhong, L., Xiao, M., Wang, S., Han, D., and Meng, Y. (2016). Foldable and High Sulfur Loading 3D Carbon Electrode for High-performance Li-S Battery Application. *Scientific Reports, 6*(1): 33871.

124. He, P., Yu, H., Li, D., and Zhou, H. (2012). Layered lithium transition metal oxide cathodes towards high energy lithium-ion batteries. *Journal of Materials Chemistry, 22*(9): 3680-3695.

125.He, Y., Chang, Z., Wu, S., and Zhou, H. (2018b). Effective strategies for long-cycle life lithium–sulfur batteries. *Journal of Materials Chemistry A, 6*(15): 6155-6182.

126.He, Y., Qiao, Y., and Zhou, H. (2018a). Recent advances in functional modification of separators in lithium–sulfur batteries. *Dalton Transactions, 47*(20): 6881-6887.

127.He, Y., Wu, S., Li, Q., and Zhou, H. (2019). Designing a Multifunctional Separator for High-Performance Li–S Batteries at Elevated Temperature. *Small, 15*(47): 1904332.

128.Zhang, L. (Ed.), Wilkinson, D. (Ed.), Chen, Z. (Ed.), Zhang, J. (Ed.). (2018b). Lithium-Ion Supercapacitors. Boca Raton: CRC Press.

129.Hencz, L., Chen, H., Ling, H. Y., Wang, Y., Lai, C., Zhao, H., and Zhang, S. (2019). Housing Sulfur in Polymer Composite Frameworks for Li–S Batteries. *Nano-micro letters, 11*(1): 17.

130.Holder, C. F., and Schaak, R. E. (2019). Tutorial on Powder X-ray Diffraction for Characterizing Nanoscale Materials. *ACS Nano, 13*(7): 7359-7365.

131.Hou, R., Gund, G. S., Qi, K., Nakhanivej, P., Liu, H., Li, F., Xia, B. Y., and Park, H. S. (2019). Hybridization design of materials and devices for flexible electrochemical energy storage. *Energy Storage Materials, 19*: 212-241.

132.Hu, C., Chen, H., Shen, Y., Lu, D., Zhao, Y., Lu, A.-H., Wu, X., Lu, W., and Chen, L. (2017). In situ wrapping of the cathode material in lithium-sulfur batteries. *Nature Communications, 8*(1): 479.

133.Hu, G., Sun, Z., Shi, C., Fang, R., Chen, J., Hou, P., Liu, C., Cheng, H.-M., and Li, F. (2017). A Sulfur-Rich Copolymer@CNT Hybrid Cathode with Dual-Confinement of Polysulfides for High-Performance Lithium–Sulfur Batteries. *Advanced Materials, 29*(11): 1603835.

134.Huang, H., and Niederberger, M. (2019). Towards fast-charging technologies in Li+/Na+ storage: from the perspectives of pseudocapacitive materials and non-aqueous hybrid capacitors. *Nanoscale, 11*(41): 19225-19240.

135.Huang, J.-K., Li, M., Wan, Y., Dey, S., Ostwal, M., Zhang, D., Yang, C.-W., Su, C.-J., Jeng, U. S., Ming, J., Amassian, A., Lai, Z., Han, Y., Li, S., and Li, L.-J. (2018). Functional Two-Dimensional Coordination Polymeric Layer as a Charge Barrier in Li–S Batteries. *ACS Nano, 12*(1): 836-843.

136.Huang, J.-Q., Zhang, Q., Peng, H.-J., Liu, X.-Y., Qian, W.-Z., and Wei, F. (2014). Ionic shield for polysulfides towards highly-stable lithium–sulfur batteries. *Energy & Environmental Science, 7*(1): 347-353.

137.Huang, Y., Li, X., Ding, R., Ying, D., Yan, T., Huang, Y., Tan, C., Sun, X., Gao, P., and Liu, E. (2020). Tetragonal MF2 (M=Ni, Co) micro/nanocrystals anodes for lithium/sodium-ion capacitors. *Electrochimica Acta, 329*: 135138.

138.Huggins, R. A. (2016). Introduction to Electrochemical Energy Storage *Energy Storage: Fundamentals, Materials and Applications* (pp. 119-144). Cham: Springer International Publishing.

139.Ivanovskii, A. L. (2013). Graphynes and graphdyines. *Progress in Solid State Chemistry, 41*(1): 1-19.

140.Jagadale, A., Zhou, X., Blaisdell, D., and Yang, S. (2018). Carbon nanofibers (CNFs) supported cobalt- nickel sulfide (CoNi2S4) nanoparticles hybrid anode for high performance lithium ion capacitor. *Scientific Reports, 8*.

141.Jagadale, A., Zhou, X., Xiong, R., Dubal, D. P., Xu, J., and Yang, S. (2019). Lithium ion capacitors (LICs): Development of the materials. *Energy Storage Materials, 19*: 314-329.

142.Jeong, T.-G., Moon, Y. H., Chun, H.-H., Kim, H. S., Cho, B. W., and Kim, Y.-T. (2013). Free standing acetylene black mesh to capture dissolved polysulfide in lithium sulfur batteries. *Chemical Communications, 49*(94): 11107-11109.

143.Jeong, Y. C., Kim, J. H., Nam, S., Park, C. R., and Yang, S. J. (2018). Rational Design of Nanostructured Functional Interlayer/Separator for Advanced Li–S Batteries. *Advanced Functional Materials, 28*(38): 1707411.

144.Jeżowski, P., Fic, K., Crosnier, O., Brousse, T., and Béguin, F. (2016). Lithium rhenium(vii) oxide as a novel material for graphite pre-lithiation in high performance lithium-ion capacitors. *Journal of Materials Chemistry A, 4*(32): 12609-12615.

145.Jiang, K., Gao, S., Wang, R., Jiang, M., Han, J., Gu, T., Liu, M., Cheng, S., and Wang, K. (2018). Lithium Sulfonate/Carboxylate-Anchored Polyvinyl Alcohol Separators for Lithium Sulfur Batteries. *ACS Applied Materials & Interfaces, 10*(21): 18310-18315.

146.Jiang, Y., and Liu, J. (2019). Definitions of Pseudocapacitive Materials: A Brief Review. *ENERGY & ENVIRONMENTAL MATERIALS, 2*(1): 30-37.

147.Jin, Z., Xie, K., and Hong, X. (2013). Electrochemical performance of lithium/sulfur batteries using perfluorinated ionomer electrolyte with lithium sulfonyl dicyanomethide functional groups as functional separator. *RSC Advances, 3*(23): 8889-8898.

148.Jin, Z., Xie, K., Hong, X., Hu, Z., and Liu, X. (2012). Application of lithiated Nafion ionomer film as functional separator for lithium sulfur cells. *Journal of Power Sources, 218*: 163-167.

149. Joshi, A. C., Rufus, A. L., and Velmurugan, S. (2018). Poly(acrylic acid-co-maleic acid), a polymer dispersant for the control of oxide deposition over nuclear steam generator surfaces. *Journal of Nuclear Materials, 498*: 421-429.

150. Kaisar, N., Abbas, S. A., Ding, J., Chen, H.-A., Pao, C.-W., Boopathi, K. M., Mohapatra, A., Chen, Y.-T., Wu, S. H., Fang, J., Jou, S., and Chu, C. W. (2019). A lithium passivated MoO3 nanobelt decorated polypropylene separator for fast-charging long-life Li–S batteries. *Nanoscale, 11*(6): 2892-2900.

151. Kaliyappan, K., Amaresh, S., and Lee, Y.-S. (2014). LiMnBO3 Nanobeads As an Innovative Anode Material for High Power Lithium Ion Capacitor Applications. *ACS Applied Materials & Interfaces, 6*(14): 11357-11367.

152. Kaliyappan, K., Samuthira Pandian, A., Son, J. N., and Lee, Y. s. (2012). Synthesis and Performance of Li2MnSiO4 as an Electrode Material for Hybrid Supercapacitor Applications. *Journal of Electrochemical Science and Technology, 3*.

153. Kamat, P. V. (2019). Lithium-Ion Batteries and Beyond: Celebrating the 2019 Nobel Prize in Chemistry – A Virtual Issue. *ACS Energy Letters, 4*(11): 2757-2759.

154. Kanamura, K., Tamura, H., Shiraishi, S., and Takehara, Z. i. (1995). XPS Analysis of Lithium Surfaces Following Immersion in Various Solvents Containing LiBF4. *Journal of The Electrochemical Society, 142*(2): 340-347.

155. Kang, W., Deng, N., Ju, J., Li, Q., Wu, D., Ma, X., Li, L., Naebe, M., and Cheng, B. (2016). A review of recent developments in rechargeable lithium–sulfur batteries. *Nanoscale, 8*(37): 16541-16588.

156. Karthikeyan, K., Amaresh, S., Aravindan, V., Kim, H., Kang, K. S., and Lee, Y. S. (2013). Unveiling organic–inorganic hybrids as a cathode material for high performance lithium-ion capacitors. *Journal of Materials Chemistry A, 1*(3): 707-714.

157. Karuppasamy, K., Kim, H.-S., Kim, D., Vikraman, D., Prasanna, K., Kathalingam, A., Sharma, R., and Rhee, H. W. (2017). An enhanced electrochemical and cycling properties of novel boronic Ionic liquid based ternary gel polymer electrolytes for rechargeable Li/LiCoO2 cells. *Scientific Reports, 7*(1): 11103.

158. Kasinathan, R., Marinaro, M., Axmann, P., and Wohlfahrt-Mehrens, M. (2018). Influence of the Molecular Weight of Poly-Acrylic Acid Binder on Performance of Si-Alloy/Graphite Composite Anodes for Lithium-Ion Batteries. *Energy technology (Weinheim, Germany), 6*(11): 2256-2263.

159. Khaligh, A., and li, Z. (2010). Battery, Ultracapacitor, Fuel Cell, and Hybrid Energy Storage Systems for Electric, Hybrid Electric, Fuel Cell, and Plug-In

Hybrid Electric Vehicles: State of the Art. *Vehicular Technology, IEEE Transactions on, 59*: 2806-2814.

160. Khomenko, V., Raymundo-Piñero, E., and Béguin, F. (2008). High-energy density graphite/AC capacitor in organic electrolyte. *Journal of Power Sources, 177*(2): 643-651.

161. Kim, D.-W., Yoo, J.-B., and Kim, Y.-J. (2019). Electrode Design for Improving Fast Charging Performance without Loss of Energy Density in Lithium Ion Batteries. *Meeting Abstracts, MA2019-01*(4): 491.

162. Kim, J. H., Seo, J., Choi, J., Shin, D., Carter, M., Jeon, Y., Wang, C., Hu, L., and Paik, U. (2016a). Synergistic Ultrathin Functional Polymer-Coated Carbon Nanotube Interlayer for High Performance Lithium–Sulfur Batteries. *ACS Applied Materials & Interfaces, 8*(31): 20092-20099.

163. Kim, K. M., Hepowit, L. R., Kim, J.-C., Lee, Y.-G., and Ko, J. M. (2015). Enhanced separator properties by coating alumina nanoparticles with poly(2-acrylamido-2-methyl-1-propanesulfonic acid) binder for lithium-ion batteries. *Korean Journal of Chemical Engineering, 32*(4): 717-722.

164. Kim, M. S., Ma, L., Choudhury, S., and Archer, L. A. (2016b). Multifunctional Separator Coatings for High-Performance Lithium–Sulfur Batteries. *Advanced Materials Interfaces, 3*(22): 1600450.

165. Knoop, J. E., and Ahn, S. (2020). Recent advances in nanomaterials for high-performance Li–S batteries. *Journal of Energy Chemistry, 47*: 86-106.

166. Kong, L., Peng, H.-J., Huang, J.-Q., Zhu, W., Zhang, G., Zhang, Z.-W., Zhai, P.-Y., Sun, P., Xie, J., and Zhang, Q. (2017). Beaver-dam-like membrane: A robust and sulphifilic MgBO2(OH)/CNT/PP nest separator in Li-S batteries. *Energy Storage Materials, 8*: 153-160.

167. Lacey, M. J., Yalamanchili, A., Maibach, J., Tengstedt, C., Edström, K., and Brandell, D. (2016). The Li–S battery: an investigation of redox shuttle and self-discharge behaviour with LiNO3-containing electrolytes. *RSC Advances, 6*(5): 3632-3641.

168. Laheäär, A., Kurig, H., Jänes, A., and Lust, E. (2009). LiPF6 based ethylene carbonate–dimethyl carbonate electrolyte for high power density electrical double layer capacitor. *Electrochimica Acta, 54*(19): 4587-4594.

169. Lai, F., Zhang, X., Wang, H., Hu, S., Wu, X., Wu, Q., Huang, Y., He, Z., and Li, Q. (2016). Three-Dimension Hierarchical Al2O3 Nanosheets Wrapped LiMn2O4 with Enhanced Cycling Stability as Cathode Material for Lithium Ion Batteries. *ACS Applied Materials & Interfaces, 8*(33): 21656-21665.

170. Lai, Y., Wang, P., Qin, F., Xu, M., Li, J., Zhang, K., and Zhang, Z. (2017). A carbon nanofiber@mesoporous δ-MnO2 nanosheet-coated separator for high-performance lithium-sulfur batteries. *Energy Storage Materials, 9*: 179-187.

171. Landi, B. J., Ganter, M. J., Cress, C. D., DiLeo, R. A., and Raffaelle, R. P. (2009). Carbon nanotubes for lithium ion batteries. *Energy & Environmental Science, 2*(6): 638-654.

172. Lang, X., Leow, W. R., Zhao, J., and Chen, X. (2015). Synergistic photocatalytic aerobic oxidation of sulfides and amines on TiO2 under visible-light irradiation. *Chemical Science, 6*(2): 1075-1082.

173. Lee, J., and Choi, W. (2015). Surface Modification of Sulfur Cathodes with PEDOT:PSS Conducting Polymer in Lithium-Sulfur Batteries. *Journal of The Electrochemical Society, 162*(6): A935-A939.

174. Lee, J. H., Kang, J., Kim, S.-W., Halim, W., Frey, M. W., and Joo, Y. L. (2018b). Effective Suppression of the Polysulfide Shuttle Effect in Lithium–Sulfur Batteries by Implementing rGO–PEDOT:PSS-Coated Separators via Air-Controlled Electrospray. *ACS Omega, 3*(12): 16465-16471.

175. Lee, W. S. V., Huang, X., Tan, T. L., and Xue, J. M. (2018a). Low Li+ Insertion Barrier Carbon for High Energy Efficient Lithium-Ion Capacitor. *ACS Applied Materials & Interfaces, 10*(2): 1690-1700.

176. Lee, W. S. V., Peng, E., Li, M., Huang, X., and Xue, J. M. (2016). Rational design of stable 4V lithium ion capacitor. *Nano Energy, 27*: 202-212.

177. Lee, Y.-S., and Ryu, K.-S. (2017). Study of the lithium diffusion properties and high rate performance of TiNb(6)O(17) as an anode in lithium secondary battery. *Scientific Reports, 7*(1): 16617-16617.

178. Lei, T., Chen, W., Lv, W., Huang, J., Zhu, J., Chu, J., Yan, C., Wu, C., Yan, Y., He, W., Xiong, J., Li, Y., Yan, C., Goodenough, J. B., and Duan, X. (2018). Inhibiting Polysulfide Shuttling with a Graphene Composite Separator for Highly Robust Lithium-Sulfur Batteries. *Joule, 2*(10): 2091-2104.

179. Lei, Y., Huang, Z.-H., Yang, Y., Shen, W., Zheng, Y., Sun, H., and Kang, F. (2013). Porous mesocarbon microbeads with graphitic shells: constructing a high-rate, high-capacity cathode for hybrid supercapacitor. *Scientific Reports, 3*(1): 2477.

180. Li, B., Dai, F., Xiao, Q., Yang, L., Shen, J., Zhang, C., and Cai, M. (2016). Activated Carbon from Biomass Transfer for High-Energy Density Lithium-Ion Supercapacitors. *Advanced Energy Materials, 6*(18): 1600802.

181. Li, B., Xiao, Z., Chen, M., Huang, Z., Tie, X., Zai, J., and Qian, X. (2017e). Rice husk-derived hybrid lithium-ion capacitors with ultra-high energy. *Journal of Materials Chemistry A, 5*(46): 24502-24507.

182. Li, B., Zheng, J., Zhang, H., Jin, L., Yang, D., Lv, H., Shen, C., Shellikeri, A., Zheng, Y., Gong, R., Zheng, J. P., and Zhang, C. (2018c). Electrode Materials, Electrolytes, and Challenges in Nonaqueous Lithium-Ion Capacitors. *Advanced Materials, 30*(17): 1705670.

183. Li, C., Ward, A. L., Doris, S. E., Pascal, T. A., Prendergast, D., and Helms, B. A. (2015b). Polysulfide-Blocking Microporous Polymer Membrane Tailored for Hybrid Li-Sulfur Flow Batteries. *Nano Letters, 15*(9): 5724-5729.

184. Li, M., Wan, Y., Huang, J.-K., Assen, A. H., Hsiung, C.-E., Jiang, H., Han, Y., Eddaoudi, M., Lai, Z., Ming, J., and Li, L.-J. (2017c). Metal–Organic Framework-Based Separators for Enhancing Li–S Battery Stability: Mechanism of Mitigating Polysulfide Diffusion. *ACS Energy Letters, 2*(10): 2362-2367.

185. Li, F., Wang, G., Wang, P., Yang, J., Zhang, K., Liu, Y., and Lai, Y. (2017b). High-performance lithium-sulfur batteries with a carbonized bacterial cellulose/TiO2 modified separator. *Journal of Electroanalytical Chemistry, 788*.

186. Li, G., Chen, Z., and Lu, J. (2018e). Lithium-Sulfur Batteries for Commercial Applications. *Chem, 4*(1): 3-7.

187. Li, G., Wang, S., Zhang, Y., Li, M., Chen, Z., and Lu, J. (2018a). Revisiting the Role of Polysulfides in Lithium–Sulfur Batteries. *Advanced Materials, 30*(22): 1705590.

188. Li, G., Yang, Z., Yin, Z., Guo, H., Wang, Z., Yan, G., Liu, Y., Li, L., and Wang, J. (2019f). Non-aqueous dual-carbon lithium-ion capacitors: a review. *Journal of Materials Chemistry A, 7*(26): 15541-15563.

189. Li, G. C., Jing, H. K., Su, Z., Lai, C., Chen, L., Yuan, C. C., Li, H. H., and Liu, L. (2015a). A hydrophilic separator for high performance lithium sulfur batteries. *Journal of Materials Chemistry A, 3*(20): 11014-11020.

190. Li, H., Sun, L., Zhao, Y., Tan, T., and Zhang, Y. (2019e). A novel CuS/graphene-coated separator for suppressing the shuttle effect of lithium/sulfur batteries. *Applied Surface Science, 466*: 309-319.

191. Li, J., Huang, Y., Zhang, S., Jia, W., Wang, X., Guo, Y., Jia, D., and Wang, L. (2017a). Decoration of Silica Nanoparticles on Polypropylene Separator for Lithium–Sulfur Batteries. *ACS Applied Materials & Interfaces, 9*(8): 7499-7504.

192. Li, J., Luo, F., Zhao, Q., Li, Z., Yuan, H., and Xiao, D. (2014c). Coprecipitation fabrication and electrochemical performances of coral-like mesoporous NiO nanobars. *Journal of Materials Chemistry A, 2*(13): 4690-4697.

193. Li, M., Wan, Y., Huang, J.-K., Assen, A. H., Hsiung, C.-E., Jiang, H., Han, Y., Eddaoudi, M., Lai, Z., Ming, J., and Li, L.-J. (2017). Metal–Organic Framework-Based Separators for Enhancing Li–S Battery Stability: Mechanism of Mitigating Polysulfide Diffusion. *ACS Energy Letters, 2*(10): 2362-2367.

194. Li, M., Wang, C., Miao, L., Xiang, J., Wang, T., Yuan, K., Chen, J., and Huang, Y. (2018b). A separator-based lithium polysulfide recirculator for high-loading and high-performance Li–S batteries. *Journal of Materials Chemistry A, 6*(14): 5862-5869.

195. Li, N.-W., Du, X., Shi, J.-L., Zhang, X., Fan, W., Wang, J., Zhao, S., Liu, Y., Xu, W., Li, M., Guo, Y.-G., and Li, C. (2018d). Graphene@hierarchical meso-/microporous carbon for ultrahigh energy density lithium-ion capacitors. *Electrochimica Acta, 281*: 459-465.

196. Li, N., Weng, Z., Wang, Y., Li, F., Cheng, H.-M., and Zhou, H. (2014a). An aqueous dissolved polysulfide cathode for lithium–sulfur batteries. *Energy & Environmental Science, 7*(10): 3307-3312.

197. Li, S., Chen, J., Cui, M., Cai, G., Wang, J., Cui, P., Gong, X., and Lee, P. S. (2017d). A High-Performance Lithium-Ion Capacitor Based on 2D Nanosheet Materials. *Small, 13*(6): 1602893.

198. Li, W., Hicks-Garner, J., Wang, J., Liu, J., Gross, A. F., Sherman, E., Graetz, J., Vajo, J. J., and Liu, P. (2014b). V2O5 Polysulfide Anion Barrier for Long-Lived Li–S Batteries. *Chemistry of Materials, 26*(11): 3403-3410.

199. Li, X., Wei, Y. J., Ehrenberg, H., Liu, D. L., Zhan, S. Y., Wang, C. Z., and Chen, G. (2009). X-ray diffraction and Raman scattering studies of Li+/e−-extracted inverse spinel LiNiVO4. *Journal of Alloys and Compounds, 471*(1): L26-L28.

200. Li, Y., Wang, W., Liu, X., Mao, E., Wang, M., Li, G., Fu, L., Li, Z., Eng, A. Y. S., Seh, Z. W., and Sun, Y. (2019b). Engineering stable electrode-separator interfaces with ultrathin conductive polymer layer for high-energy-density Li-S batteries. *Energy Storage Materials, 23*: 261-268.

201. Li, Z. (2019d). Well-dispersed Amorphous Ta2O5 Chemically Grafted onto Multi-Walled Carbon Nanotubes for High-performance Lithium Sulfur Battery. *International Journal of Electrochemical Science*: 6628-6642.

202. Li, Z., Khajepour, A., and Song, J. (2019a). A comprehensive review of the key technologies for pure electric vehicles. *Energy, 182*: 824-839.

203. Li, Z., Tang, L., Liu, X., Song, T., Xu, Q., Liu, H., and Wang, Y. (2019c). A polar TiO/MWCNT coating on a separator significantly suppress the shuttle effect in a lithium-sulfur battery. *Electrochimica Acta, 310*: 1-12.

204. Liang, T., Wang, H., Xu, D., Liao, K., Wang, R., He, B., Gong, Y., and Yan, C. (2018). High-energy flexible quasi-solid-state lithium-ion capacitors enabled by a freestanding rGO-encapsulated Fe3O4 nanocube anode and a holey rGO film cathode. *Nanoscale, 10*(37): 17814-17823.

205.Liang, X., Rangom, Y., Kwok, C. Y., Pang, Q., and Nazar, L. F. (2017). Interwoven MXene Nanosheet/Carbon-Nanotube Composites as Li–S Cathode Hosts. *Advanced Materials, 29*(3): 1603040.

206.Lin, W., Chen, Y., Li, P., He, J., Zhao, Y., Wang, Z., Liu, J., Qi, F., Zheng, B., Zhou, J., Xu, C., and Fu, F. (2015). Enhanced Performance of Lithium Sulfur Battery with a Reduced Graphene Oxide Coating Separator. *Journal of The Electrochemical Society, 162*(8): A1624-A1629.

207.Lin, X., Salari, M., Arava, L. M. R., Ajayan, P. M., and Grinstaff, M. W. (2016). High temperature electrical energy storage: advances, challenges, and frontiers. *Chemical Society Reviews, 45*(21): 5848-5887.

208.Lin, Z., Goikolea, E., Balducci, A., Naoi, K., Taberna, P. L., Salanne, M., Yushin, G., and Simon, P. (2018). Materials for supercapacitors: When Li-ion battery power is not enough. *Materials Today, 21*(4): 419-436.

209.Liu, C., Neale, Z. G., and Cao, G. (2016a). Understanding electrochemical potentials of cathode materials in rechargeable batteries. *Materials Today, 19*(2): 109-123.

210.Liu, C., Ren, Q.-Q., Zhang, S.-W., Yin, B.-S., Que, L.-F., Zhao, L., Sui, X.-L., Yu, F.-D., Li, X., Gu, D.-M., and Wang, Z.-B. (2019). High energy and power lithium-ion capacitors based on Mn3O4/3D-graphene as anode and activated polyaniline-derived carbon nanorods as cathode. *Chemical Engineering Journal, 370*: 1485-1492.

211.Liu, C., Zhang, C., Song, H., Zhang, C., Liu, Y., Nan, X., and Cao, G. (2016b). Mesocrystal MnO cubes as anode for Li-ion capacitors. *Nano Energy, 22*: 290-300.

212.Liu, J., Wang, J., Xu, C., Jiang, H., Li, C., Zhang, L., Lin, J., and Shen, Z. X. (2018b). Advanced Energy Storage Devices: Basic Principles, Analytical Methods, and Rational Materials Design. *Advanced Science, 5*(1): 1700322.

213.Liu, M.-C., Kong, L.-B., Kang, L., Li, X., Walsh, F. C., Xing, M., Lu, C., Ma, X.-J., and Luo, Y.-C. (2014). Synthesis and characterization of M3V2O8 (M = Ni or Co) based nanostructures: a new family of high performance pseudocapacitive materials. *Journal of Materials Chemistry A, 2*(14): 4919-4926.

214.Liu, M., Qin, X., He, Y.-B., Li, B., and Kang, F. (2017). Recent innovative configurations in high-energy lithium–sulfur batteries. *Journal of Materials Chemistry A, 5*(11): 5222-5234.

215.Liu, S., Zhou, Z., and Liu, D. (2019b). MoS2 coated separator as an efficient barrier for inhibiting shuttle effect of polysulfide. *Ceramics International, 45*(11): 14415-14419.

216.Liu, T., Sun, X., Sun, S., Niu, Q., Liu, H., Song, W., Cao, F., Li, X., Ohsaka, T., and Wu, J. (2019a). A robust and low-cost biomass carbon fiber@SiO2 interlayer for reliable lithium-sulfur batteries. *Electrochimica Acta, 295*: 684-692.

217.Liu, Y., He, P., and Zhou, H. (2018a). Rechargeable Solid-State Li–Air and Li–S Batteries: Materials, Construction, and Challenges. *Advanced Energy Materials, 8*(4): 1701602.

218.Liu, Z., Borodin, A., Li, G., Liu, X., Li, Y., and Endres, F. (2020a). X-ray Photoelectron Spectroscopy Probing of the Interphase between Solid-State Sulfide Electrolytes and a Lithium Anode. *The Journal of Physical Chemistry C, 124*(1): 300-308.

219.Liu, Z., Huang, J., Liu, B., Fang, D., Wang, T., Yang, Q., Dong, L., Hu, G.-H., and Xiong, C. (2020b). Constructing enhanced pseudocapacitive Li+ intercalation via multiple ionically bonded interfaces toward advanced lithium storage. *Energy Storage Materials, 24*: 138-146.

220.Long, L., Wang, S., Xiao, M., and Meng, Y. (2016). Polymer electrolytes for lithium polymer batteries. *Journal of Materials Chemistry A, 4*(26): 10038-10069.

221.Lopes, M. A. R., Antunes, C. H., and Martins, N. (2012). Energy behaviours as promoters of energy efficiency: A 21st century review. *Renewable and Sustainable Energy Reviews, 16*(6): 4095-4104.

222.Lu, C.-H., Lee, W.-C., Liou, S.-J., and Ting-Kuo Fey, G. (1999). Hydrothermal synthesis of LiNiVO4 cathode material for lithium ion batteries. *Journal of Power Sources, 81-82*: 696-699.

223.Lu, Q., Lu, B., Chen, M., Wang, X., Xing, T., Liu, M., and Wang, X. (2018). Porous activated carbon derived from Chinese-chive for high energy hybrid lithium-ion capacitor. *Journal of Power Sources, 398*: 128-136.

224.Lu, W., Yuan, Z., Zhao, Y., Zhang, H., Zhang, H., and Li, X. (2017b). Porous membranes in secondary battery technologies. *Chemical Society Reviews, 46*(8): 2199-2236.

225.Lu, Y., Gu, S., Guo, J., Rui, K., Chen, C., Zhang, S., Jin, J., Yang, J., and Wen, Z. (2017a). Sulfonic Groups Originated Dual-Functional Interlayer for High Performance Lithium–Sulfur Battery. *ACS Applied Materials & Interfaces, 9*(17): 14878-14888.

226.Lubimtsev, A., Kent, P., Sumpter, B., and Ganesh, P. (2013). Understanding the origin of high-rate intercalation pseudocapacitance in Nb2O5 crystals. *Journal of Materials Chemistry A,* 1(47):14951-14956.

227.Lukatskaya, M. R., Dunn, B., and Gogotsi, Y. (2016). Multidimensional materials and device architectures for future hybrid energy storage. *Nature Communications, 7*: 12647-12647.

228.Luo, L., Chung, S.-H., and Manthiram, A. (2016). A trifunctional multi-walled carbon nanotubes/polyethylene glycol (MWCNT/PEG)-coated separator through a layer-by-layer coating strategy for high-energy Li–S batteries. *Journal of Materials Chemistry A, 4*(43): 16805-16811.

229.Luo, X., Lu, X., Zhou, G., Zhao, X., Ouyang, Y., Zhu, X., Miao, Y.-E., and Liu, T. (2018). Ion-Selective Polyamide Acid Nanofiber Separators for High-Rate and Stable Lithium–Sulfur Batteries. *ACS Applied Materials & Interfaces, 10*(49): 42198-42206.

230.Lv, S., Zhang, X., Zhang, P., Xiang, J., Li, Y., Qiu, S., and Qin, C. (2019). One-step fabrication of nanosized LiFePO4/expanded graphite composites with a particle growth inhibitor and enhanced electrochemical performance of aqueous Li-ion capacitors. *RSC Advances, 9*(25): 14407-14416.

231.Ma, G., Huang, F., Wen, Z., Wang, Q., Hong, X., Jin, J., and Wu, X. (2016). Enhanced performance of lithium sulfur batteries with conductive polymer modified separators. *Journal of Materials Chemistry A, 4*(43): 16968-16974.

232.Ma, L., Hendrickson, K. E., Wei, S., and Archer, L. A. (2015). Nanomaterials: Science and applications in the lithium–sulfur battery. *Nano Today, 10*(3): 315-338.

233.Madabattula, G., Wu, B., Marinescu, M., and Offer, G. (2020). How to Design Lithium Ion Capacitors: Modelling, Mass Ratio of Electrodes and Pre-lithiation. *Journal of The Electrochemical Society, 167*(1).

234.Manthiram, A., Fu, Y., Chung, S.-H., Zu, C., and Su, Y.-S. (2014). Rechargeable Lithium–Sulfur Batteries. *Chemical Reviews, 114*(23): 11751-11787.

235.Manthiram, A., Fu, Y., and Su, Y.-S. (2013). Challenges and Prospects of Lithium–Sulfur Batteries. *Accounts of Chemical Research, 46*(5): 1125-1134.

236.Manthiram, A., and Kim, J. (1998). Low Temperature Synthesis of Insertion Oxides for Lithium Batteries. *Chemistry of Materials, 10*(10): 2895-2909.

237.Mei, B.-A., Munteshari, O., Lau, J., Dunn, B., and Pilon, L. (2018). Physical Interpretations of Nyquist Plots for EDLC Electrodes and Devices. *The Journal of Physical Chemistry C, 122*(1): 194-206.

238.Mi, K., Chen, S., Xi, B., Kai, S., Jiang, Y., Feng, J., Qian, Y., and Xiong, S. (2017). Sole Chemical Confinement of Polysulfides on Nonporous Nitrogen/Oxygen Dual-Doped Carbon at the Kilogram Scale for Lithium–Sulfur Batteries. *Advanced Functional Materials, 27*(1): 1604265.

239. Mikhaylik, Y. V., and Akridge, J. R. (2004). Polysulfide Shuttle Study in the Li/S Battery System. *Journal of The Electrochemical Society, 151*(11): A1969-A1976.

240. Mohd Abdah, M. A. A., Azman, N. H. N., Kulandaivalu, S., and Sulaiman, Y. (2020). Review of the use of transition-metal-oxide and conducting polymer-based fibres for high-performance supercapacitors. *Materials & Design, 186*: 108199.

241. Moorthy, B., Kwon, S., Kim, J.-H., Ragupathy, P., Lee, H. M., and Kim, D. K. (2019). Tin sulfide modified separator as an efficient polysulfide trapper for stable cycling performance in Li–S batteries. *Nanoscale Horizons, 4*(1): 214-222.

242. Moy, D., Manivannan, A., and Narayanan, S. R. (2015). Direct Measurement of Polysulfide Shuttle Current: A Window into Understanding the Performance of Lithium-Sulfur Cells. *Journal of The Electrochemical Society, 162*(1): A1-A7.

243. Moy, D., and Narayanan, S. R. (2017). Mixed Conduction Membranes Suppress the Polysulfide Shuttle in Lithium-Sulfur Batteries. *Journal of The Electrochemical Society, 164*(4): A560-A566.

244. Naguib, M., Mochalin, V. N., Barsoum, M. W., and Gogotsi, Y. (2014). 25th Anniversary Article: MXenes: A New Family of Two-Dimensional Materials. *Advanced Materials, 26*(7): 992-1005.

245. Najib, S., and Erdem, E. (2019). Current progress achieved in novel materials for supercapacitor electrodes: mini review. *Nanoscale Advances, 1*(8): 2817-2827.

246. Naoi, K. (2010). ‘Nanohybrid Capacitor’: The Next Generation Electrochemical Capacitors. *Fuel Cells, 10*(5): 825-833.

247. Niu, J., Shao, R., Liu, M., Liang, J., Zhang, Z., Dou, M., Huang, Y., and Wang, F. (2018). Porous carbon electrodes with battery-capacitive storage features for high performance Li-ion capacitors. *Energy Storage Materials, 12*: 145-152.

248. Novoselov, K. S., Fal′ko, V. I., Colombo, L., Gellert, P. R., Schwab, M. G., and Kim, K. (2012). A roadmap for graphene. *Nature, 490*(7419): 192-200.

249. Pal, B., Yang, S., Ramesh, S., Thangadurai, V., and Jose, R. (2019). Electrolyte selection for supercapacitive devices: a critical review. *Nanoscale Advances, 1*(10): 3807-3835.

250. Pan, J., Xu, G., Ding, B., Chang, Z., Wang, A., Dou, H., and Zhang, X. (2016). PAA/PEDOT:PSS as a multifunctional, water-soluble binder to improve the capacity and stability of lithium–sulfur batteries. *RSC Advances, 6*(47): 40650-40655.

251. Pan, Y., Xu, K., and Wu, C. (2019). Recent progress in supercapacitors based on the advanced carbon electrodes *Nanotechnology Reviews* (Vol. 8, pp. 299).

252. Panda, P. K., Grigoriev, A., Mishra, Y. K., and Ahuja, R. (2020). Progress in supercapacitors: roles of two dimensional nanotubular materials. *Nanoscale Advances*.

253. Paques-Ledent, M. T. (1975). Double vanadates LiMgVO4, LiMnVO4, LiCdVO4, NaCdVO4 and NaCaVO4: Structure and vibrational spectrum. *Chemical Physics Letters, 35*: 375-378.

254. Park, K., Cho, J. H., Jang, J.-H., Yu, B.-C., De La Hoz, A. T., Miller, K. M., Ellison, C. J., and Goodenough, J. B. (2015). Trapping lithium polysulfides of a Li–S battery by forming lithium bonds in a polymer matrix. *Energy & Environmental Science, 8*(8): 2389-2395.

255. Park, M.-S., Lim, Y.-G., Kim, J.-H., Kim, Y.-J., Cho, J., and Kim, J.-S. (2011). A Novel Lithium-Doping Approach for an Advanced Lithium Ion Capacitor. *Advanced Energy Materials, 1*(6): 1002-1006.

256. Pazhamalai, P., Krishnamoorthy, K., Sudhakaran, M. S. P., and Kim, S. J. (2017). Fabrication of High-Performance Aqueous Li-Ion Hybrid Capacitor with LiMn2O4 and Graphene. *ChemElectroChem, 4*(2): 396-403.

257. Pei, F., Lin, L., Fu, A., Mo, S., Ou, D., Fang, X., and Zheng, N. (2018). A Two-Dimensional Porous Carbon-Modified Separator for High-Energy-Density Li-S Batteries. *Joule, 2*(2): 323-336.

258. Prakash, D., Masuda, Y., and Chinnappanadar, S. (2012). Structural and electrical studies of LiMnVO4 cathode material for rechargeable lithium batteries. *Ionics, 18*.

259. Prakash, D., Masuda, Y., and Sanjeeviraja, C. (2013a). Structural, electrical and electrochemical studies of LiCoVO4 cathode material for lithium rechargeable batteries. *Powder Technology, 235*: 454-459.

260. Prakash, D., Masuda, Y., and Sanjeeviraja, C. (2013b). Synthesis and structure refinement studies of LiNiVO4 electrode material for lithium rechargeable batteries. *Ionics, 19*(1): 17-23.

261. Puthirath, A. B., Baburaj, A., Kato, K., Salpekar, D., Chakingal, N., Cao, Y., Babu, G., and Ajayan, P. M. (2019). High sulfur content multifunctional conducting polymer composite electrodes for stable Li-S battery. *Electrochimica Acta, 306*: 489-497.

262. Qian, X., Jin, L., Zhao, D., Yang, X., Wang, S., Shen, X., Rao, D., Yao, S., Zhou, Y., and Xi, X. (2016). Ketjen Black-MnO Composite Coated Separator For High Performance Rechargeable Lithium-Sulfur Battery. *Electrochimica Acta, 192*: 346-356.

263. Qiao, J., Hamaya, T., and Okada, T. (2005). Chemically Modified Poly(vinyl alcohol)−Poly(2-acrylamido-2-methyl-1-propanesulfonic acid) as a Novel Proton-Conducting Fuel Cell Membrane. *Chemistry of Materials, 17*(9): 2413-2421.

264. Qu, W.-H., Han, F., Lu, A.-H., Xing, C., Qiao, M., and Li, W.-C. (2014). Combination of a SnO2-C hybrid anode and a tubular mesoporous carbon cathode in a high energy density non-aqueous lithium ion capacitor: Preparation and characterisation. *J. Mater. Chem. A, 2*.

265. Raja, M., and Stephan, A. M. (2014). Natural, biodegradable and flexible egg shell membranes as separators for lithium-ion batteries. *RSC Advances, 4*(102): 58546-58552.

266. Ramya, R., Sivasubramanian, R., and Sangaranarayanan, M. V. (2013). Conducting polymers-based electrochemical supercapacitors—Progress and prospects. *Electrochimica Acta, 101*: 109-129.

267. Rana, M., Li, M., Huang, X., Luo, B., Gentle, I., and Knibbe, R. (2019). Recent advances in separators to mitigate technical challenges associated with re-chargeable lithium sulfur batteries. *Journal of Materials Chemistry A, 7*(12): 6596-6615.

268. Randin, J.-P. (1982). Ion-Containing Polymers as Semisolid Electrolytes in WO[sub 3]-Based Electrochromic Devices. *Journal of The Electrochemical Society, 129*(6): 1215.

269. Rui, X., Zhao, X., Lu, Z., Tan, H., Sim, D., Hng, H. H., Yazami, R., Lim, T. M., and Yan, Q. (2013). Olivine-Type Nanosheets for Lithium Ion Battery Cathodes. *ACS Nano, 7*(6): 5637-5646.

270. Salinas-Torres, D., Ruiz-Rosas, R., Morallón, E., and Cazorla-Amorós, D. (2019). Strategies to Enhance the Performance of Electrochemical Capacitors Based on Carbon Materials. *Frontiers in Materials, 6*(115).

271. Sandford, C., Edwards, M. A., Klunder, K. J., Hickey, D. P., Li, M., Barman, K., Sigman, M. S., White, H. S., and Minteer, S. D. (2019). A synthetic chemist's guide to electroanalytical tools for studying reaction mechanisms. *Chemical Science, 10*(26): 6404-6422.

272. Satish, R., Aravindan, V., Ling, W. C., and Madhavi, S. (2015). Carbon-coated Li3V2(PO4)3 as insertion type electrode for lithium-ion hybrid electrochemical capacitors: An evaluation of anode and cathodic performance. *Journal of Power Sources, 281*: 310-317.

273. Seh, Z. W., Wang, H., Liu, N., Zheng, G., Li, W., Yao, H., and Cui, Y. (2014). High-capacity Li2S–graphene oxide composite cathodes with stable cycling performance. *Chemical Science, 5*(4): 1396-1400.

274. Selva Roselin, L., Juang, R.-S., Hsieh, C.-T., Suresh, S., Umar, A., Selvin, R., and Hegazy, H. (2019). Recent Advances and Perspectives of Carbon-Based Nanostructures as Anode Materials for Li-ion Batteries. *Materials, 12*: 1229.

275. Shao, H., Wang, W., Zhang, H., Wang, A., Chen, X., and Huang, Y. (2018a). Nano-TiO2 decorated carbon coating on the separator to physically and chemically suppress the shuttle effect for lithium-sulfur battery. *Journal of Power Sources, 378*: 537-545.

276. Shao, Y., El-Kady, M. F., Sun, J., Li, Y., Zhang, Q., Zhu, M., Wang, H., Dunn, B., and Kaner, R. B. (2018b). Design and Mechanisms of Asymmetric Supercapacitors. *Chemical Reviews, 118*(18): 9233-9280.

277. Shard, A. G. (2020). Chapter 4.3.1 - X-ray photoelectron spectroscopy. In V.-D. Hodoroaba, W. E. S. Unger & A. G. Shard (Eds.), *Characterization of Nanoparticles* (pp. 349-371): Elsevier.

278. Shellikeri, A., Yturriaga, S., Zheng, J. S., Cao, W., Hagen, M., Read, J. A., Jow, T. R., and Zheng, J. P. (2018). Hybrid lithium-ion capacitor with LiFePO4/AC composite cathode – Long term cycle life study, rate effect and charge sharing analysis. *Journal of Power Sources, 392*: 285-295.

279. Shen, C., Xie, J., Zhang, M., Andrei, P., Hendrickson, M., Plichta, E. J., and Zheng, J. P. (2019). Self-Discharge Behavior of Lithium-Sulfur Batteries at Different Electrolyte/Sulfur Ratios. *Journal of The Electrochemical Society, 166*(3): A5287-A5294.

280. Shen, L., Lv, H., Chen, S., Kopold, P., van Aken, P. A., Wu, X., Maier, J., and Yu, Y. (2017). Peapod-like Li3VO4/N-Doped Carbon Nanowires with Pseudocapacitive Properties as Advanced Materials for High-Energy Lithium-Ion Capacitors. *Advanced Materials, 29*(27): 1700142.

281. Shi, Q. X., Pei, H. J., You, N., Wu, J., Xiang, X., Xia, Q., Xie, X. L., Jin, S. B., and Ye, Y. S. (2019). Large-scaled covalent triazine framework modified separator as efficient inhibit polysulfide shuttling in Li-S batteries. *Chemical Engineering Journal, 375*: 121977.

282. Shi, Y., Wu, C., Li, L., and Yang, J. (2017). A Lithiated Perfluorinated Sulfonic Acid Polymer Electrolyte for Lithium-Oxygen Batteries. *Journal of The Electrochemical Society, 164*(9): A2031-A2037.

283. Shrivastav, V., Sundriyal, S., Goel, P., Kaur, H., Tuteja, S. K., Vikrant, K., Kim, K.-H., Tiwari, U. K., and Deep, A. (2019). Metal-organic frameworks (MOFs) and their composites as electrodes for lithium battery applications: Novel means for alternative energy storage. *Coordination Chemistry Reviews, 393*: 48-78.

284. Simon, P., and Gogotsi, Y. (2008). Materials for electrochemical capacitors. *Nature Materials, 7*(11): 845-854.

285. Singh, A., and Kalra, V. (2019). Electrospun nanostructures for conversion type cathode (S, Se) based lithium and sodium batteries. *Journal of Materials Chemistry A, 7*(19): 11613-11650.

286. Singh, R. K., Kumar, R., and Singh, D. P. (2016). Graphene oxide: strategies for synthesis, reduction and frontier applications. *RSC Advances, 6*(69): 64993-65011.

287. Sivakkumar, S. R., and Pandolfo, A. G. (2012). Evaluation of lithium-ion capacitors assembled with pre-lithiated graphite anode and activated carbon cathode. *Electrochimica Acta, 65*: 280-287.

288. Song, J., Su, D., Xie, X., Guo, X., Bao, W., Shao, G., and Wang, G. (2016b). Immobilizing Polysulfides with MXene-Functionalized Separators for Stable Lithium–Sulfur Batteries. *ACS Applied Materials & Interfaces, 8*(43): 29427-29433.

289. Song, R., Fang, R., Wen, L., Shi, Y., Wang, S., and Li, F. (2016a). A trilayer separator with dual function for high performance lithium–sulfur batteries. *Journal of Power Sources, 301*: 179-186.

290. Song, S., Shi, L., Lu, S., Pang, Y., Wang, Y., Zhu, M., Ding, D., and Ding, S. (2018b). A new polysulfide blocker - poly(acrylic acid) modified separator for improved performance of lithium-sulfur battery. *Journal of Membrane Science, 563*: 277-283.

291. Song, X., Chen, G., Wang, S., Huang, Y., Jiang, Z., Ding, L.-X., and Wang, H. (2018c). Self-Assembled Close-Packed MnO2 Nanoparticles Anchored on a Polyethylene Separator for Lithium–Sulfur Batteries. *ACS Applied Materials & Interfaces, 10*(31): 26274-26282.

292. Song, X., Wang, S., Chen, G., Gao, T., Bao, Y., Ding, L.-X., and Wang, H. (2018a). Fe-N-doped carbon nanofiber and graphene modified separator for lithium-sulfur batteries. *Chemical Engineering Journal, 333*: 564-571.

293. Song, Y., Zhao, S., Chen, Y., Cai, J., Li, J., Yang, Q., Sun, J., and Liu, Z. (2019). Enhanced Sulfur Redox and Polysulfide Regulation via Porous VN-Modified Separator for Li–S Batteries. *ACS Applied Materials & Interfaces, 11*(6): 5687-5694.

294. Sterner, M. (2019). Energy Storage Through the Ages. In M. Sterner & I. Stadler (Eds.), *Handbook of Energy Storage: Demand, Technologies, Integration* (pp. 3-22). Berlin, Heidelberg: Springer Berlin Heidelberg.

295. Su , D. S., and Schlögl, R. (2010). Nanostructured Carbon and Carbon Nanocomposites for Electrochemical Energy Storage Applications. *ChemSusChem, 3*(2): 136-168.

296. Su, Y.-S., and Manthiram, A. (2012). Lithium–sulphur batteries with a microporous carbon paper as a bifunctional interlayer. *Nature Communications, 3*(1): 1166.

297. Sudha, V., and Sangaranarayanan, M. V. (2002). Underpotential Deposition of Metals: Structural and Thermodynamic Considerations. *The Journal of Physical Chemistry B, 106*(10): 2699-2707.

298. Sun, F., Gao, J., Zhu, Y., Pi, X., Wang, L., Liu, X., and Qin, Y. (2017). A high performance lithium ion capacitor achieved by the integration of a Sn-C anode and a biomass-derived microporous activated carbon cathode. *Scientific Reports, 7*: 40990.

299. Sun, H., She, P., Xu, K., Shang, Y., Yin, S., and Liu, Z. (2015b). A self-standing nanocomposite foam of polyaniline@reduced graphene oxide for flexible super-capacitors. *Synthetic Metals, 209*: 68-73.

300. Sun, J., Sun, Y., Pasta, M., Zhou, G., Li, Y., Liu, W., Xiong, F., and Cui, Y. (2016). Entrapment of Polysulfides by a Black-Phosphorus-Modified Separator for Lithium–Sulfur Batteries. *Advanced Materials, 28*(44): 9797-9803.

301. Sun, J., Wu, C., Sun, X., Hu, H., Zhi, C., Hou, L., and Yuan, C. (2017). Recent progresses in high-energy-density all pseudocapacitive-electrode-materials-based asymmetric supercapacitors. *Journal of Materials Chemistry A, 5*(20): 9443-9464.

302. Sun, K., Zhang, S., Li, P., Xia, Y., Zhang, X., Du, D., Isikgor, F. H., and Ouyang, J. (2015c). Review on application of PEDOTs and PEDOT:PSS in energy conversion and storage devices. *Journal of Materials Science: Materials in Electronics, 26*(7): 4438-4462.

303. Sun, W., Sun, X., Peng, Q., Wang, H., Ge, Y., Akhtar, N., Huang, Y., and Wang, K. (2019b). Nano-MgO/AB decorated separator to suppress shuttle effect of lithium–sulfur battery. *Nanoscale Advances, 1*(4): 1589-1597.

304. Sun, X., Li, Q., and Mao, Y. (2015a). Understanding the Influence of Polypyrrole Coating over V2O5 Nanofibers on Electrochemical Properties. *Electrochimica Acta, 174*: 563-573.

305. Sun, Z., Guo, Y., Li, B., Tan, T., and Zhao, Y. (2019a). ZnO/carbon nanotube/reduced graphene oxide composite film as an effective interlayer for lithium/sulfur batteries. *Solid State Sciences, 95*: 105924.

306. Sun, Z., Wang, T., Zhang, Y., Kempa, K., and Wang, X. (2019c). Boosting the electrochemical performance of lithium/sulfur batteries with the carbon nanotube/Fe3O4 coated by carbon modified separator. *Electrochimica Acta, 327*: 134843.

307. Suriyakumar, S., Kanagaraj, M., Kathiresan, M., Angulakshmi, N., Thomas, S., and Stephan, A. M. (2018). Metal-organic frameworks based membrane as a permselective separator for lithium-sulfur batteries. *Electrochimica Acta, 265*: 151-159.

308. Tan, L., Li, X., Wang, Z., Guo, H., Wang, J., and An, L. (2018). Multifunctional Separator with Porous Carbon/Multi-Walled Carbon Nanotube Coating for Advanced Lithium−Sulfur Batteries. *ChemElectroChem, 5*(1): 71-77.

309. Tang, P., Zhao, Y., Xu, C., and Ni, K. (2013). Enhanced energy density of asymmetric supercapacitors via optimizing negative electrode material and mass ratio of negative/positive electrodes. *Journal of Solid State Electrochemistry, 17*(6): 1701-1710.

310. Tomaszewska, A., Chu, Z., Feng, X., O'Kane, S., Liu, X., Chen, J., Ji, C., Endler, E., Li, R., Liu, L., Li, Y., Zheng, S., Vetterlein, S., Gao, M., Du, J., Parkes, M., Ouyang, M., Marinescu, M., Offer, G., and Wu, B. (2019). Lithium-ion battery fast charging: A review. *eTransportation, 1*: 100011.

311. Ulaganathan, M., Aravindan, V., Ling, W. C., Yan, Q., and Madhavi, S. (2016). High energy Li-ion capacitors with conversion type Mn3O4 particulates anchored to few layer graphene as the negative electrode. *Journal of Materials Chemistry A, 4*(39): 15134-15139.

312. Wang, D., Zhang, Z., Hong, B., and Lai, Y. (2019d). Self-sacrificial organic lithium salt enhanced initial Coulombic efficiency for safer and greener lithium-ion batteries. *Chemical Communications, 55*(72): 10737-10739.

313. Wang, G., Liu, Z. Y., Wu, J. N., and Lu, Q. (2012b). Preparation and electrochemical capacitance behavior of TiO2-B nanotubes for hybrid supercapacitor. *Materials Letters, 71*: 120-122.

314. Wang, H., Guan, C., Wang, X., and Fan, H. J. (2015a). A High Energy and Power Li-Ion Capacitor Based on a TiO2 Nanobelt Array Anode and a Graphene Hydrogel Cathode. *Small, 11*(12): 1470-1477.

315. Wang, J., Polleux, J., Lim, J., and Dunn, B. (2007). Pseudocapacitive Contributions to Electrochemical Energy Storage in TiO2 (Anatase) Nanoparticles. *The Journal of Physical Chemistry C, 111*(40): 14925-14931.

316. Wang, J., Yamada, Y., Sodeyama, K., Chiang, C. H., Tateyama, Y., and Yamada, A. (2016d). Superconcentrated electrolytes for a high-voltage lithium-ion battery. *Nature Communications, 7*(1): 12032.

317. Wang, J., Yang, J., Xie, J., and Xu, N. (2002). A Novel Conductive Polymer–Sulfur Composite Cathode Material for Rechargeable Lithium Batteries. *Advanced Materials, 14*(13-14): 963-965.

318. Wang, J., Yin, L., Jia, H., Yu, H., He, Y.-S., Yang, J., and Monroe, C. (2014b). Hierarchical Sulfur-Based Cathode Materials with Long Cycle Life for Rechargeable Lithium Batteries. *ChemSusChem, 7*.

319. Wang, L., Liu, J., Yuan, S., Wang, Y., and Xia, Y. (2016c). To mitigate self-discharge of lithium–sulfur batteries by optimizing ionic liquid electrolytes. *Energy & Environmental Science, 9*(1): 224-231.

320. Wang, P., Wang, R., Lang, J., Zhang, X., Chen, Z., and Yan, X. (2016b). Porous niobium nitride as a capacitive anode material for advanced Li-ion hybrid capacitors with superior cycling stability. *Journal of Materials Chemistry A, 4*(25): 9760-9766.

321. Wang, P., Zhang, Z., Hong, B., Zhang, K., Li, J., and Lai, Y. (2019c). Multifunctional porous VN nanowires interlayer as polysulfides barrier for high performance lithium sulfur batteries. *Journal of Electroanalytical Chemistry, 832*: 475-479.

322. Wang, Q., Wen, Z. H., and Li, J. H. (2006). A Hybrid Supercapacitor Fabricated with a Carbon Nanotube Cathode and a TiO2–B Nanowire Anode. *Advanced Functional Materials, 16*(16): 2141-2146.

323. Wang, R., Lang, J., Zhang, P., Lin, Z., and Yan, X. (2015b). Fast and Large Lithium Storage in 3D Porous VN Nanowires–Graphene Composite as a Superior Anode Toward High-Performance Hybrid Supercapacitors. *Advanced Functional Materials, 25*(15): 2270-2278.

324. Wang, X., Li, G., Tjandra, R., Fan, X., Xiao, X., and Yu, A. (2015c). Fast lithium-ion storage of Nb2O5 nanocrystals in situ grown on carbon nanotubes for high-performance asymmetric supercapacitors. *RSC Advances, 5*(51): 41179-41185.

325. Wang, R., Wang, S., Jin, D., Zhang, Y., Cai, Y., Ma, J., and Zhang, L. (2017c). Engineering layer structure of MoS2-graphene composites with robust and fast lithium storage for high-performance Li-ion capacitors. *Energy Storage Materials, 9*: 195-205.

326. Wang, R., Zhao, Q., Zheng, W., Ren, Z., Hu, X., Li, J., Lu, L., Hu, N., Molenda, J., Liu, X., and Xu, C. (2019e). Achieving high energy density in a 4.5 V all nitrogen-doped graphene based lithium-ion capacitor. *Journal of Materials Chemistry A, 7*(34): 19909-19921.

327. Wang, X., Liu, L., and Niu, Z. (2019b). Carbon-based materials for lithium-ion capacitors. *Materials Chemistry Frontiers, 3*(7): 1265-1279.

328. Wang, X., and Shen, G. (2015d). Intercalation pseudo-capacitive TiNb2O7@carbon electrode for high-performance lithium ion hybrid electrochemical supercapacitors with ultrahigh energy density. *Nano Energy, 15*: 104-115.

329. Wang, X., Wang, Z., Zhang, X., Peng, H., Xin, G., Lu, C., Zhong, Y., Wang, G., and Zhang, Y. (2017a). Nitrogen-Doped Defective Graphene Aerogel as Anode for all Graphene-Based Lithium Ion Capacitor. *ChemistrySelect, 2*(27): 8436-8445.

330. Wang, Y., Hong, Z., Wei, M., and Xia, Y. (2012a). Layered H2Ti6O13-Nanowires: A New Promising Pseudocapacitive Material in Non-Aqueous Electrolyte. *Advanced Functional Materials, 22*(24): 5185-5193.

331. Wang, Y., Song, Y., and Xia, Y. (2016a). Electrochemical capacitors: mechanism, materials, systems, characterization and applications. *Chemical Society Reviews, 45*(21): 5925-5950.

332. Wang, K., Wang, N., He, J., Yang, Z., Shen, X., and Huang, C. (2017b). Graphdiyne Nanowalls as Anode for Lithium−Ion Batteries and Capacitors Exhibit Superior Cyclic Stability. *Electrochimica Acta, 253*: 506-516.

333. Wang, Z., Dong, Y., Li, H., Zhao, Z., Bin Wu, H., Hao, C., Liu, S., Qiu, J., and Lou, X. W. (2014a). Enhancing lithium–sulphur battery performance by strongly binding the discharge products on amino-functionalized reduced graphene oxide. *Nature Communications, 5*(1): 5002.

334. Wang, Z., and Wang, S. (2019a). Synergistic suppression of the shuttle effect and absorption of electrolytes using a functional rich amine porous organic polymer/acetylene black-polypropylene separator in Li-S batteries. *Electrochimica Acta, 306*: 229-237.

335. Wei, H., Ma, J., Li, B., Zuo, Y., and Xia, D. (2014). Enhanced Cycle Performance of Lithium–Sulfur Batteries Using a Separator Modified with a PVDF-C Layer. *ACS Applied Materials & Interfaces, 6*(22): 20276-20281.

336. Weller, C., Pampel, J., Dörfler, S., Althues, H., and Kaskel, S. (2019). Polysulfide Shuttle Suppression by Electrolytes with Low-Density for High-Energy Lithium–Sulfur Batteries. *Energy Technology, 7*(12): 1900625.

337. Wen, Z., and Li, J. (2009). Hierarchically structured carbon nanocomposites as electrode materials for electrochemical energy storage, conversion and biosensor systems. *Journal of Materials Chemistry, 19*(46): 8707-8713.

338. Wild, M., O'Neill, L., Zhang, T., Purkayastha, R., Minton, G., Marinescu, M., and Offer, G. J. (2015). Lithium sulfur batteries, a mechanistic review. *Energy & Environmental Science, 8*(12): 3477-3494.

339. Winter, M., and Brodd, R. J. (2004). What Are Batteries, Fuel Cells, and Supercapacitors? *Chemical Reviews, 104*(10): 4245-4270.

340. Won, J. H., Jeong, H. M., and Kang, J. K. (2017). Synthesis of Nitrogen-Rich Nanotubes with Internal Compartments having Open Mesoporous Channels and Utilization to Hybrid Full-Cell Capacitors Enabling High Energy and

Power Densities over Robust Cycle Life. *Advanced Energy Materials, 7*(1): 1601355.

341. Wu, F., Qian, J., Chen, R., Zhao, T., Xu, R., Ye, Y., Li, W., Li, L., Lu, J., and Amine, K. (2015). Sulfur cathode based on layered carbon matrix for high-performance Li–S batteries. *Nano Energy, 12*: 742-749.

342. Wu, F., and Yushin, G. (2017a). Conversion cathodes for rechargeable lithium and lithium-ion batteries. *Energy & Environmental Science, 10*(2): 435-459.

343. Wu, H., Huang, Y., Zhang, W., Sun, X., Yang, Y., Wang, L., and Zong, M. (2017b). Lock of sulfur with carbon black and a three-dimensional graphene@carbon nanotubes coated separator for lithium-sulfur batteries. *Journal of Alloys and Compounds, 708*: 743-750.

344. Wu, H., Rao, C. V., and Rambabu, B. (2009). Electrochemical performance of LiNi0.5Mn1.5O4 prepared by improved solid state method as cathode in hybrid supercapacitor. *Materials Chemistry and Physics, 116*(2): 532-535.

345. Wu, Z., Li, L., Yan, J.-m., and Zhang, X.-b. (2017c). Materials Design and System Construction for Conventional and New-Concept Supercapacitors. *Advanced Science, 4*(6): 1600382.

346. Xia, H., Xu, Q., and Zhang, J. (2018). Recent Progress on Two-Dimensional Nanoflake Ensembles for Energy Storage Applications. *Nano-micro letters, 10*(4): 66-66.

347. Xia, Q., Yang, H., Wang, M., Yang, M., Guo, Q., Wan, L., Xia, H., and Yu, Y. (2017). High Energy and High Power Lithium-Ion Capacitors Based on Boron and Nitrogen Dual-Doped 3D Carbon Nanofibers as Both Cathode and Anode. *Advanced Energy Materials, 7*(22): 1701336.

348. Xiang, K., Wen, X., Hu, J., Wang, S., and Chen, H. (2019). Rational Fabrication of Nitrogen and Sulfur Codoped Carbon Nanotubes/MoS2 for High-Performance Lithium–Sulfur Batteries. *ChemSusChem, 12*(15): 3602-3614.

349. Xiang, Y., Li, J., Lei, J., Liu, D., Xie, Z., Qu, D., Li, K., Deng, T., and Tang, H. (2016). Advanced Separators for Lithium-Ion and Lithium–Sulfur Batteries: A Review of Recent Progress. *ChemSusChem, 9*(21): 3023-3039.

350. Xiang, Y., Wang, Z., Qiu, W., Guo, Z., Liu, D., Qu, D., Xie, Z., Tang, H., and Li, J. (2018). Interfacing soluble polysulfides with a SnO2 functionalized separator: An efficient approach for improving performance of Li-S battery. *Journal of Membrane Science, 563*: 380-387.

351. Xiao, W., Xin, C., Li, S., Jie, J., Gu, Y., Zheng, J., and Pan, F. (2018). Insight into fast Li diffusion in Li-excess spinel lithium manganese oxide. *Journal of Materials Chemistry A, 6*(21): 9893-9898.

352. Xie, Y., Song, F., Xia, C., and Du, H. (2015). Preparation of carbon-coated lithium iron phosphate/titanium nitride for a lithium-ion supercapacitor. *New Journal of Chemistry, 39*(1): 604-613.

353. Xin, S., Gao, H., Li, Y., and Guo, Y.-G. (2019). Introduction to Electrochemical Energy Storage *Nanostructures and Nanomaterials for Batteries: Principles and Applications* (pp. 1-28). Singapore: Springer Singapore.

354. Xiong, X., Yan, W., You, C., Zhu, Y., Chen, Y., Fu, L., Zhang, Y., Yu, N., and Wu, Y. (2019). Methods to Improve Lithium Metal Anode for Li-S Batteries. *Frontiers in Chemistry, 7*(827).

355. Xiong, Z., Yun, Y. S., and Jin, H.-J. (2013). Applications of Carbon Nanotubes for Lithium Ion Battery Anodes. *Materials (Basel, Switzerland), 6*(3): 1138-1158.

356. Xu, G., Nie, P., Dou, H., Ding, B., Li, L., and Zhang, X. (2017). Exploring metal organic frameworks for energy storage in batteries and supercapacitors. *Materials Today, 20*(4): 191-209.

357. Xu, Q., Hu, G. C., Bi, H. L., and Xiang, H. F. (2015). A trilayer carbon nanotube/Al2O3/polypropylene separator for lithium-sulfur batteries. *Ionics, 21*(4): 981-986.

358. Yamada, Y., Yaegashi, M., Abe, T., and Yamada, A. (2013). A superconcentrated ether electrolyte for fast-charging Li-ion batteries. *Chemical Communications, 49*(95): 11194-11196.

359. Yan, J., Liu, X., and Li, B. (2016). Capacity Fade Analysis of Sulfur Cathodes in Lithium–Sulfur Batteries. *Advanced Science, 3*(12): 1600101.

360. Yang, C.-C., Wu, T.-Y., Chen, H.-R., Hsieh, T.-H., Ho, K.-S., and Kuo, C.-W. (2011). Platinum Particles Embedded into Nanowires of Polyaniline Doped With Poly(Acrylic Acid-co-Maleic Acid) as Electrocatalyst for Methanol Oxidation. *International Journal of Electrochemical Science, 6*.

361. Yang, K., Zhong, L., Mo, Y., Wen, R., Xiao, M., Han, D., Wang, S., and Meng, Y. (2018a). A Functional Separator Coated with Sulfonated Poly(Styrene-ethylene-butylene-styrene) to Synergistically Enhance the Electrochemical Performance and Anti-Self-Discharge Behavior of Li–S Batteries. *ACS Applied Energy Materials, 1*(6): 2555-2564.

362. Yang, M., Zhong, Y., Ren, J., Xianlong, Z., Wei, J., and Zhou, Z. (2015). Fabrication of High-Power Li-Ion Hybrid Supercapacitors by Enhancing the Exterior Surface Charge Storage. *Advanced Energy Materials, 5*: 1500550.

363. Yang, X., Qian, X., Jin, L., Yao, S., Rao, D., Shen, X., Wang, L., and Tan, J. (2018b). Separator modified with Ketjenblack-In2O3 nanoparticles for long cycle-life lithium-sulfur batteries. *Journal of Solid State Electrochemistry, 23*.

364. Yang, Y., Wang, S., Zhang, L., Deng, Y., Xu, H., Qin, X., and Chen, G. (2019). CoS-interposed and Ketjen black-embedded carbon nanofiber framework as a separator modulation for high performance Li-S batteries. *Chemical Engineering Journal, 369*: 77-86.

365. Yao, H., Yan, K., Li, W., Zheng, G., Kong, D., Seh, Z. W., Narasimhan, V. K., Liang, Z., and Cui, Y. (2014). Improved lithium–sulfur batteries with a conductive coating on the separator to prevent the accumulation of inactive S-related species at the cathode–separator interface. *Energy & Environmental Science, 7*(10): 3381-3390.

366. Yi, R., Chen, S., Song, J., Gordin, M. L., Manivannan, A., and Wang, D. (2014). High-Performance Hybrid Supercapacitor Enabled by a High-Rate Si-based Anode. *Advanced Functional Materials, 24*(47): 7433-7439.

367. Yim, T., Han, S. H., Park, N. H., Park, M.-S., Lee, J. H., Shin, J., Choi, J. W., Jung, Y., Jo, Y. N., Yu, J.-S., and Kim, K. J. (2016). Effective Polysulfide Rejection by Dipole-Aligned BaTiO3 Coated Separator in Lithium–Sulfur Batteries. *Advanced Functional Materials, 26*(43): 7817-7823.

368. Yin, L.-C., Liang, J., Zhou, G.-M., Li, F., Saito, R., and Cheng, H.-M. (2016). Understanding the interactions between lithium polysulfides and N-doped graphene using density functional theory calculations. *Nano Energy, 25*: 203-210.

369. Yoo, H. D., Markevich, E., Salitra, G., Sharon, D., and Aurbach, D. (2014). On the challenge of developing advanced technologies for electrochemical energy storage and conversion. *Materials Today, 17*(3): 110-121.

370. Yu, P., Cao, G., Yi, S., Zhang, X., Li, C., Sun, X., Wang, K., and Ma, Y. (2018b). Binder-free 2D titanium carbide (MXene)/carbon nanotube composites for high-performance lithium-ion capacitors. *Nanoscale, 10*(13): 5906-5913.

371. Yu, S.-H., Feng, X., Zhang, N., Seok, J., and Abruña, H. D. (2018a). Understanding Conversion-Type Electrodes for Lithium Rechargeable Batteries. *Accounts of Chemical Research, 51*(2): 273-281.

372. Yu, X., Joseph, J., and Manthiram, A. (2015). Polymer lithium–sulfur batteries with a Nafion membrane and an advanced sulfur electrode. *Journal of Materials Chemistry A, 3*(30): 15683-15691.

373. Yuan, X., Wu, L., He, X., Zeinu, K., Huang, L., Zhu, X., Hou, H., Liu, B., Hu, J., and Yang, J. (2017). Separator modified with N,S co-doped mesoporous carbon using egg shell as template for high performance lithium-sulfur batteries. *Chemical Engineering Journal, 320*: 178-188.

374. Zeng, F., Jin, Z., Yuan, K., Liu, S., Cheng, X., Wang, A., Wang, W., and Yang, Y.-s. (2016). High performance lithium–sulfur batteries with a permselective

sulfonated acetylene black modified separator. *Journal of Materials Chemistry A, 4*(31): 12319-12327.

375. Zhang, H., Li, C., Piszcz, M., Coya, E., Rojo, T., Rodriguez-Martinez, L. M., Armand, M., and Zhou, Z. (2017c). Single lithium-ion conducting solid polymer electrolytes: advances and perspectives. *Chemical Society Reviews, 46*(3): 797-815.

376. Zhang, H., Zhao, H., Khan, M. A., Zou, W., Xu, J., Zhang, L., and Zhang, J. (2018c). Recent progress in advanced electrode materials, separators and electrolytes for lithium batteries. *Journal of Materials Chemistry A, 6*(42): 20564-20620.

377. Zhang, H., Zhou, M.-Y., Lin, C.-E., and Zhu, B.-K. (2015c). Progress in polymeric separators for lithium ion batteries. *RSC Advances, 5*(109): 89848-89860.

378. Zhang, L., Wan, F., Wang, X., Cao, H., Dai, X., Niu, Z., Wang, Y., and Chen, J. (2018a). Dual-Functional Graphene Carbon as Polysulfide Trapper for High-Performance Lithium Sulfur Batteries. *ACS Applied Materials & Interfaces, 10*(6): 5594-5602.

379. Zhang, L., Wang, Y., Niu, Z., and Chen, J. (2019a). Advanced nanostructured carbon-based materials for rechargeable lithium-sulfur batteries. *Carbon, 141*: 400-416.

380. Zhang, L. L., and Zhao, X. S. (2009). Carbon-based materials as supercapacitor electrodes. *Chemical Society Reviews, 38*(9): 2520-2531.

381. Zhang, R., Palumbo, A., Kim, J. C., Ding, J., and Yang, E.-H. (2019b). Flexible Graphene-, Graphene-Oxide-, and Carbon-Nanotube-Based Supercapacitors and Batteries. *Annalen der Physik, 531*(10): 1800507.

382. Zhang, S. (2013). Liquid electrolyte lithium/sulfur battery: Fundamental chemistry, problems, and solutions. *Journal of Power Sources, 231*: 153-162.

383. Zhang, S., Li, C., Zhang, X., Sun, X., Wang, K., and Ma, Y. (2017b). High Performance Lithium-Ion Hybrid Capacitors Employing Fe3O4–Graphene Composite Anode and Activated Carbon Cathode. *ACS Applied Materials & Interfaces, 9*(20): 17136-17144.

384. Zhang, X., Lu, C., Peng, H., Wang, X., Zhang, Y., Wang, Z., Zhong, Y., and Wang, G. (2017c). Influence of sintering temperature and graphene additives on the electrochemical performance of porous Li4Ti5O12 anode for lithium ion capacitor. *Electrochimica Acta, 246*: 1237-1247.

385. Zhang, Z., Lai, Y., Zhang, Z., Zhang, K., and Li, J. (2014). Al2O3-coated porous separator for enhanced electrochemical performance of lithium sulfur batteries. *Electrochimica Acta, 129*: 55-61.

386. Zhang, Z., Wang, G., Lai, Y., Li, J., Zhang, Z., and Chen, W. (2015a). Nitrogen-doped porous hollow carbon sphere-decorated separators for advanced lithium–sulfur batteries. *Journal of Power Sources, 300*: 157-163.

387. Zhang, Z., Zhang, Z., Li, J., and Lai, Y. (2015b). Polydopamine-coated separator for high-performance lithium-sulfur batteries. *Journal of Solid State Electrochemistry, 19*(6): 1709-1715.

388. Zhao, D., Qian, X., Jin, L., Yang, X., Wang, S., Shen, X., Yao, S., Rao, D., Zhou, Y., and Xi, X. (2016). Separator modified by Ketjen black for enhanced electrochemical performance of lithium–sulfur batteries. *RSC Advances, 6*(17): 13680-13685.

389. Zhao, J., Wang, L., He, X., Wan, C., and Jiang, C. (2008). Determination of Lithium-Ion Transference Numbers in LiPF6–PC Solutions Based on Electrochemical Polarization and NMR Measurements. *Journal of The Electrochemical Society, 155*(4): A292-A296.

390. Zhao, M., Li, B.-Q., Peng, H.-J., Yuan, H., Wei, J.-Y., and Huang, J.-Q. (2020). Challenges and Opportunities towards Practical Lithium–Sulfur Batteries under Lean Electrolyte Conditions. *Angewandte Chemie, Accepted Author Manuscript. doi:10.1002/ange.201909339*.

391. Zhao, Q., Zhu, Q., Miao, J., Zhang, P., and Xu, B. (2019). 2D MXene nanosheets enable small-sulfur electrodes to be flexible for lithium–sulfur batteries. *Nanoscale, 11*(17): 8442-8448.

392. Zhao, X., Johnston, C., and Grant, P. S. (2009). A novel hybrid supercapacitor with a carbon nanotube cathode and an iron oxide/carbon nanotube composite anode. *Journal of Materials Chemistry, 19*(46): 8755-8760.

393. Zheng, J., Zhang, Y., Wang, N., Zhao, Y., Tian, F., and Meng, C. (2016). Facile synthesis and characterization of LiV3O8 with sheet-like morphology for high-performance supercapacitors. *Materials Letters, 171*: 240-243.

394. Zhong, C., Deng, Y., Hu, W., Qiao, J., Zhang, L., and Zhang, J. (2015). A review of electrolyte materials and compositions for electrochemical supercapacitors. *Chemical Society Reviews, 44*(21): 7484-7539.

395. Zhou, G., Pei, S., Li, L., Wang, D.-W., Wang, S., Huang, K., Yin, L.-C., Li, F., and Cheng, H.-M. (2014). A Graphene–Pure-Sulfur Sandwich Structure for Ultrafast, Long-Life Lithium–Sulfur Batteries. *Advanced Materials, 26*(4): 625-631.

396. Zhou, J., Guo, Y., Liang, C., Cao, L., Pan, H., Yang, J., and Wang, J. (2018). A new ether-based electrolyte for lithium sulfur batteries using a S@pPAN cathode. *Chemical Communications, 54*(43): 5478-5481.

397. Zhou, J., Zhao, H., Mu, X., Chen, J., Zhang, P., Wang, Y., He, Y., Zhang, Z., Pan, X., and Xie, E. (2015). Importance of polypyrrole in constructing 3D

hierarchical carbon nanotube@MnO2 perfect core–shell nanostructures for high-performance flexible supercapacitors. *Nanoscale, 7*(35): 14697-14706.

398. Zhou, W., and Greer, H. F. (2016). What Can Electron Microscopy Tell Us Beyond Crystal Structures? *European Journal of Inorganic Chemistry, 2016*(7): 941-950.

399. Zhou, X., Liao, Q., Tang, J., Bai, T., Chen, F., and Yang, J. (2016). A high-level N-doped porous carbon nanowire modified separator for long-life lithium–sulfur batteries. *Journal of Electroanalytical Chemistry, 768*: 55-61.

400. Zhou, X., Luo, X., Wang, H., Yang, J., Xu, H., Jia, M., and Tang, J. (2019). Reduced graphene oxide@CoSe2 interlayer as anchor of polysulfides for high properties of lithium–sulfur battery. *Journal of Materials Science, 54*(13): 9622-9631.

401. Zhu, J., Chen, C., Lu, Y., Zang, J., Jiang, M., Kim, D., and Zhang, X. (2016b). Highly porous polyacrylonitrile/graphene oxide membrane separator exhibiting excellent anti-self-discharge feature for high-performance lithium–sulfur batteries. *Carbon, 101*: 272-280.

402. Zhu, J., Ge, Y., Kim, D., Lu, Y., Chen, C., Jiang, M., and Zhang, X. (2016a). A novel separator coated by carbon for achieving exceptional high performance lithium-sulfur batteries. *Nano Energy, 20*: 176-184.

403. Zhu, J., Zhu, P., Yan, C., Dong, X., and Zhang, X. (2019a). Recent progress in polymer materials for advanced lithium-sulfur batteries. *Progress in Polymer Science, 90*: 118-163.

404. Zhu, K., Wang, C., Chi, Z., Ke, F., Yang, Y., Wang, A., Wang, W., and Miao, L. (2019b). How Far Away Are Lithium-Sulfur Batteries From Commercialization? *Frontiers in Energy Research, 7*(123).

405. Zhu, P., Zhu, J., Zang, J., Chen, C., Lu, Y., Jiang, M., Yan, C., Dirican, M., Kalai Selvan, R., and Zhang, X. (2017). A novel bi-functional double-layer rGO–PVDF/PVDF composite nanofiber membrane separator with enhanced thermal stability and effective polysulfide inhibition for high-performance lithium–sulfur batteries. *Journal of Materials Chemistry A, 5*(29): 15096-15104.

406. Zhu, Y., Xiao, S., Shi, Y., Yang, Y., and Wu, Y. (2013). A trilayer poly(vinylidene fluoride)/polyborate/poly(vinylidene fluoride) gel polymer electrolyte with good performance for lithium ion batteries. *Journal of Materials Chemistry A, 1*(26): 7790-7797.

407. Zhuang, T.-Z., Huang, J.-Q., Peng, H.-J., He, L.-Y., Cheng, X.-B., Chen, C.-M., and Zhang, Q. (2016). Rational Integration of Polypropylene/Graphene Oxide/Nafion as Ternary-Layered Separator to Retard the Shuttle of Polysulfides for Lithium–Sulfur Batteries. *Small, 12*(3): 381-389.

408. Zukalová, M., Kalbáč, M., Kavan, L., Exnar, I., and Graetzel, M. (2005). Pseudocapacitive Lithium Storage in TiO2(B). *Chemistry of Materials, 17*(5): 1248-1255.

409. Zuo, W., Li, R., Zhou, C., Li, Y., Xia, J., and Liu, J. (2017). Battery-Supercapacitor Hybrid Devices: Recent Progress and Future Prospects. *Advanced Science, 4*(7): 1600539.

LIST OF PUBLICATIONS BASED ON THE THESIS

Related to Thesis

1. Haritha, H., Reshma, C., and Mary Gladis, J. (2018). Effect of crystallite size on the intercalation pseudocapacitance of lithium nickel vanadate in aqueous electrolyte. *Journal of Solid State Electrochemistry, 22*(1): 1-9.

2. Haritha, H., Reshma, C., and Mary Gladis, J. (2018). Micro- and Nanocrystalline Inverse Spinel $LiCoVO_4$ for Intercalation Pseudocapacitive Li^+ Storage with Ultrahigh Energy Density and Long-Term Cycling. *ACS Applied Energy Materials, 1*(2): 393-401.

3. Haritha, H., Reshma, C., and Mary Gladis, J., Shruti, S., and Stephan, A. M. (2019). Sulfonic groups stemmed ionic shield for polysulfides towards high performance Li–S batteries. *Electrochimica Acta, 321*: 134697.

4. Haritha, H., Reshma, C., and Mary Gladis, J. Ion-selective PEDOT:PSS decorated separator as a potential polysulfide immobilizer for lithium-sulfur batteries (*Under review in New J. Chem*.)

5. Haritha, H., Reshma, C., and Mary Gladis, J. Nanoscale $LiMnVO_4$ as an intercalation-type anode for high-energy lithium-ion capacitors (*Manuscript under preparation*).

6. Haritha, H., Reshma, C., and Mary Gladis, J. Inhibiting the shuttle effect in lithium-sulfur batteries using a carboxylate anchored permselective separator. (*Manuscript under preparation*).

Other Publications

7. Reshma, C., Haritha, H., Raja, M., Mary Gladis, J., and Stephan, A. M. (2017). Enhanced cyclability using a polyindole modified cathode material for lithium sulphur batteries. *Sustainable Energy & Fuels, 1*(8): 1774-1781.

8. Reshma, C., Haritha, H., Raja, M., Mary Gladis, J., and Stephan, A. M. (2017). Sulfur-Immobilized Nitrogen and Oxygen Co-Doped Hierarchically Porous Biomass Carbon for Lithium-Sulfur Batteries: Influence of Sulfur Content and Distribution on Its Performance. *ChemistrySelect*, 2: 10484–10495.

9. Reshma, C., Haritha, H., and Mary Gladis, J. (2019). Hierarchical Porous Carbon Material with Multifunctionalities Derived from Honeycomb as a Sulfur Host and Laminate on the Cathode for High-Performance Lithium–Sulfur Batteries. *ACS Sustainable Chemistry & Engineering, 7*(24): 19344-19355.

10. Reshma, C., Haritha, H., Mary Gladis, J. (2020). Template free one pot synthesis of heteroatom doped porous Carbon Electrodes for High performance symmetric supercapacitor. *Electrochimica Acta* 337:135698.

Scientific Article

- Haritha, H., and Mary Gladis, J., Metal Oxides for Supercapattery-An Emerging Electrochemical Energy Storage Technology, IIM METNEWS, Vol.36, No.1, July 2018.

PRESENTATIONS IN CONFERENCES/SEMINARS

Oral Presentations

1. Haritha, H., and Mary Gladis, J. Synthesis and electrochemical properties of $LiNiVO_4$ for supercapacitor applications, ICAFM 2017, organized by Central university of Tamil Nadu & Anna University, Chennai from January 6-8 2017.

2. Haritha, H., and Mary Gladis, J. High Energy Intercalation Pseudocapacitive Electrode Materials for Supercapattery, Materials Research Society of India Trivandrum Chapter - Annual Technical Meeting, IISER Thiruvananthapuram, 24 March 2018.

3. Haritha, H., and Mary Gladis, J. Ionic Shield for Polysulfides Towards High-Performance Lithium-Sulfur Battery, Indian Institute of Metals Trivandrum Chapter - Research Scholars Symposium on Materials Science and Engineering, CSIR-NIIST Thiruvananthapuram, 6 April 2018. ***(Best Presentation Award)***

4. Haritha, H., and Mary Gladis, J. Polyelectrolyte Decorated Separator to Prolong Lithium-Sulfur battery life, National Conference on Emerging Trends in Science, Technology & Application of Electron Microscope (STAEM 2018), CSIR-NIIST Thiruvananthapuram, 19-21 December 2018. ***(Best Presentation Award)***

5. Haritha, H., Sreekala, K., and Mary Gladis, J. Modified separator performing dual functions to inhibit the shuttle of polysulfides for lithium-sulfur batteries, 12th International Symposium on Advances in Electrochemical Science and Technology (iSAEST-12), Hotel Trident, Chennai, 8-10 January 2019. ***(Best Paper Award)***

Poster Presentations

6. Haritha, H., and Mary Gladis, J. High-energy asymmetric supercapacitors based on Li^+ intercalation into a nanocrystalline inverse spinel $LiCoVO_4$, Bengaluru INDIA NANO, organized by JNCASR & Govt. of Karnataka, Bengaluru from December 7-8 2017.

7. Haritha, H., and Mary Gladis, J. Inverse spinel nanocrystalline $LiCoVO_4$ with ultrahigh energy density as Li^+ intercalation pseudocapacitor material, ADMAT SkyMat 2017, organized by ASM India National Council, IIM, MRSI, SAME, NIAS, INAE with the active support of ISRO, Trivandrum from December 14-16 2017.

8. Haritha, H., and Mary Gladis, J. Functional Separator as an Effective Ionic Shield for Polysulfides Towards High Performance Li-S Batteries, International Conference on Recent Trends in Materials Science & Technology (ICMST 2018), Thiruvananthapuram, 10-13 October 2018.

9. Haritha, H., and Mary Gladis, J. Bifunctional Separator as a highly efficient polysulfide mediator for Li-S batteries, International Conference on Advanced Materials and Manufacturing Processes for Strategic Sectors (ICAMPS 2018), Thiruvananthapuram, 25-27 October 2018. ***(Best Poster Award)***

10. Haritha, H., and Mary Gladis, J. High performance supercapacitors based on nanocrystalline inverse spinel $LiCoVO_4$, International Symposium on Solid State Chemistry of Transition Metal Oxides, JNCASR Bengaluru, November 30 - December 01, 2018.

11. Haritha, H., and Mary Gladis, J. Inhibiting Polysulfide Shuttling with a Polyelectrolyte Decorated Separator for High Performance Li-S Batteries, International Winter School on Frontiers in Materials Science 2018, JNCASR Bengaluru, 3-7 December 2018.

12. Haritha, H., and Mary Gladis, J. Ion-selective PEDOT:PSS coated functional separator for effective suppression of polysulfide shuttle effect in lithium-sulfur batteries, National Conference on Materials Science And Technology (NCMST-2019), IIST Thiruvananthapuram, 18-20 December 2019.

13. Haritha, H., and Mary Gladis, J. Inhibiting the shuttle effect in lithium-sulfur batteries using a carboxylate anchored permselective separator, National Convention of Electrochemists (NCE-21), VIT Chennai Campus, Chennai, 30-31 January 2020.